Ultrasonic Viewing of Structures and Components for Immersion Applications

By

EAGLEKUMAR G. TARPARA

ENGG 01201404023

Bhabha Atomic Research Centre, Mumbai

A thesis submitted to the

Board of Studies in Engineering Sciences

In partial fulfillment of requirements
for the Degree of

DOCTOR OF PHILOSOPHY
of
HOMI BHABHA NATIONAL INSTITUTE

January, 2020

Homi Bhabha National Institute[1]

Recommendations of the Viva Voce Committee

As members of the Viva Voce Committee, we certify that we have read the dissertation prepared by Eaglekumar G. Tarpara entitled "Ultrasonic Viewing of Structures and Components for Immersion Applications" and recommend that it may be accepted as fulfilling the thesis requirement for the award of Degree of Doctor of Philosophy.

Chairman – Dr. A .P. Tiwari	24.1.2020
Guide / Convener - Dr. V. H. Patankar	V.H. Patan 24-01.2020
Co-guide - —	—
Examiner - Dr. M. R. Bhat	24/01/2020
Member 1- Dr. A. K. Bhattacharjee	AKBhattacharjee 24/01/2020
Member 2- Dr. S. Kar	SKar 24/01/2020
Technology Advisor- Dr. Kallol Roy	Kallol Roy 24/01/20

Final approval and acceptance of this thesis is contingent upon the candidate's submission of the final copies of the thesis to HBNI.

I/We hereby certify that I/we have read this thesis prepared under my/our direction and recommend that it may be accepted as fulfilling the thesis requirement.

Date: 24.01.2020

Place: Mumbai-94

—

Signature

Co-guide (if any)

V.H. Patankar

Signature

Guide

Dr. V. H. PATANKAR

[1] This page is to be included only for final submission after successful completion of viva voce.

STATEMENT BY AUTHOR

Eaglekumar G. Tarpara
ENGG 01201404023

DECLARATION

I, hereby declare that the investigation presented in the thesis has been carried out by me. The work is original and has not been submitted earlier as a whole or in part for a degree / diploma at this or any other Institution / University.

Eaglekumar G. Tarpara
ENGG 01201404023
Email: eagle252525@gmail.com

List of Publications arising from the thesis

Journals (Published)

1. Eaglekumar G. Tarpara, V.H. Patankar, "Reconfigurable Hardware Implementation of Coherent Averaging Technique for Ultrasonic NDT Instruments", Accepted in *Ultrasonics*, 2019. (Accepted, I.F.=2.59, *Elsevier*)

2. Eaglekumar G. Tarpara, V.H. Patankar, Harshit Jain, N. Pavan Kumar "Ultrasonic Camera: A Matrix-based Real-time Ultrasonic Imaging System for Immersion Applications ", *Journal of Instrumentation*, vol. 14, no. 11, pp. 11033, 2019. (I.F.=1.36, *IOPscience*)

3. Eaglekumar G. Tarpara, V.H. Patankar, "Design and Development of Reconfigurable Embedded System for Real-time Acquisition and Processing of Multichannel Ultrasonic Signals", *IET Science, Measurement and Technology*, vol. 13, no. 7, pp. 1048-1058, 2019. (I.F.=1.89, *IET*)

4. Eaglekumar G. Tarpara, V.H. Patankar, "Real time implementation of empirical mode decomposition algorithm for ultrasonic nondestructive testing applications", *Review of Scientific Instruments* , vol. 89, no. 12, pp.125118, 2018. (I.F=1.58, *AIP*)

5. Eaglekumar G. Tarpara, V.H. Patankar, "Lossless and lossy modeling of ultrasonic imaging system for immersion applications: Simulation and experimentation", *Computers & Electrical Engineering*, vol. 71, pp. 251 - 264, 2018. (I.F.=2.18, *Elsevier*)

Journals (Under Review)

1. Eaglekumar G. Tarpara, V.H. Patankar "Real-time Imaging of Immersed Fuel-Sub Assemblies using Multi-channel Ultrasonic Camera ", submitted to *Review of Scientific Instrumentation*, on November 18, 2019.

Technical Report

1. Eaglekumar G. Tarpara, V.H. Patankar and N. Vijayan Varier, "Under Sodium Ultrasonic Viewing for Fast Breeder Reactors: A Review", *INIS Report, IAEA Geneva*, BARC/2016/E/014, October, 2016.

Conferences

1. Eaglekumar G. Tarpara, V.H. Patankar and N. Vijayan Varier, "Design and Development of Matrix based Ultrasonic Imaging Instrumentation for Immersion Applications ", 15^{th} *Asia Pacific Conference for Non-Destructive Testing APCNDT 2017*, Singapore, 13-17 Nov., 2017. (Oral presentation)

2. Eaglekumar G. Tarpara and V. H. Patankar, "Design and development of high voltage ultrasonic spike pulser for immersion applications", *2017 IEEE International Conference on Intelligent Computing, Instrumentation and Control Technologies (ICICICT)*, pp. 640-645, Kannur, 2017. (Oral presentation) (**This paper received Best Paper award**)

3. Patankar V. H., Eaglekumar Tarpara and N. Vijayan Varier, "Perspective on Under-Sodium Ultrasonic Instrumentation Systems for In-Service-Inspection of SFRs", *DAE-VIE 2016 Symposium on Emerging Trends on I&C and Computer Systems*, IGCAR, Kalpakkam, 23-24 June, 2016. (Oral presentation)

4. Patankar V. H., Eaglekumar Tarpara, "Advances in Ultrasonic Instrumentation for Core-mapping of Fast Breeder Reactors", *Proceedings of NDE 2015 Seminar*, Hyderabad, 26-28 Nov., 2015. (Oral presentation)

Eaglekumar G. Tarpara
ENGG 01201404023

Acknowledgements

First and foremost, I would like to express my deep and sincere gratitude to my guide, Prof. V. H. Patankar, Electronics Division, BARC for formulating this research topic and for the guidance and encouragement to work to the best of my abilities. His knowledge, insightfulness and consistent care for the best output have been great assets without which this research would not have been possible. He willingly took the pain, shouldered the responsibility of providing me guidance despite the day-to-day office activities and encouraged me to pursue my research interests.

I would like to thank my technical advisor Dr. Kallol Roy, Chairman & Managing Director, BHAVINI for his keen interest, constructive suggestion, valuable guidance, constant encouragement, and motivation throughout my entire research tenure. I am extremely thankful to Shri. Vijayan Varier. Ex-Head TC&QCD, IGCAR, Mumbai for his invaluable suggestions emanating from several discussions and his able guidance have finally ensured that this research work sees the light of the day.

I am indebted to the doctoral committee-V chairman Prof. A. P. Tiwari and other members of the doctoral committee Prof. A. K. Bhattacharjee and Prof. S. Kar for their critical evaluation of my research activities, sincere review, suggestions and kind cooperation during the review presentations, oral general comprehensive examination and pre-synopsis viva-voce.

It gives me great pleasure in acknowledging the help and support of Shri M. M. Kuswarkar and Mrs. Asha Jadhav of ED, BARC, regarding the assemblies of PCBs and the making of various types of cables for my research work. I also thank to Shri. L. V. Murali Krishna, Shri. Sanjay Patil and other staff of the ED workshop for the designing and manufacturing of mechanical assemblies and fixtures for my thesis work. I am also thankful to Shri. K. V. Panchal and Shri. Dinesh Kushwaha of drawing office, ED, BARC for support to prepare Engg. drawings of mechanical fixtures.

I express my sincere gratitude to my reviewers Prof. Anthony Croxford, University of Bristol, UK and Prof. M. R. Bhat, IISc Banglore for their timely review and valuable suggestions for further improvement of the thesis.

I am extremely grateful to my father Shri. Girdharbhai Tarpara, my mother Smt. Induben Tarpara and my younger brother Pratik Tarpara for their encouragement and support throughout the entire tenure of my education. Last but not least, I am grateful to my wife Smt. Ankita Desai and all Tarpara and Desai family members for their moral support and blessings.

Eaglekumar G. Tarpara

Abstract

Ultrasonic inspection is one of the most widely used Non-Destructive Testing (NDT) techniques suitable for quality assessment, identification, detection, and characterization of flaws in metallic structures. The manual or contact inspection technique is not beneficial to acquire information of the entire volume of the component under test. It is difficult to utilize manual scanning for the ultrasonic flaw detection due to instability of acoustic coupling with material and lack of positional accuracy and scanning positions. Though, this will be possible by immersion technique and particular by B-Scan or C-Scan automated imaging method to conduct precision scanning of the entire volume of the specimen. Conventional single-channel and linear array-based multi-channel ultrasonic imaging techniques usually take very long inspection time to investigate entire immersed mechanical structures/components. For immersion-based phased-array imaging, the main issue is that it is difficult to determine the focal index point due to presence of two distinct mediums. Furthermore, it is also not possible to arrange multiple single-element transducers of high frequency in a linear manner for phased-array configurations for the satisfaction of delay-laws. Therefore, phased-array technique is difficult to implement for immersion-based ultrasonic imaging due to the unavailability of phased-array immersion transducers. Particularly if large areas need to be examined, the matrix-based immersion ultrasonic system can improve the speed of inspection and can extend the coverage of the transducer. The main objective of the thesis is to propose a novel real-time matrix-based ultrasonic imaging technique which can enhance the inspection time and provide real-time images of immersed objects. Such immersion-based ultrasonic imaging systems are useful for many industrial applications. One of the major applications is in the nuclear industry, for viewing or core-mapping of liquid sodium submerged Fuel-Sub Assemblies (FSA) located in the core of the fast breeder reactor (FBR) at 200 °C during the Fuel-Handling (FH) campaign when a reactor is in shutdown stage. Throughout the world, ultrasonic imaging systems suitable for FBR are qualified for the water-immersion method and further extended to under-sodium ultrasonic imaging applications.

The model of the immersion-based ultrasonic pulse-echo measurement system involves combined consideration of both mechanical vibrations and non-ideal electrical properties of the ultrasonic transducer and transceiver circuits. Electronic driver circuits required to energize ultrasonic transducer includes non-linear switching devices and semiconductor networks like HV MOSFET, MOSFET driver, HV diodes, damping network, etc. which directly influence the excitation High-Voltage (HV) excitation pulses and received echo signals. The conventional model approach of the ultrasonic pulse-echo system utilizes ideal assumptions of front-end electronics and they do not consider their influences on ultrasonic echo signals. For modeling of a transducer, the Leach-model has been chosen which involves controlled current and controlled voltage sources. Two types of transmission line models have been considered for the modeling of propagation medium: (1) lossless model and (2) lossy/low-loss model. The absorption losses are modeled by the R parameter of the lossy transmission line. The effects of cable length on pulse-echo time-domain waveforms have been calculated at constant temperature and constant frequency. Effects of non-ideal frequency-dependent behaviour of front-end transceiver electronics have been considered in simulation, for practical pulse-echo measurement equipment. Experiments have been conducted by developing a PC based real-time ultrasonic pulse-echo measurement system. The simulation model is validated by comparing both simulated (lossless and lossy) and experimented pulse-echo waveforms in the time domain. The results show that TOF and amplitude of both lossy simulation and experimental results provide very good quantitative agreements in the time domain as well as in the frequency domain.

Noise is a universal limitation that can occur from a variety of sources for sensing applications. Because of temporal incoherence of noise (incoherent noise), repeating the corresponding measurement and averaging it with a previous measurement, provides a reduction in random/incoherence noise i.e. enhancement of Signal to Noise Ratio (SNR). However, averaging of the signal is not advantageous in all conditions. Specifically, sometimes repeating the measurement initiates identical scatterings events inside the material. Since it remains synchronized and consequently repeats similar measurements of both noise and signal, such type of noise is called coherent noise. For that reason, a two-stage noise filtering scheme has been proposed and implemented in the presence of both incoherent noise and coherent noise. The incoherent noise will be filtered by the coherent averaging algorithm (Stage 1) and further, coherent noise will be filtered by the Empirical Mode Decomposition (EMD) algorithm (Stage 2).

A novel reconfigurable hardware architecture has been proposed which utilizes minimum hardware for complete coherent averaging operation. For that purpose, single-port, read-first block-RAM has been implemented in the FPGA platform. The proposed approach reduces the required additional time for summing operations. The summing and division operations need only 1 adder and 1 divisor, respectively. For a conventional coherent averaging scheme, the required number of memory bytes and hardware adders depend upon the number of averages N_{Avg}. For a higher number of averages, it is difficult to manage large memory storage and hardware adders. However, the number of memory storage and adders for the proposed averaging architecture are independent of the number of averages N_{Avg} which allows users to increase the number of averages and hence SNR. The performance of implemented coherent averaging technique has been presented by various applications such as removal of RF random false echoes, smoothing of A-Scan waveforms and speckle removal of B-Scan images.

The ultrasonic echo signal is non-linear and non-stationary. To remove coherent noise from such a signal, the EMD algorithm is adopted for coherent noise filtering, signal analysis and processing in the time domain. The EMD operation needs many iterative calculations and therefore, it cannot be implemented using parallel architecture. Real-time implementation of EMD based filtering scheme has been presented for better visualization and identification of ultrasonic pulse-echo signals. The original signal $x(t)$ is decomposed into small number of Intrinsic Mode Functions (IMFs) ($c_1(t)$, $c_2(t)$,..., $c_n(t)$) and a residue function $r(t)$. The partial reconstruction algorithm has been adopted for EMD reconstruction. The cubic spline tridiagonal matrix is solved by the Thomas algorithm for the intention of real-time processing. The total time complexity functions for both implemented Piece-wise Linear Interpolation (PLI) and Cubic Spline Interpolation (CSI) based EMD method have been computed. The baseline correction and noise filtering applications have been presented using EMD based visual software. The real-time practicability and efficiency of this method were validated through ultrasonic NDT experimentation for improvement in time domain resolution of ultrasonic A-Scan raw data.

A novel hardware-based architecture of a reconfigurable embedded system has been implmneted for a multi-channel ultrasonic immersion-based system. It provides an address-based analog multiplexing scheme that requires only one data acquisition unit and common on-chip storage for the multi-channel imaging system. The hardware also provides a unique channel reconfigurable facility to the user to modify the number of channels, by installing only partial front-end hardware (pulser, pre-amplifier) and without modifying remaining data acquisition hardware (common-amplifier, digitizer) and back-end embedded system. The developed system also supports dynamic on-line reconfiguration of analog front-end hardware, real-time hardware-based data processing and data transfer operation. For experimentation, a complete 4-channel ultrasonic imaging system has been designed, developed and validated using immersion test set-up in the laboratory. The performance evaluation of the developed multi-channel system has been completed by carrying out B-Scan and C-Scan image acquisition of water-immersed mechanical components.

The novel matrix-based real-time ultrasonic imaging, using an ultrasonic camera for immersion application has been proposed and implemented in the thesis. The proposed ultrasonic camera (25-Channels for P-E mode and 50-Channels for T-R mode) provides real-time C-Scan images of mechanical components and the image size is equal to the field of view of the matrix-based transducer assembly. For matrix-based ultrasonic imaging, an address-based analog multiplexing scheme has been implemented in such a way that all channels in the specific row are selected concurrently for transducer excitation, data acquisition, data processing and transferring operation. Similarly, the row-wise operation is performed for the remaining rows sequentially. The developed real-time ultrasonic camera also supports dynamic on-line reconfiguration of analog front-end hardware, real-time hardware/software-based data processing and data transfer operation. For experimentation, an entire matrix-based (5×5) ultrasonic imaging system has been designed, developed and evaluated in the laboratory using immersion test set-up. The performance of the developed matrix-based ultrasonic camera was validated by imaging of FSA top-head of Prototype Fast Breeder Reactor (PFBR) for detection of growth and bowing in under-water, automated test set-up at 70 °C. Imaging results in water can be extended to liquid sodium for ease of testing the real-time 5×5 matrix-based ultrasonic camera for core-mapping of FBR in liquid sodium at 200 °C, during FH operation, at the shut-down stage of the reactor.

Contents

List of Figures

List of Tables

Abbreviations

1-D	**O**ne-**D**imensional
ADC	**A**nalog to **D**igital **C**onverter
AMS	**A**nalog and **M**ixed-**S**ignal
ARM	**A**dvanced **R**ISC **M**achine
BRAM	**B**lock **R**andom **A**ccess **M**emory
BW	**B**ack-**W**all
CMOS	**C**omplementary **M**etal–**O**xide–**S**emiconductor
CMRR	**C**ommon **M**ode **R**ejection **R**atio
CMSE	**C**onsecutive **M**ean **S**quare **E**rror
COR	**C**orrelation co-efficient
CSI	**C**ubic **S**pline **I**nterpolation
DAQ	**D**ata **A**c**Q**uisition
DLL	**D**ynamic **L**ink **L**ibrary
EDF	**E**nvelope **D**etection **F**ilter
EMD	**E**mpirical **M**ode **D**ecomposition
FBH	**F**lat **B**ottom **H**ole
FBR	**F**ast **B**reeder **R**eactor
FFT	**F**ast **F**ourier **T**ransform
FIFO	**F**irst-**I**n **F**irst-**O**ut
FPGA	**F**ield **P**rogrammable **G**ate **A**rray
FSA	**F**uel **S**ub-**A**ssembly
GPIF	**G**eneral **P**urpose **I**nter**F**ace

GPIO	**G**eneral **P**urpose **I**nput/**O**utput
GUI	**G**raphical **U**ser **I**nterface
HV	**H**igh **V**oltage
IF	**I**nter**F**ace
IMF	**I**ntrinsic **M**ode **F**unction
ISE	**I**ntegrated **S**ynthesis **E**nvironment
LUT	**L**ook**U**p **T**able
MOSFET	**M**etal **O**xide **S**emiconductor **F**ield **E**ffect **T**ransistor
MSPS	**M**ega **S**ample **P**er **S**econd
NDE	**N**on-**D**estructive **E**valution
NDT	**N**on-**D**estructive **T**esting
PC	**P**ersonal **C**omputer
PCB	**P**rinted **C**ircuit **B**oard
P-E	**P**ulse-**E**cho
PIV	**P**eak **I**nverse **V**oltage
PLI	**P**iecewise **L**inear **I**nterpolation
PLL	**P**hase-**L**ocked **L**oop
PPI	**P**iecewise **P**olynomial **I**nterpolation
PRT	**P**ulse **R**epetition **T**ime
PRF	**P**ulse **R**epetition **F**requency
PW	**P**ulse **W**idth
PZT	Lead zirconate titanate
RG	**R**adio Guide
SD	**S**tandard **D**eviation
SDH	**S**ide-**D**rilled **H**ole
SNR	**S**ignal to **N**oise **R**atio
SPICE	**S**oftware **P**rocess **I**mprovement and **C**apability d**E**termination
SMD	**S**urface-**M**ount **D**evices
TDMA	**T**ri**D**iagonal **M**atrix **A**lgorithm

TOF	**T**ime **O**f **F**light
TOFD	**T**ime-**O**f-**F**light **D**iffraction
T-R	**T**ransmit-**R**eceive
TTL	**T**ransistor-**T**ransistor **L**ogic
USB	**U**niversal **S**erial **B**us
VHDL	**V**HSIC **H**ardware **D**escription **L**anguage

Symbols

F_T, f_c	central frequency of transducer
C_0	static capacitance between piezoelectric plates
t_W	pulse width
N_{burst}	number of pulse trains
t_R	rise time
t_F	fall time
Q	quality factor
S_1, S_2	strain component
ρ	density of material
A_z	cross-section area of piezoelectric plate along the length
u_p	phase velocity
ε^s	permittivity with constant strain
l_z	distance between two faces of crystal
e_{33}	piezoelectric stress Constant
h	transmitting constant
α_v	coefficient of attenuation due to viscous losses
$\alpha_{thermal}$	Coefficient of attenuation due to thermal losses
Z_0	characteristic impedance
γ	propagation constant
c_l	longitudinal velocity
c_s	shear velocity

$c_i(t)$	i^{th} IMF
$r(t)$	residue function
k_c	optimal index
ADD	addition/subtraction
MUL	multiplication
DIV	division
$COMP$	comparison
SFT	shifting
n	number of data sample
n_f	number of IMF
n_{pf}	number of inner loop iteration
n_e	number of extrema
n_k	optimal mode number of IMF
$O(\cdot)$	complexity function
N_R	number of accumulated data sample
T_s	sampling time
N_{Avg}	number of averages
σ	standard deviation
f_s, f_{aq}	sampling/acquisition frequency
T_{clk}	pulse width of clock
f_{sys}	system frequency

Dedicated to my Family...

Chapter 1

Introduction

1.1 Ultrasound in NDT

At beginning of '50s, NDT (Non-Destructive Testing) personnel knew only radiography (x-ray or radioactive isotopes) as a method for the detection of internal flaws in addition to methods for NDT of material surfaces, e.g. dye penetration and magnetic particle method. After the second world war, the ultrasonic technique was described by Sokolovin in 1935 and applied by Firestonein in 1940 [1]. It was further developed so that very soon instruments were available for ultrasonic testing of materials. The ultrasonic principle is based on the fact that solid materials are good conductors of sound waves. Detecting flaws are not sufficient and thus, further information is needed such as the position of the flaw and its size. Especially the defense and nuclear industry are interested in new solutions. It resulted in that perfect solution to this problem is Ultrasonic Testing.

The relation between the frequency, wavelength and sound velocity is given by

$$f = \frac{v}{\lambda} \tag{1.1}$$

where v is the sound velocity (m/s), f is the frequency (MHz) and λ is the wavelength (m) of the ultrasonic wave. Generally, ultrasonic waves used for NDT in a frequency range between about 0.5 MHz to 25 MHz and that the resulting wavelength is in 3 mm to 0.06 mm in water ($v = 1500$ m/s).

1.1.1 Wave propagation in material

Ultrasonic testing is based on time-varying deformations or vibrations in materials that use mechanical waves. All material substances are comprised of discrete atoms, which may be forced into vibrational motion about their equilibrium positions. Many patterns of vibrational motion occur at the atomic level; however, few are not routinely employed for acoustics and ultrasonic testing. When a material is not stressed in tension or compression beyond its elastic limit, its individual particles perform elastic oscillations. When particles of a medium are displaced from their equilibrium positions, internal (electrostatic) restoration forces arise, it behaves like a spring model. It is these elastic restoring forces between particles, combined with the inertia of particles that leads to oscillatory motions of the medium.

There are many types of waves that can propagate in the material. They can be divided by the direction of vibration with respect to the direction of the propagation in the material [1, 2].

- **Longitudinal wave**: This type of wave generally occurs in the material. The vibration of particles has the same direction as the wave direction of propagation. They can propagate in solids, liquids, and gases. Since the compressional forces are active in it, it is also called pressure or compression waves. They are also sometimes called density waves because their particle density fluctuates as they move.

- **Shear wave**: It has the same importance as longitudinal waves and propagates only in solids. It has perpendicular particle vibration direction with respect to the direction of propagation in solids. So it is also called a transverse wave. Shear waves are relatively weak when compared to longitudinal waves. In fact, shear waves are normally generated in materials using some of the energy from longitudinal waves. It has a lower velocity than longitudinal waves. So solid material produces two distinct wavelengths by applying the same frequency of input wave.

- **Rayleigh (Surface) wave**: Surface waves travel the surface of a relatively thick solid material penetrating to a depth of one wavelength. Surface waves associate both a longitudinal and transverse motion to generate an elliptic orbit motion. The major axis of the ellipse is perpendicular to the surface of the solid. As the depth of an individual atom from the surface increases, the width of its elliptical motion decreases. Surface waves are produced when a longitudinal wave intersects a surface near the second critical angle and they travel at a velocity between 0.87 and 0.95 of a shear wave. Rayleigh waves are beneficial because they are very sensitive to surface defects (and surface details) and they follow the surface around curves.

- **Plate wave**: They are similar to surface waves except they can only be generated in materials a few wavelengths thick. Lamb waves are the most commonly used plate waves in NDT. Lamb waves are complex vibrational waves that propagate parallel to the test surface throughout the thickness of the material. Propagation of Lamb waves depends on the density and the elastic material properties of a component. They can also be changed by the test frequency and material thickness. So usually, they have two types: Symmetric lamb wave and Asymmetric Lamb wave. Both are propagating with different velocity and wavelength. Lamb waves are generated at an incident angle in which the parallel component of the velocity of the wave in the source is equal to the velocity of the wave in the test material. Lamb waves will travel several meters in steel and so are useful to scan plate, wire, and tubes. "Guided Lamb Waves"can be defined as Lamb-like waves that are guided by the finite dimensions of real test objects.

1.1.2 Characteristics of Acoustic Impedance, Transmission, Reflection, Refraction and Diffraction

The multiplication of density of material and velocity of the ultrasonic wave is called the acoustic impedance of the material. Material with high acoustic impedance called sonically hard and in contrast sonically soft materials [1].

$$Z = \rho v_L \tag{1.2}$$

where ρ is the material density (kg/m^3) and v_L (m/s) is the longitudinal velocity of material. For example, stainless steel has a density 7890 kg/m^3 and longitudinal velocity 5790 m/s. Thus, the acoustic impedance is equal to 45.7 $\times 10^6 kg/m^2/s$.

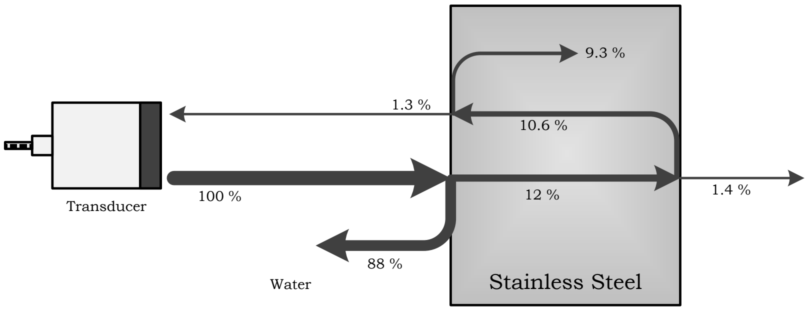

FIGURE 1.1: Percentage of receiving ultrasonic energy after multiple interfaces.

The ultrasonic wave is reflected from the interface of the dissimilar materials where there is a difference in acoustic impedance. If the material concerned borders on an empty space, no wave can go beyond boundary as such wave always requires the presence of particles of materials. If the impedance difference of both materials is higher, the wave will be reflected with the higher energy. If material 1 and 2 have acoustic impedance Z_1 and Z_2 respectively, the amount of reflection coefficient r by the perpendicular incident of the ultrasonic wave from material 1 to 2 is given by below equation [1].

$$r = \frac{Z_2 - Z_1}{Z_2 + Z_1} \tag{1.3}$$

and transmission coefficient τ is given by

$$\tau = \frac{2Z_2}{Z_2 + Z_1} \tag{1.4}$$

The amount of reflected energy E_R and transmitted energy E_T by the material is given by the below equation.

$$E_R = \left(\frac{Z_2 - Z_1}{Z_2 + Z_1}\right)^2, E_T = 1 - E_R \tag{1.5}$$

From the below example, it is observed that only small percentage (1.3%) of energy is reflected back to the ultrasonic transducer from the bottom of the steel boundary, due to impedance difference between water and steel. Here, the amount of energy due to absorption and attenuation is neglected.

If the plane ultrasound wave strikes a plane interface obliquely at an incident angle of θ_i to the perpendicular of the boundary, reflected and transmitted waves are produced as occurring in optics. The transmitted wave is called the refracted wave because their direction has changed relative to the direction of propagation. The direction of reflected and refracted waves are determined by the general law of refraction called Snell's law [1].

$$\frac{sin\theta_i}{sin\theta_t} = \frac{v_1}{v_2} \tag{1.6}$$

where θ_i and θ_t are the incident and refracted angle respectively, v_1 and v_2 are the velocities of material 1 and 2.

When sound propagates through a solid material, one form of wave energy can be transformed into another form. For example (Fig. 1.2), when a longitudinal wave hits an interface at an angle, some of the energy can create particle movement in the transverse direction to begin a shear (transverse) wave. It is called the mode conversion and it occurs when a wave encounters an interface between materials of different acoustic impedance and the incident angle is not normal to the interface.

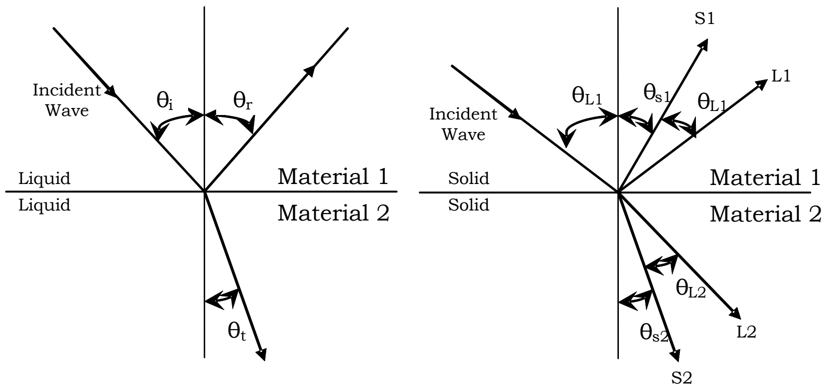

FIGURE 1.2: Mode conversion of ultrasonic wave at interface.

Another important phenomenon is the diffraction effect. Diffraction involves a change in direction of waves as they pass through an opening or around a barrier in their path. When plane waves pass through the diaphragm with the sharp edge, the elementary waves appear in the central zone of the diaphragm. But due to edge effect, in the case of straight edge, the elementary wave produces cylindrical waves while in the case of circular edge an annular wave is produced as shown in Fig.1.3. Superposition upon this plane wave produces maxima and minima of sound pressure. This is called the Huygens' Principle. The ratio of the oscillator diameter D and wavelength determines the ultrasound field spread and the number of minima and maxima.

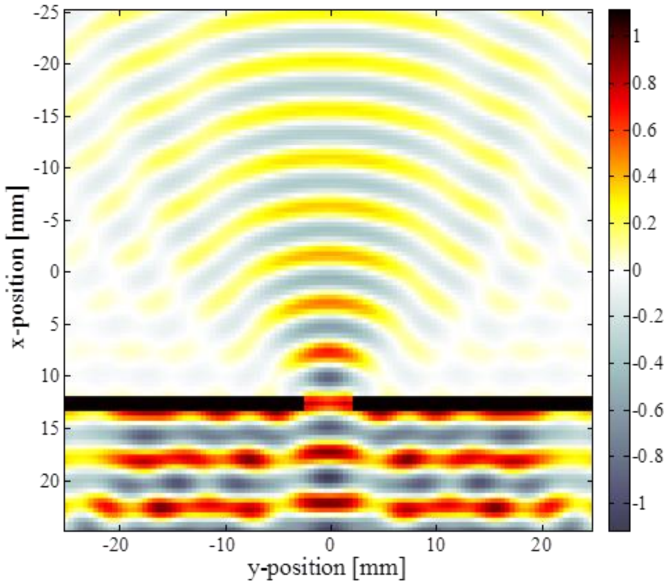

FIGURE 1.3: Diffraction of plane wave when passing through an edge.

1.1.3 Near field, Far field, Beam spread and Half angle

The pressure field between the transducer and last pressure maximum is called *Near field* N_F, and field beyond that it is called a *Far field* as shown in Fig.1.4. The sound pressure on the axis of a flat-disk circular transducer is given by the formula [1].

$$p = p_0 2 sin\left(\frac{\pi}{\lambda}\left[\sqrt{\left(\frac{D}{2}\right)^2 + z^2} - z\right]\right) \tag{1.7}$$

where D (mm) is the radiator diameter, λ (mm) is the wavelength of wave and z (mm) is the axial distance from the center of the radiator disk. Fig.1.5 shows the variation in normalized pressure of a flat transducer.

By solving Eq.1.7, it is possible to determine the near field distance from the center of the circular disk. The formula for N_F is given by [1]

$$N_F = \frac{D^2 - \lambda^2}{4\lambda} \tag{1.8}$$

In most practical cases the diameter of the piezoelectric crystal is much larger than the wavelength and the above equation can be rewritten as

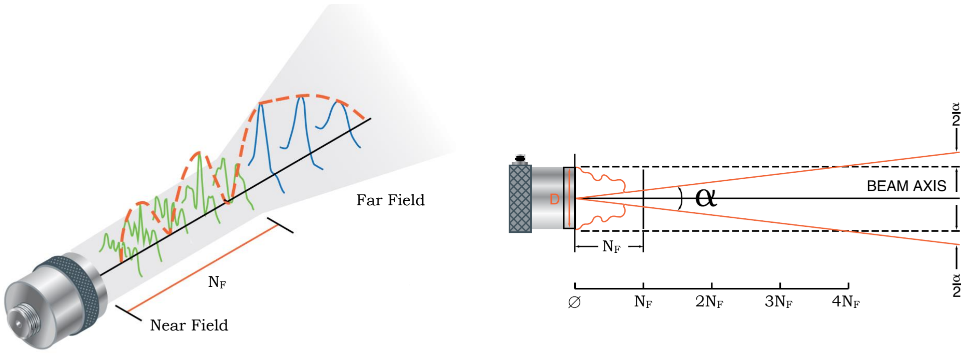

FIGURE 1.4: Near field and far field of transducer.

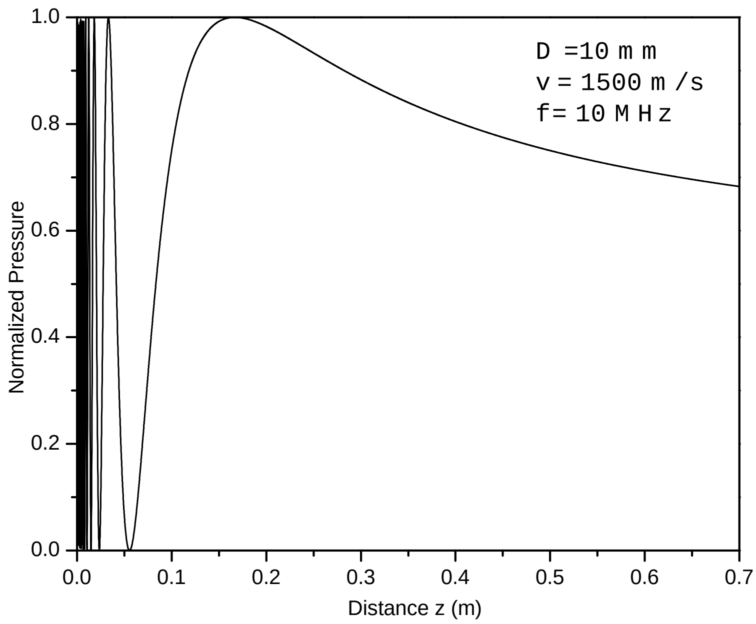

FIGURE 1.5: Normalized pressure of a Flat disk unfocused transducer.

$$N_F = \frac{D^2}{4\lambda} \tag{1.9}$$

Here, it is observed that a circular flat-disk transducer have a quasi-focus at the end of the near field and it is naturally produced by the diffraction phenomenon. But to achieve higher sensitivity and resolution, additional focusing is required. It is achieved by using the curved mirrors or lenses which are able to focus a beam at a fixed axial distance. The axial pressure for spherically curved circular disk transducer is given as [1],

$$p = p_0 2\left|\frac{2}{1-\frac{z}{r}}\right|\left|sin\left(\frac{\pi}{\lambda}\left[\sqrt{\left(\frac{D}{4}\right)^2 + (z-h)^2} - z\right]\right)\right| \tag{1.10}$$

where $h = r - \sqrt{r^2 - \frac{D^2}{4}}$ and r is the radius of curvature of transducer lens or axial focal distance from the center of disk.

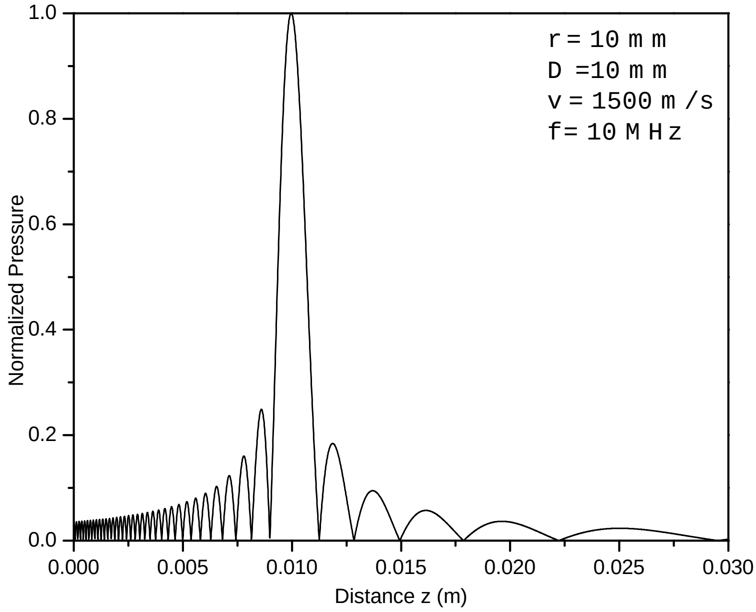

FIGURE 1.6: Normalized pressure of a focused transducer with $r = 10$ mm.

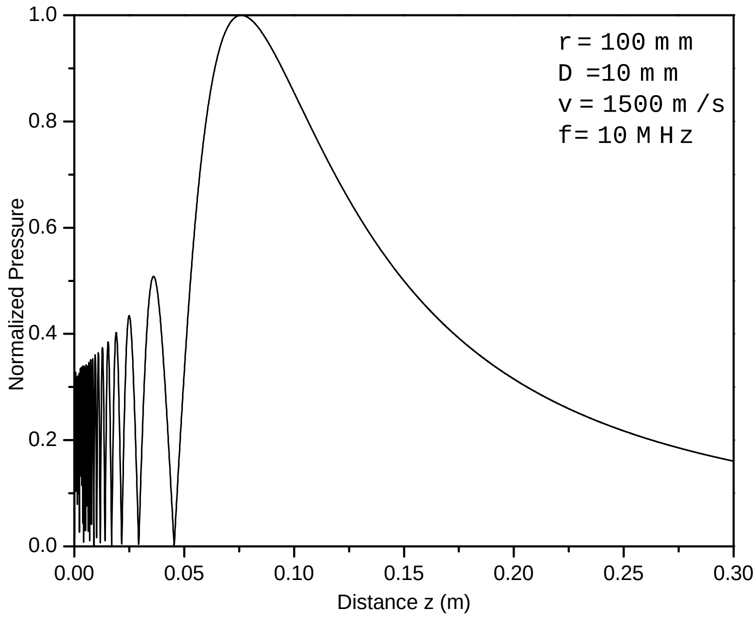

FIGURE 1.7: Normalized pressure of a focused transducer with $r = 100$ mm.

From the Fig.1.6, it is observed that normalized pressure field have a maximum pick at given focus point 10 mm but for focal distance 100 mm, it is observed that maximum pressure value is not at a focal distance as expected as seen in Fig.1.7. By considering only the geometric condition, it would have infinite value. But it has finite value because diffraction effect causes a slight change in maximum pressure. The ratio of the focus distance z_f to the near field length N_F of the unfocused transducer is called focus factor, and it is always less than 1 [1].

$$K = \frac{z_f}{N_F} \tag{1.11}$$

where $0 < K \leq 1$. For a small value of r the curve follows approximately the law $z_f = r$, but for the larger value of r, it approaches unity asymptotically. The focal distance can never be larger than the near-field length N_F.

All ultrasonic beams of transducers diverge. Fig.1.4 provides for a flat transducer with a simplified view of a sound beam spread. The beam has a complex narrow shape in the near field while the beam diverges in the far field. The -6dB pulse-echo beam spread angle is given as [3]

$$Sin\left(\frac{\alpha}{2}\right) = \frac{0.514v}{fD} \tag{1.12}$$

where $\alpha/2$ = Half Angle Spread between -6 dB points.From this equation, it can be seen that it is possible to reduce the beam spread from a transducer by selecting a transducer with a higher frequency or a larger diameter of the element or both.

1.1.4 Attenuation of signal

Consideration of how the physical properties of test material/object will affect sound transmission is essential in an ultrasonic test. When sound propagates within a medium, its intensity decreases with distance. In idealized materials, sound pressure (signal amplitude) is just diminished by the spreading of waves. But all-natural materials produce an effect that further weakens sound. These additional weakening effects occur from scattering and absorption. Scattering is a reflection of sound in directions different than its original direction of propagation. Absorption is the conversion of sound energy to another form of energy. The mixed effect of scattering and absorption is called attenuation. Attenuation and scattering in test objects are usually limiting factors in high-frequency testing. The loss of amplitude due to a given sound path is the sum of absorption effects that increase linearly with frequency. The scattering effect varies through three zones depending upon the ratio of grain boundaries or other scatterers to wavelength [4]. There will be a specific attenuation coefficient for a given material at a given temperature, tested at a given frequency, commonly expressed in Nepers per centimeter (Np/cm). Once this coefficient of attenuation is known, losses can be calculated according to the below equation in a given sound path

$$p = p_0 e^{-\alpha d} \tag{1.13}$$

where p is the output pressure at the end of path, p_0 is the source pressure at the beginning of path, α is attenuation co-efficient and d is the total path length of object.

1.1.5 Water path effect

The attenuation effect of water must be considered for immersion measurements where the ultrasonic wave is coupled within a water bath or water column. Because higher frequency components of a broadband pulse will be attenuated faster than lower frequency components, long water paths will effectively shift transducer's center frequency downwards, and this effect will increase as the water path's length increases. This frequency downshift in received signal will also affect the shape of the focal zone as focused beam diameter and focal zone length from a transducer of a given element diameter and lens design vary with frequency. This effect can be significant when using long water paths. As a practical matter, in order to avoid significant downshift in effective test frequency, water paths must be kept very short at high frequencies.

The downshift in the peak frequency of a broadband pulse traveling within water may be estimated from the below equation [5]

$$f_{Shifted} = \frac{f_0}{2\alpha d_w \sigma^2 + 1} \tag{1.14}$$

where $f_{Shifted}$ is the shifted peak frequency, f_0 is the original central frequency, $\alpha(Np/m)$ is the attenuation co-efficient of water, $d_w(cm)$ is the total water path length and $\sigma = f_0(\%bandwidth)/236$.

1.2 Contact and Immersion method

Ultrasonic inspection is one of the most successful and widely used non-destructive testing (NDT) technique for quality assessment, identification, detection, and characterization of flaws in metal structures. The signal reflected by discontinuities/ flaws includes the information about anomalies, based on which one can identify its location, size, and category. But it should be noted that these types of investigations such as sampling/manual or contact inspection (1.8(a)) are not beneficial to collect information of the entire volume of production. For analysis of quality control, it is desirable that information of complete volume be gathered. It is difficult to utilize ultrasonic flaw detection by manual scanning of the entire volume due to instability of acoustic coupling with material and inaccuracy of scanning interval. Though, this has been possible by immersion type ultrasonic scanning system (1.8(b)), C-scan imaging system, design and developed such as a way to conduct precision scanning flaw detection of the entire area of the specimen. There are many benefits of immersion-based ultrasonic testing compared to contact-based ultrasonic testing such as

- It is possible to utilize high-frequency focused transducer for better detectability in water.
- Problems associated with variation in the thickness and inadequacy of couplant are absent as liquid couplant is always present.
- Simplicity of changing the refraction angle in the medium without changing of transducer.
- Scanning accuracy and scanning resolution are superior.
- Automated stable data/image record can be obtained.
- Scanning process can be under the control of computer.

Generally, the immersion technique requires an object in a specific liquid (typically water) and immersion transducers will interact with an object within the liquid, which functions as a coupling agent. The mechanical pulse generated by transducers travels through liquid into the object. This incident pulse will separate into different reflected pulses that will come back to the transducer and various transmitted pulses that will travel away from the transducer on another side of the object. Each of those reflected and transmitted pulses can be measured.

1.3 Applications of immersion ultrasonic testing

Immersion-based ultrasonic imaging systems are extensively utilized in many industrial areas such as on-line thickness gauging, automatic scanning, high-speed

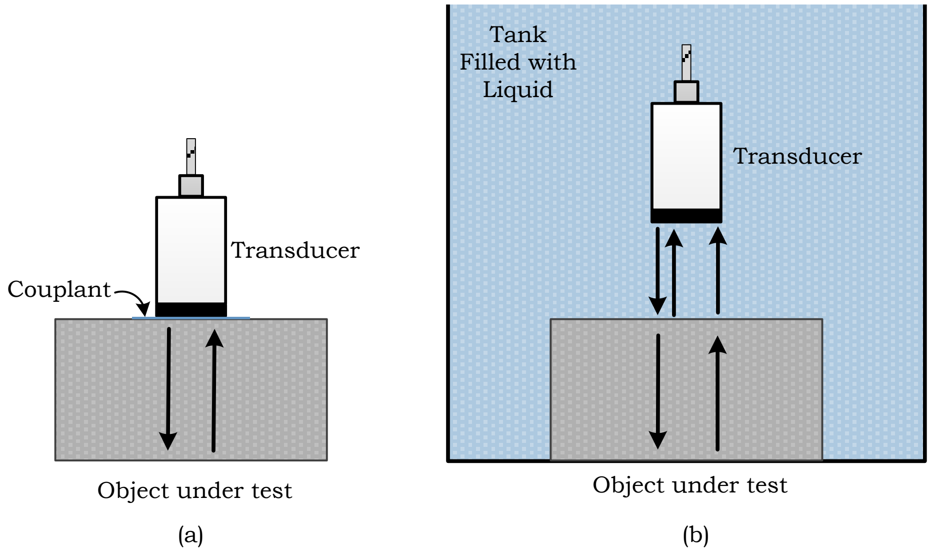

FIGURE 1.8: Ultrasonic testing methods: (a) Contact method and (b) Immersion method.

flaw detection in pipe/bar/tube/plate/other similar components, time-of-flight or amplitude-based imaging, detection of hydrogen-induced cracking (HIC) in steels in oil and gas industries, scanning of side-drilled hole (SDH) and flat-bottom hole (FBH) inside ingot, quality evaluation of magnetically impelled arc butt welded drive shafts of motor vehicles and many more. One of the main application of the immersion-based ultrasonic system is viewing or core-mapping of FSA which are usually submerged in liquid sodium environment at high temperature in fast breeder reactor (FBR) core, during reactor shutdown period [6].

In sodium-cooled fast reactor (SFR), in-service inspection is necessary to examine the integrity of safety-related structures of SFR. During maintenance and fuel handling, prototype fast breeder reactor PFBR (India) presently under commissioning stage, will be in shut down condition, coolant temperature will be at 180°C, neutron flux will be 120 $n/cm^2/s$, gamma levels decrease to 1.2×10^3 Sv/h (Sieverts per hour), sodium flow velocity will be 0.91 m/s and sodium pressure will be up to 500 $mbar$. At reactor shutdown, sodium temperature will be lowered to $150 - 180$ °C and therefore, in-service inspection (ISI) needs to be performed at this temperature. Since liquid sodium is optically opaque and electrically conductive, a conventional visual inspection cannot be used for observing internal structures under a harsh sodium environment and electromagnetic methods are also significantly limited due to the nature of metal and salt ions in a molten state. So ultrasonic imaging is the only technique that can be effectively used for viewing submerged components in the core of the reactor, core supports, and refueling hardware [6]. The other applications of this type of ultrasonic system are: identifying in-vessel core sub-assemblies, determining the orientation of hexagonal core components and other remotely placed equipment, ascertaining structural integrity of materials and structures during reactor operation, determining elevation and lateral profiles of fuel duct assemblies and searching of missing components in core inside reactor [6].

1.4 Objectives of Thesis

The conventional single-channel and linear array-based multi-channel ultrasonic imaging techniques for immersion applications usually take very long inspection time to investigate complete immersed mechanical structures/components. Particularly if large areas have to be examined, a matrix-based immersion ultrasonic system can improve the speed of testing and extend coverage on the field of view of sensors. Therefore, the main aim of the research is to propose a novel real-time matrix-based ultrasonic imaging technique which can enhance inspection time and provide real-time images of immersed objects. Furthermore, multi-channel real-time ultrasonic imaging system tested, calibrated and qualified in water can be further suitable for imaging/viewing of FBR and many other immersion-based real-time imaging applications.

- Modeling, simulation and experimental validation of the complete ultrasonic pulse-echo measurement system for immersion applications.
- Proposal and utilization of signal processing algorithms for the noise filtering and SNR enhancement of ultrasonic signals and the real-time implementation of the noise filtering algorithms in programmable hardware and software environment
- Proposal of the new real-time matrix-based ultrasonic imaging technique which can enhance the inspection time and provide real-time images of immersed objects
- Under-water ultrasonic viewing of mechanical components using the matrix-based (5×5) ultrasonic imaging system and experimental validation in hot-water environment

- Quantification of bowing measurement of FSA using 25-channel ultrasonic imaging system, in real-time mode and experimental validation in hot-water

1.5 Literature Review

The ultrasonic inspection method for immersion applications is well known and widely used for NDT and assessment of mechanical structures in many industrial sectors. Conventional or manual ultrasonic testing methods are increasingly being replaced by automated ultrasonic inspection systems in the field of NDT particularly for immersion applications. For the identification and/or assessment of the amplitude and time-of-flight (TOF) of the received signal (A-scan) in the test medium, traditional ultrasonic instruments are needed and, when it is connected to an automatic scanner, this configuration can be used to obtain cross-sectional images (B-scan, C-scan) [7]. For basic and immediate inspection of the material, a single-channel ultrasonic system is applicable. But particularly if large dimensional objects have to be examined, the multi-channel immersion system improves the speed of testing and extend the coverage on the field of view of the transducers [8]. Furthermore, it is difficult to inspect uneven, irregular and complex components using a single element transducer and it is not feasible to use a single element transducer because the complex surface reflects ultrasonic beams in different directions which is difficult to receive.

Normally, for a contact method, the medium is the same for ultrasonic pulse-echo imaging and thus, focal laws of phased array system are simply computed by applying simple trigonometric rules [9]. But, for immersion applications, transducers are immersed in a liquid (or water) and hence, water paths must be accommodated in focal laws calculations. The main issue with two distinct mediums is that they have distinct acoustic velocities and it is difficult to determine the index point between medium [10]. Furthermore, it is also not possible to arrange multiple single-element transducers in a linear manner for phased array configuration because, for the satisfaction of delay laws, element to element distance i.e. pitch must be at least equal to half wavelength ($\lambda/2$) in water [11]. For the case of 10 MHz transducers in water, calculated half-wavelength (pitch) is equal to 0.074 mm and therefore, it is not practicable to keep pitch distance so low as each individual transducer probe has a 10 mm diameter. Therefore, for high-frequency ultrasonic imaging especially for immersion application, it is impractical to use a phased array technique for real-time imaging.

For contact-based ultrasonic imaging, there are some commercially available camera-based instruments or imaging systems [12–14] that provide real-time images of material under test. Some researchers have also developed a laser-based ultrasonic camera for photoacoustic imaging [15, 16]. However, these instruments/systems can not be used for imaging of water-immersed structures and components. Furthermore, these instruments have a limited axial thickness range for contact mode imaging such as they have a thickness range of 0-150 mm for steel[17], 0-16 mm for CFRP [18] and 0-60 mm for metal[14]. If we use these types of contact-based instruments/cameras for immersion application, maximum axial thickness range will be decreased significantly because it is obvious that acoustic velocity of liquid couplant is lower than acoustic velocity of metal and measured thickness (d) is proportional to acoustic velocity (v) of material ($d \propto v$) [19]. For such a case, the acoustic velocity of water is approximately 4 times lower than the acoustic velocity of aluminium so the maximum thickness range of contact-based instruments will be further decreased by 4 times. Therefore, for immersion-based ultrasonic imaging, the thickness range must be large so that ultrasonic waves can easily strike the surface of immersed mechanical components.

1.5.1 Core-Mapping of FSA

In a fast breeder reactor, the heat is generated by nuclear fission in the core where core consists of the large number of FSAs. Each FSA consists of a hexagonal wrapper tube which contains bundles of clad tubes or fuel pins, filled with fuel pellets. For example, in PFBR (India), there are 181 FSAs which are arranged in a triangular array. Each FSA consists of 217 fuel pins [20]. During normal operation of the reactor, the temperature of liquid sodium is more than 550 °C and the neutron flux levels are about two orders of magnitude higher as compared to equivalent thermal reactors. Deformation of various components of the SAs can occur due to void swelling, thermal creep and irradiation creep. Differential swelling can occur because of gradients in flux and difference in temperature at various locations in the reactor core due to the inter-assembly heat transfer. Wrapper deformation is expected to be limited; otherwise, the interaction between wrappers will lead to obstruction in fuel handling. At the center of the core, sub-assemblies are expected to remain straight with an elongation and an increase of distance across surfaces of adjacent SAs. But at the periphery, sub-assemblies can tend to bow outwards called as “flowering” due to differential void swelling on the opposite faces of the wrapper tube as a consequence of neutron flux gradient. There would be differential thermal expansion and differential swelling across the width of the SA. Hence, the SA will tend to bow to accommodate the differential expansion. Higher the neutron flux gradient, bowing will be more. The extent of bowing is dependent on its location in the core as the flux gradually reduces towards the core periphery. Due to high temperature and flow of liquid sodium, there is also a possibility of growth of FSAs [21–23]. The variation in pins is the result of the combined action of swelling and irradiation creep. Once swelling exceeds 15-20%, failure can occur under the liquid sodium by swelling and irradiation creep, leading to mechanical interference with neighboring FSAs and support structure during attempts to extract the ducts from the core [23].

In the FBR core, small motions in the fuel region can lead to changes in the core reactivity. Since positive reactivity is added when the core assemblies displace radially inward, the phenomena of bowing have importance for safety and control point of view. So does the Core-mapping is required to locate, identify and measure the growth and bowing of FSAs. For inspection and viewing, the system based on ultrasonic imaging is generally deployed during the shutdown campaign of the reactor when the temperature of liquid sodium is around 180 °°C. Previously, many types of ultrasonic imaging system have been developed for such application. The single channel ultrasonic imaging system developed has been developed by India[24], Germany [25] and Japan [26] for the under-sodium viewing. The multi-channel ultrasonic imaging system such as the USA has developed the azimuthally-scanner with the linear array of eight focused ultrasonic transducers for fast flux test facility (FFTF) [27, 28] and the 12-channel linear array system for under sodium imaging in sodium-cooled fast reactor [29], India has developed the 8-channel automated under sodium ultrasonic scanner (USUSS) for the growth and bowing measurements [30], the UK has developed the 12-channel rigid under sodium viewer (RUSV) for the in-service operation of the prototype fast reactor core [31, 32] and linked sweep-arm scanner (LSAS) system for deployment in commercial demonstration fast reactor (CDFR)[33], France has developed an ultrasonic orthogonal array system "IMARSOD" for in-service inspection and repair technique developments (ISI&R) in french liquid metal fast reactors (LMFR) [34], Germany used eight receiving transducers with focal lenses fitted circularly around the central focused transmitter-receiver sensor [35], Japan has developed a 2D matrix array based imaging system for FBR [36]. However, all these developed ultrasonic imaging systems are not the real-time system as they usually take a long acquisition and processing time for the viewing of FSA such as the system developed by Japan took the approximately 3 minutes time to take the image using single transducer [26] and further it took approximately 7.2 seconds for one frame scan and several minutes to obtain image using the multi-channel imaging system [36]. The conventional single-channel and linear array based multi-channel ultrasonic imaging techniques for immersion applications usually take very long inspection time to investigate the immersed mechanical structures/components. Therefore, the one of objective is to propose a new real-time matrix-based imaging technique which can enhance the inspection time and provide real-time images of immersed FSAs.

1.5.2 SPICE models of ultrasonic transducer and comparisons between different models

Simulation is an essential tool for designers to understand the effect of system parameters in any field. One approach is based on the equivalent electrical circuit and implementation using simulation tools like Spice (P-Spice) [37–40] or VHDL-AMS [41]. Here SPICE (software process improvement and capability determination) simulator has been utilized to simulate the complete ultrasonic pulse-echo measurement system. It is more convenient use of the equivalent circuit of the ultrasonic transducer where both the mechanical and electrical section of the transducer is characterized by only electrical equivalents. The equivalent circuit of each type of piezoelectric transducer can be derived by applying its equation of motions (acoustic wave equations) and applicable piezoelectric equations.

- Mason has proposed equivalent electric circuit for the ultrasonic transducer with three different conditions based on direction of electric field and mechanical force: (1) Length expander bar with parallel electric field, (2) Length expander bar with electric field perpendicular to length and (3) Thickness modes with electric field parallel to the thickness [42]. Each equivalent model comprises one pair of electrical terminals and two pairs of mechanical terminals which can be represented by the three couple of equations describing the transducer system in terms of three depended and three independent variables. For that, the thickness mode transducer model[43] is considered.

- M. Redwood [44] has proposed a method to solve the transient response of the piezoelectric transducer. This model consists of a transmission line which is utilized to represent the time delay which is necessary for mechanical signals to travel from one face of the transducer to the other face. An ideal transformer represents the conversions of electrical quantities to mechanical quantities and vice versa. One capacitor of the model has a negative value and is unlike any real electrical element. Its magnitude is equal to the transformed static capacity, and therefore when there is no electrical contact to the transducer, the transducer behaves as a length of the mechanical transmission line.

- Krimholtz R. et al. [45] has proposed new equivalent circuit for piezoelectric transducers. The circuit involves frequency-depended components attached to the center of the transmission line. In the new circuits, on the other hand, the acoustic forces appear directly across the transmission-line terminals. In the KLM model, the electromechanical transformer is directly connected to the center of the acoustic transmission line of a piezoelectric element without additional circuit component. Those acoustic structures such as piezoelectric active layers, backing, (front) matching, and other passive layers can also be simply added or omitted along with the transmission line of the model. Therefore, the KLM model is more appropriate for the simulation of multilayer structures. However, modeling of multiple-active-layer structures having more than one interaction sources between electrical and acoustic signals is much-complicated [46].

- The Redwood version of Mason's equivalent circuit has been proposed by [39] to provide the computer simulation. The modified circuit comprises a hybrid representation of electromechanical transformer, an accurate approximation of the negative capacitor C and modified coupling from the transformer to the acoustic transmission line. Equivalent model of Mason [42, 43], Redwood [44], KLM [45] have not implemented for circuit analysis as they consist of frequency depended components. The Mason model consists of a capacitance C_0, a negative capacitance $-C_0$, an ideal transformer and a transmission line. Given a particular transducer, SPICE model can be used to simulate the important characteristics of the transducer, e.g. electrical and acoustic input impedance, port-to-port transfer functions, received time response, and drive time response. Electrical matching can be provided by introducing the matching network in the circuit.

The thickness mode plate transducer is considered mainly for simulation, since it has very significant practical applications in the generation and detection of longitudinal waves in solids, fluids, and gases [42]. It is more suitable to use the equivalent circuit of the ultrasonic transducer where both mechanical and electrical portions of the transducer are represented by only electrical equivalents. The equivalent circuit of each type of piezoelectric transducer can be determined using its acoustic wave equations and piezoelectric equations. Mason et al. [43] have proposed equivalent electric circuit for ultrasonic transducer based on the direction of electric field and mechanical force. The model comprises an ideal transformer which represents the conversions of electrical quantities to mechanical quantities and vice versa. The model also contains a negative value capacitor C_0, the static capacitance of the transducer. M. Redwood [44] has proposed a method to solve the transient response of a piezoelectric transducer. The Redwood model consists of a transmission line which is used to represent a time delay which is necessary for mechanical signals to travel from one face of the transducer to the other face. Krimholtz et al. [45] have proposed new equivalent KLM Model for piezoelectric transducers. They modified mason's model equations for the thickness expander plate. Its circuit contains frequency depended on components connected to the middle of the transmission line. The acoustic forces emerge directly across the transmission-line terminals, unlike in mason model where the forces are not developed across the transmission line only but are developed partially across the line terminals and the secondary of the transformer. KLM model is more favorable for simulation of multilayer structures [46]. However, these models are difficult to implement in spice as they contain frequency dependant transformers and a negative value capacitor. Morris et al. [39] have come up with a Redwood version of Mason's equivalent circuit to provide the computer simulation which subsists of the hybrid representation of electromechanical transformer, an accurate approximation of the negative capacitor and modified coupling from the transformer to the acoustic transmission line. Leach et al. [40] have proposed a spice simulation model which involves the controlled current and controlled voltage sources instead of a transformer and a negative value capacitor. The spice model of the sandwiched piezoelectric ceramic ultrasonic transducer has been proposed by Wei X et al. [47] using the leach model for high power applications.

1.5.3 Noise sources and real-time implementation of noise-filtering algorithms

Several conditions provoke the occurrence of noise in the ultrasonic signal. There are many causes of the noise appearance in ultrasonic data such as the physical interaction between the sound waves and the propagation medium, the propagation of sound in a matter [48], the formation of the ultrasound pulse (i.e. ultrasound beam characteristics) and the acquisition, processing and reconstruction of reflected echoes. In order to detect small planer cracks or flaws in highly scattered or coarse grain materials such as stainless steel, the noise from the grain boundaries called grain noise and backscattering noise play a major role as this noise value can be higher than the desired flaw echoes. Thus, the detection of flaws in the presence of noise becomes very difficult [49]. The same type of effect is observed while carrying out the time-of-flight diffraction (TOFD) technique. However, electronics front-end hardware of the ultrasonic instrumentation also introduces the noise in the feeble echo signals. Noise can also be caused by improper scanning techniques, although these noises can be avoidable. Most of the noise is introduced due to the AC power-line interference, electromagnetic interference (EMI), ADC quantization error, improper impedance matching, cross-talk between channels and high-frequency interference [50].

In experimental science, noise equals any random fluctuation in data which obstructs discernment of the desired signal. Many of these noises can be misinterpreted as real discontinuities in the reconstructed data, therefore it is essential to reduce them either during the time of acquisition (pre-processing enhancement techniques, see for example [51]) or after data acquisition using signal and image processing methods (post-processing enhancement techniques).

Coarse-grained materials are used widely in modern industry. For example, 304/304L type austenitic stainless steel has been used widely in the chemical reaction vessels and piping, liquid and gas storage and transportation as well as nuclear power and other industrial units. During the cooling stage, the austenitic steels are processed without phase change, resulting in coarse dendritic grain. These result in extensive ultrasonic scattering in austenitic stainless steel. Ultimately, the attenuation for scattering is increased, and the reflected signal strength from the defect is greatly reduced, thus reducing the SNR. The non-destructive testing (NDT) of coarse-grained ingredients, such as austenitic castings, forgings, welded joints, and coated steel plates, is necessary both in the production process and in the regular maintenance and repair [52]. To improve the SNR and the reliability of ultrasonic testing of coarse-grained materials, a lot of research has been carried out using different methods of signal processing.

Background noise disturbs a variety of applications for radar, sonar, optic, and ultrasonic detection and imaging. The background noise also called the grain noise for the ultrasonic applications. This type of noise usually occurs from the small randomly distributed scatters compared to the ultrasonic wave's wavelength. Therefore, it is difficult to distinguish the resulting signal interference pattern between target echos and noise. Since the targeted echoes from the scatter shows no phase and amplitude variations with time and therefore they can not be suppressed by the time or coherent averaging [53].

The main problem in ultrasonic imaging is also the speckle noise and the mentioned speckle noise is not generated due to grain noise.. Arising artifacts or speckles in B-scan images can be due to the physical interaction between the sound waves and the improper surface of medium [54], the formation of the ultrasound waves (i.e. ultrasound beam), acquisition of reflected echoes, data processing, and waveform reconstruction techniques. Speckles can also be generated by improper scanning techniques although these artifacts can be avoidable [48]. Speckle diminishes the quality of ultrasonic images, it specifically blurs edges and lose details in the B-scan image. Additionally, material produces a granular texture occurring in the background of the B-scan image. Thus, it is also called the background noise [55]

During characterizations or calculations of TOF, the sound speed is considered to be uniform within the medium. Although there may be variations in the sound speed depending on the medium's characteristics. The variation in the speed of sound will produce a distortion in the appearance, shape, and size of the object being examined [56, 57].

When a strong absorber (high reflector) is observed (air void), the attenuation type artifacts occur in the image because it reflects most of the incoming waves. The waves that pass through the strong absorber are thus weakened. This produces a shadowing effect in the image that appears after the strong absorber. The returning echo will be higher from the object under the weak absorber. This effect causes an increment in the intensity of the received signal [48].

Material microstructure and surface geometry of the inspected object can also have a significant effect among many factors that influence the performance of an NDT system. These may result in additional scattering and attenuation of the ultrasonic pulse-echo signal that dramatically changes a transducer's beam pattern. For example, a polycrystalline metal can generate backscattering and grain noise that can mask the signals reflected in pulse-echo inspections from small flaws [58]. The backscattering can also attenuate both the incident signal and the flaw signal and can hence adversely affect the detection of flaws. Backscattering and attenuation, however, can also be used to benefit material characterization, such as determining grain size that influences mechanical properties.

In terms of surface geometry, both surface curvature and roughness may in some circumstances have significant effects on ultrasonic beam patterns [59]. For example, the transmitted beam could be significantly defocused or focused on a curved surface, depending on whether the surface is convex or concave. As a result, signals from the corresponding flaw for the convex surface could be weaker and stronger for the concave surface compared to flaw signals for a smooth surface. However, for different flaw depths, these effects will be distinctive.

Furthermore, surface curvature may also change the amplitudes of backscattered grain noise. This means that raising the flaw signal does not necessarily mean raising the SNR. In addition to the direct reflection from the surface, surface roughness can also modify an incident beam and result in further dispersion. One important type of surface roughness is in the form of periodic grooves, normally present on the surface of machined metallic parts and it has a peak-to-valley height ranging from a few micrometers to a few hundred micrometers which are close to ultrasonic wavelengths used in NDE [59]. Although the magnitude of the roughness might be small, it could still generate significant noise in flaw detection. Therefore, noise is a universal limitation that can occur from a variety of described sources on sensing applications. Thus, the two types of noise exist in the ultrasonic pulse-echo signal while performing ultrasonic testing: coherent noise and incoherent noise [60–63].

The software implementation of the averaging process involves the accumulation of each scanned ADC output into an allocated controller memory which can be connected to the ADC chip directly or through the onboard memory (FIFO/RAM). Because of the non-availability of parallel hardware architecture, this induces the limitations on overall acquisition time. Many commercially available ultrasonic NDT instruments/flaw detectors do not provide the data averaging feature, but it can be implemented by the user in the computer-based host software environment. This post-processing operation typically reduces the overall acquisition speed of the system. The digital storage oscilloscope (DSO) can provide data acquisitions with the standard number of averages (i.e. 4, 16, 32, etc.). But it has a limited number of averaging options and it is more costly [64, 65]. Furthermore, it is suitable for one-scan ultrasonic measurements and it may introduce some ambiguities in the acquired scan data as the ultrasonic pulser and digitizer circuit within DSO have separate clock sources. Thus, it can result in random and asynchronous time delays between the pulser trigger and the scan acquisition trigger of each A-scan data. This leads to temporal incoherence between successive scan records in a coherent averaging. To resolve these issues, there must be a provision of precise time and phase synchronizations between the pulser trigger and the trigger associated with the data acquisition board. Previously, many authors have proposed the hardware-based architecture for the coherent averaging [66–73]. The conventional architecture [67, 71] of coherent averaging accommodates large hardware and takes more execution time for the averaging process. The reconfigurable ultrasonic smart sensor platform (RUSSP) comprises of parallel coherent architecture using the 4 block-RAM and 4 adders [72, 74]. Later, a single block-RAM based architecture was proposed only for the summation process and the remaining division operation was performed in the software environment [68].

As ultrasonic echo is non-linear and non-stationary, to process this kind of signal with coherent noise, various signal processing techniques have been used such as cross-correlation processing [75], discrete wavelet filtering [75–77], undecimated wavelet transform (UWT) [78, 79], sparse de-convolution [80], time reversal processing [81], split spectrum processing (SSP) [82, 83], moving bandwidth polarity thresholding (MBPT) [84], Wiener filtering [85], Wigner Ville transform (WCT) processing [86], matching pursuit (MP) method [87], Bayesian learning approach [88], etc. Here every technique has some advantages and drawbacks like cross-correlation is the easy method for implementation but it is not an efficient to reduce the noise because if the noise and signal have the same amplitude in the same frequency range then it would be impossible to discriminate between them [75]. The linear filtering methods like wiener filtering [85] are also easy to design and implement. But it is not effective when the signal contains sharp edges and impulses of short period. The non-linear methods like wavelet transform is the most popular due to its time and frequency localization properties. But it requires the selection of the mother wavelet function and scale of it for signal enhancement.

1.6 Thesis outline

In chapter 2, the design and development of the matrix-based ultrasonic system are presented. For that purpose, the beam-splitter based approach for both P-E and T-R mode of imaging has been proposed. This beam-splitter based matrix-transducer approach allows the user to switch the mode of transmission from P-E to T-R or vice versa by using the same transducer holder/assembly. Furthermore, the overall imaging scheme of the matrix-based (5×5) ultrasonic imaging is presented. The presented multi-channel ultrasonic imaging scheme combines sequential and parallel mode of acquisition and processing in real-time. This chapter provides the proposed matrix-based ultrasonic imaging scheme by performing real-time imaging of water-immersed mechanical components. Furthermore, the real-time imaging and bowing measurement of water-immersed FSA in high-temperature environment are also presented.

In chapter 3, the one-dimensional simulation modeling of the entire ultrasonic pulse-echo measurement system for immersion application is presented. The modeling of the entire ultrasonic pulse-echo measurement system is a complex task which involves an understanding of acoustic physics of transducer, acoustic properties of propagating medium, transmission cables and analog front-end electronics for generating and receiving of ultrasonic signals. For validation purpose, a single channel real-time ultrasonic imaging system is designed and developed for laboratory application and it contains high voltage ultrasonic spike pulser, high voltage protection circuits, ultrasonic receiver amplifiers, co-axial cables, and the ultrasonic transducer. The lossless and lossy (low-loss) simulations are performed for ultrasonic transducer and propagation medium using the transmission line model. Effects of non-ideal, frequency-dependent and non-linear components in high voltage excitation circuit (pulser), the receiver circuit and the effects of cables are also considered for modeling and simulation. We will see that the validation results of the entire ultrasonic imaging system provide very close agreement with lossy simulated results.

In chapter 4, the two-stage noise filtering technique for the both coherent and incoherent noise is proposed. The first stage is described in chapter 4 and the second is described in chapter 5. In chapter 4, the proposed novel hardware (FPGA) implementation of the coherent averaging architecture for the reconfigurable ultrasonic NDT system is presented. The proposed hardware architecture uses the addressing-based shifting technique for the addition operation and Radix-2 non-restoring algorithm for the division operation. Since the amount of hardware required by the proposed averaging scheme is independent of the number of averages, it supports on-the-fly control on the number of averages. The developed system further supports dynamic on-line reconfiguration of the analog front-end hardware, real-time data acquisition, real-time hardware-based data processing, and data transfer operations. The performance of implemented coherent averaging is presented by various applications such as removal of RF random false-echoes, smoothing of A-scan waveforms and speckle removal of B-scan images.

In chapter 5, the real-time empirical mode decomposition (EMD) algorithm based ultrasonic imaging system is developed for both contact and immersion NDT applications. It is difficult to implement the EMD based signal processing algorithm in real time because it is a totally data-driven process which comprises numerous sifting operations. In this chapter, the EMD algorithm is implemented in the visual software environment. The EMD implementation encompasses two types of interpolation methods, piecewise linear interpolation (PLI) and cubic spline interpolation (CSI). The cubic spline tridiagonal matrix will be solved by the Thomas algorithm for the intention of real-time processing. The total time complexity functions for both implemented PLI and CSI based EMD method will be computed. For signal filtering, the partial reconstruction algorithm is adopted. The baseline correction and noise filtering applications are presented using EMD based visual software. The real-time practicability and efficiency of this method will be validated through ultrasonic NDT experimentation for improvement in the time domain resolution of the ultrasonic A-scan raw data. The practical results will explain that in the noisy environment, it is possible to enhance the signal-to-noise ratio (SNR) for the visualization and identification of ultrasonic pulse-echo signals in real time.

In chapter 6, a novel hardware-based architecture using the reconfigurable embedded system for the multi-channel immersion ultrasonic system is proposed. It provides the addressing-based analog multiplexing scheme which requires only one data acquisition unit and common on-chip storage for the multi-channel imaging system. It also provides unique channel reconfigurable facility to the user to modify the number of channels (up to 256 for pulse-echo (P-E) and 512 for transmit-receive (T-R) mode by installing only the partial front-end hardware (pulser, pre-amplifier) and without modifying the remaining data acquisition hardware (common-amplifier, digitizer) and back-end embedded system. The developed system further supports dynamic on-line reconfiguration of the analog front-end hardware, real-time hardware-based data processing, and data transfer operation. For the experimentation, the complete 4-channel ultrasonic imaging system for immersion testing is designed, developed and evaluated in the laboratory. Furthermore, this study describes the capability of the proposed system by performing multi-channel real-time data acquisition, hardware-based coherent averaging, channel multiplexing-demultiplexing, reconfigurable control, and software-based post-processing. Here the performance evaluation of the developed multi-channel system will be presented by carrying out the B-scan and C-scan image acquisition of the water-immersed mechanical components.

In chapter 7, the design and development of the matrix-based ultrasonic camera system are presented. For that purpose, we have proposed the beam-splitter based approach for both P-E and T-R mode of imaging. This beam-splitter based matrix-transducer approach allows the user to switch the mode of transmission from P-E to T-R or vice versa by using the same transducer holder/assembly. Furthermore, the overall imaging scheme of the matrix-based (5×5) ultrasonic imaging is also presented. The presented multi-channel ultrasonic imaging scheme combines sequential and parallel modes of acquisition and processing in real-time. This chapter provides the proposed matrix-based ultrasonic imaging scheme by performing real-time imaging of water-immersed mechanical components. Furthermore, the real-time imaging and bowing measurement of water-immersed FSA in the high-temperature environment is also presented.

Chapter 2

Design and Hardware Implementation of Single-channel and Multi-channel Ultrasonic Imaging System

2.1 Overview of single-channel ultrasonic imaging system

Experimental setup for the complete real-time ultrasonic imaging system is presented in Fig. 2.1. The ultrasonic imaging system comprises high voltage ultrasonic spike pulser for generation of high voltage negative spike pulse for ultrasonic transducer; ultrasonic receiver amplifier for amplification of echo signals; Analog-to-Digital Converter (ADC) (100 MSPS, 8-Bit) for the digitization of echo signals; Spartan-6 FPGA chip for accumulating and digital processing of received data of echo signals; USB ARM controller which operates as a master controller between data acquisition system and host PC; and a GUI application software for the user interface to control the full imaging system through PC. GUI application produces real-time plotting of A-Scan waveform and B-Scan cross-sectional Image.

Fig. 2.2 shows a detailed block diagram of high voltage ultrasonic spike pulser. Ultrasonic pulser is composed of four sections: DC power supply which produces electrical energy, the low voltage section consists of a TTL buffer to interface with MOSFET driver, MOSFET driver drives the power MOSFET and the high

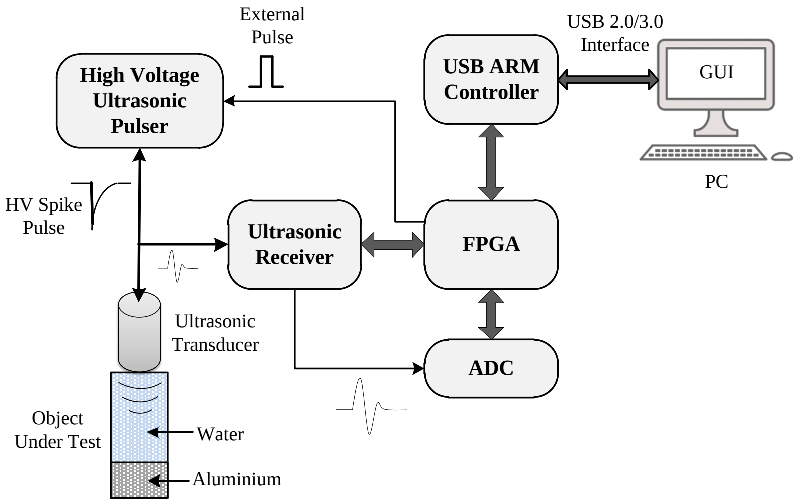

FIGURE 2.1: Block diagram of ultrasonic imaging system for experimentation.

voltage N-channel MOSFET which is used to generate the high voltage spike signal for excitation of the ultrasonic transducer. The external input pulse trigger has been provided through the external devices (FPGA/Processer) with sufficient Pulse Width (PW) (100 ns) and Pulse Repetition Frequency (PRF) (100 Hz to 1 kHz). The output pulse energy of the pulser is enhanced by raising the pulse width. PRF is the number of pulses of a periodic signal in a specific time and it is set such that received echo should not get superimposed on other echoes. The high-voltage section is the most important part of the ultrasonic pulser. This stage supplies the electrical pulse of the sufficient amplitude to the ultrasonic transducer. Convention pulser topology for high voltage spike generation has been depicted in Fig. 2.3. Here only one active element is utilized for leading edge spike pulse. RC network is used between the output of driver and gate of the power MOSFET to prevent DC voltage reaching to MOSFET. The circuit includes damping resistor R_d, charging capacitor C_C and resistor R_P in order to get the efficient electrical matching between pulser and transducer. The fast damping of the electrical signal is achieved by the proper selection of the damping resistor. Low capacitance C_C provides fast trailing edge during charging of the external capacitor. But the disadvantage is that peak overshoot is increased which causes oscillations during the excitation of the transducer. So there is a trade-off between peak overshoot and storage time of charging the capacitor. The other solution is to the reduce drain resistance RC. It also causes a fast trailing edge response, but it produces a large voltage drop when the MOSFET is turned "ON" and power can be reduced by using a short width of the trigger pulse.

A fast CMOS RF gate driver is used to drive power MOSFET. It sources and

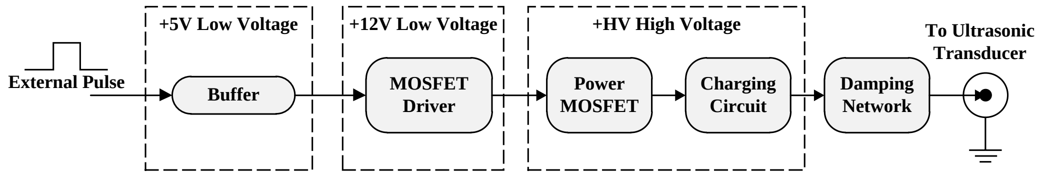

FIGURE 2.2: Schematic block diagram of high voltage ultrasonic pulser .

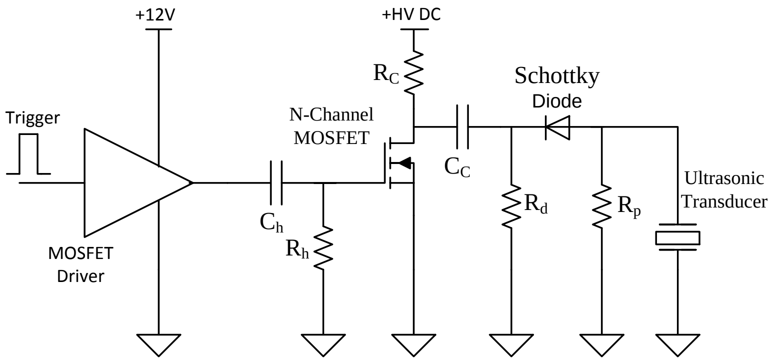

FIGURE 2.3: High voltage section of ultrasonic spike pulser.

sinks up to 30A peak pulse current while producing the voltage rise and fall times of less than 4 ns and minimum pulse widths of 8 ns. High-speed dual MOSFET driver can be utilized to enhance the drive capability of pulser. The maximum source and sink current of the driver is 2A and driving capacity of the driver can be increased by connecting two drivers in parallel. N-Channel Enhancement switch mode MOSFET is used for high voltage switching operation. The MOSFET has 40A peak drain pulse current ID_{peak} and 2.1Ω output resistance R_{DS} during “ON” condition of MOSFET. It has 1200 V maximum drain voltage V_{DSS} and 2500 V high isolation voltage. It has a very low rise time of 4 ns and fall time of 5 ns during 900 V supply voltage. Here 5W wire wound metalized film resistor is adopted as a drain resistor. The ultrafast Schottky diode is used to create the discharging path with less resistance. This diode has 1000V Peak Inverse Voltage (PIV) and 70 ns forward recovery time and 100 ns reverse recovery time. The typical performance of the pulser also depends on the quality of DC power supply voltage. A low voltage resistor is connected between the +12 V supply and driver supply pin to reduce the di/dt effect. The high voltage capacitors 1nF/1000V and 0.01uF/1000V are utilized as bypass capacitors at +HV supply terminals.

Fig. 2.4 shows the schematic block diagram of the ultrasonic receiver amplifier. It consists of limiter circuit which provides protections from high voltage transients

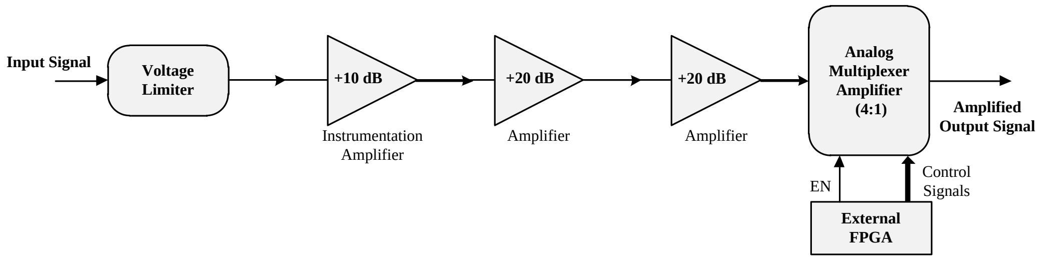

FIGURE 2.4: Ultrasonic receiver amplifier.

connected inadvertently to this stage, +10dB instrumentation amplifier for high CMRR, op-amp based +20 dB non-inverting amplifier and a 4:1 analog multiplexer amplifier. The analog multiplexer has four input signals which are controlled by the external FPGA device. The bridge diodes architecture is used as a voltage limiter. All diodes are forward biased by a dual DC power supply. High voltage signals pass through a single diode pair into the ground while low voltage echo signals pass through to the receiver. In this protection circuit, a DC power supply is needed to bias the diode–bridge structure. The ultrafast rectifying diodes are used for limiter diode-bridge. These diodes have 1000V PIV and 70 ns forward recovery time and 100 ns reverse recovery time. For single diode pair, fast switching diodes are used. It has 4ns reverse recovery time. The limiter circuit has an output voltage of 1.6V to 1.7V. The 400 MHz small signal bandwidth, low power and high performance operational amplifiers are used as non-inverting feedback amplifier with individual gain of +20 dB. The output of the three stage cascaded amplifiers are connected to the analog multiplexer. The analog multiplexer offers high speed disable feature allowing the output to be placed into high impedance state for shorting output stages of all the channels, which does not load the output bus to the off channels. This will allow receiver boards to be used in larger arrays.

The 8-Bit, 100 MSPS, low power ADC is adopted for analog-to-digital conversion as indicated in Fig. 2.5. It involves on-chip track and hold circuit and power-down facility to put the device in the high impedance state. ADC is interfaced with Spartan-6 (XC6SLX9-3CSG324) FPGA. Here control signals are generated by the FPGA which provides clock and power-down signal to ADC. The 8-bit output data from ADC are accumulated in on-chip FIFO inside the FPGA for further processing of A-Scan waveform data. Before storing into the FIFO, data are synchronized with the FPGA system clock. The system clock frequency of the FPGA is 100 MHz. The On-chip 8 bit FIFO with 8 Kbyte Block memories has been configured using VHDL language in ISE 14.7 Xilinx development tool. FIFO has an independent clock domain for writing and reading of data which is

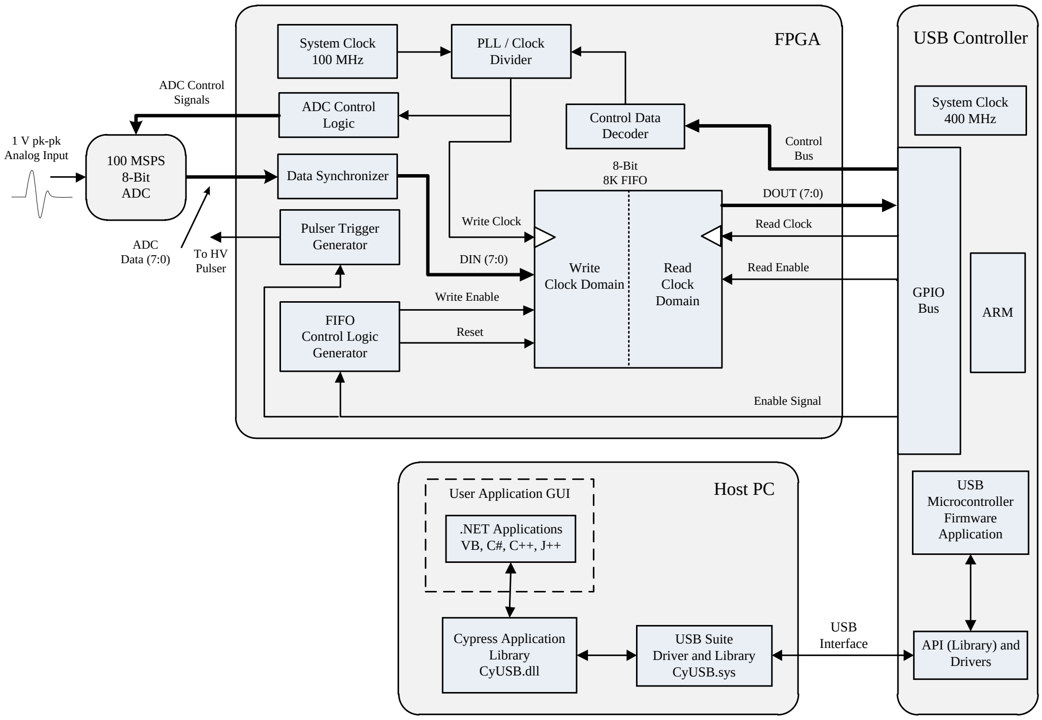

FIGURE 2.5: General block diagram of digital section for pulse-echo data transfer.

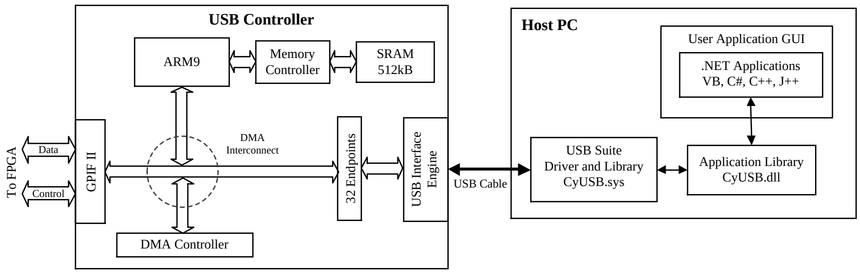

FIGURE 2.6: Interfacing architecture between USB controller and host PC.

needed to transfer data asynchronously. The signals in the write-clock domain are synchronous to the input system clock and all signals in the read-clock domain are synchronous to the USB controller. The Read Clock domain is entirely controlled by the external device which has a system clock of 400 MHz and works asynchronously with the FPGA system. The controlled signals are provided by the GPIO of the USB controller. The detailed interfaces between ADC, FPGA and USB controller are depicted in Fig.2.5.

Interfacing between USB microcontroller and host PC has two distinct sections, ARM-based USB microcontroller section and host PC section. USB 3.0 peripheral controller has an on-chip 32-bit, 200-MHz ARM926EJ-S core CPU. The USB application firmware has been developed using C++ language. The host PC and target USB microcontroller board are connected through the USB interface. The driver CyUSB.sys is able of transmitting with several devices that comply with the USB 2.0/3.0 specifications. These drivers and supported application libraries (CyUSB.dll) are provided by the device manufacturers. So any Windows.Net application can communicate with the microcontroller using the CyUSB.dll libraries and these can be accessed from the Microsoft Visual Studio .NET managed languages. Here the GUI application has been developed in a visual studio environment using Visual C# language.

2.2 Overview of multichannel (Matrix 2×2) ultrasonic imaging system

The multichannel ultrasonic imaging system is subdivided into four sections: (1) Transmitter section, (2) Front-end receiver section (3) Back-end Digital section and (4) System GUI software. Transmitter section comprises high voltage ultrasonic spike pulser boards which excite the ultrasonic transducers. Front-end Analog Receiver section consists of pre-amplifier and Main-amplifier boards to amplify ultrasonic echo signals and digitizer boards for analog to digital (A-D) conversion for further processing of echo signals. Back-end digital processing section consists of on-chip FIFO based digital architecture in FPGA for digital processing like storage, averaging, etc.; ARM-based USB microcontroller for high-speed data transfer to host PC. This ultrasonic imaging system has a PC based GUI application for plotting of A-Scan and B-Scan real-time images.

2.2.1 Transmitter section

High voltage ultrasonic spike pulser has been designed and developed especially for immersion applications requiring high material penetration due to long water path and multiple interfaces. It consists of four sub-sections: high and low voltage DC power supplies, low voltage trigger generator which generates trigger pulses, MOSFET driver which drives the power MOSFET and the high voltage RF MOSFET switch which is needed to generate the HV (up to 600V) negatively spike signal for excitation of the ultrasonic transducer. High voltage pulser has been tested under different conditions like with no load, with 50Ω output load and with the ultrasonic transducer load [89]. The Fig. 2.7 shows the transmitter section consisting of pulser module '1'and '2'for row 1 and row 2, respectively.

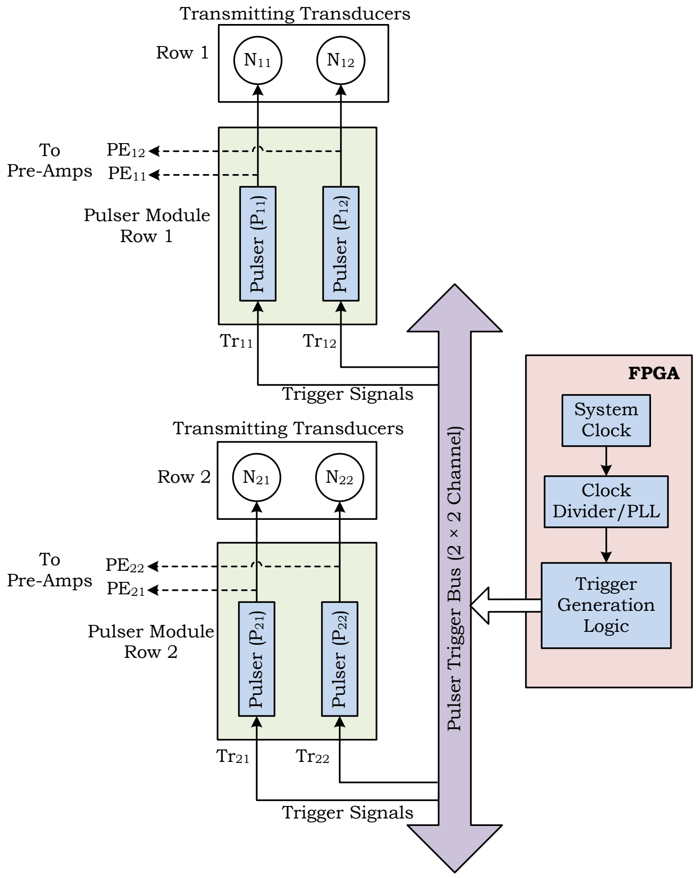

FIGURE 2.7: Transmitter section of ultrasonic imaging system for 2×2 channels.

Each pulser module (1 & 2) consists of two pulser boards (P_{11}, P_{12} and P_{21}, P_{22}) and each pulser board is connected to individual transmitting transducer (N_{11}, N_{12} and N_{21}, N_{22}). For P-E mode, received four ultrasonic echo signals (PE_{11} to PE_{22}) are taken from rows of pulser modules. Received P-E mode echo signals are fed to the pre-amp modules for amplification. All pulser boards are parallel triggered by the external trigger pulse generator using FPGA.

2.2.2 Front-end analog receiver section

Fig. 2.8 shows the schematic block diagram of the front-end ultrasonic receiver section. It comprises ultrasonic receiving transducers (N_{1-2} to N_{2-2}) for T-R mode, pre-amplifier boards (PA_{11} to PA_{22}) for fixed gain amplification, main-amplifier boards (M_1-M_2) for variable gain amplification and digitizer boards (A_1-A_2) for A-D conversion. Each pre-amplifier board consists of diode bridge limiter circuits for input signals in P-E and T-R mode which protect further amplifier stages from a high voltage transient, inadvertently received from pulser modules.

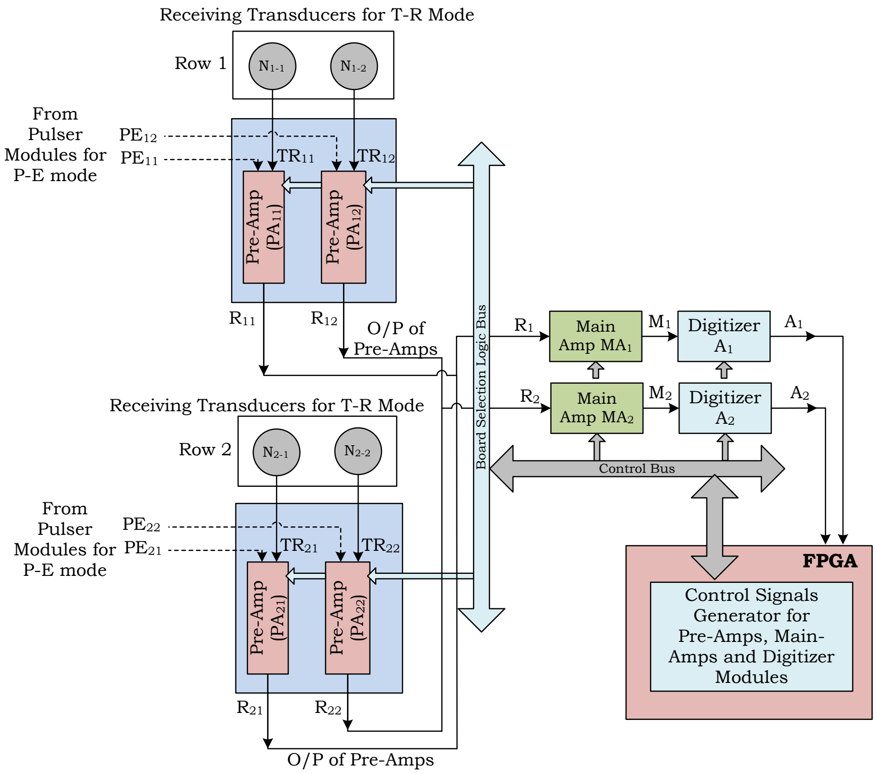

FIGURE 2.8: Front-end Analog Receiver section of ultrasonic imaging system.

Pre-amps also consists of relay logic which is used for selection of P-E (PE_{11} to PE_{22}) and T-R (TR_{11} to TR_{22}) mode signals, Instrumentation amplifier for high CMRR, Op-Amp based non-inverting Amplifier and a 4:1 analog multiplexer amplifier. Inputs of the analog multiplexer are controlled by the selection logic input from the board control logic circuit. The board selection logic circuit is used to select the specific pre-amplifier board using addressing logic which is controlled by the external FPGA. Each main-amplifier board consists of a variable gain amplifier for user selectable amplification of echo signals. Each digitizer board consists of 8-Bit 100 MSPS A-D converter chip with onboard synchronous FIFO device. Both main-amplifier and digitizer boards are controlled by FPGA.

2.2.3 Back-end digital section

Digitizer boards and Back-end digital section of imaging system is depicted in Fig. 2.9. It consists of FPGA-6 for interfacing of ADCs and ARM based USB controller. ADCs have on chip track and hold circuit and power-down facility to bring high impedance output. ADCs are interfaced with Spartan-6 FPGA. Here control signals are generated by the FPGA which provides clocks and power-down

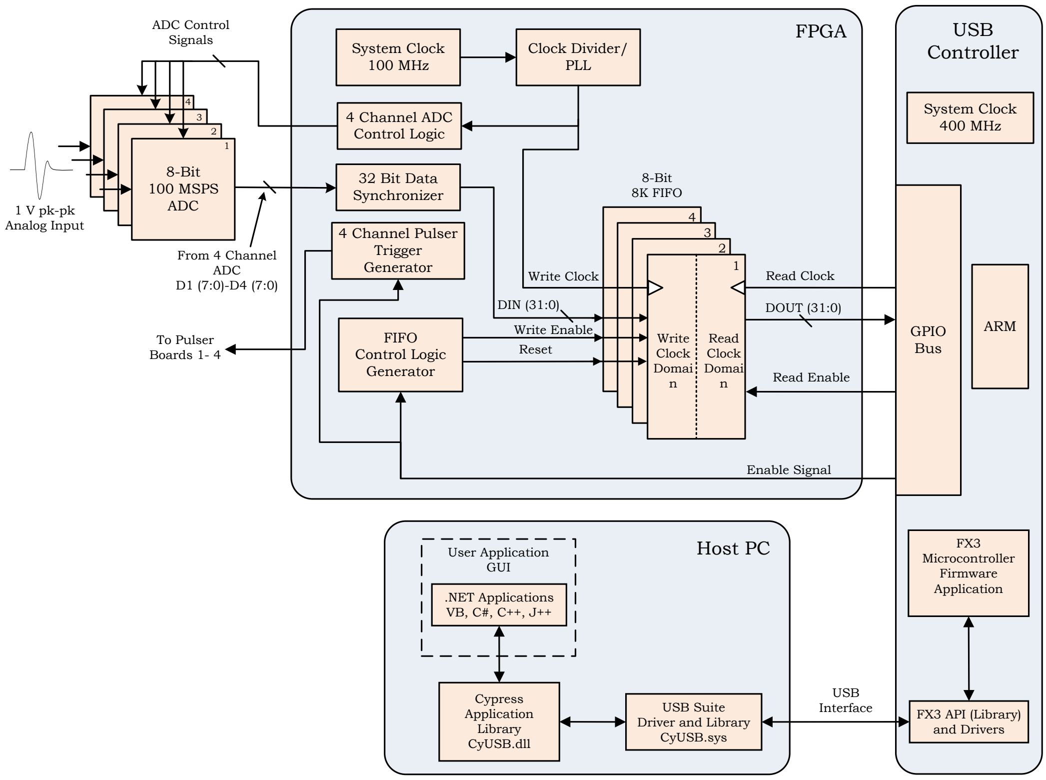

FIGURE 2.9: Back-end Digital section of ultrasonic imaging system.

signals to the ADCs. The 8-bit output data of the each ADC are stored in on chip 8 bit FIFO with 8 Kb memory inside FPGA for further processing of data. Before storing in FIFO, data must be synchronized with the FPGA chip clock. Each FIFO has independent clock domain for writing and reading of data to transfer data asynchronously. All the logical blocks are developed in FPGA using VHDL language in ISE 14.7 Xilinx tool. Fig. 2.9 shows the asynchronous interfacing between FPGA with USB controller. Here write clock domain has been controlled by the internal FPGA control logic and read clock domain has been controlled by the external control device. The clock divider circuit uses the 100 MHz system clock as base frequency. The external Enable Signal also provides the control to the trigger signal generator which provides trigger to the pulser units. The controlled signal provided by the Complex GPIO unit of the FX3 device.

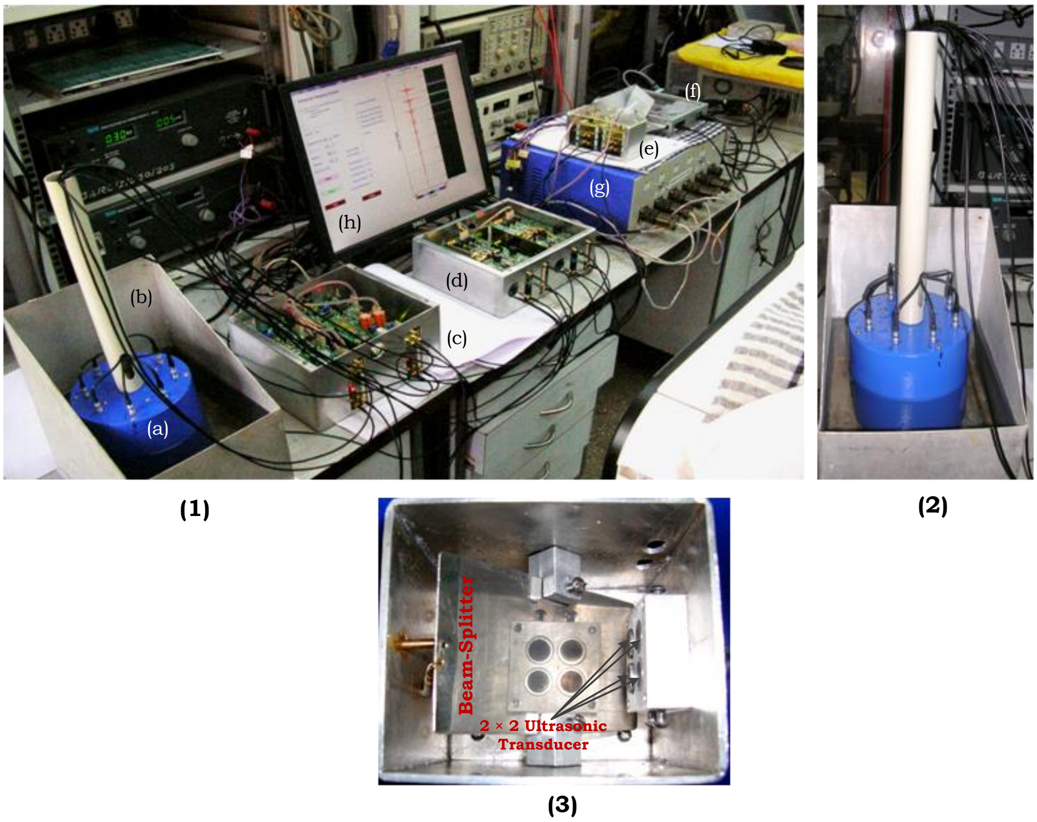

FIGURE 2.10: (1) Experimental setup for matrix based ultrasonic imaging system: (a) 8 channel transducer assembly with two sets of (2×2) array transducers, (b) Tank filled with water, (c) HV spike pulser boards, (d) Ultrasonic Receiver amplifier boards, (e) Digitizer boards, (f) Digital Section with FPGAs and USB Controllers, (g) Power supply unit, (h) GUI application S/W for A-Scan and B-Scan image; (2) Photograph of transducer array assembly; (3) Photograph of 8 channel transducer assembly with two sets of (2×2) array transducers for P-E and T-R modes.

2.3 Overview of matrix-based (5×5) multi-channel ultrasonic imaging system (Ultrasonic Camera)

2.3.1 Reconfigurable analog front-end circuits

The analog front-end section consists of UPR modules and common-amplifier module. For the $NrNc-$channel ultrasonic camera, total Nc number of UPR modules are required and each UPR module contains the Nr numbers of HV pulsers and Nr numbers pre-amplifiers.

2.3.1.1 Ultrasonic Pulser-Receiver (UPR) Module

As shown in Fig 2.11, the Nr number of HV pulsers ($P_{1,1}$, $P_{2,1}$,..., $P_{Nr,1}$) simultaneously energize the Nr number of ultrasonic transducers ($T_{1,1}$, $T_{2,1}$,..., $T_{Nr,1}$), respectively. The received ultrasonic signals from the same transmitting transducers are pre-amplified by their corresponding pre-amplifiers ($AP_{1,1}$, $AP_{2,1}$,..., $AP_{Nr,1}$). Likewise, for T-R mode, the receiving ultrasonic transducers ($R_{1,1}$, $R_{2,1}$,..., $R_{Nr,1}$) are connected to their corresponding Nr number of pre-amplifiers ($AT_{1,1}$, $AT_{2,1}$,..., $AT_{Nr,1}$). The outputs of both types of pre-amplifiers ($AP_{1,1}$ and $AT_{1,1}$) are multiplexed together through the analog multiplexer $M_{1,1}$. Likewise, all outputs of analog multiplexers ($M_{1,1}$, $M_{2,1}$,..., $M_{Nr,1}$) are connected via daisy-chaining connection. Therefore, such kind of arrangement provides only single amplified output (Out_1) of the single UPR board (PR_1) for the Nr number of channels. In such a way, all UPR boards are connected with their corresponding ultrasonic transducers such as UPR PR_X is connected with the Nr number of P-E mode transducers ($T_{1,X}$, $T_{2,X}$,..., $T_{Nr,X}$) and Nr number of T-R mode transducers ($R_{1,X}$, $R_{2,X}$,..., $R_{Nr,X}$).

As shown in Fig 2.11, the Nr number of high voltage pulsers ($P_{1,1}$, $P_{2,1}$,..., $P_{Nr,1}$) are energized the Nr number of ultrasonic transducers ($T_{1,1}$, $T_{2,1}$,..., $T_{Nr,1}$), respectively. The received ultrasonic signals from the same transmitting transducers are pre-amplified by their corresponding pre-amplifiers ($AP_{1,1}$, $AP_{2,1}$,..., $AP_{Nr,1}$). Likewise, for T-R mode, the receiving ultrasonic transducers ($R_{1,1}$, $R_{2,1}$,..., $R_{Nr,1}$) are connected with their corresponding Nr number of pre-amplifiers ($AT_{1,1}$, $AT_{2,1}$,..., $AT_{Nr,1}$). The outputs of both types of pre-amplifiers ($AP_{1,1}$ and $AT_{1,1}$) are multiplexed together through the analog multiplexer $M_{1,1}$. Likewise, all outputs of analog multiplexers ($M_{1,1}$, $M_{2,1}$,..., $M_{Nr,1}$) are connected together via daisy-chaining connection. Therefore, such kind of arrangement provides only single amplified output (Out_1) of the single UPR board (PR_1) for the Nr number of channels. In such a way, all UPR boards are connected with their corresponding ultrasonic transducers such as UPR PR_X is connected with the Nr number of P-E mode transducers ($T_{1,X}$, $T_{2,X}$,..., $T_{Nr,X}$) and Nr number of T-R mode transducers ($R_{1,X}$, $R_{2,X}$,..., $R_{Nr,X}$).

Each HV pulser circuit is triggered by the individual 3.3-volt, rising edge signal from the FPGA. This CMOS level trigger signal is converted to the TTL 5-volt signal using 50 Ω line driver. The output signal of the line driver is supplied to the MOSFET driver (EL7202, Intersil Corp., SA) that provides +12 volt rising edge

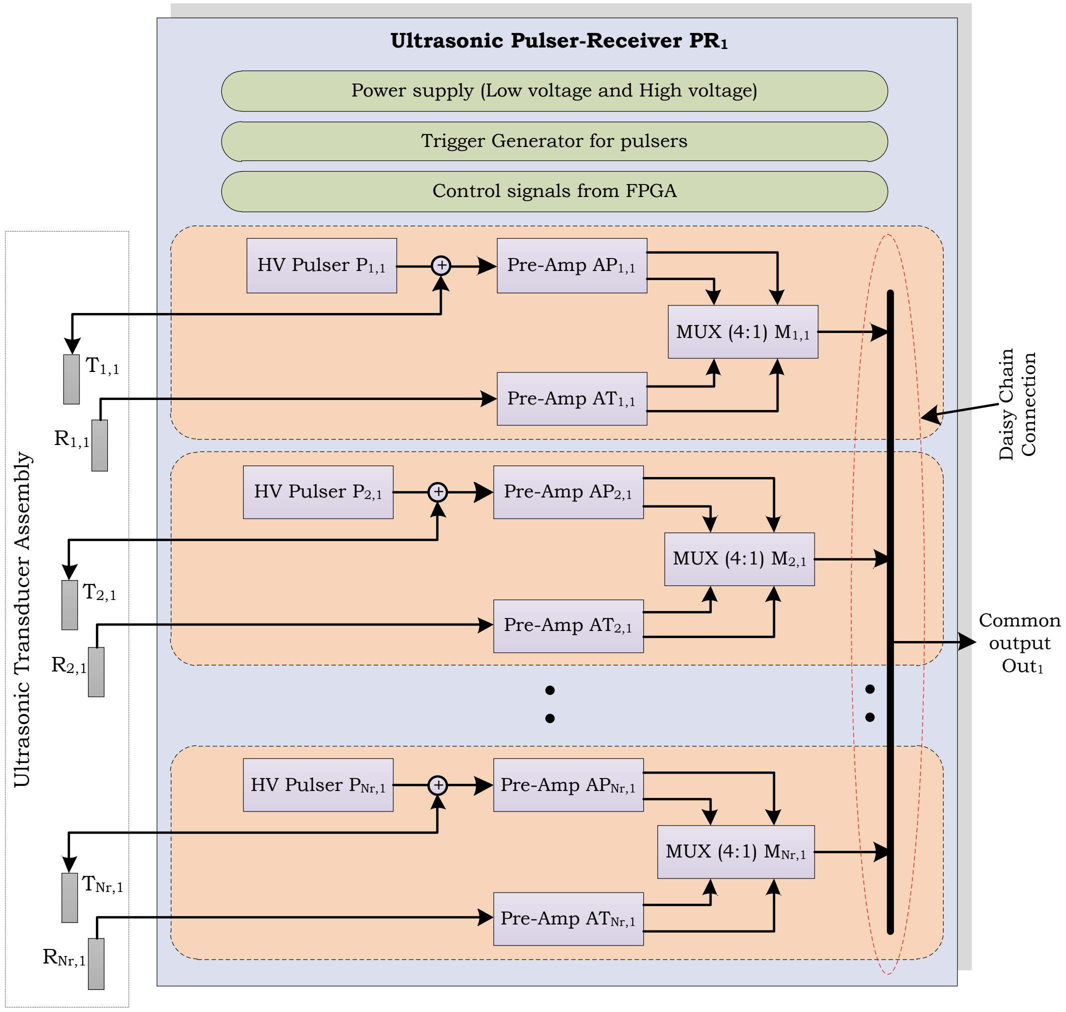

FIGURE 2.11: Schematic block diagram of the single UPR board.

pulse for driving the power MOSFET (IXZ308N120, IXYS RF, CA) as displayed in Fig. 2.12(a).

Fig.2.12(b) shows the schematic block diagram of one of the ultrasonic receiver pre-amplifier. It comprises the diode bridge limiter circuit which provides protections for further amplifier hardware stage from HV spike pulses received from the pulser circuit. Each preamplifier section includes two-stage op-amp based feedback amplifiers (AD8014, Analog Devices Inc.) in non-inverting configuration with an individual gain of +20 dB and a bandwidth of 400 MHz. The passive band-pass filters with -3dB cut-off frequencies from 50 kHz to 50 MHz are also used directly after the terminals of all amplifiers. These cascaded amplifiers are connected to the analog multiplexer (AD8174, Analog Devices Inc.) for the selection of appropriate amplified output signal. It provides a high speed disable feature allowing the output of the all pre-amplifier boards to be put into a high impedance state

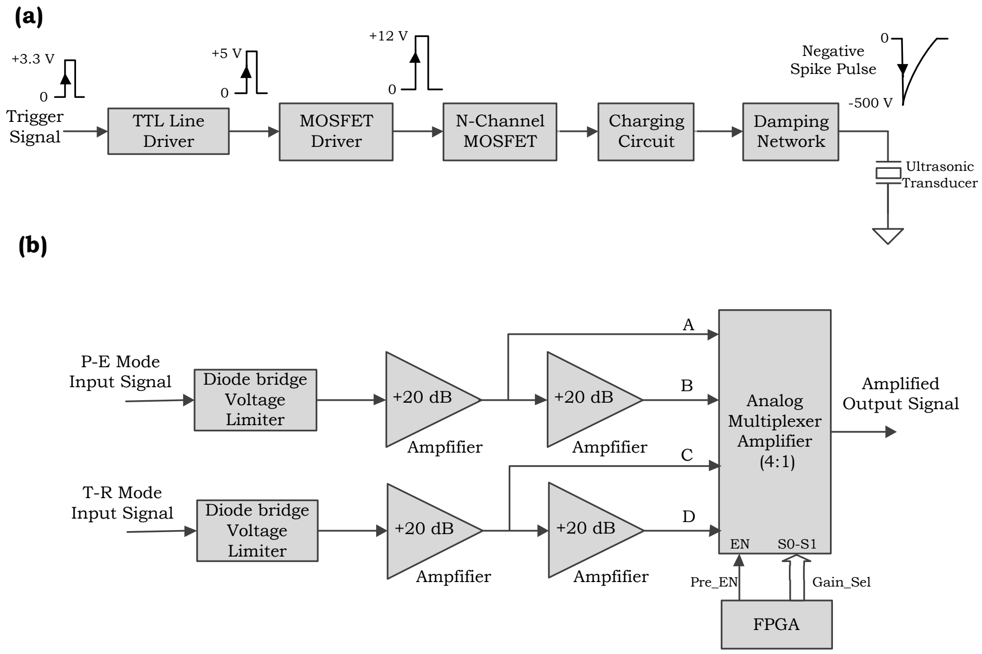

FIGURE 2.12: Schematic block diagram of pulser ($P_{1,1}$) and receiver pre-amplifier section ($AP_{1,1}$ and $AT_{1,1}$) of the UPR (PR_1).

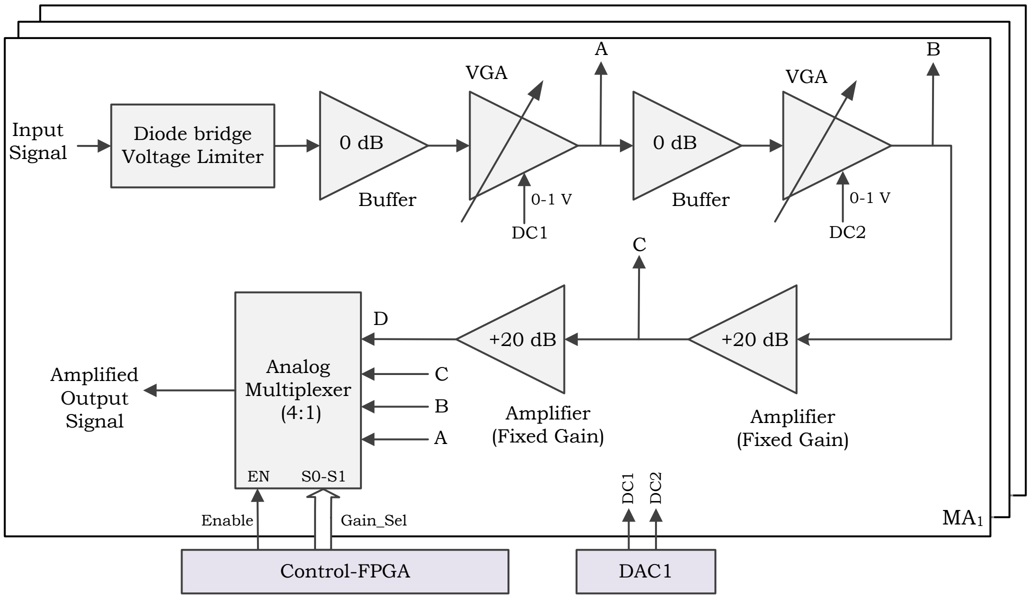

FIGURE 2.13: Schematic block diagram of main-amplifier board (MA_1.

for cascading configuration so that the off pre-amplifier channels (boards) do not load the output bus and allow them to be used in larger channels.

2.3.1.2 Common-amplifier Module

The common-amplifier module/board consist of the Nc number of the main-amplifier sections (MA_1, MA_2,..., MA_{Nc}). Each main-amplifier section (i.e. MA_1) has five-stage cascade amplifiers such as variable gain amplifiers (0-30 dB) with buffer, two fixed gain amplifier (+20 dB) and an analog multiplexer amplifier (+10 dB). The programmable gain-adjustable amplifiers (AD603, Analog Devices) are utilized where the gain is controlled by the DC output (0-1 V) of the 8-bit DAC (DAC1). Before the amplified signal is fed to the analog-digital converter (ADC), a high-speed analog multiplexer is used to select the appropriate gain of the analog outputs. The enable and input selection logic has been provided by the control-FPGA. Likewise, all main-amplifier sections (MA_1, MA_2,..., MA_{Nc}) have been controlled by the control-FPGA and fine-gain has been tuned by the respective DACs (#1 to #N_c).

2.3.2 Digital Back-end Module

The digital master module comprises the four type of sections namely 1) Digitizer section for multi-channel digitization of analog signals, 2) DAC section for the fine gain adjustment, 3) FPGA section which contains two FPGAs: data-FPGA and control-FPGA and 4) USB controller for the communications between the system and user PC.

2.3.2.1 Digitizer section

As shown in Fig. 2.14 , there are Nc number of digitizers are used each for each Nc number of columns. Each digitizer contains RC filters, amplifier, voltage limiter and analog-to-digital converter (ADC). The high-pass filter with lower cut-off frequency $f_l = 200kHz$ is used to block the DC component from the incoming analog signal. Since the input analog signals may contain the high voltage pulses, the diode-bridge based voltage limiter is used. Furthermore, for the proper signal-conditioning, the signal is amplified by the fixed gain amplifier and filtered by the band-pass RC filter with lower cutoff frequency $f_l = 500kHz$ and higher cutoff frequency $f_h = 12MHz$. In the final stage, the 8-bit, 100 MSPS ADC (AD9283, Analog Devices Inc.) is used for the analog-to-digital conversion. The clock and the power-down signals of ADC are provided by the data-FPGA. The 8-bit output data of the ADC are accumulated in FIFO implemented in data-FPGA for further processing of data. Before storing in FIFO, data are synchronized with the data-FPGA system clock. This section also includes the Nc number of digital-to-analog conversion circuits for the fine-amplifications of the analog signal and these Nc channel analog outputs of DACs are provided to the common-amplifier module through the motherboard. The 8-bit digital inputs and controls of all DACs (MAX505, Maxim Integrated, CA) are provided by the control-FPGA.

2.3.2.2 Development of GUI based signal processing software

The GUI has been implemented in visual software environment using visual C# and WPF application. Once the appropriate connection between the host and the USB controller is established, the control endpoint is utilized to send/receive the sample data to/from the external device. The control endpoint is only one endpoint that serves as a bidirectional data connectivity. So before every transfer operation, the direction of control endpoint has been fixed. The *Request code* is also transmitted from host to device along with the control data.

The developed GUI software includes different sequential stages for imaging operations such as data fetching from the external device, channel demultiplexing, channel allocation, noise suppression, base-line correction, and scan conversion from raw data to different scan/image format (i.e. A-scan, B-scan, and C-scan). The $NcNc$-channel raw data are fetched from the device and separated into the specific storage arrays. Thereafter, these raw data samples are fed to the envelope detection filter (EDF) based envelope generation block.

The FPGA plays a significant role for the $NrNc$ -channel ultrasonic processing unit that controls pulse/trigger transmission, channel selection, front-end hardware control, channel multiplexing, data acquisition, pre-processing of the A-scan data sets and data transfer. Therefore, the FPGA code is appropriately designed and developed such that it is reconfigurable to re-optimize the speed and usage of the relevant resources in the multi-channel ultrasonic imaging system.

2.3.3 FPGA based digital system

2.3.3.1 Data-FPGA

The block diagram of the data-FPGA (XC6SLX45-2CSG324, Xilinx, CA) code for the $NrNC$ $(= 25)$-channel imaging system is shown in Fig.2.15. The code

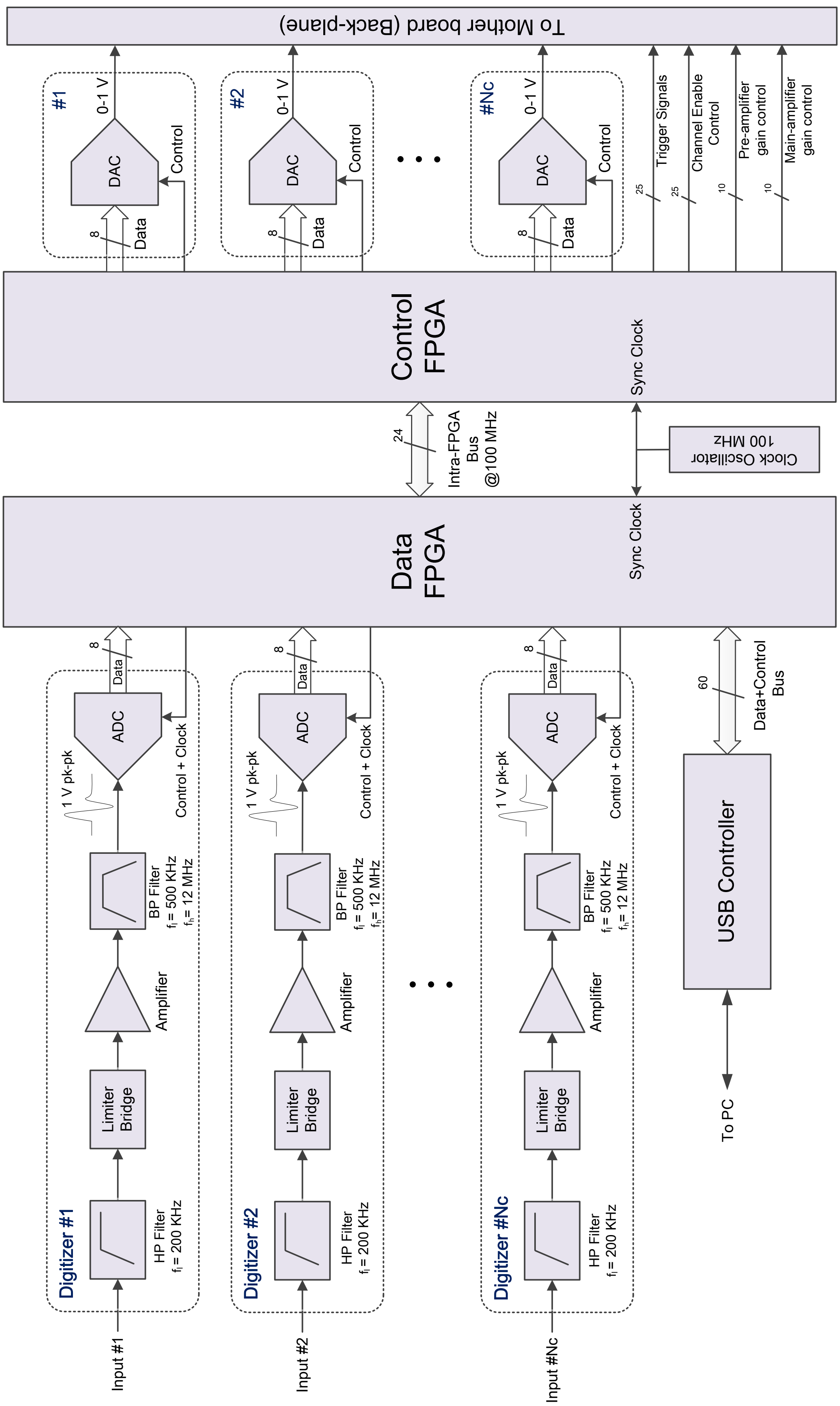

Figure 2.14: Schematic block diagram of Digital back-end module.

was written in VHDL based hardware description language (HDL). It comprises a channel selection logic section that produces sequential control signals for the specific channels after getting the command from the USB controller. The Nc number of ADC outputs are decoded as parallel, single-ended, and binary-offset outputs at 100 MHz speed. After that, all parallel data streams are synchronized with the system clock and stored in the respective block-RAM of the data averaging module when the appropriate control signals are received from the data-FPGA master controller. The master controller handles the overall flow of the data and provides the reconfigurable feature of the code, which is ultimately controlled by the control signals from the USB controller. After completion of coherent averaging, it generates *Data_ready* signal. The master controller makes its decisions based on the trigger signal timing and *Data_ready* signal to control FIFO module and USB-controller interface. The functions of the main blocks are summarized in the rest of this section.

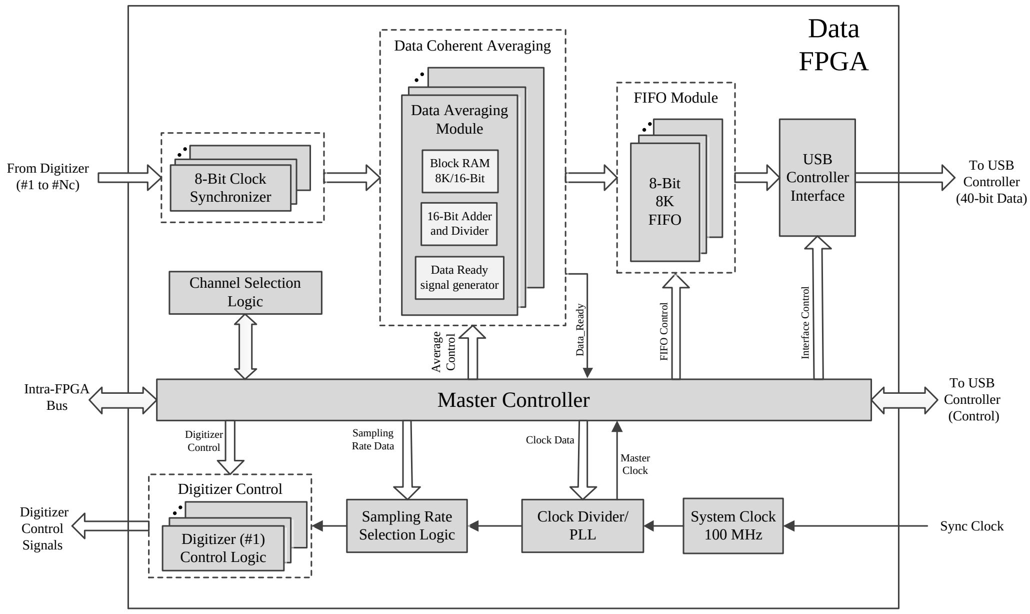

FIGURE 2.15: The overall block diagram of the data-FPGA code

2.3.3.2 Overall scheme of data acquisition

To begin the acquisition process, a user interface control built up in a visual application is initialized first. The GUI software calculates the control parameters such as channel selection, mode selection (P-E/T-R) sampling rate, acquisition memory size and number of coherent averages. During the running acquisition, it also calculates the control parameters for the front-end hardware such as pre-amplifier

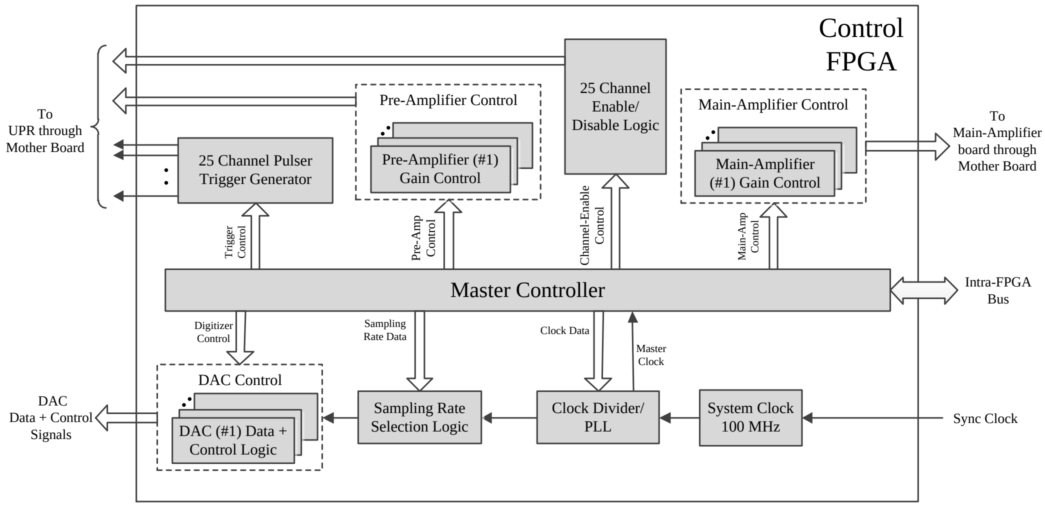

FIGURE 2.16: The overall block diagram of the control-FPGA code.

gain control, common-amplifier gain control, fine-gain adjustable for VGA. These all parameters are calculated based on the respective transducer channel and the scan type (i.e., A-scan, B-scan, and C-scan). After initialization, all parameters are downloaded into the USB controller via the USB interface, which distributes them to both FPGAs and front-end hardware. The pulse trigger signal to the next activated sequence is fed via the control-FPGA after completion of the acquisition process of the formerly activated channel. Some of the control signals are transferred to the control-FPGA through intra-FPGA bus st the speed of 100 MHz.

Once all parameter values are transferred to the control-FPGA, it triggers all the HV pulsers sequentially and parallelly. Then, it simultaneously fills the receiving block-RAM with the corresponding A-scan stream of data until the block-RAM is full. After that, it waits for the next trigger pulse to start filling the block-RAM again. This process is repeated for N_{Avg} times while the data sets of specific channels are averaged simultaneously and transferred immediately to the FIFO module. The FIFO module consists of the Nc number of FIFO blocks with 8-bit, 8-Kbye memory. Afterward, the accumulated data sets from Rx-B FIFO are transferred to the USB controller via parallel GPIF II interface. Once the controller receives all A-scan data sets of all $NcNr$ number of channels, they will be transferred to the PC via USB interface. Thereafter, the post-processing operations like channel demultiplexing, envelope generation, and scan conversions are performed in the host GUI. In the end, imaging is performed in three distinct modes: A-scan, B-scan, and C-scan.

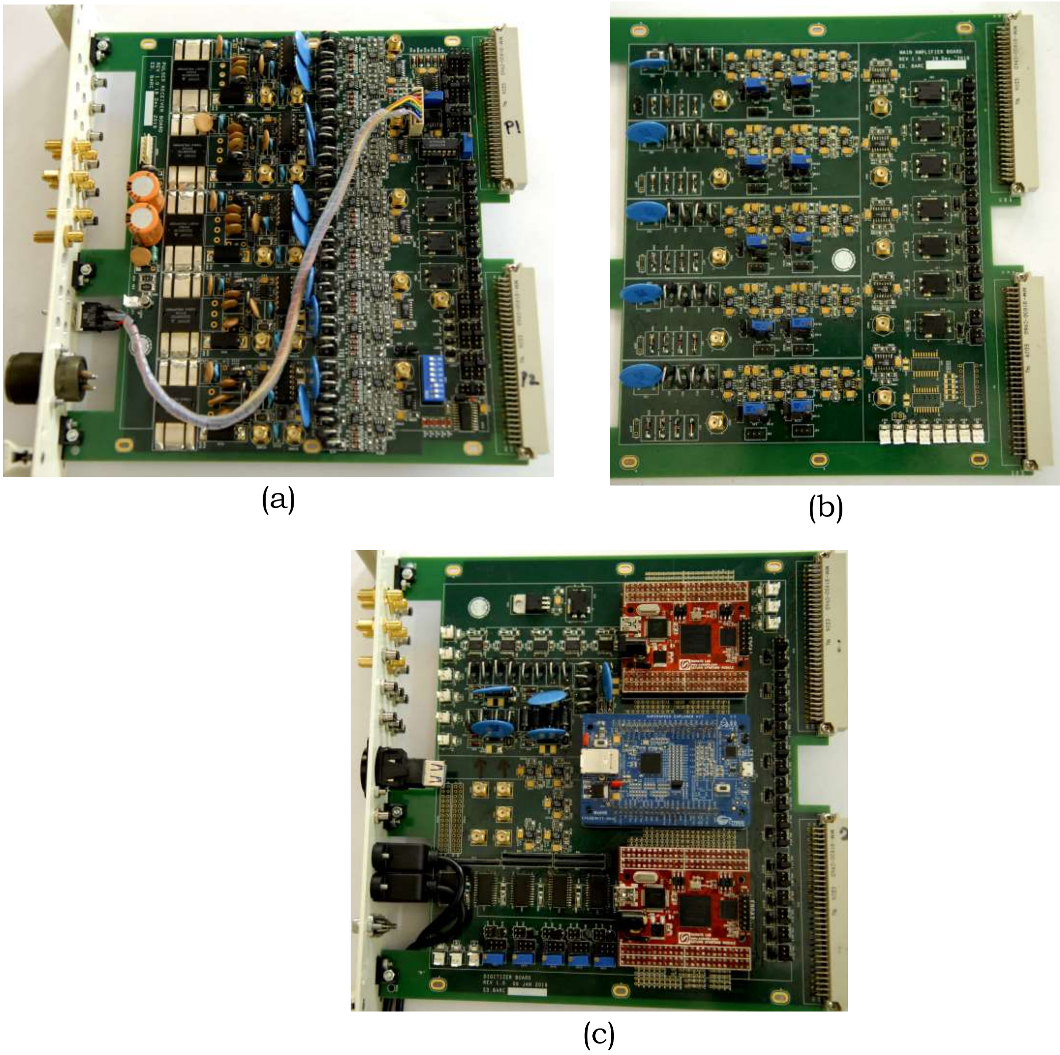

FIGURE 2.17: PCBs of the 25-channel real-time ultrasonic imaging system: (a) 5-channel UPR board, (b) Common-amplifier board and (c) Digital back-end board.

2.3.3.3 Control-FPGA

Control-FPGA contributes the all control logic for the entire multi-channel ultrasonic imaging system. The control signals from the host devices are received through the data-FPGA at the speed of 100 MHz. After receiving controls from intra-bus, the master controller of it generates various time delay signals for the different sections of the control-FPGA. The channel-enable module generates enable/disable signal for the selection of the appropriate channel while simultaneously it produces the low voltage trigger signal for the corresponding pulser. Meanwhile, it generates the simultaneously Nc number (row 1) of trigger signals and enables control signals. Furthermore, this procedure will be repeated for

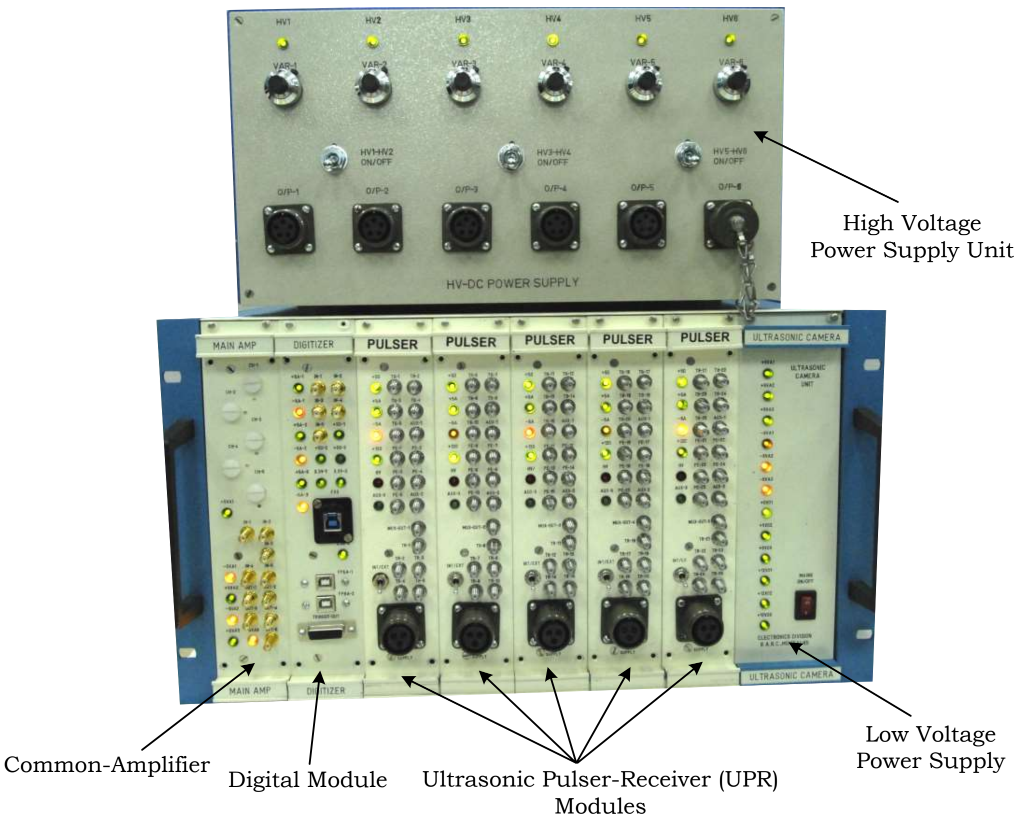

FIGURE 2.18: Photograph of real-time matrix-based ultrasonic camera system (6U-chassis with 7 pluggable PCB modules with built-in LV power supply (LV) DC power supply and separate HV-DC power supply unit (0-550 V)).

every consecutive row (Nr number). The pre-amplifier control section and main-amplifier control section provides the appropriate controls to the $2NrNc$ number of pre-amplifiers and Nc number of main-amplifiers. The controls and data of the Nc number of the DACs (#1 to #Nc) are also provided by the control-FPGA. All these control signals are serially received from the USB controller through data-FPGA using common 8-bit control-bus and 4-bit address bus.All these control signals are serially received by the USB controller through data-FPGA using common 8-bit control-bus and 4-bit distinct address bus. The addresses from address-bus are serially decoded and control/data from the control-bus are stored by the master controller of control-FPGA. Then, all control signals are distributed to the respective section such as the pre-amplifier gain controls are transferred to the pre-amplifier control section. This section classifies the gain controls to the specific pre-amplifier through the motherboard.

The photographs of fabricated, assembled, tested and calibrated PCBs namely a UPR (5-channel pulser-receiver), 5-channel main-amplifier and digital modules are shown in Fig 2.17. For the 25-channel ultrasonic imaging, the five UPR, one common-amplifier and one digital module are fitted in the 6U-double euro motherboard inside the 6U-chassis as shown in 2.18. The motherboard contains two 96-pin euro connectors for every pluggable (PCB) module. The HV-DC power supply unit contains 6 number of isolated and variable power supplies with the range of 0-550 V and resolution of 5V. The final real-time ultrasonic imaging system is capable of accommodating, acquisition and processing of 25-channel ultrasonic transducers for P-E mode and 50-channel ultrasonic transducers for T-R mode. This system is used for the A-Scan, B-Scan and C-Scan imaging of the immersed mechanical components in real-time.

In the next chapter, the one-dimensional simulation modeling of the entire ultrasonic pulse-echo measurement system for immersion application will be presented. The validation results of the entire ultrasonic imaging system provide very close agreement with lossy simulated results.

Chapter 3

Lossless and Lossy Modeling of Ultrasonic Pulse-Echo Measurement System for Immersion Applications: Simulation and Validation

The design, modeling, optimization, and development of the entire ultrasonic imaging system is a complex task which involves an understanding of acoustic physics of transducer, acoustic properties of propagating medium, transmission cables and analog front-end electronics for generating and receiving of ultrasonic signals. This chapter provides one-dimensional simulation modeling of the entire ultrasonic imaging system. For validation purpose, a single channel real-time ultrasonic imaging system has been designed and developed for laboratory application and it contains high voltage ultrasonic spike pulser, high voltage protection circuits, ultrasonic receiver amplifiers, co-axial cables, and the ultrasonic transducer. The lossless and lossy (low-loss) simulations have been performed for ultrasonic transducer and propagation medium using the transmission line model. Effects of non-ideal, frequency-dependent and non-linear components in high voltage excitation circuit (pulser), the receiver circuit and the effects of cables are also considered for modeling and simulation. Validation results of the entire ultrasonic imaging system provide very close agreement with lossy simulated results. This model was intended to simulate and validate the single-channel ultrasonic imaging system such that it will become easy to scale such a single-channel hardware configuration for the multi-channel ultrasonic imaging system development.

3.1 Introduction

Modeling of the immersion-based ultrasonic pulse-echo measurement system is a real challenge because it involves combinations of both mechanical vibrations and non-ideal electrical properties of transducer and transceiver circuits. Use of higher frequencies for NDT inspections are more desirable since they provide higher axial resolution inside the material, but the major challenge is the high attenuation because of adoption of higher frequencies in the liquid medium which reduces the higher penetration depth inside the material. So there is a trade-off between material penetration depth and axial resolution. To handle this situation, one has to increase the dynamic range of the receiver amplifier. But the front-end electronics must have low noise and large signal handling capability for large dynamic range amplifier because it would amplify the random as well as synchronized noise in the path at the same time, degrading the signal-to-noise (SNR) ratio of the receiver path [90]. Cable mismatch and its parasitic losses also add noise to the overall noise figure of the system. An additional difficulty is the high Q of the transducer; it can ring for a long time once it is energized by a high voltage pulse, this requires high electrical damping to shorten the pulse length. On the other hand, the higher number of ringing periods provide lower axial resolution. A big drawback of electrical damping is the loss of energy, which demands a higher input voltage pulse for a given total energy. Another challenge is the acoustic impedance mismatch between the ultrasonic transducer and the front-end electronics like high voltage pulser. The electrical impedance matching network is needed for optimum energy transmission to the ultrasonic transducer [91]. As the higher frequency components of a broadband pulse attenuate more rapidly than the lower frequency components, long water path shifts the center frequency of the transducer downward. This effect increases as the length of the water path increases [92]. Additionally, this frequency downshifts in the received signal will influence the shape of the focal zone because the focused beam diameter and focal zone length of a transducer and lens vary with frequency and signal get attenuated by bandwidth mismatch with analog high-pass filter banks in the receiver circuit. Electronics interfacing with ultrasonic transducer probes normally includes non-linear switching devices and semiconductor networks like MOSFET, MOSFET Driver, Diodes, etc., which influence directly to the excitation high voltage pulses and received echo signals [93]. Conventional approaches of pulse-echo system modeling use the ideal assumptions for the front-end electronics and they do not consider their influences on ultrasonic echoes. These non-ideal frequency dependent electrical components may influence the transducer excitation circuit (pulser) and limiter circuits.

In section 3.2, spice model of the ultrasonic transducer has been described. In section 3.3, both lossless and low-loss leach spice models for propagation mediums have been presented, having approaches in order to consider absorption losses due to the viscosity of the material. In the later section 3.4, the development of spice simulation setup is described in the simulator which covers all the stages of an ultrasonic imaging system like an ultrasonic transducer, high voltage spike pulser, limiter circuit, receiver amplifier, co-axial cables, and propagation mediums. In the last section 3.5, simulation results obtained from both lossless and lossy models are analyzed and compared with the experimental results. Validated results show that lossy simulated waveforms have very good agreements with the experimental measurement.

3.2 Spice modeling of ultrasonic transducer

An ultrasonic transducer contains different material layers. The design, optimization, and development of an ultrasonic transducer are a complicated task which involves the physics of acoustic, acoustic properties of materials, analog electronics. This chapter presents the simulation solution of the ultrasonic transducer which is based on mechanical and electrical analogies. This simulation utilizes a standard simulation tool such as SPICE. The characteristics of transducers depend on the type of mechanical vibration in which it operates and the equivalent circuits present slight differences corresponding to whether the vibration is mainly compressional, shear, flexural, or torsional. Two transducers are reviewed here: the “plate” vibrating in a compressional thickness mode and the “bar” vibrating in a compressional length mode. These are adopted because their equivalent circuits present important differences; other types of transducer usually have equivalent circuits very identical to one of these two. The thickness mode plate is considered in more detail here since it has very significant practical applications in the generation and detection of compressional waves in solids, fluids, and gases. The designer has to simulate the possible effects of backing materials, quarter-wave layers, electrical matching schemes and other design variables on the time response of the transducer former to transducer fabrication.

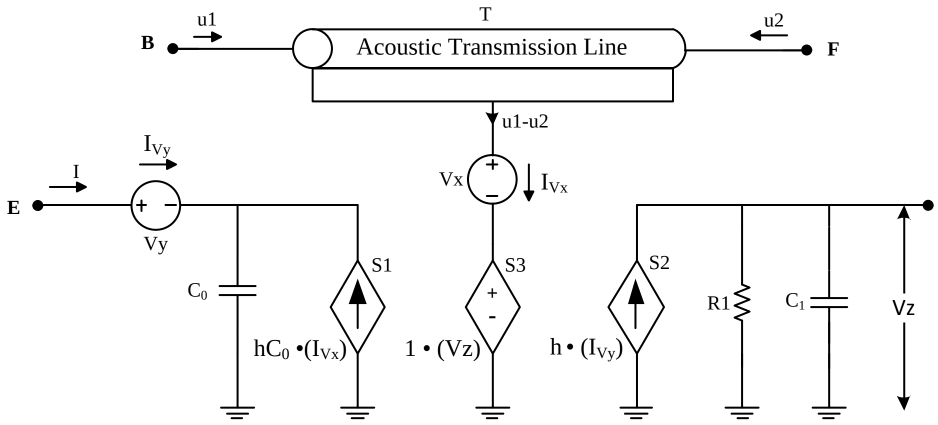

FIGURE 3.1: Leach model of ultrasonic thickness mode transducer.

The thickness mode ultrasonic transducer has been simulated using the leach model as shown in Fig. 3.1. The model consists of three terminals: E (Electrical), F (Front-end) and B (Back-end). Here $u1$ and $u2$ are the acoustic velocity at the back (B) and front (F) surface of the piezoelectric plate, C_0 is the static capacitance between the two electrodes, ρ is the acoustic density, h is the piezoelectric constant and c is the relative elastic constant. Like Redwood's version of the Mason model [39], the circuit also involves a transmission line. The circuit is valid for a balanced line for which both leads exhibit series inductance. The model does not have any transformer and negative value capacitor. The coupling between an electrical analogous circuit and a mechanical analogous circuit is modeled by two controlled sources. The controlled sources measure the voltage (current) at any node (branch) in the circuit and modify the measured signal according to a function and provide an output as voltage or current sources. Here, controlled sources form the connection between the mechanical and electrical section of the model. The controlled source in the mechanical part has the voltage hi/s and electrical part has $h(u1-u2)/s$. The $1/s$ term from the controlled source is eliminated from the Norton equivalent circuit, connecting the capacitor and the controlled current source in parallel. Here, the velocity difference $(u1-u2)$ controls the input current of the $S1$ source with gain hC_0, which can directly affect the current of $S2$ source. $S2$ source is also controlled by the current from C_0 capacitor with gain h. Its output needs to be integrated to obtain the total charge on the electrodes. The capacitor $C1$ and resistor $R1$ are performed as an integrator.

3.3 Spice modeling of propagation medium

The wave propagation medium can be modeled by the various implementations of a transmission model [37, 38, 47, 94–96]. Losses are introduced in the model by simulation of the effect of attenuation of the propagating wave. Diffraction occurs during propagation of acoustic wave since waves do not propagate as a plane wave, but they propagate as a spherical wave, so they spread away as they depart from the emitting source and receiving transducer cannot receive all transmitted energy. Johansson et al. [94] have measured diffraction losses experimentally and introduced this effect into the spice model via the G parameter of the lossy transmission line. The same way absorption losses are modeled by the R parameter of the lossy transmission line [37]. Some researchers have used the analytical expression instead of an experiment to calculate the diffraction losses and inserted them in the spice model via the G parameter [95, 96]. Nonlinearity also plays a significant role during the propagation of the ultrasonic wave in the medium. It is because of variation in ultrasonic phase velocity while propagating into the distorted medium and it causes wave distortion in the time domain. The effect of nonlinearity of ultrasonic wave can be introduced in the spice model from the Burger's equation [41, 97]. Aouzale et al. [97, 98] has proposed a computational spice model for nonlinear ultrasonic wave propagation. Guelaz et al. [41, 99] have presented the VHDL-AMS language based modeling approach for non-linear propagation using the Redwood transducer model. To define the level of nonlinearity, materials have a nonlinearity parameter "B/A". The non-linearity effect occurs mostly in liquid propagation medium having a higher B/A nonlinear parameter. As water has a low B/A compared to other liquids like ethanol, etc., the effect of non-linearity is not being considered for analysis. The absorption of the acoustic wave is the conversion of acoustic energy into heat while propagating thought medium and it is mainly due to the viscosity of the propagating material. So, only the losses due to viscous effect have been considered for simulation of the ultrasonic transducer, propagation mediums, and co-axial cables.

3.3.1 Lossless model of propagation medium

The electrical transmission line equations are given as [100],

$$-\frac{\mathrm{d}V}{\mathrm{d}z} = R + LsI, \quad -\frac{\mathrm{d}I}{\mathrm{d}z} = C + GsV \tag{3.1}$$

Where R is the resistance in the conductors per unit length in Ω/m, L is the inductance in conductors per unit length in H/m; G is the conductance of the dielectric media per unit length in S/m and C is the capacitance between the conductors per unit length in F/m. For lossless transmission line, $R = G = 0$. Comparing electrical transmission line equations (1) with leach model equations as described in [40], obtained lossless transmission line parameters are:

$$L = \rho A_z, \;\; C = \frac{1}{A_z c} \tag{3.2}$$

The phase velocity is given by $u_p = (1/LC)^{1/2} = (c/\rho)^{1/2}$ and the characteristics impedance is:

$$Z_0 = (L/C)^{1/2} = A_z(\rho c)^{1/2} = A_z \rho u_p \tag{3.3}$$

For lossless condition, the delay time T_D (s) for transmission line is given as

$$T_D = l_z/u_p \tag{3.4}$$

Where length l_z (m) is the acoustic distance between two faces of the piezoelectric crystal and it is selected such that the transducer can resonate at its centre frequency. With fixed ends for thickness mode piezoelectric plate, the length l_z is

$$l_z = u_p/2f \tag{3.5}$$

Here u_p (m/s) is the acoustic velocity in the propagating medium and f (Hz) is the center frequency of transducer. In electrical part, the static capacitance is given by,

$$C_0 = \varepsilon^s A_z/l_z \tag{3.6}$$

Where, ε^s (C^2/Nm^2) is the permittivity with constant strain [42]. The controlled sources of $S2$ and $S1$ have gain equals to h and hC_0. Here h (N/C) is the transmitting constant. It is the ratio of the piezoelectric stress constant e_{33} (C/Nm^2) in the direction of propagation and the permittivity with constant strain ε^s for the thickness mode plate:

$$h = e_{33}/\varepsilon^{s} \tag{3.7}$$

3.3.2 Lossy (Lowloss) model of propagation medium

Acoustic losses are important to take into account when transducer having a low Q factor [38]. Lossy transmission line consists of lumped ladders with elements R, L, G and C per unit length dz, as described in (3.8). The propagation behaviour of sinusoidal waves traveling along the z direction can be described with the two complex quantities, the characteristic impedance Z_0 and propagation function γ [100].

$$Z_0 = \sqrt{\frac{R + j2\pi fL}{G + j2\pi fC}} \tag{3.8}$$

$$\gamma = \sqrt{(R + j2\pi fL)(G + j2\pi fC)} \tag{3.9}$$

The real part of γ is the attenuation coefficient α (Np/m) of the transmission line and the complex part β (rad/m) is the phase constant. The phase velocity v_p (m/s) of the transmission line is

$$v_p = 2\pi f/\beta \tag{3.10}$$

For low-loss approximation, the resistive component R is much more less than $2\pi fL$ $(R \leq 2\pi fL)$ and G is much more less than $2\pi fC$ $(G \leq 2\pi fC)$. However, since the loss is very small and when one require the calculation of losses along the transmission line, one can use the value of the attenuation constant α by substituting this condition: $R \leq 2\pi fL$ and $G \leq 2\pi fC$. From (3.9),

$$\gamma = \sqrt{(j2\pi fL)\,(j2\pi fC)\left(1 + \frac{R}{j2\pi fL}\right)\left(1 + \frac{G}{j2\pi fC}\right)} \tag{3.11}$$

$$\gamma = j2\pi f\sqrt{LC}\sqrt{1 - j\left(\frac{R}{2\pi fL} + \frac{G}{2\pi fC}\right) - \frac{RG}{(2\pi f)^2\,LC}} \tag{3.12}$$

Since $RG \leq (2\pi f)^2\,LC$,

$$\gamma = j2\pi f\sqrt{LC}\sqrt{1 - j\left(\frac{R}{2\pi fL} + \frac{G}{2\pi fC}\right)} \tag{3.13}$$

By using the Taylor approximation: $\sqrt{1+x} \approx 1 + x/2$, propagation constant γ can be approximated by,

$$\gamma \approx j2\pi f\sqrt{LC}\left[1 - \frac{j}{2}\left(\frac{R}{2\pi fL} + \frac{G}{2\pi fC}\right)\right] = \frac{1}{2}\sqrt{LC}\left(\frac{R}{L} + \frac{G}{C}\right) + j2\pi f\sqrt{LC} \tag{3.14}$$

The same way, using Taylor approximation: $1/\sqrt{1+x} \approx 1 - x/2$, (3.8) can be approximated by,

$$Z_0 \approx \sqrt{\frac{L}{C}}\left[1 - \frac{j}{4\pi f}\left(\frac{R}{L} - \frac{G}{C}\right)\right] \tag{3.15}$$

Here, the second term in (3.15) is negligible, so the characteristic impedance becomes

$$Z_0 \approx \sqrt{\frac{L}{C}} \tag{3.16}$$

From (3.14), real part of γ is the attenuation coefficient:

$$\alpha = \frac{1}{2}\sqrt{LC}\left(\frac{R}{L}\right) + \frac{1}{2}\sqrt{LC}\left(\frac{G}{C}\right) \tag{3.17}$$

In (3.17), the first term is the coefficient of attenuation (α_v) due to viscous losses, and the second term is the coefficient of attenuation ($\alpha_{thermal}$) due to thermal conduction [37]. As the attenuation occurs mainly due to viscous losses only, attenuation coefficient α becomes:

$$\alpha \approx \alpha_v = \frac{1}{2}\sqrt{LC}\left(\frac{R}{L}\right) \tag{3.18}$$

Substituting Z_0 from (3.16),

$$\alpha = \frac{1}{2}\sqrt{\frac{C}{L}}R = \frac{R}{2Z_0} \Rightarrow Z_0 = \frac{R}{2\alpha} \tag{3.19}$$

The characteristic impedance of acoustic transmission line is given as [37],

$$Z_T = \rho c \sqrt{1 + j2\pi f \tau} \tag{3.20}$$

where τ is the relaxation time, which is the time for pressure to reach the value $1/e$ of its initial value when subjected to a sudden step change. For low-loss condition $2\pi f \tau \leq 1$, acoustic impedance is $Z_T = \rho c$. In an acoustic system analogy, the force is represented by voltage and the velocity is represented by the current. So the relationship between the characteristic impedance of acoustic and electric transmission line is given by,

$$Z_0 = Z_T A_z \Rightarrow \frac{R}{2\alpha} = \rho c A_z \Rightarrow 2\rho c A_z \alpha \tag{3.21}$$

where A_z (m^2) is the beam cross-section area of acoustic waves. For lowloss approximation, transmission line parameters are [37, 38, 95],

$$L = A_z \rho \tag{3.22}$$

$$C = \frac{1}{A_z \rho c^2} \tag{3.23}$$

$$R = 2\rho c A_z \alpha \tag{3.24}$$

$$G = 0 \tag{3.25}$$

In (3.24), α is the coefficient of attenuation due to viscous losses. It is assumed that there is negligible loss due to the diffraction of the pressure field in radial and axial direction. So the conductance parameter is taken as $G = 0$.

3.4 Simulation

The LTspice XVII (Linear Technology Corporation) simulator has been used for simulation of the complete ultrasonic imaging system. The analogous circuit setup is described in Fig. 3.2. The sub-circuit of it contains the PZT-5A ultrasonic transducer. The spice models of all components are described in Appendix A.

A high voltage pulser is being fed by the external pulse generator Vpulse (Trigger). Spice model has been prepared according to MOSFET Driver and N-channel Power MOSFET as shown in Fig. 2.3. Ultrasonic receiver amplifier contains diode bridge

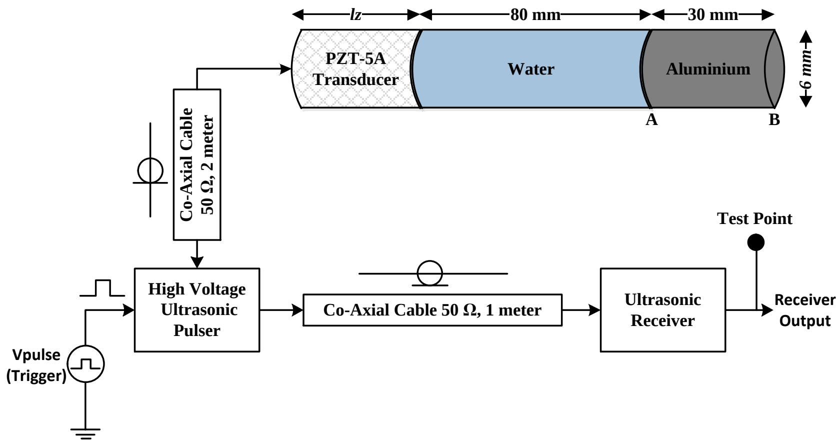

FIGURE 3.2: Spice simulation setup for immersion ultrasonic system.

limiter circuit for high voltage protection and front-end receiver amplifier circuit which is used for amplification of echo signals. Here the amplifier gain of 0 dB has been chosen for simulation as well as for experimentation, because the echo signal has an adequate amplitude for further data acquisition process.

PZT-5A crystal with 6 mm diameter and 10MHz central frequency is used for simulation. The material data of PZT-5A are obtained from [101] as shown in Table 3.1. The material characteristics of PZT-5A modify with temperature. But in this study, constant temperature ($20C$) has been assumed for analysis. The front surface matching layer has been omitted for simulation. The backing material has been considered to overcome the ringing effect, and it is modeled as a backing resistor.

TABLE 3.1: Internal parameters of PZT-5A transducer

Internal parameters of PZT-5A transducer	Values
Crystal diameter ($10^{-3}m$)	6
Crystal thickness ($10^{-3}m$)	0.22
Acoustic density of ceramic ρ (kg/m^3)	7750
Longitudinal velocity in ceramic c (m/s)	4350
Permittivity ε^S (C^2/Nm^2)	73.5×10^{-9}
Piezoelectric stress constant e_{33} (C/Nm^2)	15.8
Crystal central frequency f (MHz)	10

For immersion application, water is utilized as the propagation medium between the transducer and the object under the test. Aluminium object is adopted as a reflecting medium as shown in Fig. 3.2. Here the water path distance is 80 mm and aluminium object has 30 mm thickness. Both water and aluminium object has cross-section diameter of 6 mm. The attenuation coefficient of acoustic waves in a water medium is proportional to the square of the ultrasonic central frequency [1] and it is affected by the frequency downshift effect due to long water path.

$$\alpha(f) = 25.3 \times 10^{-15} f^2 \ Np/m/Hz \tag{3.26}$$

Material data used in simulation for water and aluminium sample are described in Table 3.2 [1].

TABLE 3.2: Parameters of liquid and solid medium

Parameters	Liquid (Water)	Solid (Aluminium)
Acoustic density ρ (kg/m^3)	1000	2700
Longitudinal velocity c (m/s)	1497	6420
Length of propagation $(10^{-3}m)$	80	30
Acoustic attenuation α (Np/m)	2.53 $(@10MHz)$	2.99

The electrical resistance in long cables leads to signal loss which is rising with cable length. For this purpose, in an ultrasonic imaging system where precise tracking of echo amplitude is important, like B-Scan, C-Scan, etc., instrument sensitivity should be calibrated with the real cable being utilized for inspection. For experimentation and simulation, co-axial RG-174U cable with 2-meter length is used between PZT-5A transducer and pulser board. The same cable with 1-meter length is used between pulser and receiver boards. RG-174U has 50 Ω characteristic impedance and 66 % velocity of propagation. The model parameters of co-axial cable are given by [102] as explained below.

$$R = 127.820 \times 10^{-6}\sqrt{2\pi f} \tag{3.27}$$

$$L = 2527 \times 10^{-9} \tag{3.28}$$

$$G = 0.1000428 \times 10^{-12} 2\pi f \tag{3.29}$$

$$C = 101.08 \times 10^{-12} \tag{3.30}$$

The frequency downshift due to long water path reduces the attenuation of co-axial cable because the resistance R is proportional to the square root of the frequency and conductance G is proportional to the frequency of propagation wave.

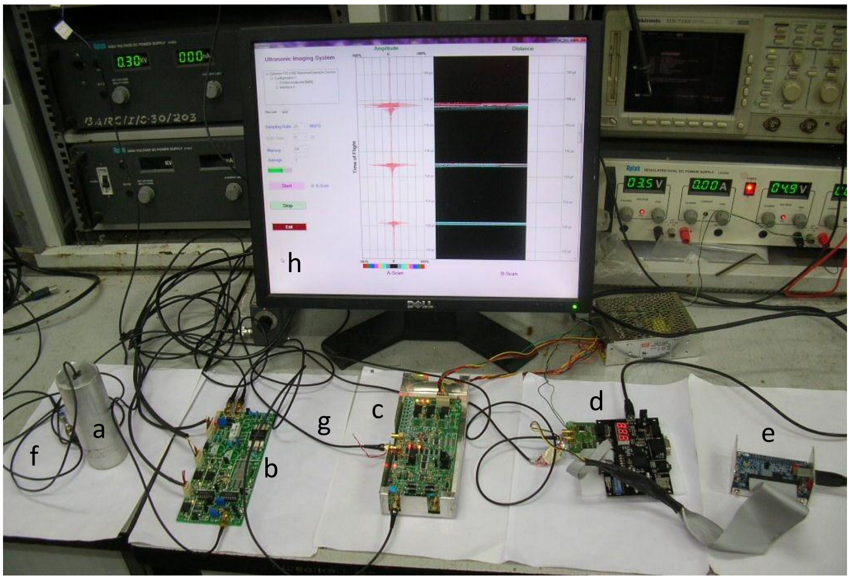

FIGURE 3.3: Experiment setup: (a) aluminum setup with PZT-5A transducer, (b) high voltage ultrasonic pulser board, (c) ultrasonic receiver board, (d) digitizer and FPGA boards, (e) USB controller board, (f) 2 meter RG-174U cable, (g) 1 meter RG-174U cable and (h) GUI application in host PC.

3.5 Results and Discussions

For the ultrasonic pulse-echo experimentation, 10 MHz unfocused un-damped 6 mm crystal diameter water immersed PZT-5A transducer; high voltage ultrasonic pulser with 300V DC supply voltage; ultrasonic receiver with the diode bridge limiter and operational amplifiers; RG-174U cables and aluminium test setup are utilized as shown in Fig. 3.3.

3.5.1 High voltage driving pulser response

High voltage ultrasonic spike pulser has been simulated and tested under three different output load conditions: (1) without external load, (2) with 50Ω load, and (3) with an ultrasonic transducer load. Simulations and experimental results provide satisfactory results under all conditions. Fig. 3.4 shows the comparison between simulation and experimental high voltage spike waveform at a supply voltage of 900 V without piezoelectric transducer load. There is a good agreement between both waveforms in the time domain as well as in amplitude. Here the effect of frequency dependent switching devices, impedance matching circuit and damping network are also considered for the simulation.

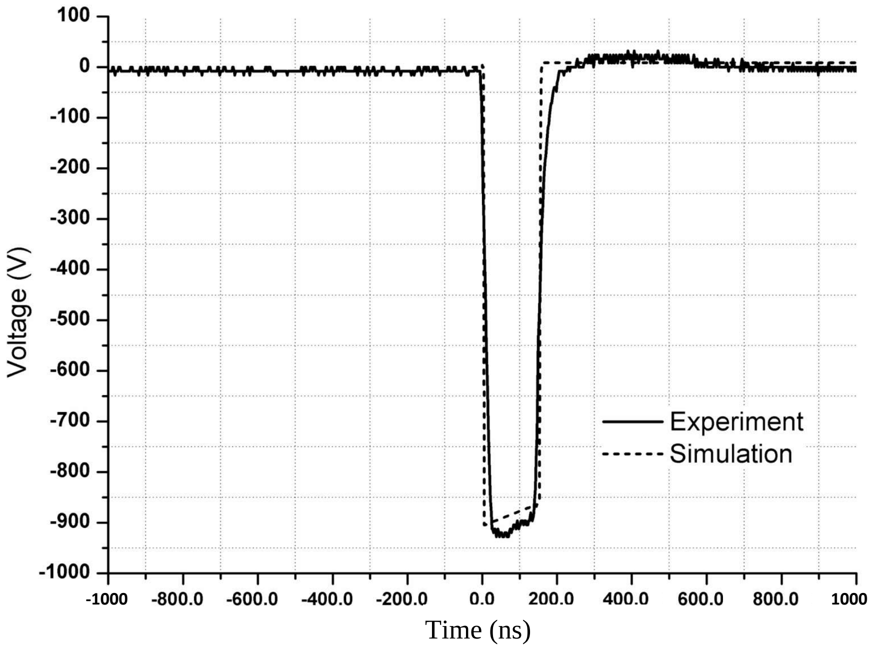

FIGURE 3.4: Output pulse responses of spike pulser with no load condition: $+HV = 900V$,$C_C = 12.3nF$,$R_d = 333\Omega$, $P_w = 130ns$, $PRF = 100Hz$.

3.5.2 Pulse-echo responses from lossless and lossy ultrasonic imaging system

Lossless and Lossy spice simulations of the ultrasonic transducer, propagation mediums, and co-axial cables have been performed using lossless and low-loss transmission line models, respectively. The front-end electronics have equal responses from both lossless and lossy simulations for constant frequency. Spice models of both lossless and lossy PZT-5A transducer, water, and aluminium propagation medium and RG-174 co-axial cables are provided in Appendix. Fig. 3.5 provides the simulated (lossless and lossy) and experimented echo signal, which is reflected from the front surface of aluminium test block. For simplification, the diffraction and non-linearity effect of propagation medium is not considered for modeling. The difference between both simulations are the following: for lossless simulation, no losses were considered, whereas, for lossy simulation, mechanical losses in the piezoelectric material, absorption losses in the propagation medium due to viscosity, and attenuation in water depending on the frequency (f^2) were considered. From the simulation, it is observed that the experimented results are marginally matches with the lossy simulated results.

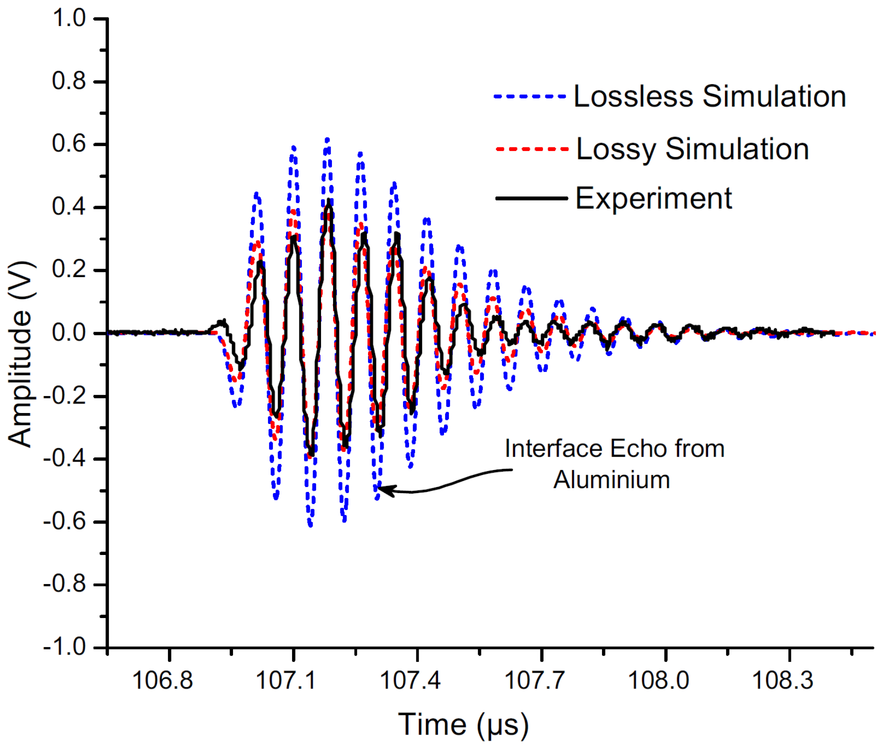

FIGURE 3.5: Lossless and Lossy echo responses of the entire ultrasonic imaging system and comparison with the measured echo response.

3.5.3 Cable length effects on pulse-echo waveforms

The majority of ultrasonic inspections are performed in the frequency range from 200 kHz to 20 MHz, with transducer co-axial cables whose length does not extend beyond just about 2 meters. On the other hand, in operations relating higher experiment frequencies or longer cables, it is necessary to be familiar with the probable effects of increasing cable length and adjust them as needed. As the transducer cable is part of the total distance or thickness measurement during the inspection, the electrical transit time should also be considered. Long cables can add considerable time to the echo signal measurement and can generate distance measurement errors. Effects of cable length on pulse-echo time domain waveforms have been calculated at the constant temperature and constant 10 MHz frequency. Here the only effect of co-axial cable between high voltage pulser and ultrasonic transducer has been considered because the cable connection between the transducer and front-end electronics play a significant role for the immersion-based ultrasonic application. The simulated pulse-echo responses with different cable lengths as depicted in Fig. 3.6, demonstrate that cable length causes the effect on voltage amplitude as well as on phase delay of the echo signal in time domain. Fig. 3.7 indicates that the normalized amplitude of the pulse-echo signals has been

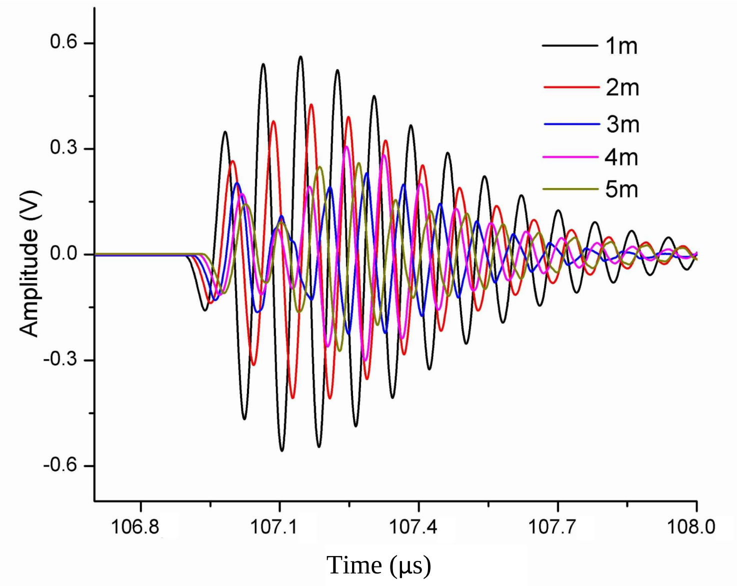

FIGURE 3.6: Pulse Echo waveforms of the complete ultrasonic imaging system with different cable lengths.

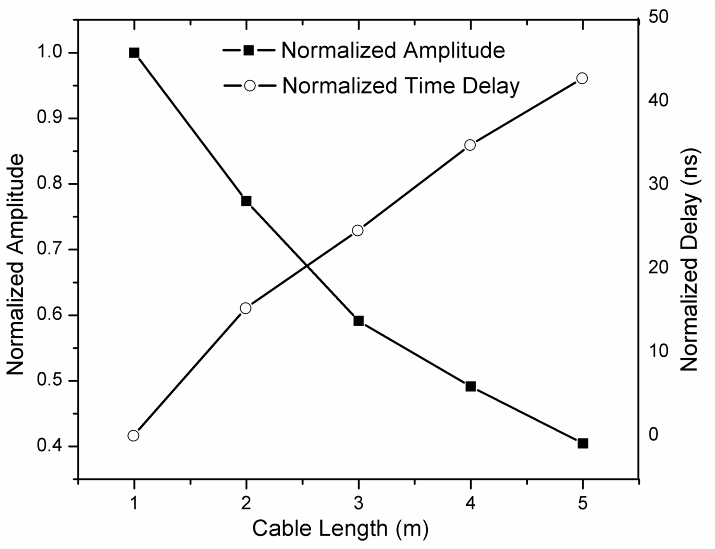

FIGURE 3.7: Cable length effect on the pulse echo amplitude and time delay.

dropped due to the series resistance of the lossy cable. The phase delay has been raised by cable length and it is calculated as [103]:$t_p = len\sqrt{\varepsilon_r}/c$, where len is the length of cable, ε_r is the dielectric constant of the dielectric material occupying the area between the center and the outer conductor of the coaxial cable and c is the light velocity in the vacuum.

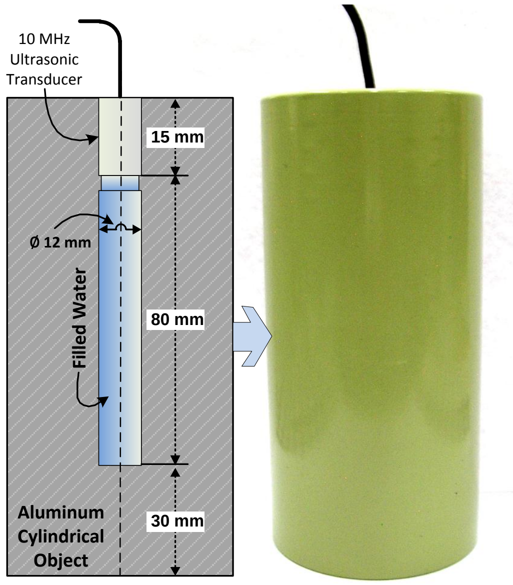

FIGURE 3.8: Aluminium test block of 40 mm diameter for testing of pulse-echo response with transducer assembly diameter: 10 mm and PZT-5A crystal diameter: 6 mm.

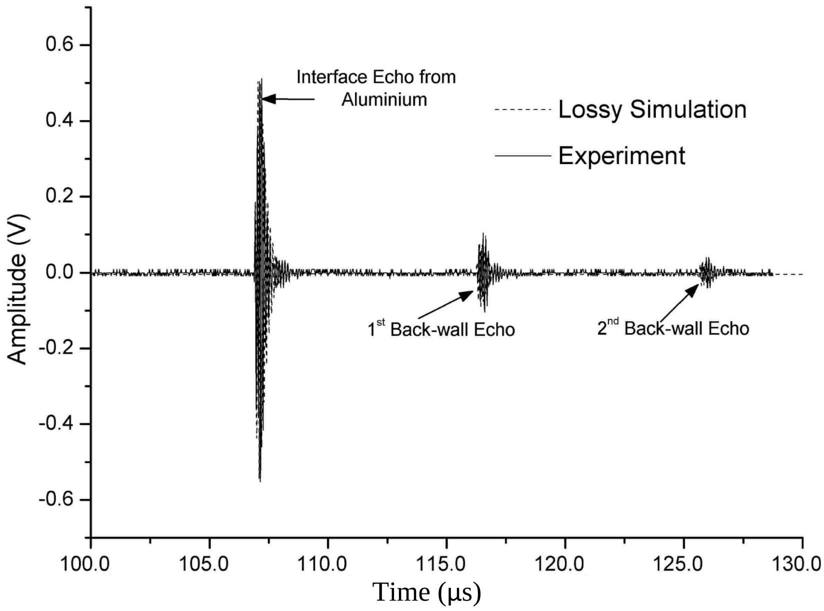

FIGURE 3.9: Time domain pulse-echo responses from aluminum test block by lossy simulation and experimentation.

3.5.4 Validation of pulse-echo simulation results in time domain

Aluminium block based experimental setup has been constructed in the laboratory for pulse-echo measurement as shown in Fig. 3.8. The setup consists of 80

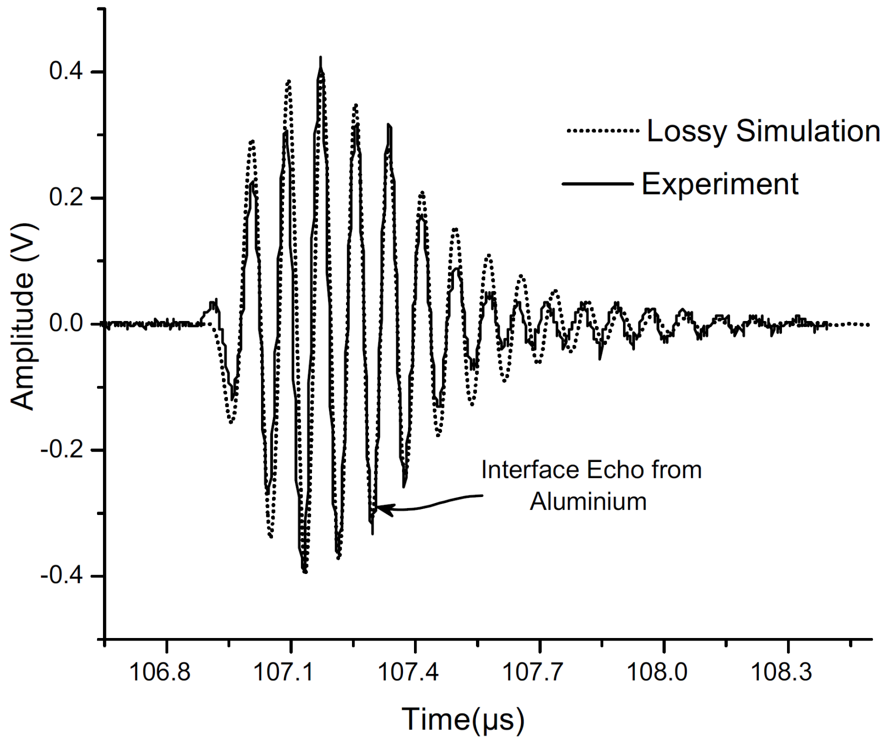

FIGURE 3.10: Amplitude comparison of both lossy simulated and measured interface echo signal.

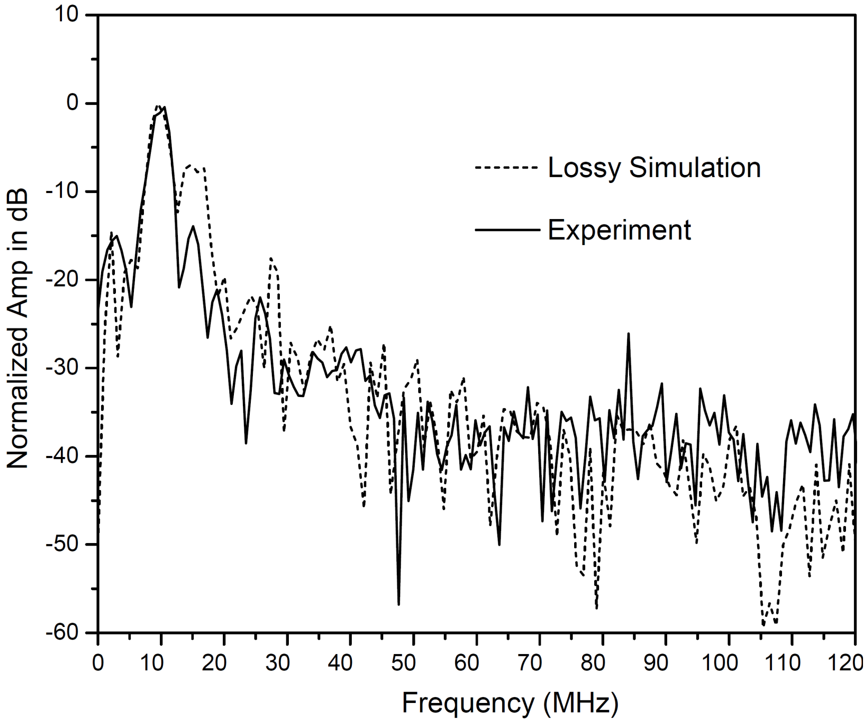

FIGURE 3.11: Frequency domain responses (FFT) of both simulated and measured echo signals.

mm water path and 30 mm aluminium path for pulse-echo measurement. So after high voltage excitation of the ultrasonic transducer, the first echo is observed from the water-aluminium interface and the second echo is observed from the back wall surface of aluminium test block. Fig. 3.9 provides pulse echo responses from the aluminium block immersed in water. The time of flight (TOF) of the detected echo signals from both simulation and experiment provides very close agreements. The interfaced echo response is depicted in Fig. 3.10. The detected simulated and measured voltage amplitudes of pulse-echo waveforms are almost identical and observed that there is a minor mismatch between both results due to diffraction and non-linearity effects in the medium which has not been considered for spice simulation. Frequency response curves of the received echo signal from the simulations and experimentations are shown in Fig. 3.11. It was measured using a rectangular window with a sampling interval of 0.5 ns. The overall shape of the simulated frequency response and the shape of the experimental data are matched. Both have the highest normalized amplitude peak at 9.22 MHz frequency. The measured -3dB bandwidth is 1.4 MHz from frequency response. So the quality factor of the ultrasonic transducer is 6.5857, which is acceptable.

In the next chapter, the two-stage noise filtering technique for both coherent and incoherent noise is proposed. The first stage is described in chapter 4 and the second is described in chapter 5. In chapter 4, the proposed novel hardware (FPGA) implementation of the coherent averaging architecture for the reconfigurable ultrasonic NDT system is presented.

Chapter 4

Signal Processing for SNR Enhancement of Ultrasonic Signals

This chapter provides the various causes of noise in ultrasonic data. Furthermore, this chapter proposed novel hardware (FPGA) implementation of the coherent averaging architecture for the reconfigurable ultrasonic NDT system. The proposed hardware architecture uses the addressing-based shifting technique for the addition operation and Radix-2 non-restoring algorithm for the division operation. Since the amount of hardware required by the proposed averaging scheme is independent of the number of averages, it supports on-the-fly control on the number of averages. The performance of implemented coherent averaging has been presented by various applications such as removal of RF random false-echoes, smoothing of A-scan waveforms and speckle removal of B-scan images.

4.1 Two-stage noise filtering scheme

Ultrasonic inspection is one of the most successful and widely used non-destructive testing (NDT) technique for quality assessment, identification, detection, and characterization of flaws in metal structures. The signal reflected by discontinuities/flaws includes the information about the anomalies, based on which one can identify its location, size, and category.

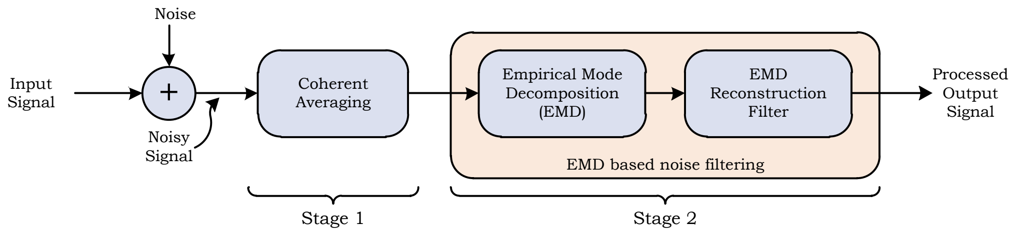

FIGURE 4.1: Two-stage filtering scheme for SNR enhancement of ultrasonic signal.

As explained in Section 1.5.3, there are two types of noise exist in the ultrasonic pulse-echo signal while performing ultrasonic testing: coherent noise and incoherent noise [60–63]. The noise coming from the stationary scatters exhibits no change in amplitude and phase variation with time. It is called the coherent noise [60, 63]. On the other hand, incoherent noise is randomly distributed noise. The correlation between different incoherent noise signals is quick low [62]. Because of its temporal incoherence of noise, repeating the same measurement and averaging it with a previous measurement, provides a reduction in noise by a factor which is ordained by the square-root of the number of averages. Therefore, in the absence of the time limit, any SNR is attainable as long as incoherence with time is satisfied. However, averaging of the signal is not advantageous for all conditions. Specifically, repeating as a measurement initiates the same scatterings events inside the material as it remains stable, consequently repeating the similar measurement of both noise and signal. Correspondingly, in an attempt to recover a loss in SNR, raising the excitation signal amplitude simply raises the noise linearly and therefore retains the same SNR in the presence of coherent noise. [60].

Thus, the main aim is the noise suppression and echo identification of ultrasonic pulse-echo signals in real time using the developed experimental setup under noisy environment. For those reasons, the noise filtering algorithms in the presence of both incoherent noise and coherent noise have been proposed and implemented. The incoherent noise will be filtered by the coherent averaging algorithm (stage 1) and further, the coherent noise will be filtered by the empirical mode decomposition algorithm (stage 2) as shown in Fig. 4.1

In section 4.2, the analysis and basic requirements for reconfigurable hardware architecture of the coherent averaging is presented. In section 4.3, the FPGA implementation of the reconfigurable coherent averaging architecture is presented for the SNR enhancement and compared with the conventional architecture. The single ultrasonic imaging system designed and developed by the authors for the experimentation is briefly elaborated in section 4.4. The experimented pulse-echo signal has been processed through the proposed real-time, coherent hardware and the results are evaluated with different averaging values as described in section 4.5.

4.2 Coherent averaging and implementation

Ultrasonic imaging involves beam-forming technique when various delayed signals from various transducers are combined to enhance the detectability but it is the most complex technique and requires more hardware. Therefore, for the SNR enhancement, the coherent averaging scheme is adopted [104–107]. In the coherent averaging process, the multiple sets of samples of the noisy experimented signal are collected synchronously and the time phases of each accumulated set of samples must be identical. The main condition is that the acquired signal waveforms should remain coherent in time-domain. However, the frame jitter reduces this coherence [108] and the best procedure of its contraction is that there must be synchronization between pulser excitation trigger and data acquisition unit of the system[66]. Here, the novel parallel hardware architecture is proposed which has utilized minimum hardware for the complete coherent averaging operation compared to the previous hardware architecture as explained in Section 1.5.3.

4.2.1 Coherent averaging

Assume that a noisy signal $x(t)$ is superimposed by the actual signal $x_a(t)$ and the random noise $n(t)$: $x(t) = x_a(t)+n(t)$. The aim is to find the approximate $X_{Avg}(t)$ of the noisy signal $x(t)$ using the coherent averaging. The noise $n(t)$ has following properties: $n(t)$ is stationary, $n(t)$ is normally distributed with zero mean and variance σ^2, and the samples of $n(t)$ are uncorrelated with each other and also with the sample rate. After the digital conversion with sampling time T_s, the input signal $x(t)$ can be described as

$$x(t + kT_s) = x_a(t + kT_s) + n(t + kT_s) \tag{4.1}$$

where $0 \leq k \leq N_R - 1$ and N_R is the total number of accumulated data samples. The coherent averaged signal $X_{Avg}(t)$ is given as

$$
\begin{aligned}
X_{Avg}(t) &= \frac{1}{N_{Avg}} \sum_{k=0}^{N_{Avg}-1} x(t+kT_s) \\
&= \frac{1}{N_{Avg}} \sum_{k=0}^{N_{Avg}-1} x_a(t+kT_s) + \frac{1}{N_{Avg}} \sum_{k=0}^{N_{Avg}-1} n(t+kT_s)
\end{aligned}
\tag{4.2}
$$

Since it is assumed that actual signal $x_a(t)$ is invariant with time. So (4.2) can be written as [109]

$$
X_{Avg}(t) = x_a(t) + \frac{1}{N_{Avg}} \sum_{k=0}^{N_{Avg}-1} n(t+kT_s) \tag{4.3}
$$

It indicates that coherent averaging can reduce the undesirable random noise from the noisy signal. In order to observe the uncertainty behavior of coherent averaging, it is necessary to compare the standard deviation of the averaged signal (σ_{Avg}) with the standard deviation of the input noisy signal (σ_x).

$$
\sigma_{Avg} = \frac{\sigma_x}{\sqrt{N_{Avg}}} \tag{4.4}
$$

It illustrated that the averaged data $X_{Avg}(t)$ will not vary much compared to the original signal $x(t)$. Therefore, the $X_{Avg}(t)$ data set is less noisy than any $x(t)$ data set, and further if we increase the average number N_{Avg}, the more closely an individual signal $X_{Avg}(t)$ will match with the actual value of $x(t)$. The improvement in the signal-to-noise ratio of signal amplitude is given by the signal-to-noise ratio gain factor (SNR_{gain}) as stated below [109, 110].

$$
\begin{aligned}
SNR_{gain} &= \frac{\sigma_x}{\sigma_{Avg}} = \sqrt{N_{Avg}} \\
SNR_{gain}(dB) &= 20 \log_{10} \sqrt{N_{Avg}} = 10 \log_{10} N_{Avg}
\end{aligned}
\tag{4.5}
$$

Through averaging, (4.5) stated that signal-to-noise ratio improvement is proportional to the square root of the number of averages.

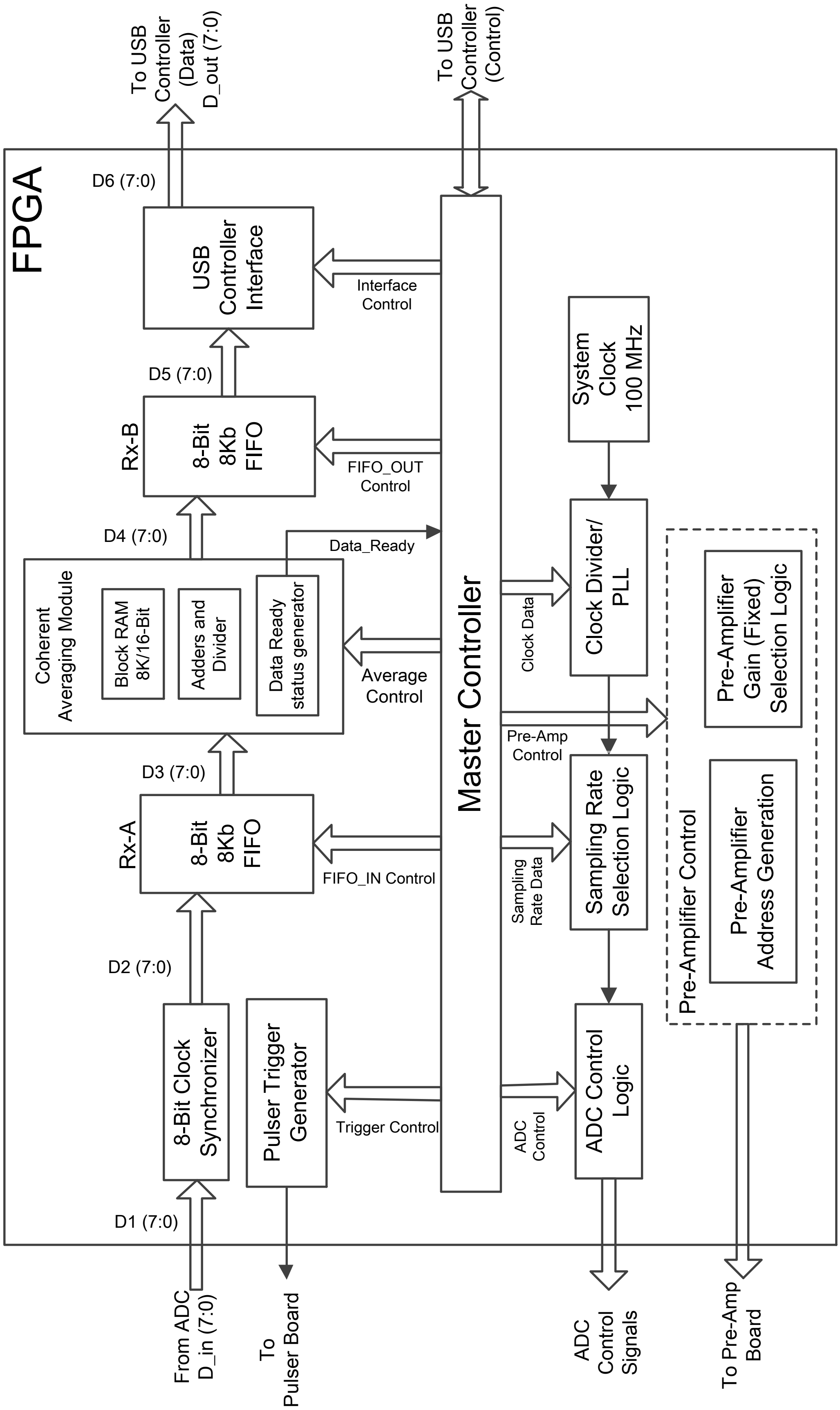

FIGURE 4.2: Block diagram of FPGA code.

4.3 Hardware (FPGA) implementation of coherent averaging

The transformation of electronics technology has created accessible devices such as field-programmable gate arrays (FPGAs) and digital signal processors (DSPs) consisting of banks of gates and/or multiple cores, which have a capability to perform concurrently in terms of data processing and control of other front-end hardware systems [111, 112]. The block diagram of the FPGA code for the single channel system is shown in Fig. 4.2. The code was written in VHDL based hardware description language (HDL). It comprises pulser trigger generators that produce sequential pulses after getting the command from external controller. The ADC outputs are decoded to parallel single-ended outputs at 100 MHz sampling frequency. After that, the parallel data stream is synchronized with the system clock and stored in the Rx-A FIFO when the appropriate control signals are received from the FPGA master controller. Later, it is transferred to the data averaging module for coherent averaging process. The master controller handles the overall flow of the data and provides the reconfigurable feature of the code, which is ultimately controlled by the control signals from USB controller. After completion of coherent averaging, it generates *Data_ready* signal. The master controller makes its decisions based on the trigger signal timing and *Data_ready* signal to control the Rx-A and Rx-B FIFO, to enable/disable pre-amplifier channel, and to select memory size data storage. The functions of the main blocks are summarized in the residue of this section.

The two types of hardware-based architecture of coherent averaging are presented: Conventional and Proposed. Both provide hardware averaging of each subsequent A-scan data stream, as well as there is a perfect clock synchronizations between the ultrasonic pulser trigger and scan acquisition trigger. This hardware-based averaging architecture can be reconfigured on-line during the scanning operations by continuously downloading the parameters from host PC. After completion of each averaging operation, FPGA notifies the host via proper interface.

4.3.1 Conventional architecture of coherent averaging

For the N_{Avg} number of averaging operations, a selected channel of the pulser is triggered by N_{Avg} times with the pulse repetition frequency (PRF) of $1\,kHz$. So after every pulse repetition time (PRT= $1ms$), the trigger will be generated for the

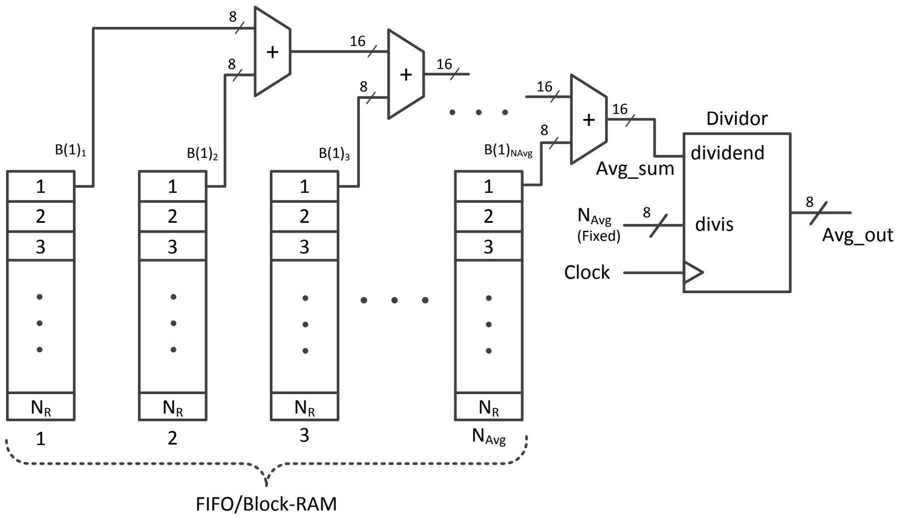

FIGURE 4.3: Conventional architecture of data averaging scheme.

individual channel. Then the RF pulse-echo signal is amplified, digitized via ADC, accumulated A-scan data in Rx-A FIFO and these processes will be repeated for N_{Avg} times in every $1\,ms$ interval. After that, all RF A-scan data are coherently averaged by the conventional architecture as illustrated in (4.3).

The time complexity function is analyzed for conventional averaging scheme using the hardware architecture as indicated in Fig.4.3. First, it accumulates the samples of one scan (frame) and each byte of it is added with the formerly accumulated respective byte of the previous scan sample. After summing of all bytes of consecutive A-scans, the each bytes of the summed data are divided by the number of average N_{Avg}. The used operations include shifting (SFT), addition/subtraction (ADD), and division (DIV). Let each of the input sample $B(i)_j$, output sample $Byte_j$, and average number N_{Avg} have same bit-length n number. The RAM memory comprises total N_R registers with each involving n-bit length. During each trigger pulse transition, the total time required for the shifting operations are equal to $N_R \cdot N_{Avg} \cdot SFT$. But it is assumed that the all acquired data samples are accumulated in the Rx-A FIFO during the time duration of PRT. Thus, the total time required for the shifting operations are equal to $N_{Avg} \cdot PRT$ because the PRT is always greater than the total acquisition time $(PRT > N_R \cdot SFT)$. Likewise, the number of addition requires $(N_{Avg} - 1) \cdot N_R \cdot ADD$ operations. After the completion of addition, the division is performed, and it requires $N_R \cdot DIV$ operations. Therefore, the total number of operations or time needed by the conventional averaging architecture is

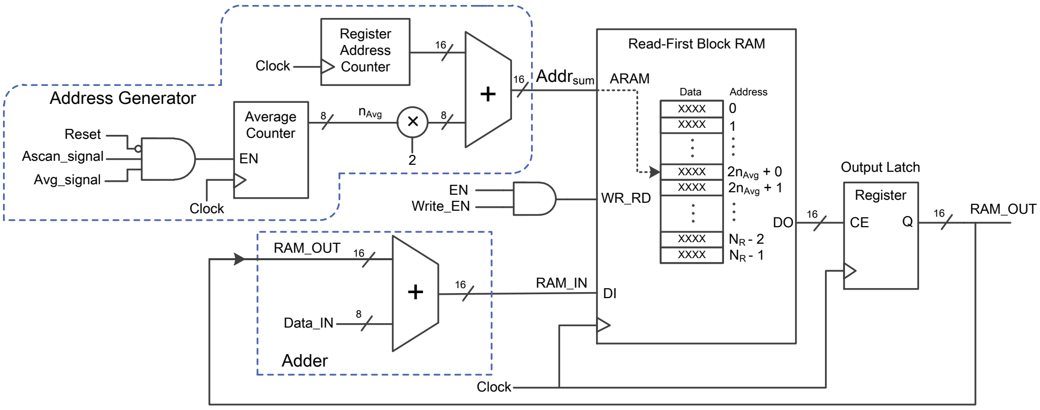

FIGURE 4.4: Data accumulation and summation schemes of coherent averaging module.

$$T_{C-Avg} = PRT \cdot N_{Avg} + ((N_{Avg} - 1) \cdot ADD + DIV) \cdot N_R \tag{4.6}$$

Here, it is assumed that all arithmetic operations require the same amount of time $ARTH$. So (4.6) can be written as

$$\begin{aligned} T_{C-Avg} &= PRT \cdot N_{Avg} + ARTH \cdot N_{Avg} \cdot N_R \\ T_{C-Avg} &= (PRT + N_R \cdot ARTH) \cdot N_{Avg} \end{aligned} \tag{4.7}$$

The total memory storage required for the conventional average module are $N_{Avg} \cdot N_R$ byte as shown in Fig. 4.3. The summing and division operations need total $N_{Avg} - 1$ number of adders and 1 divisor, respectively.

4.3.2 Proposed hardware based implementation of coherent averaging architecture

Here the unique architecture for the data averaging scheme is proposed that requires minimum hardware and less processing time. For that purpose, a single-port, read-first block-RAM with $2N_R$ ($16K$) bytes of memory is adopted. The summation process of data averaging module is shown in Fig. 4.4. Unlike the conventional average scheme, it requires only $2N_R$ memory storage. The control signals of block-RAM like enable and write signals are controlled by the master controller. The major benefit of this scheme is that the data summing operation is performed for every byte before the writing operation. In this mode of block-RAM, the data stored in the previous address comes out in the output latch, while the input data is being accumulated in a memory of same address. Therefore, it is also called a *Read-Before-Write* mode of block-RAM. It requires two rising edge clock cycles. The first rising edge clock is for read and second is for write operations. For such a case, it is impractical to add (8-bit summation) the incoming data with the formerly accumulated block-RAM data during the execution of same clock cycle. To overcome this problem, the addressing based method is proposed to shift the upcoming block-RAM address using (4.8) such that the already accumulated output latch data and the input data sample can be added during the rising edge of the same clock cycle. Later, the added data will be written into the block-RAM during next consecutive clock cycle. This approach reduces the additional time needed for summing operations. The input block-RAM address for summing operation is expressed by the following equation.

$$SAddr = (n_{Avg} \times 2) + Cont_{Addr}$$
$$Addr_{sum} = \begin{cases} SAddr & \text{if } SAddr < N_R \\ SAddr - N_R & \text{if } SAddr \geq N_R \end{cases} \tag{4.8}$$

where $0 < n_{Avg} \leq N_{Avg} - 1$ and $0 \leq Cont_{Addr} \leq N_R - 1$. The n_{Avg} is the number of trigger event during the n_{Avg} scan operations. The maximum block-RAM address is $N_R - 1$. If the block-RAM address is greater than N_R, it will start from the initial memory address as described in (4.8). The implementation of this condition is not displayed in Fig. 4.4. Before transferring the data samples to the block-RAM, the A-scan data samples are added with the previously latched block-RAM data (RAM_OUT) and accumulated in the same address location as described in below equation.

$$RAM\_IN(Addr_i) = RAM\_OUT(Addr_i) + Data\_IN(Addr_i) \tag{4.9}$$

where $0 \leq i < N_R - 1$, $Data\_IN$ is the input 8-bit data sample, RAM_IN is the input 16-bit data sample of block-RAM and RAM_OUT is the output 16-Bit latch data of block-RAM.

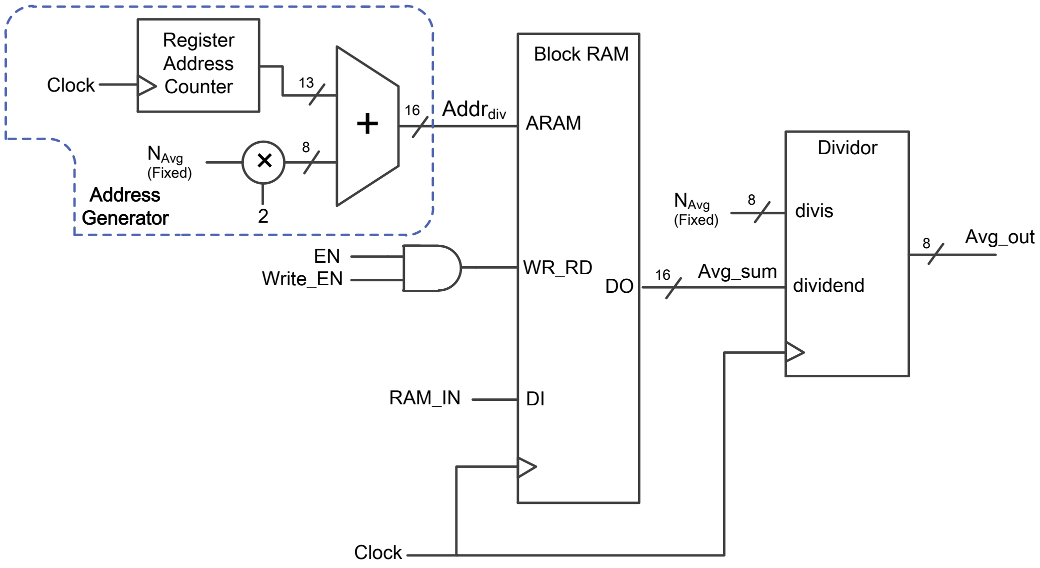

FIGURE 4.5: Division scheme of coherent averaging module.

4.3.2.1 Division implementation

The division is the most complex procedure and toughest to speed up because hardware designs are equally larger and more complex. Here the Radix-2 non-restoring algorithm is adopted for the division operation. The design of implemented division algorithm is fully pipelined. Assume that the calculated quotient Avg_out and reminder R as n-bit binary integers for the given dividend Avg_sum (Q) and divisor N_{Avg}. The pseudo-code for the implemented Radix-2 non-restoring algorithm is illustrated below [113].

Step 1. Assume that $Avg\_sum = N_{Avg} \times Q + R$; $N_{Avg} \neq 0$;

Step 2. $D = |Avg\_sum|$; $R_n = N_{Avg}$;
For $i = n-1$ to 0 Do
If $R_{i+1} = 0$ then Do
$Q = [q_{n-1}\, q_{n-2} \cdots q_0] = [0\,0 \cdots 0]$; $R = 0$;
Go to $STOP$;
End If
If $R_{i+1} < 0$ then Do
$q_i = -1$ else $q_i = 1$;
End If
$R_i = R_{i+1} - q_i \cdot 2^i \cdot D$;
End For

Step 3. $Q = [q_{n-1}\, q_{n-2} \cdots q_0]$;

If $Avg\_sum > 0$ and $R_0 < 0$ then Do

$R = R_0 + D$; $Q = Q - 1$;

Else If $Avg\_sum < 0$ and $R_0 > 0$ then Do

$R = R_0 - D$; $Q = Q + 1$;

Else $R = R_0$;

End If

Step 4. $STOP$: If $Avg\_sum < 0$ then Do

$X = -Q$ else $X = Q$;

End If

Step 5. Avg_out=2's complement of X

Since the X is obtained as sequence of -1 and 1 (Step 4), the final averaged output $Avg\_out = [a_{n-1}, a_{n-2}, \cdots, a_0], a_i \epsilon \{0, 1\}$ can be obtained by the 2's complement representational of the X (Step 5). Thus, after every summing and writing of A-scan raw data, final summing output Avg_sum is divided by the number of average N_{Avg} as presented in Fig. 4.4. The RAM address for the division operation is given as:

$$DAddr = (N_{Avg} \times 2) + Cont_{Addr}$$
$$Addr_{div} = \begin{cases} DAddr & \text{if } DAddr < N_R \\ DAddr - N_R & \text{if } DAddr \geq N_R \end{cases} \tag{4.10}$$

where N_{Avg} is fixed and $0 \leq Cont_{Addr} \leq N_R - 1$.

4.3.2.2 Timing of control signals

The proposed architectural flow is controlled by the finite state machine (FSM) as displayed in Fig. 4.7. The control unit of the averaging circuit uses three timing control signals as shown in Fig. 4.6. Here, the $Total\_avg\_signal$ determines the full data acquisition window width and it totally depends on the total number of averages. Likewise, the $Ascan\_signal$ represents the trigger pulse repetition signal width which is constant during the each transducer excitation and the Avg_signal describes the signal width of total accumulated acquisition samples in the FIFO. The time width t_2 described the frame or scan time span between each successive trigger event of the transducer and it has to be wide enough such that the high

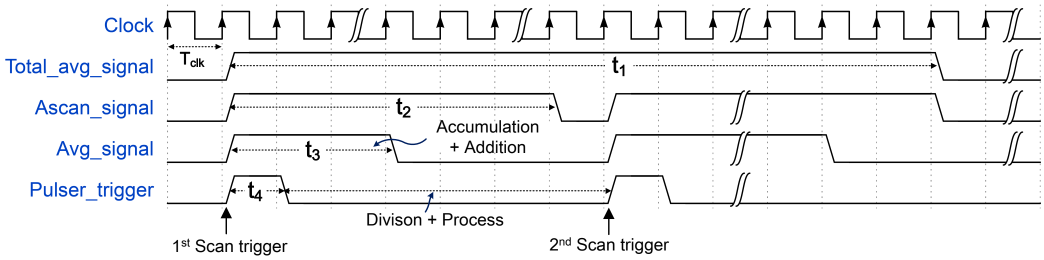

FIGURE 4.6: Timing diagram for proposed coherent averaging architecture

voltage pulser can take sufficient time to set in the original state. The time width t_3 of each scan is depended on the number of acquisition samples. The conditions that applies to t_3 is that it must not exceed the available FIFO depth and it should be less than the PRT ($t_3 < PRT$). It is essential to define the number of averages before the start of data acquisition because it is responsible for the time width t_3 and it is always greater than the PRT ($t_1 > (t_2, t_3)$). The choice of the average number N_{Avg} is very important since it causes the trade-off between the total available data acquisitions time t_1 and the expected SNR_{Avg} as described in (4.5). The T_4 represents the pulse width of the pulser trigger signal. The timing parameters are calculated as per the following equations.

$$\begin{aligned} t_1 &= N_{Avg} \cdot PRT \\ t_2 &= PRT - 1 \cdot T_{clk} \\ t_3 &= \text{int}\left[N_R/f_s\right] \\ t_4 &= (1 \cdot T_{clk}) \text{ to } (15 \cdot T_{clk}) \end{aligned} \tag{4.11}$$

4.3.2.3 Comparisons with conventional averaging scheme

The total shifting operations required for the data writing/accumulating operation using the proposed averaging architecture are $PRT \cdot N_{Avg}$ that is analogous to the conventional averaging scheme. But the major advantage over the previous method is that the both operations (summing of data samples and reading of output latch data samples) are executed simultaneously during the same clock cycle. The number of operations required for the summing operations are $(N_{Avg} \cdot N_R) \cdot ADD$. After the completion of the addition operation, division is performed, and it requires $N_R \cdot DIV$ operations. Therefore, the total number of operations or time taken by the proposed averaging architecture is

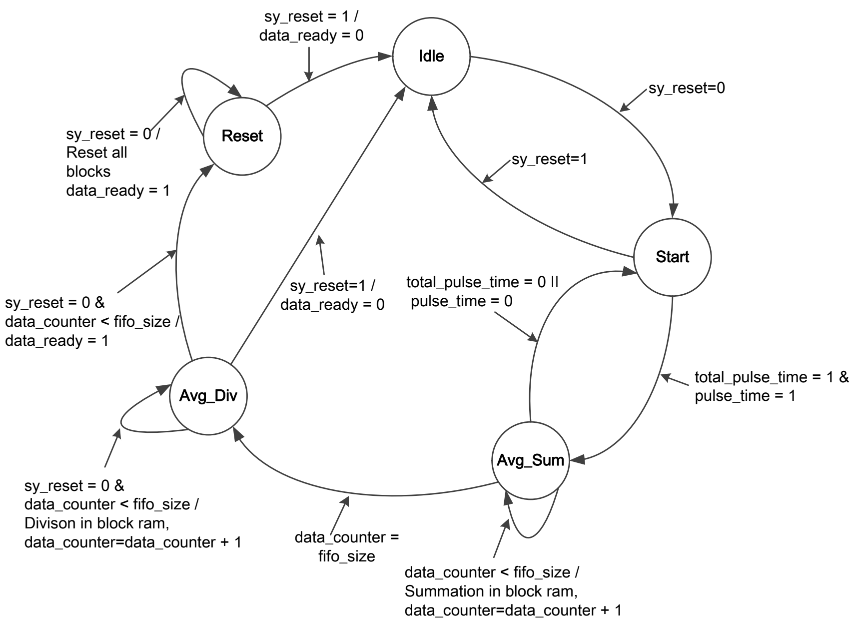

FIGURE 4.7: Finite state machine (FSM) flow of coherent averaging implementation.

$$
\begin{aligned}
T_{P-Avg} &= \max\left[(N_{Avg} \cdot N_R) \cdot ADD,\ PRT \cdot N_{Avg}\right] + DIV \cdot N_R \\
T_{P-Avg} &= PRT \cdot N_{Avg} + DIV \cdot N_R
\end{aligned}
\tag{4.12}
$$

Like (4.6), it is assumed that all arithmetic operations require the same amount of time $ARTH$. So (4.12) is equal to

$$
T_{P-Avg} = PRT \cdot N_{Avg} + ARTH \cdot N_R \tag{4.13}
$$

Unlike the conventional averaging method, overall memory storage required for the proposed averaging architecture is only $2N_R$ bytes as displayed in Fig. 4.4. The summing and division operations need only 1 adder and 1 divisor, respectively. Table 4.1 and 4.2 correspondingly describe the total time complexity and hardware requirements for the both conventional and proposed averaging scheme. It can be seen that the number of memory bytes and adders depend upon the number of averages (N_{Avg}) for the conventional coherent averaging scheme. For the higher averages, it is difficult to manage such kind of large memory storage and hardware adders. However, the number of memory storage and adders for the proposed averaging architecture are independent of the amount of averages (N_{Avg}) and that allows user to increase the averages and hence SNR.

TABLE 4.1: Time complexity comparisons between conventional and proposed architecture

Architectures	Time complexity
Conventional	$T_{C-Avg} = (PRT + N_R \cdot ARTH) \cdot N_{Avg}$
Proposed	$T_{P-Avg} = PRT \cdot N_{Avg} + ARTH \cdot N_R$

TABLE 4.2: Hardware comparisons between conventional and proposed architecture

Architectures	Storage (Byte)	Adder	Divisor
Conventional	$N_{Avg} \cdot N_R$	$N_{Avg} - 1$	1
Proposed	$2N_R$	1	1

The maximum number of averaging is restricted by the memory size of FIFO/block-RAM. From (4.8), the highest permissible average number for the proposed architecture is $N_R/2$. So for the case of block-RAM size $N_R = 8192$, the highest permissible average number is 4096.

4.4 Experimentation Setup

The overall block diagram of the single channel ultrasonic inspection system is shown in Fig. 4.8. It consists of five different types of hardware boards interfaced together and a PC based GUI software for post-processing and displaying of images. The pulser board is connected to the pulse-echo mode ultrasonic transducer and the same connection is provided to the pre-amplifier board. In similar manner, the transmit-receive mode transducer is also connected with pre-amplifier board.

As shown in the system block diagram in Fig. 4.8, the personal computer (PC) serves as the master host. Upon each pulse trigger sign provided through graphical user interface (GUI), the microprocessor inside the USB controller sequentially sends out control signals to other blocks of the imaging system. The trigger generator circuit inside FPGA sends the trigger signal to the pulser board sequentially for the excitation of transducer. Coaxial cables are used to connect transducers and interconnection of analog front-end boards. The amplified echoes are first digitized using 8-bit analog-to-digital converter at 100 MSPS and then synchronized by the FPGA for data averaging process. Later, the averaged data are transferred to PC through the USB port for display.

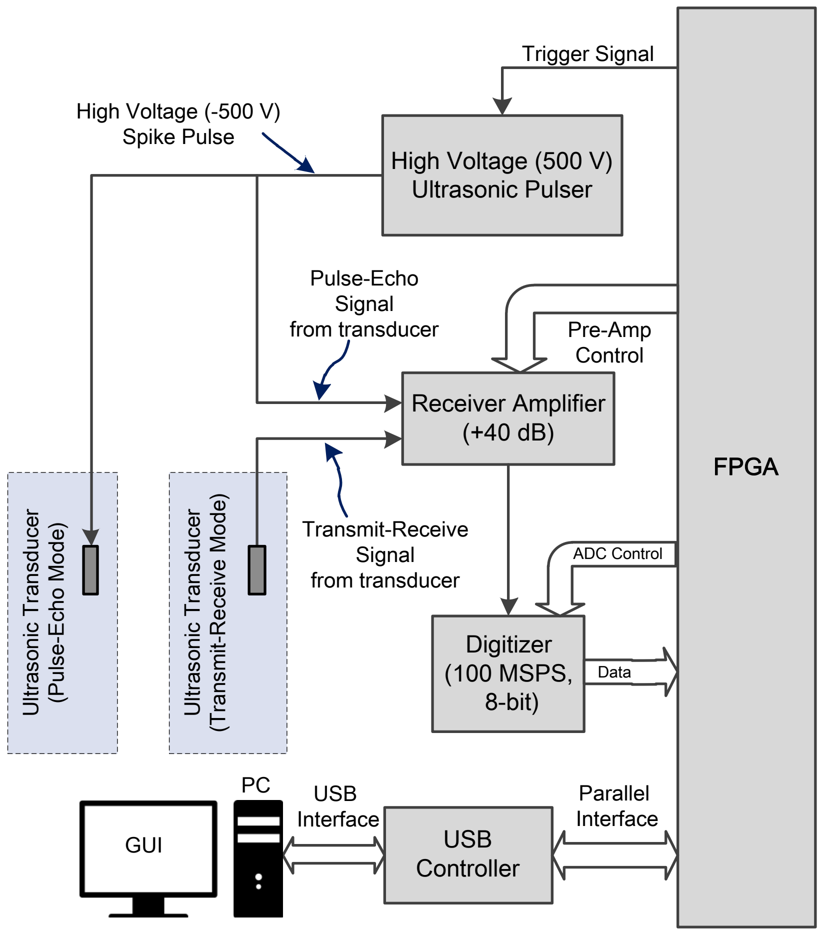

FIGURE 4.8: The overall Block diagram of Single channel ultrasonic imaging system.

4.4.1 Overall scheme of data acquisition

To begin the acquisition process, a user interface control built up in a visual application is started first. The software calculates control/DAQ parameters for the sampling rate selection, acquisition memory size option, and data averaging control. These all parameters are based on the user-selected transducer element and the scan type (i.e., A-Scan, B-Scan and C-Scan). After that, the all required data acquisition parameters are downloaded into the USB controller via USB, which distributes them to the FPGA.

Once the all parameters are transferred to FPGA, it triggers the high voltage pulser sequentially and simultaneously fills the receiving (Rx-A) FIFO by acquiring pulse-echo A-lines (i.e., A-scan data) until the *Full* signal of FIFO is activated. After that, it waits for the next trigger pulse to start filling the FIFO again. This process is repeated for N_{Avg} number of averages times while the RF data are averaged

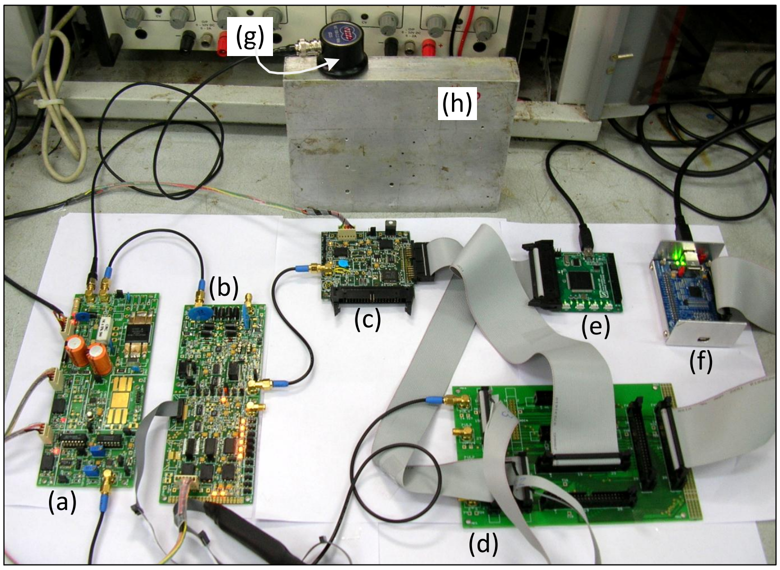

FIGURE 4.9: Experimental setup of ultrasonic imaging system: (a) High voltage ultrasonic pulser board, (b) Receiver pre-amplifier and main-amplifier board, and (c) Digitizer, (d)Interface board, (e) FPGA board, (f) USB controller board, (g) 2.5 MHz ultrasonic contact transducer, (h) Aluminium block under test.

simultaneously and transferred immediately to the Rx-B FIFO. Afterwards, the accumulated data sets from Rx-B FIFO will be transferred to the USB controller via parallel GPIF II interface. Once the controller receives the entire A-scan data set, they will be transferred to the PC via USB interface. Later, the post-processing operations of envelope detections and scan conversions are performed in the host PC. Finally, the imaging is performed using B-scan or C-scan modes.

Photograph of the electronics boards utilized for the experimental setup are shown in Fig. 4.9 which consist of a high voltage pulser board, multi-stage pre-amplifier board, digitizer board, FPGA and USB controller board.

TABLE 4.3: Total FPGA resource utilization

Type	# Utilization	% Utilization
Slice Registers	713	6 %
Slice LUTs	639	11 %
LUT-FF pairs	450	61 %
IO buffers	27	26 %
Block-RAM/FIFO	8	25 %

Table 4.3 shows the total FPGA resource utilizations for the proposed coherent averaging implementations and required control operations. The power estimation of the various on-chip resources are also calculated using the Xilinx Power Estimator (XPE) tool as shown in Table 4.4. For the power estimation, it is assumed that

TABLE 4.4: On-chip FPGA power estimation under the assumptions: $f_{sys} = 100\,MHz$, $f_{aq} = 25\,MHz$, and $f_{rd} = 25\,MHz$

On-chip	Power (W)
Clocks	0.008
Logic	0.002
Signals	0.002
BRAMs	0.001
IOs	0.012
Leakage	0.014
Total	**0.039**

FPGA system clock frequency is $f_{sys} = 100\,MHz$, ADC data acquisition rate is $f_{aq} = 25\,MHz$, and reading clock frequency for the FIFO (Rx-B) is $f_{rd} = 25\,MHz$. The total approximated estimated power of the FPGA is $39\,mW$.

4.5 Results and Discussions

Assume that the number of preferred average is $N_{Avg} = 64$, the memory depth of RAM is $N_R = 8192$ bytes and pulse repetition time is $PRT = 1\,ms$. The processing time by the hardware based arithmetic circuits is totally dependent on the system clock frequency, operation type and optimized hardware design. To reduce the complications, it is assumed that the approximated arithmetic processing time is $ARTH = 60\,ns$. Under these conditions, Table 4.5 shows that there is 96.875% (i.e. $100\% \times [524288 - 16384]/524288$) reduction in the memory storage and 98.41% (i.e. $100\% \times [63 - 1]/63$) reduction in the number of adders by the proposed averaging scheme. The number of dividers are same for the both averaging architectures. The total percentage reduction in processing time under the given condition is 32.439% (i.e. $100\% \times [95.4573 - 64.4915]/95.4573$). Fig.4.10 and Fig.4.11 respectively display the percentage reduction in hardware cost (memory and adder) and the percentage reduction in processing time by the proposed averaging scheme compared to the conventional averaging. Both graphs show that percentage reduction in hardware, as well as the processing time, is increased with the number of averages and after the particular average number the increment of percentage reduction modifies gradually. Since the PRT is higher compared to the hardware based arithmetic calculation time, the total processing time is dominated by the PRT.

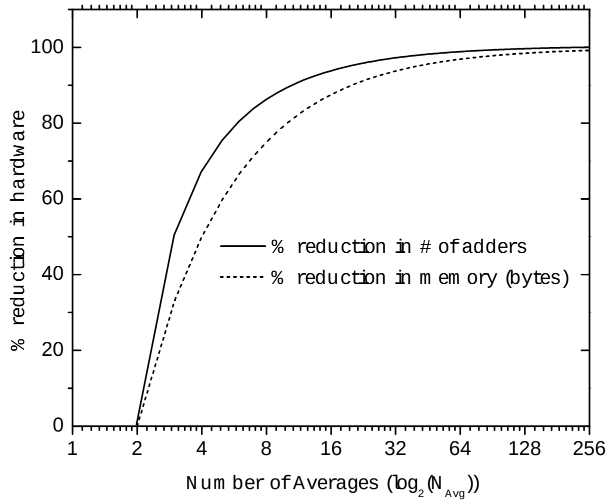

FIGURE 4.10: Percentage reduction in required hardware (memory storage and adder) by the proposed averaging scheme compared to conventional scheme. $N_R = 8192$, $PRT = 1\,ms$.

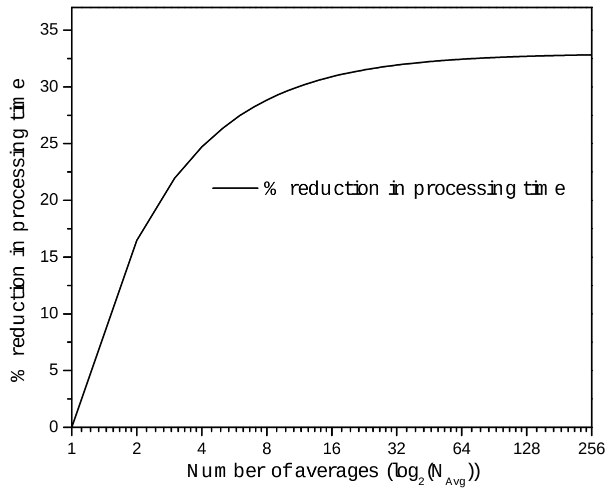

FIGURE 4.11: Percentage reduction in processing time by the proposed averaging scheme compared to conventional scheme. $N_R = 8192$, $PRT = 1\,ms$, $ARTH = 60\,ns$ (Approximate)

TABLE 4.5: Comparisons between averaging architectures for the case: $N_{Avg} = 64$, $N_R = 8192$, $PRT = 1\,ms$, $ARTH = 60\,ns$ $(Approximate)$

Architectures	Storage (#Byte)	#Adder	#Divisor	Time (ms)
Conventional	524288	63	1	95.4573
Proposed	16384	1	1	64.4915

4.5.1 Removal of random False-echoes and Smoothing of RF A-scan signal using hardware based implementation of coherent averaging

Generally, for materials with a non-homogeneous or coarse-grained structures, the transmit signal energy gets reduced due to scattering, so it is usually difficult to identify small flaws in practical applications. Sometimes, material generates spurious signals that are randomly distributed in the time domain and have the frequency band very analogous to that of the echoes received from the defects to be detected. These echoes are generally specified as backscattering noise. Both unwanted backscattering noise and noise from electronic instrumentation have to be canceled without suppressing the original echoes that characterize material flaws. Fig. 4.12 shows the aluminium block with three side-drilled holes $N1$, $N2$ and $N3$ in the beam direction. During the measurements, the experimented pulse-echo signal has been acquired from the holes using a contact transducer of 2.5 MHz frequency and 25 mm casing diameter. The sampling rate of 16 MHz with 8-bit resolution is chosen for the data acquisition. Fig. 4.13(a) displays the experimented ($N_{Avg} = 1$) signal with unwanted false-echoes and random spurious coherent noise. From the Fig. 4.13(b), it can be observed that unwanted false-echoes are removed by the coherent averaging ($N_{Avg} = 16$) of time domain waveforms. Further, the smoothing of A-scan waveforms and reduction of random spurious noise can be achieved by increasing the number of averages ($N_{Avg} = 64$).

Fig. 4.14 shows the frequency spectrum of the pulse-echo signal detected from the

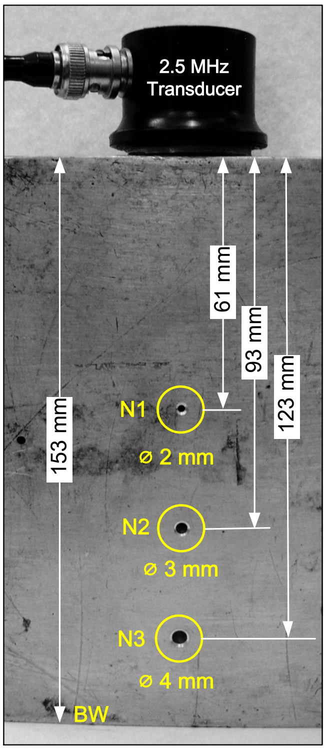

FIGURE 4.12: Aluminium test block for ultrasonic pulse-echo measurements with three side-drilled holes $N1$, $N2$, and $N3$

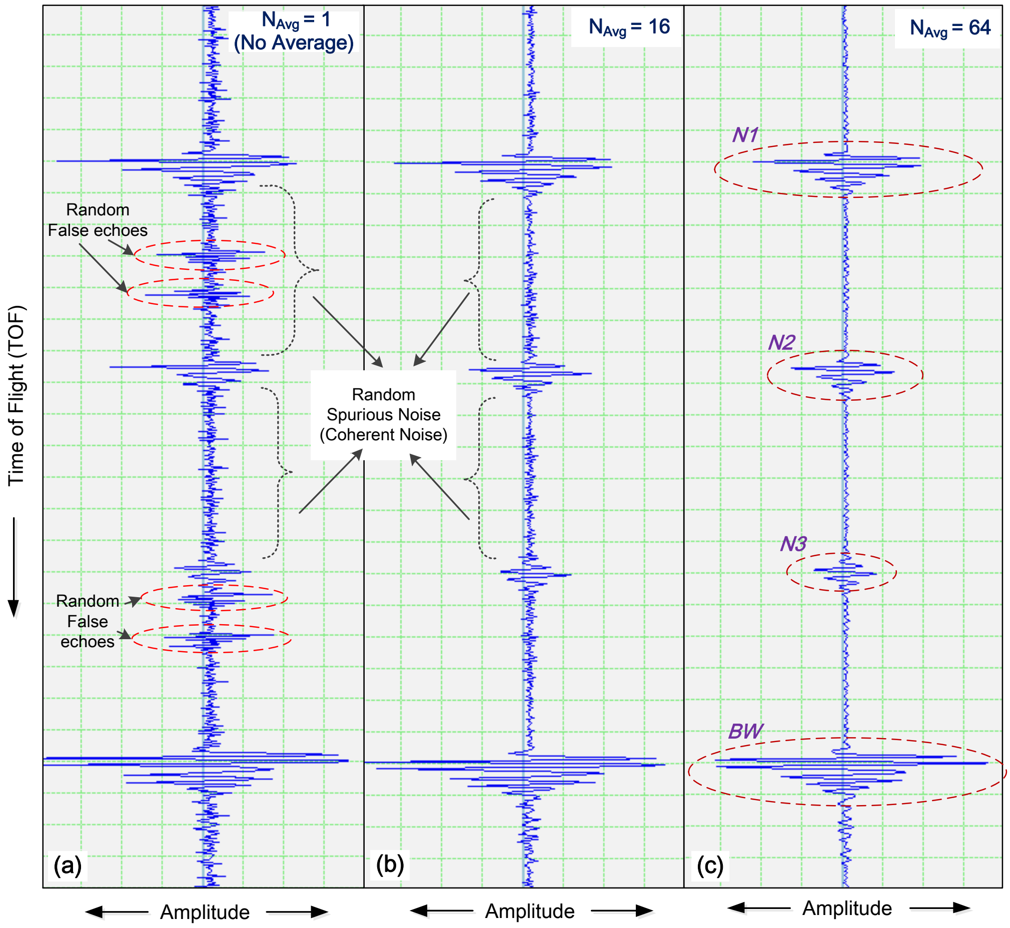

FIGURE 4.13: Random spurious/false-echo removal and smoothing of A-scan RF signal using hardware based data averaging. The number of averages are: (a) $N_{Avg} = 1$ (Experimented) (b) $N_{Avg} = 16$, and (c) $N_{Avg} = 64$.

hole $N1$ with different average numbers. The measured center frequency of transducer is 2.5 MHz and the -6 dB bandwidth ranged from 2.1 MHz to 3.0 MHz. From that, the calculated fractional bandwidth is 36 % (i.e., $(3.0-2.1) \times 100/2.5$). The lower frequency components of the spectrum ranged from 1.38 MHz to 3.4 MHz are identical for the experimental (no average) and averaged pulse-echo signals. But the magnitude of very low frequency ($<$ 1.38 MHz) and high frequency components ($>$ 3.4 MHz) are varied according to the number of averages. As shown in Fig. 4.14, the frequency spectrum of the experimental (no average) signal becomes prominent at the higher frequency range that cause noise and false-echoes in time domain. Other than fundamental frequency (2.5 Mhz), its frequency spectrum includes two other highest peaks at 7.2 MHz and 11.5 MHz frequency with the magnitude of -7.5 dB. As the number of averages increase, the magnitude of higher frequency component are reduced. For the case of 64

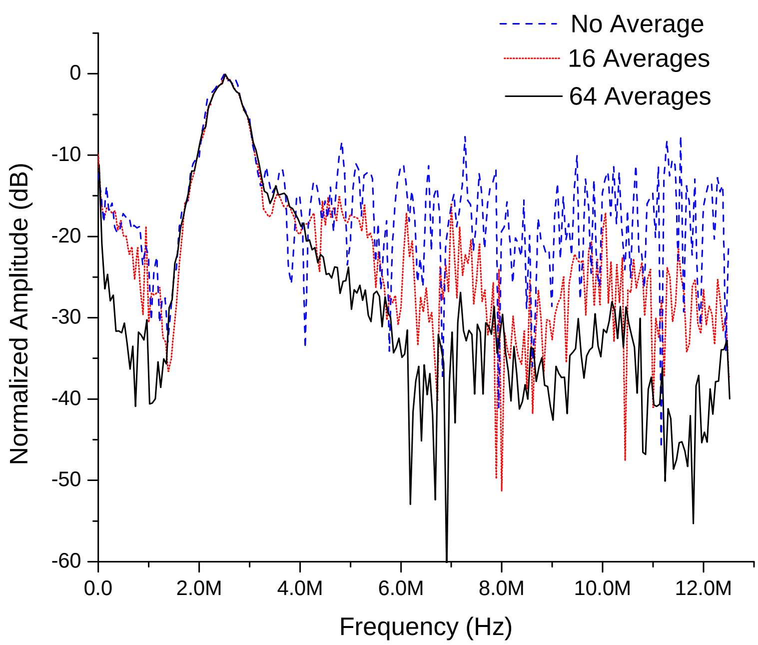

FIGURE 4.14: Frequency spectrum of the pulse-echo signal from hole $N1$ with no average (dashed blue line), 16 averages (dotted red line) and 64 averages (black line).

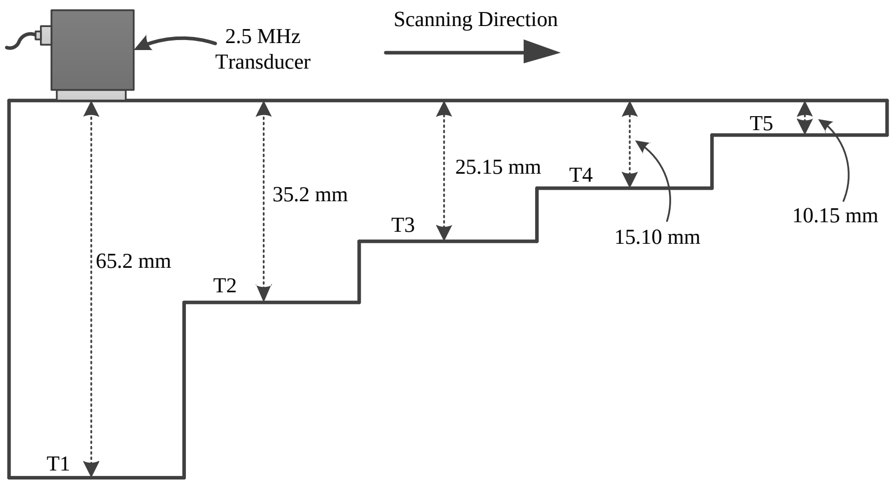

FIGURE 4.15: Calibrated aluminium Step Block for B-scan imaging

averages, the all higher frequency components ($> 3.4\ MHz$) have the amplitude of $< -30\ dB$ which is acceptable for pulse-echo imaging.

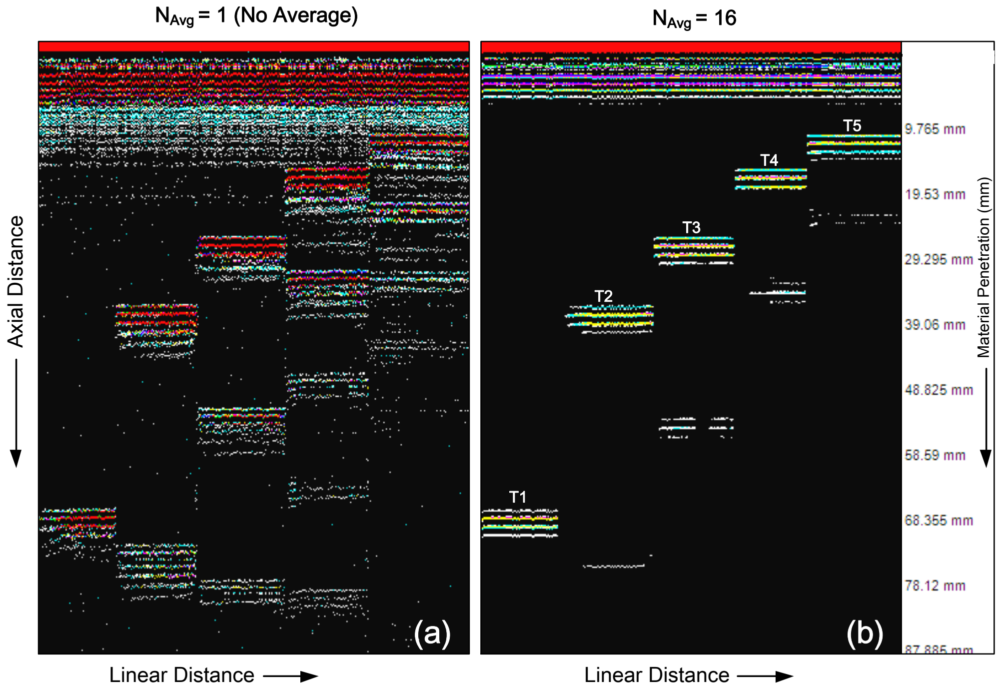

FIGURE 4.16: Speckle removal of ultrasonic B-scan image using hardware based data averaging. The number of averages are: (a) $N_{Avg} = 1$ (Experimented), and (b) $N_{Avg} = 16$.

4.5.2 Speckle removal of ultrasonic B-scan images by hardware based coherent averaging scheme

Arising artifacts or speckles in B-scan images are mainly due to the system noise [54], the formation of the ultrasound waves (i.e. ultrasound beam), acquisition of reflected echoes, data processing, and waveform reconstruction techniques. Speckles can also be generated by improper scanning techniques although these artifacts can be avoidable [48]. The mentioned speckle noise is not generated due to grain noise. Speckle diminishes the quality of ultrasonic images, it specifically blurs edges and lose details in the B-scan image. Additionally, material produces a granular texture occurring in the background of the B-scan image. Thus, it is also called the background noise [55]. Since this is not grain noise speckle, it can be removed by the coherent noise. The calibrated step block with 5 different steps (T1-T5) has been used for the B-scan imaging using 2.5 Mhz transducer as shown in Fig. 4.15. The horizontal manual scanning has been performed from the maximum thickness (T1) to the minimum thickness (T5). The experimented B-scan image encompasses the background noise, speckles and artifacts which degrades the edges as well as the quality of the image as displayed in Fig. 4.16(a). In order to improve quality of the image, hardware-based coherent averaging with the $N_{Avg} = 16$ number averages is used as shown in Fig. 4.16(b).

In the next chapter, the real-time empirical mode decomposition (EMD) algorithm based ultrasonic imaging system is developed for both contact and immersion NDT applications. The practical results will explain that in the noisy environment, it is possible to enhance the signal-to-noise ratio (SNR) for the visualization and identification of ultrasonic pulse-echo signals in real-time.

Chapter 5

Real Time Implementation of Empirical Mode Decomposition Algorithm for Ultrasonic SNR Enhancement

Real-time empirical mode decomposition (EMD) algorithm based ultrasonic imaging system is presented for the filtering of coherent noise from the ultrasonic signals. It is difficult to implement the EMD based signal processing algorithm in real time because it is a totally data-driven process which comprises numerous sifting operations. In this chapter, the EMD algorithm is implemented in the visual software environment. The EMD implementation encompasses two types of interpolation methods, piecewise linear interpolation (PLI) and cubic spline interpolation (CSI). The cubic spline tridiagonal matrix will be solved by the Thomas algorithm for the intention of real-time processing. The total time complexity functions for both implemented PLI and CSI based EMD method will be computed. For signal filtering, the partial reconstruction algorithm is adopted. The baseline correction and noise filtering applications are presented using EMD based visual software. The real-time practicability and efficiency of this method will be validated through ultrasonic NDT experimentation for improvement in the time domain resolution of the ultrasonic A-scan raw data.

5.1 Introduction

In this chapter, the empirical mode decomposition (EMD), proposed by Huang et al. [114], is utilized for the signal analysis and processing in the time domain. This data-driven decomposition algorithm is used for de-noising of non-linear and non-stationary ultrasonic data sample sequences. EMD decomposes the signal into a series of narrow-band oscillatory components with different features and a residue function. Each oscillatory component is called an intrinsic mode function (IMF). Different from other methods such as wavelet, the EMD does not require pre-defined basis function or mother wavelet for the signal decomposition. The process of decomposition using EMD is totally non-model based data-driven.

The EMD requires many iterative calculations and thus, it cannot be implemented using parallel architecture[115]. Many real-life applications require real-time results such as detection of faults in operating machines, real-time inspection of material integrity using NDT, etc. However, real-time fast implementation of EMD is a major challenge. In the past few years, many authors have presented EMD based real-time implementation in hardware, software, and hardware-software mix environment [115–119]. Ultrasonic noise suppression and signal identification using non-real time EMD have been described in [120, 121]. The EMD based algorithm should be performed in real-time especially for applications (or instruments) where on-line visual inspections of signals/waveforms are mandatory such as NDT instruments, ECG instruments, digital oscilloscope, etc. In this chapter, an on-line implementation of EMD based filtering scheme has been presented for better visualization and identification of ultrasonic pulse-echo signals in real-time.

5.2 EMD and Signal Reconstruction

5.2.1 EMD Algorithm

The original signal $x(t)$ is decomposed into the small number of IMFs and a residue function. The IMFs and finite residue sequences are produced through the sifting process of the signal. Using the EMD, the original signal $x(t)$ can be decomposed as [114]

$$x(t) = \sum_{i=1}^{n_f} c_i(t) + r(t). \tag{5.1}$$

where n_f denotes the number of extracted IMFs, $c_i(t)$ and $r(t)$ are the IMF and the finite residue of the original signal $x(t)$, respectively. The EMD algorithm flow is depicted in Fig. 5.1

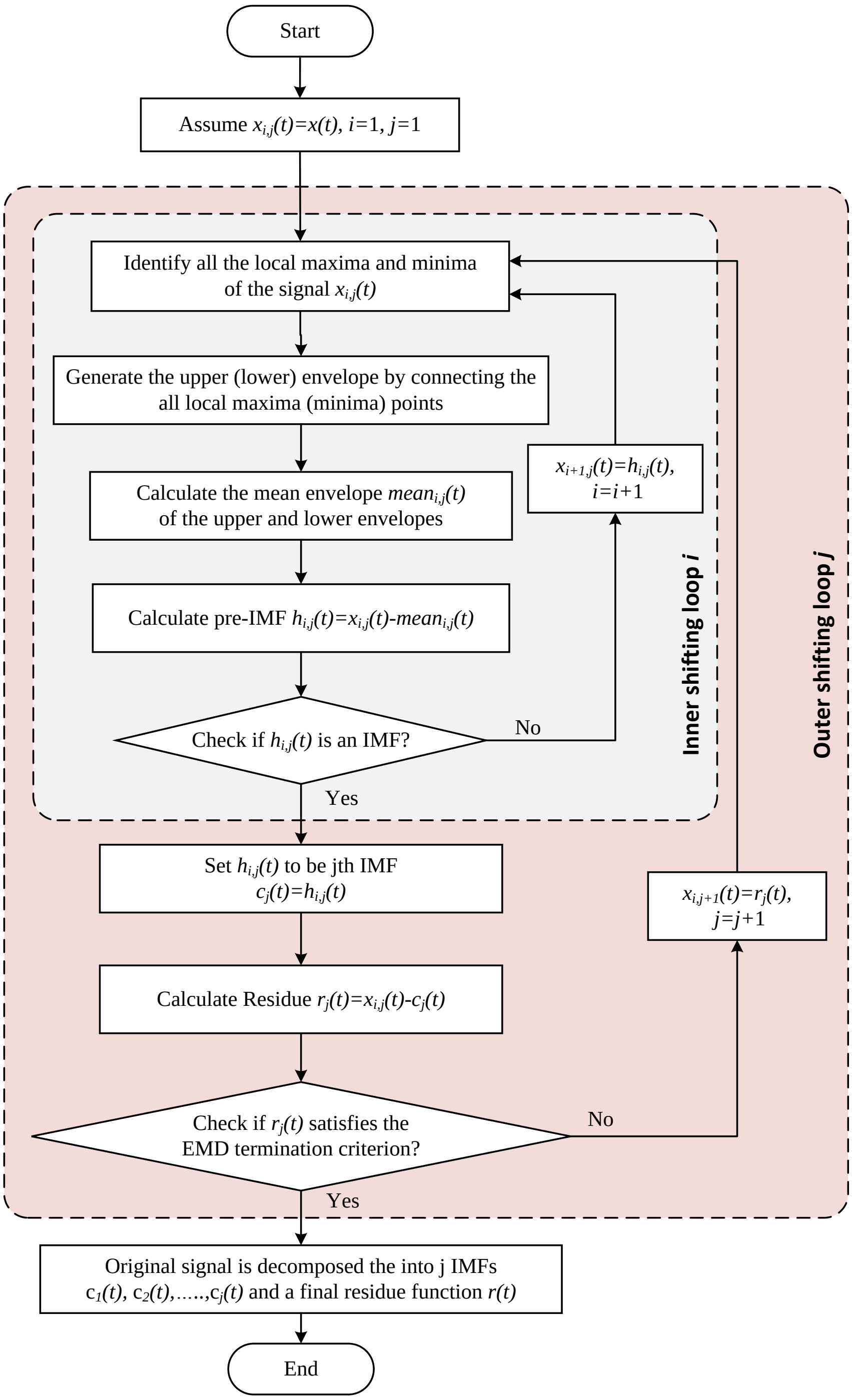

FIGURE 5.1: EMD algorithm flow.

An IMF must satisfy the following two conditions:

1) In the given whole data sets, the number of extrema points (local minima and maxima) and zero crossing points should be equal to each other or differ by at the most by one.

2) The mean values of envelopes defined by the local minima and maxima should be equal to zero at any point of the signal.

The steps of the EMD procedures are described as follows:

1. Let i and j denotes the inner and outer iterative loop indices, respectively. Initially assume $x_{i,j}(t) = x(t)$.
2. Identify all the local maxima and minima of the signal $x_{i,j}(t)$.
3. Interpolate these local minima and maxima points by CSI or PLI and generate lower envelope $le(t)$, and upper envelope $ue(t)$.
4. Calculate the mean envelope $mean(t)$ by averaging both envelopes: $mean_{i,j}(t) = [le(t) + ue(t)]/2$
5. Take the difference between data $x_{i,j}(t)$ and $mean_{i,j}(t)$: $h_{i,j}(t) = x_{i,j}(t) - mean_{i,j}(t)$.
6. Check if $h_{i,j}(t)$ accomplishes conditions defining an IMF. If $h_{i,j}(t)$ is not an IMF, then it is treated as original data: $x_{i+1,j}(t) = h_{i,j}(t)$ and repeat the step 1 to 5. If $h_{i,j}(t)$ is an IMF, then save the IMF component $c_j(t) = h_{i,j}(t)$.
7. Obtain the remaining residue function $r_j(t)$ by using $r_j(t) = x_{i,j}(t) - c_j(t)$.
8. If residue $r_j(t)$ satisfies the EMD termination criterion: number of extrema in $r_j(t) < 2$, then stop the shifting process and $r_j(t)$ becomes the final residue function $r(t)$; otherwise, treat $r_j(t)$ as a new set of data $x_{i,j+1}(t) = r_j(t)$ and repeat the step 1 to 7 to find other IMFs $c_1(t), c_2(t), ..., c_{n_f}(t)$

Thus, the original signal $x(t)$ is decomposed into the n_f IMFs: $c_1(t), c_2(t), ..., c_{n_f}(t)$ and a final residue function $r(t)$.

5.2.2 Signal Reconstruction using EMD

The EMD sequentially extracts the signal into the energy associated with different intrinsic time scales, starting from the narrower time scales (or high-frequency modes) to a coarser one (or low-frequency modes). The filtering scheme depends on the basic idea that most of the signals are usually concentrated on lower frequency components (last IMFs) and decrease toward high-frequency modes (first IMFs).

For the signal that is corrupted by white Gaussian noise, SNR is higher at low frequencies than at the higher one. Here the partial filtering algorithm is adopted which is proposed by Boudraa and Cexus[122] because it is a fully data-driven approach and hence it does not require any pre-possessing and post-processing of data. Thus, the actual signal $x_a(t)$ superimposed by white Gaussian noise $n_g(t)$ is described as:

$$x(t) = x_a(t) + n_g(t) \tag{5.2}$$

The main objective is to find an approximation $\tilde{x}_a(t)$ from the noisy signal $x(t)$. There is a certain mode index k, after which, the c_k (k^{th}IMF) allows us to retrieve the most of the information of the actual signal from the noisy signal. Thus, the modes after c_k dominate the signal, whereas the previous modes contain high-frequency components. So for the signal reconstruction, high-frequency dominated components will not be used. The signal $\tilde{x}_a(t)$ is reconstructed using selected $(n_f - k + 1)$ IMFs and from (5.1), it is given as:

$$\tilde{x}_a^k(t) = \sum_{i=k}^{n_f} c_i(t) + r(t) \tag{5.3}$$

where $k = 2, 3, ..., n_f$. The consecutive mean square error (CMSE) has been used which does not require any information of $x_a(t)$. The CMSE measures the squared Euclidean length between two consecutive reconstructions of the signal [122].

$$\begin{aligned} CMSE(\tilde{x}_a^k, \tilde{x}_a^{k+1}) &= \frac{1}{N}\sum_{i=1}^{N}[\tilde{x}_a^k(i) - \tilde{x}_a^{k+1}(i)]^2 \\ &= \frac{1}{N}\sum_{i=1}^{N}[c_k(i)]^2 \end{aligned} \tag{5.4}$$

where, $k = 1, 2, ..., n_f - 1$ and N is the data length of signal. Here, the CMSE is reduced to the energy of the k^{th} IMF. The main aim of the signal reconstruction is to find the optimal index $k = k_c$ after which CMSE has minimum value or it has significant change in the IMF energy. It is given as:

$$k_c = \underset{1 \leq k \leq n_f - 1}{argmin}[CMSE(\tilde{x}_a^k, \tilde{x}_a^{k+1})] \tag{5.5}$$

Thus, the steps for the signal reconstruction are as follows: 1) Decompose the signal $x(t)$ using (5.1), 2) Compute $CMSE(\tilde{x}_a^k, \tilde{x}_a^{k+1})$, for $k = 1, 2, ..., n_f - 1$ using

(5.4), 3) Find optimal value $k = k_c$ using (5.5), and 4) Reconstruct the filtered signal $\tilde{x}_a(t)$ using (5.3).

5.3 Online Implementation of EMD based Signal Processing Algorithm

5.3.1 Envelope Generation

The local extrema extraction is the first step of the EMD algorithm. The First Derivative method is adopted to extract the local minima and maxima points. The function $F(x)$ has

Local maxima at c, if $F^{'}(c-1) > 0$ and $F^{'}(c) < 0$

Local minima at c, if $F^{'}(c-1) < 0$ and $F^{'}(c) > 0$

No local extrema at c, if *otherwise*.

The envelope generation is a most complex phenomenon of EMD. It involves proper interpolation of data points between two nearest local maxima or minima. An appropriate interpolation algorithm must be implemented to connect the local extrema points to form an envelope. In this design, two interpolation methods, PLI and CSI, are considered for envelope generation. Fig. 5.2 shows an example of 5 points and its generated PLI and CSI curves connecting them all together.

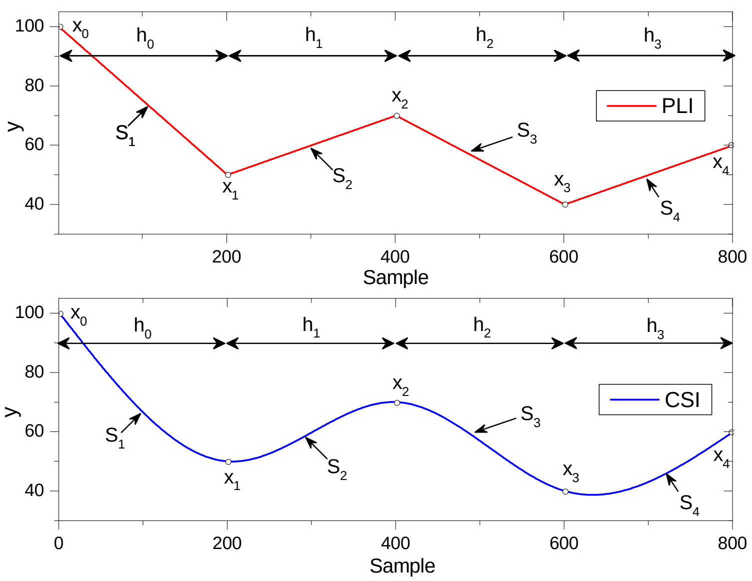

FIGURE 5.2: PLI and CSI curve connecting to 5 data points, x_0 to x_4.

The piecewise polynomial interpolation (PPI) splits the data points (x_0, y_0), (x_1, y_1) ,..., (x_n, y_n) into a set of intervals for $j = 0, 1, ..., n - d$ and constructs a separate polynomial of degree d for all intervals. These polynomials attach together at data points, and thus, the resulting curve is continuous. Here the PLI (degree 1) is chosen which connects pairs of data points with a straight linear line. The full curve $S(x)$ is given as

$$S(x) = \sum_{i=1}^{n} S_i(x) \tag{5.6}$$

where each $S_i(x)$ is the polynomial in the interval $[x_{i-1}, x_i]$. For the PLI, each curve $S_i(x)$ is given as

$$S_i(x) = \begin{cases} y_k + \frac{y_{k+1} - y_k}{x_{k+1} - x_k}(x - x_k) & \text{if } x_k \leq x \leq x_{k+1} \\ 0 & \text{if } otherwise \end{cases} \tag{5.7}$$

This method of interpolation can be extended by constructing a new set of interpolating polynomial $S_i(x)$ of higher degree ($d = 3$). As we increase the degree of the polynomial, the $S_i(x)$ can be chosen such that resulting curve has a number of continuous derivatives. A piecewise polynomial interpolant of degree d with $d-1$ continuous derivatives is called a spline, if less than $d - 1$ continuous derivatives are present, then it is called a sub-spline. To derive mathematical formulas of the cubic spline, assumed extrema points are

$$a = x_0 < x_1 < \cdots < x_n = b, \quad h_i = |x_{i+1} - x_i| \tag{5.8}$$

The cubic spline is a third degree piecewise cubic polynomial and it is given as,

$$S_{i+1}(x) = a_i(x - x_i)^3 + b_i(x - x_i)^2 + c_i(x - x_i) + d_i \tag{5.9}$$

where $i = 0, 1, .., n - 1$. For the $n + 1$ points, the cubic spline curve is calculated as described in (5.1).

The cubic spline interplant has following properties,

1) $S_i(x_i) = y_i$. The cubic spline interpolant passes through each and every data points.

2) $S_i(x_{i+1}) = S_{i+1}(x_{i+1})$. The cubic spline curve is continuous at the data points so it continues everywhere in the interpolation interval.

3) $S_i^{'}(x_{i+1}) = S_{i+1}^{'}(x_{i+1})$. The cubic spline curve has continuous first derivative for the smoothness of the interval.

4) $S_i^{''}(x_{i+1}) = S_{i+1}^{''}(x_{i+1})$. The cubic spline curve has continuous second derivative.

To construct a cubic spline curve from a given set of data points, the coefficients a_i, b_i, c_i and d_i of the cubic polynomials must be solved. There are four coefficients in each cubic polynomial curve, therefore, we have $4n$ unknowns. The interpolation data points impose $n+1$ constraints. Properties 2), 3), and 4) each supply an additional $n-1$ constraint. Thus $n+1+3(n-1) = 4n-2$ constraints are specified for the $4n$ unknown coefficients. In order to solve the all coefficients, two more constraints are must required. For the extra two boundary conditions, there are various alternatives like,

1) Natural Spline: $S_0^{''}(x_0) = 0$ and $S_{n-1}^{''}(x_n) = 0$.

2) End Slope Spline: $S_0^{'}(x_0) = y_0^{'}$ and $S_{n-1}^{'}(x_n) = y_n^{'}$.

3) Periodic Spline: $S_0^{'}(x_0) = S_{n-1}^{'}(x_n)$ and $S_0^{''}(x_0) = S_{n-1}^{''}(x_n)$.

4) Not-a-Knot Spline: $S_0^{'''}(x_0) = S_1^{'''}(x_1)$ and $S_{n-2}^{'''}(x_{n-1}) = S_{n-1}^{'''}(x_{n-1})$.

The natural cubic spline is rarely used because it does not provide an adequately precise approximation $S_i(x)$ near the ends of the interval $[a, b]$. This may be probable from the fact that the values on the second derivatives forced to be zero because these are not unavoidably values of the second derivative of the function from which the data measures. Here we have considered the end slope spline conditions to solve unknown cubic coefficients. It is also called the complete cubic spline. The first derivative values of the data may not be readily available but they can be replaced by exact approximations. By using these conditions, following relation holds for $i = 0, 1, ..., n-1$.

$$
\begin{aligned}
a_i &= \frac{m_{i+1} - m_i}{6h_i} \\
b_i &= \frac{m_i}{2} \\
c_i &= \frac{y_{i+1} - y_i}{h_i} - \frac{2m_i h_i + h_i m_{i+1}}{6} \\
d_i &= y_i
\end{aligned}
\tag{5.10}
$$

Here h_i and y_i are the known values from the data points so all that remains is to solve for m_i. After combining all the equations, one can obtain the system of linear equation $Am = B$ where

$$Am = B \tag{5.11}$$

where

$$A = \begin{bmatrix} a_{00} & a_{01} & 0 & \cdots & 0 & 0 & 0 \\ a_{10} & a_{11} & a_{12} & \cdots & 0 & 0 & 0 \\ 0 & a_{21} & a_{22} & \cdots & 0 & 0 & 0 \\ \vdots & \vdots & \vdots & \cdots & \vdots & \vdots & \vdots \\ 0 & 0 & 0 & \cdots & a_{n-1,n-2} & a_{n-1,n-1} & a_{n-1,n} \\ 0 & 0 & 0 & \cdots & 0 & a_{n,n-1} & a_{nn} \end{bmatrix}$$

$$\begin{aligned} a_{00} &= 2h_0 & a_{22} &= 2(h_1 + h_2) \\ a_{01} &= h_0 & a_{n-1,n-2} &= h_{n-2} \\ a_{10} &= h_0 & a_{n-1,n-1} &= 2(h_{n-2} + h_{n-1}) \\ a_{11} &= 2(h_0 + h_1) & a_{n-1,n} &= h_{n-1} \\ a_{12} &= h_1 & a_{n,n-1} &= h_{n-1} \\ a_{21} &= h_1 & a_{nn} &= 2h_{n-1} \end{aligned} \tag{5.12}$$

Here A is the tridiagonal matrix and the system of linear equations $Am = B$ is stated as,

$$A \begin{bmatrix} m_0 \\ m_1 \\ m_2 \\ \vdots \\ m_{n-1} \\ m_n \end{bmatrix} = \begin{bmatrix} \frac{6}{h_0}(y_1 - y_0) - 6y_0' \\ \frac{6}{h_1}(y_2 - y_1) - \frac{6}{h_0}(y_1 - y_0) \\ \frac{6}{h_2}(y_3 - y_2) - \frac{6}{h_1}(y_2 - y_1) \\ \vdots \\ \frac{6}{h_{n-1}}(y_n - y_{n-1}) - \frac{6}{h_{n-2}}(y_{n-1} - y_{n-2}) \\ 6y_n' - \frac{6}{h_{n-1}}(y_n - y_{n-1}) \end{bmatrix} \tag{5.13}$$

5.3.2 EMD based visual software for data processing

EMD based algorithm has been implemented in the visual software environment using visual C# as depicted in Fig. 5.3. In order to verify the EMD based denoising technique for ultrasonic inspection, two types of input data schemes have been utilized, one is the continues noisy sinusoidal waveform generator and second is the on-line actual ultrasonic pulse-echo raw data that are acquired directly from the ultrasonic imaging system. The local upper and lower envelope has been constructed using both techniques, PLI and CSI. In contrast to the CSI implementation, it is easy to implement the PLI algorithm in real time as it requires fewer metamathematical computations.

For the CSI implementation, as described earlier, the matrix A can be solved by a sequential method of removing unknowns from equations using the forward elimination followed by the back substitution and this is called a general Gaussian elimination or Naive Gaussian elimination method. The total numbers of addition/subtraction and multiplication/division for the general Gaussian Elimination can be written as [123],

$$\underbrace{\frac{2n^3}{3}}_{\substack{\text{Forward}\\ \text{Elimination}}} + \underbrace{n^2}_{\substack{\text{Back}\\ \text{Substitution}}} \xrightarrow{as\, n\, increases} \underbrace{\sim O(n^3)}_{\substack{\text{Total}\\ \text{Computations}}} \tag{5.14}$$

where n is the total number of linear equations. As the number of equations increase, the required computation cost and, hence computational time also increases. Here most of the efforts are incurred in the elimination step. So, for example if n is equal to 1000, we have the numbers of computations that are required in order to use Gaussian elimination are of the order of approximately 10^9.

In our case, A is the tridiagonal matrix because in this matrix structure diagonal, super-diagonal and sub-diagonal elements may be the nonzero value but everything else in this structure elements are zero. In order to solve the tridiagonal system of equations, the TriDiagonal Matrix Algorithm (TDMA), also known as Thomas Algorithm is adopted which is a simplified form of Gaussian elimination [124]. The Thomas algorithm proceeds in two stages. At the first stage, the tridiagonal system is transformed into a bidiagonal system called forward elimination. At the second stage, this bidiagonal system is solved by back substitution. The pseudo code for the Thomas algorithms is provided in Table 5.1.

The actual idea behind this forward elimination method is to reduce the linear equations into a single unknown because such equations are trivial to solve. Such a reduction is achieved by manipulating the equations in the system in such a way that the solution does not change, but unknowns are eliminated from selected equations until; we obtain an equation having only a single unknown. These manipulations are called elementary row operations or forward gauss eliminations. The basic forward elimination procedure using equation k to operate on equations $k+1, k+2, ..., n$ is

$$
\begin{aligned}
a_{ij} &= a_{ij} - (\frac{a_{ik}}{a_{kk}})a_{kj} \\
B_i &= B_i - (\frac{a_{ik}}{a_{kk}})B_k
\end{aligned}
\tag{5.15}
$$

where $k \leq j \leq n$, $k \leq i \leq n$, $a_{kk} \neq 0$. This algorithm requires approximately $2(n-1)$ arithmetic operations and $4(n-1)$ multiplication/division operations. So the total computations required by using this algorithm is only $\sim O(n)$, in contrast to the computations cost $O(n^3)$ required for the general Gaussian elimination algorithm. The next step for the Thomas algorithm is back substitution and the final equation for the system solution is given as

$$
m_n = \frac{B_n}{a_{nn}} \tag{5.16}
$$

This result can be back-substituted into the $(n-1)^{th}$ equation to solve for m_{n-1}. Likewise, the remaining m_i can be calculated by the following formula:

$$
m_i = \frac{B_i - \sum_{j=i+1}^{n} a_{ij} m_j}{a_{ii}} \ , \quad i = n-1, n-2, ..., 1 \tag{5.17}
$$

TABLE 5.1: Peseudo code for TDMA

Thomas Algorithm
Step 1: Formation of $[A/B] = m$ system of linear equations
Step 2: For $i = 1$ to n Do
$t = A[i+1, i]/A[i, i]$
For $j = 1$ to $i + 1$ Do
$A[i+1, j] = A[i+1, j] - t * A[i, j]$
End For
End For
Step 3: $m[n] = A[n+1, n+1]/A[n+1, n+2]$
For $i = n-1$ to 0 Do
$sum = 0$
For $j = 1$ to $i - 1$ Do
$sum = sum + A[i, j] * m[i]$
End For
$m[i] = (A[i, n] - sum)/A[i, i]$
End For

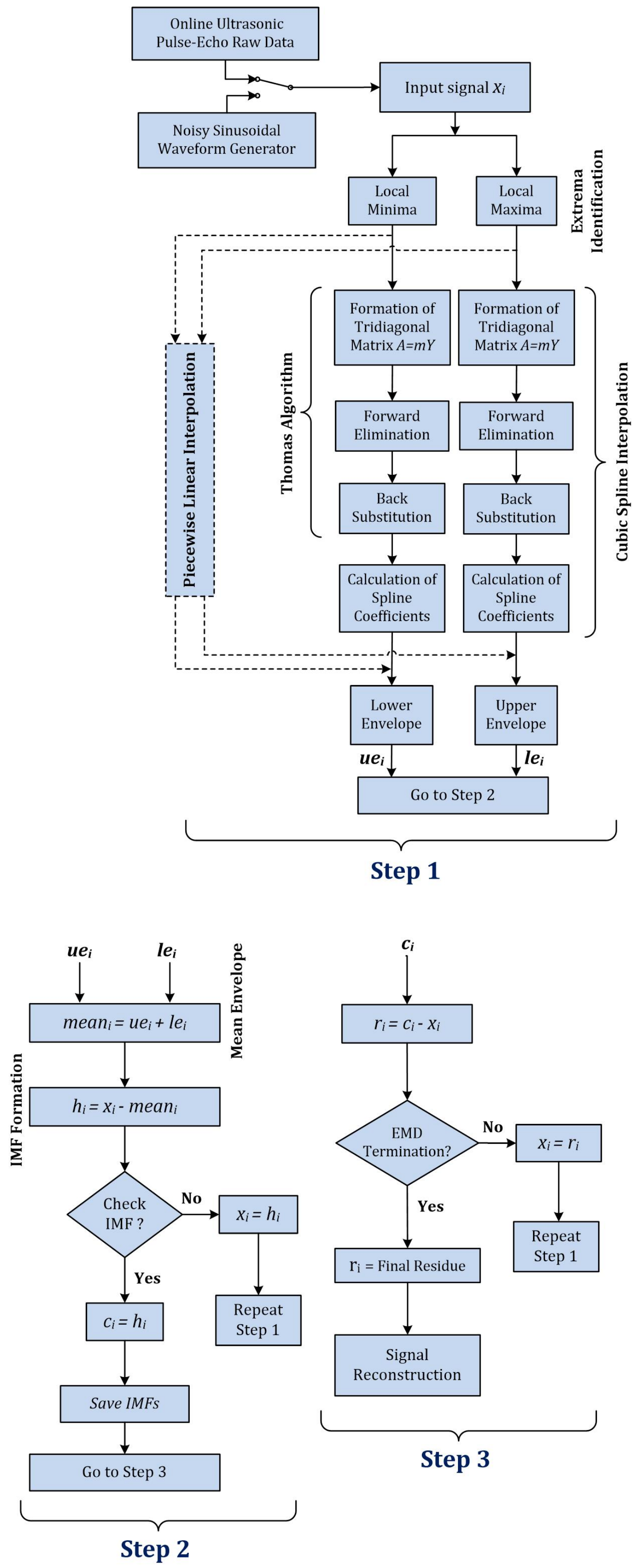

FIGURE 5.3: Block diagram of implemented EMD based architecture.

5.3.3 IMF Stoppage Shifting Criteria

To get physically meaningful IMFs, the stoppage shifting criteria should be defined accordingly. Previously various stoppage criteria have been proposed such as the Cauchy type criterion [114], the mean value criterion [125], the S-number criterion [126] and the fixed shifting time criterion [127]. The Cauchy type shifting criteria is chosen because it is easy to implement. The IMF shifting process will stop when the SD (Standard deviation) is smaller than the fixed predefined value ζ.

$$SD = \sum_{i=1}^{N} \frac{\left|d_{j(k-1)}(i) - d_{jk}(i)\right|^2}{d^2_{j(k-1)}(i)} \leq \zeta \tag{5.18}$$

where N is the total data length, ζ is the threshold number ($\zeta = 0.3$), and $d_{jk}(i)$ is the k^{th} shifting result of inner shifting loop of j^{th} mode.

5.4 Time Complexity of Implemented EMD

In this section, the time complexity of the implemented EMD algorithm is analyzed. The previously published work [128] does not encompass the computations of IMF stoppage criteria and signal reconstruction. The arithmetic operation includes addition/subtraction (ADD), multiplication (MUL), division (DIV), and comparison (COM). Here the float data type is used for the arithmetic data operations. The computational time complexity of the both PLI and CSI based EMD has been calculated. The main procedures like extrema identification, IMF calculations, mean envelope calculations, checking of IMF stopping criteria etc. are identical for both types of EMD. The detailed descriptions are provided below.

Let each of the input $x(t)$, *pre*-IMF, *post*-IMF $c(t)$, residue $r(t)$, mean, upper/lower envelope $ue(t)/le(t)$ have equal length n. The decomposition results of EMD consist of total n_f IMFs each with length n. So it requires total $n \cdot n_f$ storage for all IMFs. The inner loop of EMD comprises multiple iterations for every unsatisfied IMF stoppage criteria. Thus, the inner loop requires total $n_{pf} \cdot n_f$ iterations where n_{pf} is the number of each inner loop iteration. Assume, there are $n_{ue}(f)$ maxima and $n_{le}(f)$ minima points for each IMF. So the total number of extrema for each IMF are $n_e(f) = n_{ue}(f) + n_{le}(f)$. The optimal mode number of IMF is represented by n_k using (5.5). The total time complexity of implemented EMD functions are provided in Table 5.2. The total time required for each arithmetic operations like

ADD, MUL, DIV, and $COMP$ depends on the implemented hardware architecture. Different hardware has different time speed for the individual arithmetic operations such as multiplication/division requires more operational time compared to addition/comparisons. Here, it is assumed that all arithmetic operations require the same amount of time for the numerical calculations. Total shifting operation requires $(2ADD)n_{pf} \cdot n_f \cdot n$ operations. The mean of the upper and lower envelope needs $(1ADD + 1DIV)n_{pf} \cdot n_f \cdot n$ operations. The total time complexity for the calculations of shifting and mean operations is:

$$T_{shift} = (3ADD + 1DIV)\, n_{pf} \cdot n_f \cdot n \tag{5.19}$$

IMF stoppage criteria is also being consideration for the calculations of total cost function of EMD. Because the Cauchy type criterion has been used as described in 5.18, the total time complexity for the IMF stoppage criteria is:

$$T_{SD} = (2ADD + 1MUL + 1DIV + 1COMP)\, n_{pf} \cdot n_f \cdot n \tag{5.20}$$

In order to identify the extrema of signal, the first derivative test has been used. The first derivative calculation $x^{'}(t)$ has been performed at the every point of the signal followed by the comparison operation to identify extrema. This operation requires $(1ADD + 1COMP)n_{pf} \cdot n_f \cdot n$ operations. After extrema point identification, one more comparison operation is needed to separate both maxima and minima points. But this operation has been performed only at extrema points of each IMFs and requires only $(1COMP)n_{pf} \sum n_e(f)$ operation. Here $n_e(f)$ is the number of total extrema of the signal. Hence, the total time complexity for extrema identification operation is:

$$T_{extr} = \left[(1ADD + 1COMP)n_f \cdot n + (1COMP) \sum_{f=1}^{n_f} n_e(f) \right] n_{pf} \tag{5.21}$$

The total amount of time count for the PLI based EMD from the Table 5.2 is,

$$\begin{aligned} T_{PLI-EMD} &= T_{shift} + T_{stop} + T_{extr} + T_{PLI} + T_{reco} \\ T_{PLI-EMD} &= (11n_{pf} + 4)n_f n + 1n_k n + 9 \sum_{f=1}^{n_f} n_e(f) n_{pf} \end{aligned} \tag{5.22}$$

Here, $\underset{1\le k\le n-1}{max}(n_k) = n_f$. So (5.22) can be written as

$$T_{PLI-EMD} = \left[11n_f n\left(1+\frac{5}{11n_{pf}}\right)\right] n_{pf} + 9\sum_{f=1}^{n_f} n_e(f) n_{pf} \tag{5.23}$$

Since $11n_{pf} >> 5$, (5.23) can be reduced

$$T_{PLI-EMD} = \left[11n_f \cdot n + 9\sum_{f=1}^{n_f} n_e(f)\right] \cdot n_{pf} \tag{5.24}$$

TABLE 5.2: Time Complexity of EMD Functions

Function	T	Time Complexity
Shifting	T_{shift}	$(3ADD + 1DIV)n_{pf} \cdot n_f \cdot n$
IMF Stoppage Criteria	T_{stop}	$(2ADD + 1MUL + 1DIV$ $+1COMP)n_{pf} \cdot n_f \cdot n$
Extrema Identification	T_{extr}	$[(1ADD + 1COMP)n_f \cdot n$ $+(1COMP)\sum_{f=1}^{n_f} n_e(f)] \cdot n_{pf}$
PLI Envelope Generation	T_{PLI}	$(4ADD + 2DIV + 2COMP)$ $\cdot n_{pf}\sum_{f=1}^{n_f} n_e(f)$
CSI Envelope Generation	T_{CSI}	$[(6ADD + 6MUL)n_f \cdot n + (13ADD$ $+9MUL + 7DIV)\sum_{f=1}^{n_f} n_e(f)] \cdot n_{pf}$
Signal Reconstruction	T_{reco}	$(1ADD + 1MUL + 1DIV$ $+1COMP)n_f \cdot n + (1ADD)n_k \cdot n$

As mentioned earlier, CSI envelope generation is divided into three stages: formation of a tridiagonal matrix, forward elimination and backward substitution. All arithmetic operations repeat for each IMF and hence, the total time complexity function for the matrix formulation is $T_{math} = (5ADD{+}2MUL{+}1DIV)n_{pf}\sum n_e(f)$. The time complexity function for the forward elimination is $T_{for} = (2ADD + 2MUL + 1DIV)n_{pf}\sum n_e(f)$. The same way for the backward substitution, the time complexity function is $T_{back} = (2ADD + 1MUL + 1DIV)n_{pf}\sum n_e(f)$. From the (5.10), the numbers of required operations for the coefficient calculations are $T_{coef} = (4ADD + 4MUL + 4DIV)n_{pf}\sum n_e(f)$. The total number of required arithmetic calculations for the spline curve generation are $T_{cubic} = (6ADD + 4MUL)n_{pf} \cdot n_f \cdot n$. Like (5.23), the total time complexity of implemented CSI based EMD algorithm can be calculated as

$$\begin{aligned} T_{CSI-EMD} = T_{CSI}(&= T_{mat} + T_{for} + T_{back} + T_{coef} \\ &+ T_{cubic}) + T_{shift} + T_{stop} + T_{extr} + T_{reco} \end{aligned} \tag{5.25}$$

$$\begin{aligned} T_{CSI-EMD} = &\left[23n_f \cdot n \left(1 + \frac{5}{23n_{pf}}\right)\right] n_{pf} \\ &+ 30 \sum_{f=1}^{n_f} n_e(f) \cdot n_{pf} \end{aligned} \tag{5.26}$$

Since $23n_{pf} >> 5$, (5.26) can be reduced as

$$T_{CSI-EMD} = \left[23n_f \cdot n + 30 \sum_{f=1}^{n_f} n_e(f)\right] \cdot n_{pf} \tag{5.27}$$

Since, $\underset{1 \le f \le n_f}{max}\, n_e(f) \approx n$, (5.24) and (5.27) can be written as

$$\begin{aligned} T_{PLI-EMD} &\approx 20 \cdot n_{pf} \cdot n_f \cdot n \\ T_{CSI-EMD} &\approx 53 \cdot n_{pf} \cdot n_f \cdot n \end{aligned} \tag{5.28}$$

The EMD behaves as a dynamic filter bank in which the Fourier spectra of all IMFs fall into the single step along the axis of period logarithm [129]. So for the n number of data samples, the total number of *pre*-IMFs required for the EMD algorithm are $n_f \le \log_2 n$ [130]. Assume that the number of *post*-IMF n_{pf} is fixed. Thus, the reduced time complexity functions are given as

$$\begin{aligned} T_{PLI-EMD} &\le 20 \cdot n_{pf} \cdot (\log_2\ n) \cdot n \\ T_{CSI-EMD} &\le 53 \cdot n_{pf} \cdot (\log_2\ n) \cdot n \end{aligned} \tag{5.29}$$

Thus, the total time complexity for the PLI and CSI based EMD is equal to the $O(n \log n)$.

5.5 Experimental Setup

The presented (Fig. 5.4) real time EMD based ultrasonic imaging system for NDT application consists of four main sections: (1) Test setup for NDT, (2) Analog front-end electronics boards, (3) Digital section (boards), and (4) GUI software for the data processing and waveform displaying. The experimental setup is shown in Fig. 4.9. The USB application firmware has been developed using the C++ language. The GUI software has been developed in Visual Studio platform using visual C# language. It encompasses the EMD based implementation as depicted in Fig. 5.4

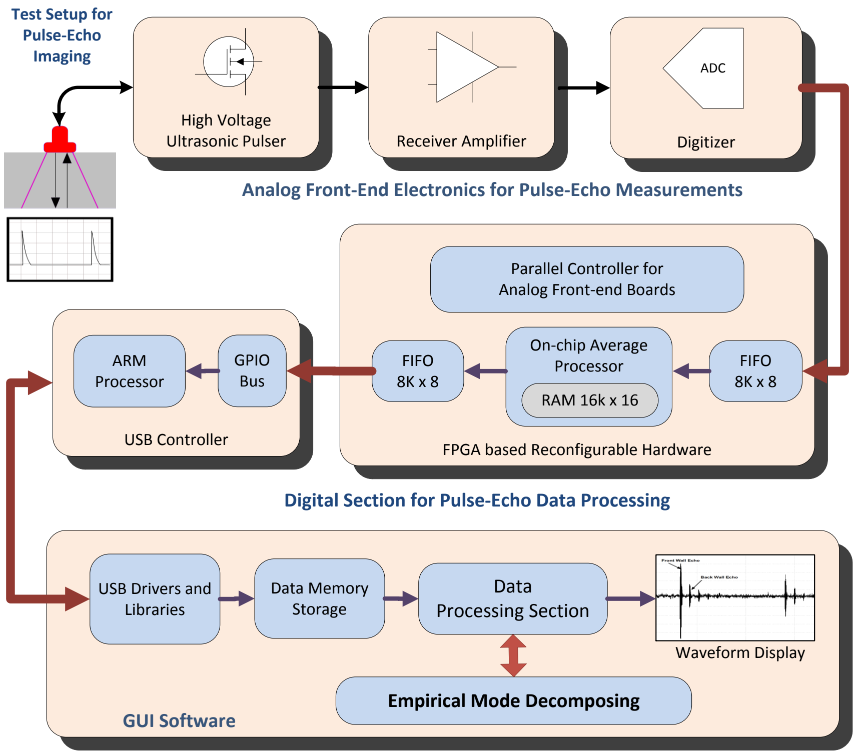

FIGURE 5.4: Schematic block diagram of developed experimental setup for ultrasonic pulse-echo measurements.

5.6 Results and Discussions

The EMD algorithm has been implemented in visual software platform for the real-time denoising of detected ultrasonic echo signals. It is common practice among researchers to model the present noise as Gaussian noise and apply appropriate denoising filter on the actual signal for its SNR improvement. Thus, the partial reconstruction method is used for signal filtering. Both PLI and CSI based EMD software have been implemented but we will mainly focus on the CSI based EMD as it has better interpolation accuracy. First of all, the decomposition capability of the implemented CSI-EMD has been checked using multi-frequency sinusoidal signal. Then the baseline correction and the denoising performance of the CSI-EMD algorithm have been verified by introducing external random white Gaussian noise into the sinusoidal signal with DC offset. Further, the actual noisy ultrasonic

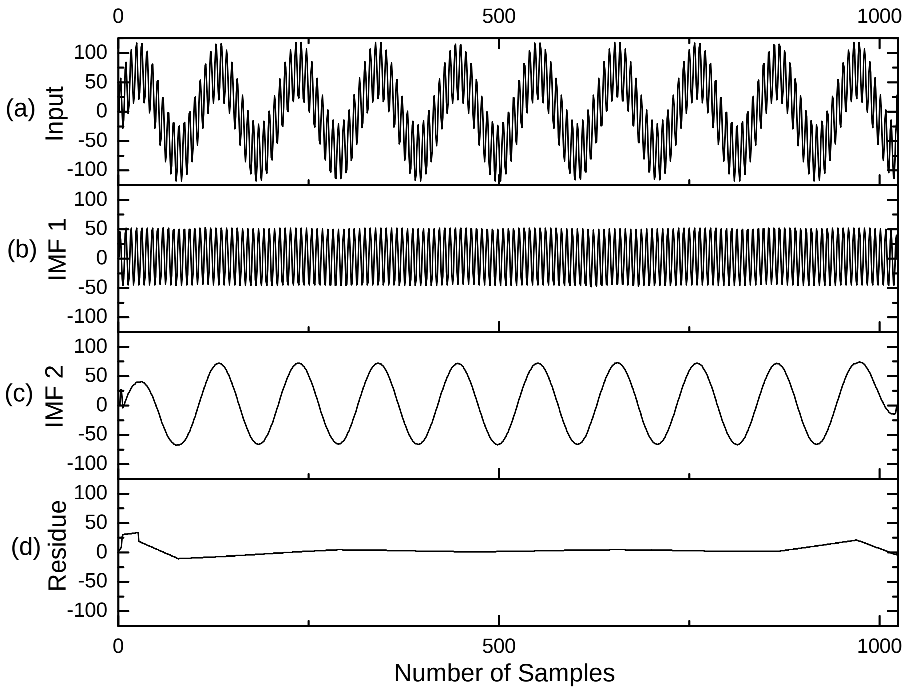

FIGURE 5.5: Decomposition results by CSI-EMD: (a) Input, (b) $IMF1$, (c) $IMF2$, and (d) Residue r.

pulse-echo signal has been filtered through the EMD software for the real-time denoising filtering analysis.

5.6.1 Decomposition results by implemented EMD software

This section provides the decomposition capability of the implemented EMD algorithm using sifting operations to split the signal into its components with different frequencies. The numerical equation of the sinusoidal signal has been implemented in a visual software environment using C# and it is described as:

$$x(i) = 70 \cdot sin(2 \cdot \pi \cdot 0.01i) + 50 \cdot sin(2 \cdot \pi \cdot 0.15i),\ 0 < i \leq 1024 \tag{5.30}$$

where i is the number of samples and the data acquisition/sampling rate is chosen as 10 MSPS. So the signal $x(t)$ is composed of two different frequency components 1500 kHz and 100 kHz. The implemented sinusoidal input has been plotted as shown in Fig. 5.5. It shows that signal has been decomposed in $IMF1$ (1500 kHz), $IMF2$ (100 kHz) and residue function r. It can be observed that $IMF2$ and residue r have end-effect errors at both extreme ends because in most cases, the first and last endpoints of the signal are not the extreme points, and this cause

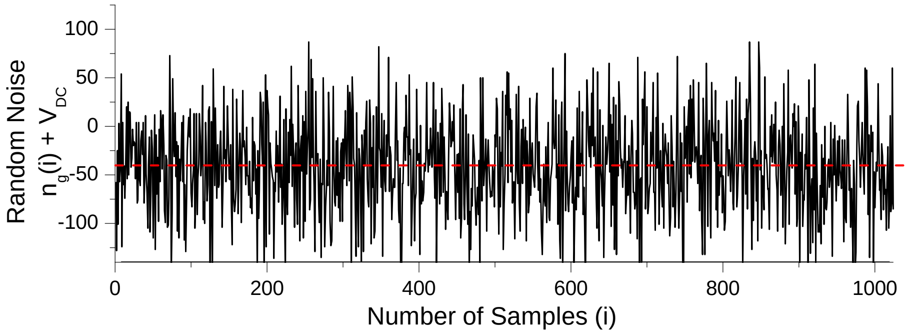

FIGURE 5.6: Random white gaussian noise $A \cdot n(t)$ with negative DC baseline.

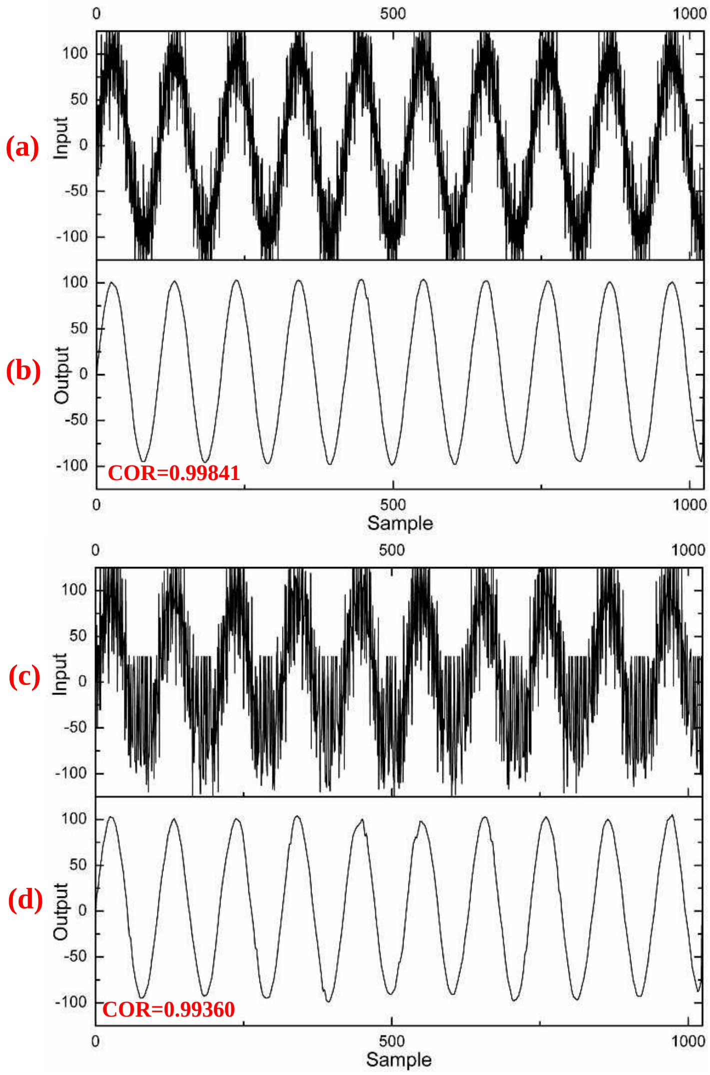

FIGURE 5.7: Baseline correction and noise filtering of sinusoidal noisy signals using the EMD software. Input waveforms are the noisy signals $x(t)$ with SNR of (a) 16.48 dB and (c) 12.04 dB. Output waveforms are the EMD processed signals $\tilde{x}_a(t)$ with COR of (b) 0.99841, and (d) 0.99260.

upper/lower envelope become divergent at both end parts. This leads to the waveform distortion at the ends of the decomposed signal.

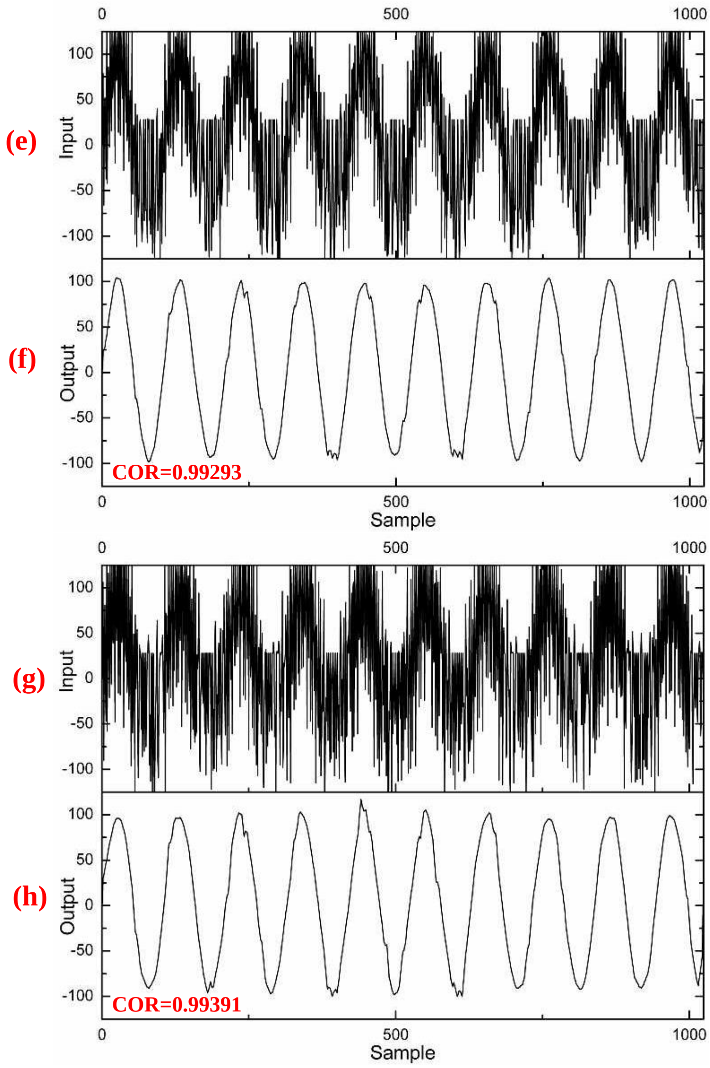

FIGURE 5.8: Baseline correction and noise filtering of sinusoidal noisy signals using the EMD software. Input waveforms are the noisy signals $x(t)$ with SNR of (e) 9.118 dB and (g) 6.020 dB. Output waveforms are the EMD processed signals $\tilde{x}_a(t)$ with COR of (f) 0.99293 and (h) 0.99191.

5.6.2 Baseline correction and noise filtering by EMD

The signal noise suppression and baseline correction capability of the implemented EMD have been described in this section. The noisy signal has been filtered using the partial reconstruction algorithm as described earlier. The numerical expression for the noisy sinusoidal signal is given as

$$x(i) = 100 \cdot sin(2 \cdot \pi \cdot 0.01i) + A \cdot n_g(i) + V_{DC} \tag{5.31}$$

where $0 < i \leq 1024$, A indicates the multiplication factor and $n_g(i)$ is the spatially uniformly distributed random white Gaussian noise which is introduced with the sinusoidal signal of 100 kHz frequency. The DC baseline of $n_g(i)$ is shifted in the negative value V_{DC} with $A = 100$ as shown in Fig. 5.6. This random white Gaussian noise has been captured from the Tektronix AFG3103C function generator with different voltage amplitude A. The signal-to-noise ratio (SNR) of the noisy signal is calculated as $SNR = 20 \cdot \log_{10}(max_i(x(i))/max_i(An_g(i)),\ 0 < i \leq 1024$. Fig. 5.7 provides the waveform plots of noisy sinusoidal inputs $x(t)$ and its EMD filtered outputs $\tilde{x}_a(t)$. It can be observed that EMD processed signal $\tilde{x}_a(t)$ provides the smooth sinusoidal signal with zero DC baseline. The obtained IMF index k_c is 1 for the signal reconstruction. The similarity between actual signal $x_a(t)$ and EMD processed signal $\tilde{x}_a(t)$ has been analyzed by calculating the Pearson correlation coefficient [131] as described in (5.32). The $\bar{x}$ and $\bar{y}$ are the mean values of the signal $x_a(t)$ and $\tilde{x}_a(t)$, respectively. It is observed that there is a decrement in COR of the signal due to the increment of noise. However, the COR of 0.99192 was obtained from the noisy signal with SNR of 6.020 dB as shown in Fig. 5.7(h),

$$COR = \frac{\sum_{i=1}^{N}(x_a(i) - \bar{x})(\tilde{x}_a(i) - \bar{y})}{\sqrt{\sum_{i=1}^{N}(x_a(i) - \bar{x})^2 \sum_{i=1}^{N}(\tilde{x}_a(i) - \bar{y})^2}} \tag{5.32}$$

5.6.3 Ultrasonic pulse-echo measurements using EMD based denoise system

For the NDT experimentation, two types of testing methods have been used: (1) Contact bases NDT and (2) Immersion based NDT. Ultrasonic echo signals have been detected by the ultrasonic transducer from the flaws in the material. Here the random white Gaussian noise $n(t)$ has been superimposed with the ultrasonic actual signal $x_a(t)$. Fig. 4.12 shows the aluminium block with three artificial side-drilled holes $N1$, $N2$ and $N3$ in the beam direction. During the measurements, the experimented pulse-echo signal has been acquired from the holes of the aluminium object using a contact transducer of 2.2 MHz frequency and 25 mm casing diameter. The sampling rate of 16 MHz with 8-bit resolution is chosen for the data acquisition. The actual signal $x_a(t)$, noisy (non-EMD) signal $x(t)$ and its EMD processed signal $\tilde{x}_a(t)$ are captured in GUI software as shown in Fig. 5.9. The obtained IMF index k_c is 2 for the contact ultrasonic testing. The modified SNR function is used to analyze the enhancement of the pulse-echo signal using EMD based signal filtering [120]. The SNR function is:

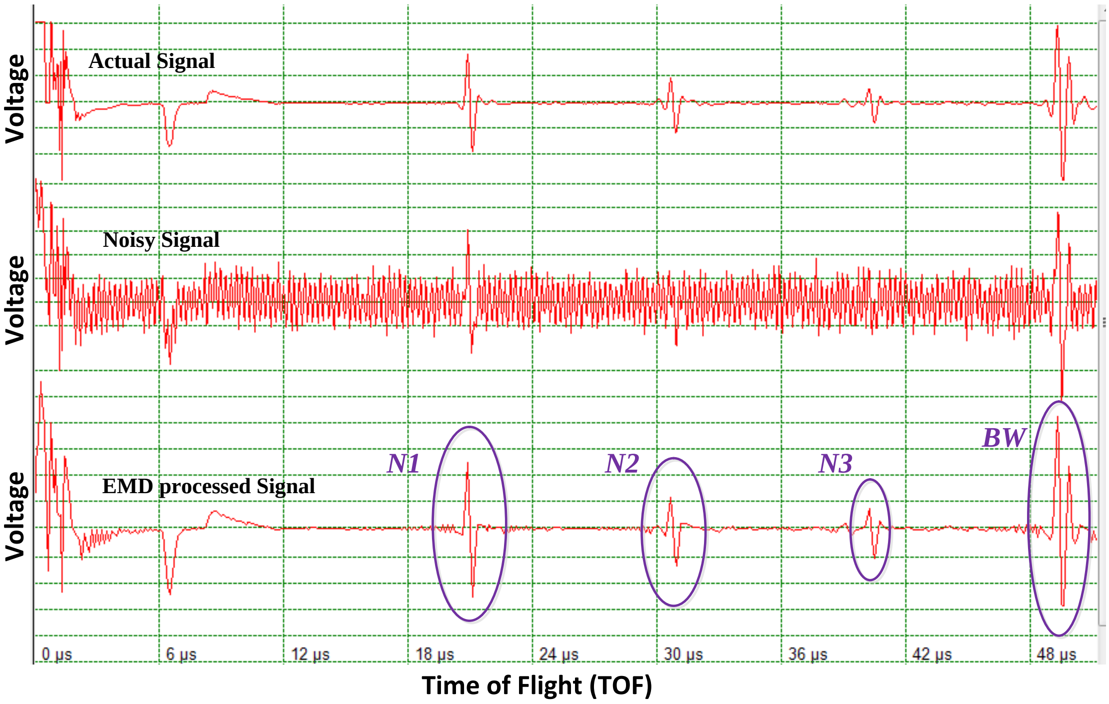

FIGURE 5.9: Screenshot of GUI software for online viewing of actual signal $x_a(t)$, noisy signal $x(t)$ and EMD processed signal $\tilde{x}_a(t)$: $k_c = 3$, $n = 1024$, sampling rate $f_s = 16MHz$, and transducer frequency $f_T = 2.2MHz$.

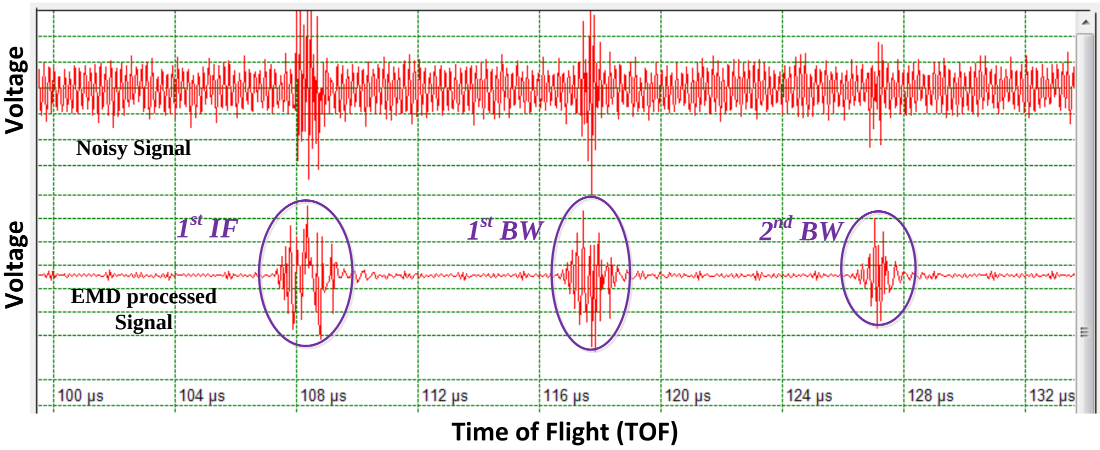

FIGURE 5.10: Screenshot of GUI software for online viewing of noisy signal $x(t)$ and EMD processed signal $\tilde{x}_a(t)$: $k_c = 2$, $n = 1024$, sampling rate $f_s = 25MHz$, and transducer frequency $f_T = 10MHz$.

$$SNR = 10 \cdot \log_{10} \left[\frac{\sum_{i=T-W/2}^{T+W/2} x^2(i)}{\sum_{i=1}^{n} x^2(i) - \sum_{i=T-W/2}^{T+W/2} x^2(i)} \right] \tag{5.33}$$

where T is the location of flaw/hole and W is the pulse width of the echo signal. These parameters are obtained manually through visual examination. The same SNR function is used for noisy input and its EMD processed output. Here it can be observed that ultrasonic echoes from the three holes $N1$, $N2$, $N3$ and a

TABLE 5.3: SNR enhancement of ultrasonic signals

Echoes	Depth from Transducer	SNR Noisy Signal $x(t)$	SNR EMD Processed Signal $\tilde{x}_a(t)$	SNR Enhancement
		Contact Testing		
$N1$	61 mm	-14.2239	$+10.3968$	$+24.6207$
$N2$	93 mm	-17.2012	$+8.6246$	$+25.8258$
$N3$	123 mm	-18.5110	$+3.7801$	$+22.2911$
BW	153 mm	-12.5792	$+15.1700$	$+27.7492$
		Immersion Testing		
1^{st} IF	80 mm	-27.1326	-0.8853	$+26.2473$
1^{st} BW	110 mm	-29.6862	-7.4857	$+22.2005$
2^{nd} BW	140 mm	-36.0773	-17.1687	$+18.9086$

back-wall BW are clearly detected and visualized in EMD processed output signal with the SNR enhancement (Table 5.3) of $> 22\,dB$.

A 10 MHz, unfocused, un-damped, 6 mm crystal diameter, water immersible transducer is used for the immersion NDT. The Aluminium based mechanical cylindrical object has been made in the laboratory as shown in Fig. 3.8. After the high voltage excitation of the ultrasonic transducer, first echo (1^{st} IF) is detected from the water-aluminium interface and second echo (1^{st} BW) is detected from the back wall surface of aluminium block. Fig. 5.10 provides pulse-echo responses from the aluminium block. The obtained IMF index k_c is 3 for immersion ultrasonic testing. The SNR improvement of the EMD processed pulse-echo signals are 26.25 dB, 22.20 dB, and 18.91 dB for the signals 1^{st} IF, 1^{st} BW, and 2^{nd} BW, respectively. For the PLI-EMD implementation, the SNR enhancement of the $1^{st}BW$ echo is 26.43 dB.

TABLE 5.4: Calculated parameters of EMD based denoise system

	Envelope Generation Method	Sampling Rate	Processing Time	Data Samples #
Current Work	CSI	50 MHz	0.001500 s	1000
Current Work	PLI	50 MHz	0.0000491 s	1000

5.6.4 Performance of the EMD based denoise system

Table 5.4 describes the calculated parameters of the real-time EMD based denoise system. The hardware-accelerated method for EMD data processing has been developed in [116] but these are not real-time results as they require 1.43 second to process 2048 data samples. The method described in [117] for ECG system divides the whole dataset into the multiple sections of 1000 data byte samples where each section needs 2.48 second for EMD processing. However, the complete FPGA based implementation of PLI based EMD requires 0.0001 second as described in [115]. The method in [132] developed the fast EMD implementation and needs only 0.000075 second for the processing of 1000 samples using PLI-EMD. Our proposed PLI-EMD implementation needs least processing time of 0.0000491 second, compared to all previously implemented PLI-EMD. The processing time for the implemented CSI-EMD is 0.00150 second. The current EMD implementation has no limitation on memory cost or area. The sampling rate for the current implementation can be increased up to 100 MHz. The highest sampling rate for the current system implies the feasibility of the real time ultrasonic measurement systems. The work presented in[115] filters simply the high-frequency sinusoidal interference from the ultrasonic data. But the current work describes the noise filtering application applying the actual ultrasonic signal which is degraded by the white Gaussian noise.

In the next chapter, a novel hardware-based architecture using the reconfigurable embedded system for the multi-channel immersion ultrasonic system is proposed. It provides the addressing-based analog multiplexing scheme which requires only one data acquisition unit and common on-chip storage for the multi-channel imaging system. Here the performance evaluation of the developed multi-channel system will be presented by carrying out the B-scan and C-scan image acquisition of the water-immersed mechanical components.

Chapter 6

Reconfigurable Embedded System for Real-time Acquisition and Processing of Multichannel Ultrasonic Signals

This chapter proposes a novel hardware-based architecture of the reconfigurable embedded system for the multi-channel immersion ultrasonic system. It provides the addressing-based analog multiplexing scheme which requires only one data acquisition unit and common on-chip storage for the multi-channel imaging system. It also provides unique channel reconfigurable facility to the user to modify the number of channels by installing only the partial front-end hardware (pulser, pre-amplifier) and without modifying the remaining data acquisition hardware (common-amplifier, digitizer) and back-end embedded system. The developed system further supports dynamic on-line reconfiguration of the analog front-end hardware, real-time hardware-based data processing, and data transfer operation. For the experimentation, the complete 4-channel ultrasonic imaging system for immersion testing has been designed, developed and evaluated in the laboratory. Here the performance evaluation of the developed multi-channel system will be presented by carrying out the B-scan and C-scan image acquisition of the water-immersed mechanical components.

In section 6.1, the differences between conventional and proposed multi-channel ultrasonic imaging system are described. In the section 6.2, the overall system description has been presented for the multi-channel configuration which consists of multi-channel reconfigurable analog front-end circuits, interfacing architecture between various boards and development of GUI software. In the next section 6.3, the FPGA based reconfigurable implementation of the coherent averaging is presented for the SNR enhancement. The prototype-based 4-channel ultrasonic imaging system for immersion testing has been designed and developed for experimentation and it is discussed in section 6.4. During experimentation, the pulse-echo signal has been processed through real-time signal processing hardware and the entire imaging system is evaluated using the 4 channel matrix based transducer assembly. Furthermore, the B-scan and C-scan imaging applications are also presented using the developed multi-channel system.

6.1 Overview of proposed multi-channel ultrasonic imaging system

Ultrasonic inspection technique for immersion applications is well established and broadly utilized for non-destructive testing (NDT) and evaluation (NDE), specifically of mechanical structures in numerous industries. Traditional ultrasonic instruments are required for flaw detection and/or estimation of amplitude and time-of-flight (TOF) of the received signal (A-scan) in the test medium and, when it is connected with an automatic scanner, this setup can be employed to acquire images (B-scan, C-scan). A single-channel system is actually relevant for basic and instant inspection of the material. On the other hand, the multi-channel immersion system can enhance the speed of testing and expand the coverage on the field of view of the sensors, especially if large areas have to be examined. The approach behind a multichannel immersion system is that each transducer element takes care of the inspection of a metal specimen (for example aluminium) with a width equivalent to the active transducer diameter. Here it is assumed that the acoustic intensity at the borders of a transducer is zero. Therefore, the transducers should spatially be arranged as adjacent as possible in order to ensure 100% coverage of the material under inspection.

The conceptual architecture of multi-channel ultrasonic imaging system for immersion application is shown in Fig. 6.1 (a) [89, 133–137]. The research-purposed ultrasonic imaging system should ideally allow the researcher to implement or develop new real-time imaging algorithm, customization of the waveform data pattern, and access to the unprocessed receiver data. Furthermore, its hardware components should be designed with a reconfigurable tool such that data processing scheme can be easily programmed or modified. The front-end hardware of a

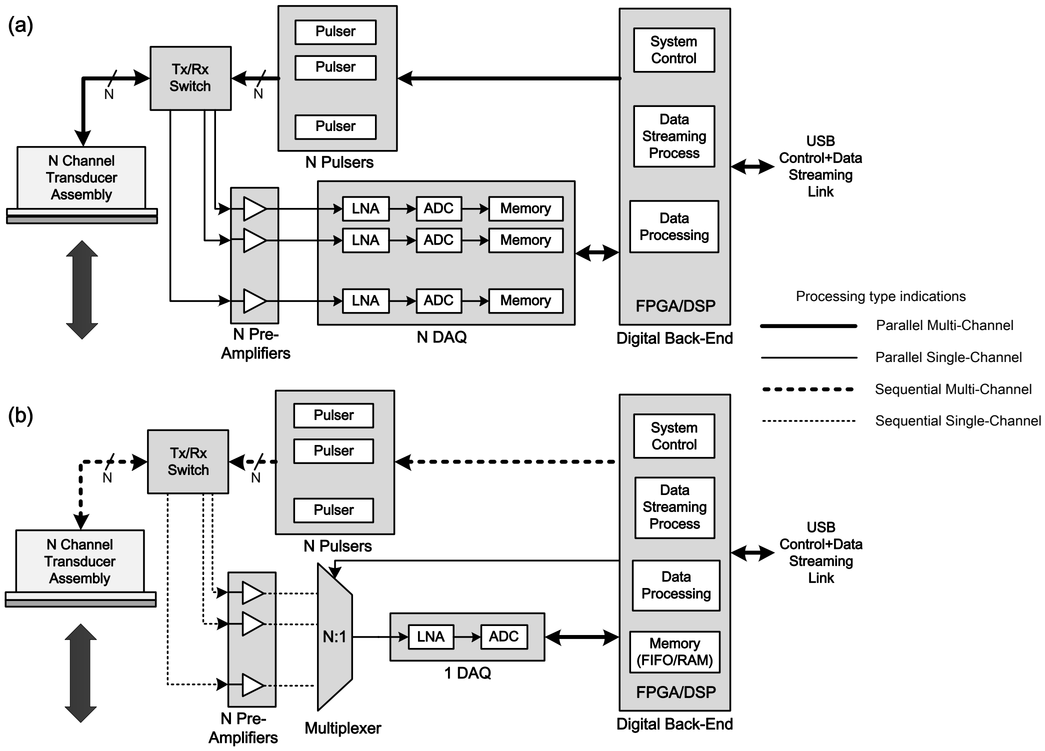

FIGURE 6.1: Conceptual view of multichannel ultrasonic imaging system for immersion system. Here line pattern indicates the type of processing/operation (Parallel/Sequential) (a) General architecture of such system and (b) Proposed architecture of multichannel imaging system.

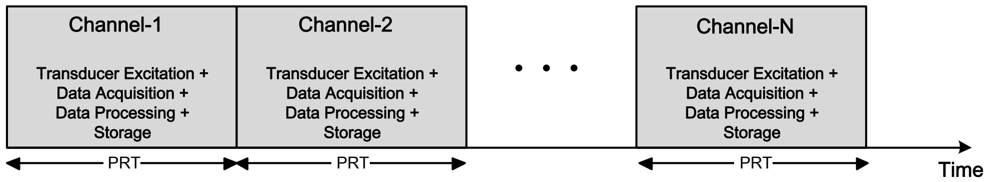

FIGURE 6.2: Ultrasonic data acquisition and processing time diagram for the proposed system.

general multi-channel ultrasonic system (Fig. 6.1 (a)) includes N-channel pulsers, Tx/Rx switch, and N-channel pre-amplifiers. The primary role of the front-end electronic is to interface the imaging system with the connected transducer probes on a channel-by-channel basis. The outputs of pre-amplifier boards are connected with the N-channel data acquisition (DAQ) unit. It consists of N number low-noise amplifiers (LNAs), analog-to-digital converters (ADCs) and memory storages (FIFO/RAM). Since it is the multi-channel parallel arrangement, it is not feasible to utilize the on-chip FIFO/RAM of the FPGA or DSP chip for the further processing of the A-scan raw data. However, such type of systems does not have the modular design approach to facilitate the scaling of the system. The system scaling i.e. increment in the number of channels enhances the complexity in terms of front-end hardware, DAQ hardware, programmability of FPGA/DSP, memory management, I/O management, and back-end hardware complexity. The such kind of 4-channel ultrasonic imaging system has been implemented as described in section 2.2. To overcome this problem, the novel architecture is proposed specifically for multichannel immersion system as presented in Fig. 6.1 (b). As the main role of the front-end hardware (pulser, Tx/Rx switch, pre-amplifier) is the same, both architectures have the identical front-end hardware. the addressing based analog multiplexing scheme is proposed to overcome the use of multiple DAQ hardware and digital back-end complexity for the multi-channel system. In that case, the N-channel immersion system requires only one DAQ unit for the multiplexed signal and a memory (FIFO/RAM) can be implemented in digital back-end hardware. Thus, it has a fixed number of physical I/O lines and on-chip storage memory. The proposed architecture includes both parallel and sequential configuration. The front-end hardware (pulsers and pre-amplifiers) operations are preformed in a sequential manner while the DAQ and back-end digital hardware are performed in a parallel manner as shown in Fig. 6.1 (b). The timing diagram of the ultrasonic data acquisition and processing is shown in Fig. 6.2. It shows that each channel is executed sequentially one by one with one pulse repetition time (PRT). Therefore, for the N-channel ultrasonic imaging system, it requires $N \cdot PRT$ time for the entire execution. While the data processing of each channel is performed in both parallel and sequential way as presented in Fig. 6.7. The detailed architecture is described in section 6.2.

Since the ultrasonic frequency for immersion testing is ranging from 0.1-20 MHz, the data processing operation becomes very vital to the system configuration. Main parameters determining such a complex imaging system comprises signal processing, computational speed, data transfer speed, and hardware cost. This chapter also provides an efficient hardware-based reconfigurable architecture which is designed and implemented to meet the demands of multi-channel, high-performance and reconfigurable ultrasonic imaging system. The proposed developed reconfigurable embedded system provides the unique channel reconfigurable facility to the user to change the number of channels of the imaging system by introducing only the partial front-end analog hardware (pulser and pre-amplifier) and dynamically modifying few parameters of the back-end embedded system. This capability provides the user to convert this reconfigurable system from 1-channel to 512-channel (256 channel for pulse-echo (P-E) mode as well as 512 channel for transmit-receive

(T-R) mode) system without changing the digital back-end hardware and DAQ hardware (i.e. common-amplifier, digitizer). The developed imaging system also supports dynamic on-line reconfiguration of the analog front-end hardware, the real-time data processing, and data transfer operation.

6.2 System Description

The overall block diagram of the multichannel ultrasonic imaging system is shown in Fig. 6.3. Since this system is a modular system, it allows the number of channels to be upgraded up to the 512 channels (256 for P-E and 512 for T-R mode). For the N-channel ultrasonic imaging system, it comprises six different types of electronics boards interfaced together and a PC based GUI software for post-processing and displaying of images. The N numbers of pulser boards $(P_1, P_2, ..., P_N)$ are connected to the N number of pulse-echo mode ultrasonic transducers $(TP_1, TP_2, ..., TP_N)$. The same connections are provided to the N number of respective pre-amplifier boards $(Pr_1, Pr_2, ..., Pr_N)$. Same way, N number of transmit-receive mode transducers $(TT_1, TT_2, ..., TT_N)$ are also connected with pre-amplifier boards. The outputs of all N-channel pre-amplifier boards are connected via daisy chaining for the analog multiplexing and the final multiplexed output is given to the common-amplifier board.

As displayed in the system block diagram in Fig. 6.3, the personal computer (PC) serves as the user interface. Upon each trigger sign provided by the graphical user interface (GUI), the processor inside the USB controller sequentially sends out control signals to alternate blocks of the imaging system. The trigger generator circuit inside FPGA sends trigger signals to the pulser boards sequentially for the excitation of the respective transducer. Coaxial cables are used to connect transducers and interconnect analog front-end boards. The amplified echoes are first digitized using analog-to-digital (ADC) converter and later aligned by the FPGA for the further data processing. Afterward, the processed data is transferred to PC through the USB interface for display purpose. The GUI software is developed using Visual C++ for the real-time displaying of A-scan waveforms and B-scan/C-scan images.

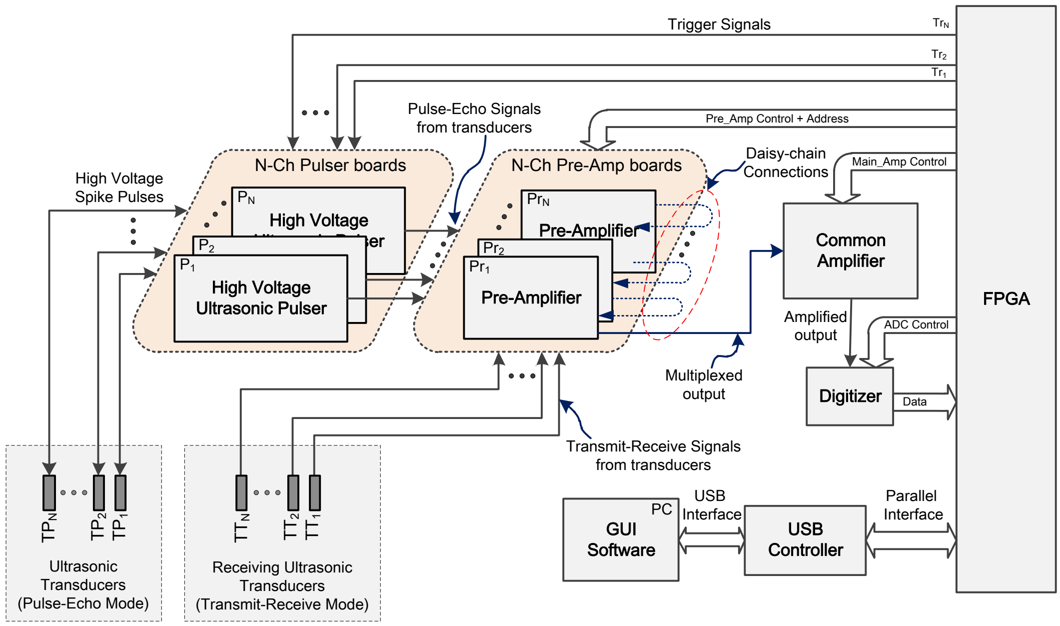

FIGURE 6.3: The overall block diagram of proposed N-channel (Maximum 256 channel for P-E and 512 channel for T-R mode) ultrasonic imaging system for immersion applications.

6.2.1 Reconfigurable analog front-end circuits

The analog front-end circuit comprises four types of group boards namely: high voltage (HV) pulser board, multi-stage pre-amplifier board, common-amplifier board having the variable gain amplification (VGA) and digitizer board.

Fig.6.4(b) shows the schematic block diagram of ultrasonic receiver pre-amplifier. It comprises the diode bridge limiter circuit which provides protections for further amplifier hardware stage from HV spike pulses received from the pulser circuit. The relay with low resistance and capacitance in ON condition is used to select the corresponding activated P-E or T-R signal. Each preamplifier board includes two-stage op-amp based feedback amplifiers (AD8014, Analog Devices Inc.) in non-inverting configuration with an individual gain of +20 dB and a bandwidth of 400 MHz. The passive band-pass filters with -3dB cut-off frequencies from 50 kHz to 50 MHz are also used directly after the terminals of all amplifiers. These cascaded amplifiers are connected to the analog multiplexer (AD8174, Analog Devices Inc.) for the selection of appropriate amplified output signal. It provides a high speed disable feature allowing the output of the all pre-amplifier boards to be put into a high impedance state for cascading configuration so that the off pre-amplifier channels (boards) do not load the output bus and allow them to be used in larger channels.

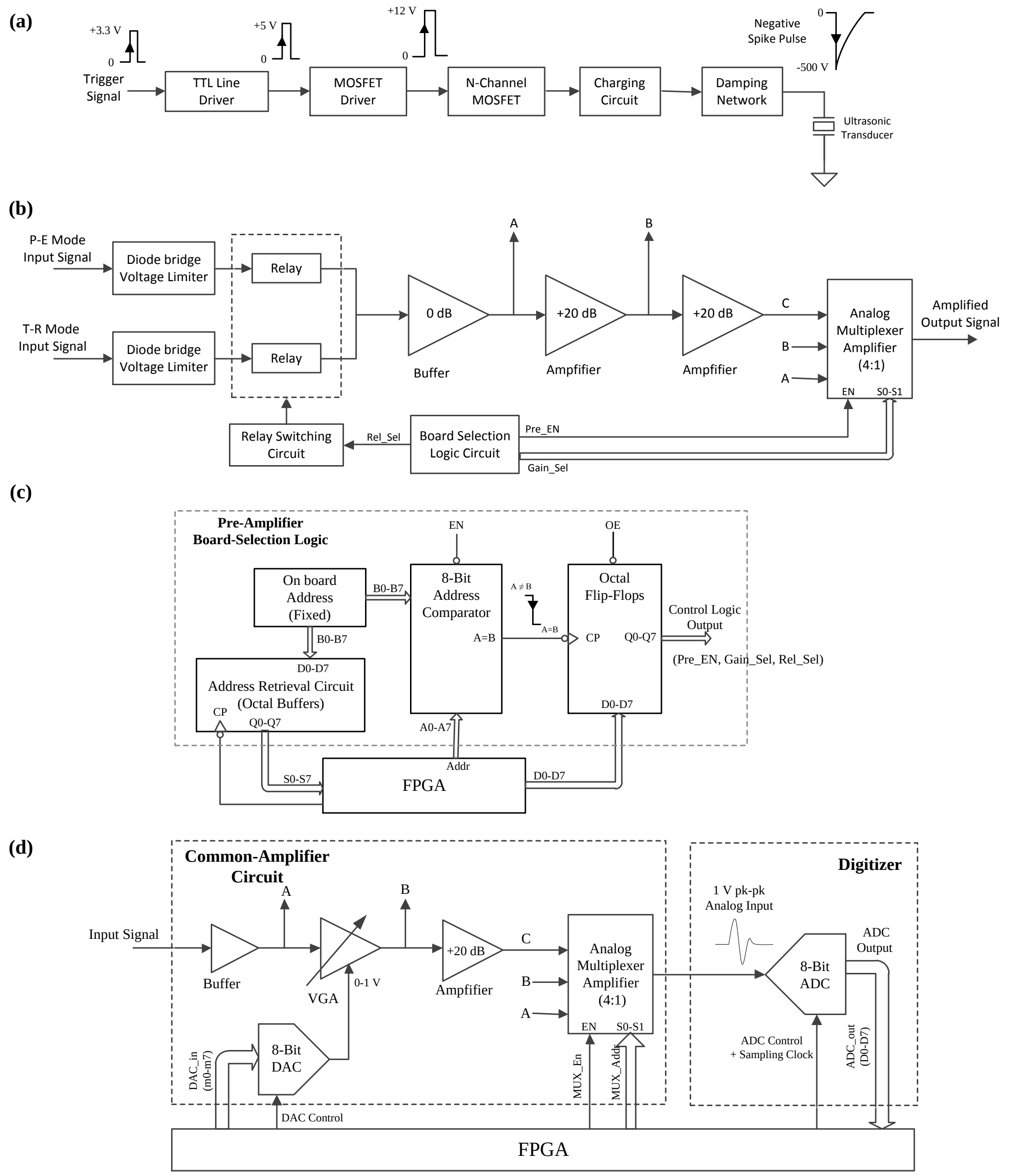

FIGURE 6.4: (a) Each channel of HV ultrasonic pulser, (B) Each channel of pre-amplifier circuit, (C) Board selection logic circuit for each pre-amplifier, and (D) Common-amplifier and Digitizer board with an interface to FPGA.

6.2.1.1 Multiplexing scheme

The four input signals of the analog multiplexer are entirely controlled by the board selection logic circuit. The board selection logic circuit selects the specific pre-amplifier board for the corresponding energized ultrasonic transducer. Every pre-amplifier board has its own 8-bit address (B0-B7) that is the pre-defined set by the user i.e. the pre-defined address for channel 1 (pre-amplifier 1) is 0x01. The FPGA continuously generates the external address (A0-A7) corresponding

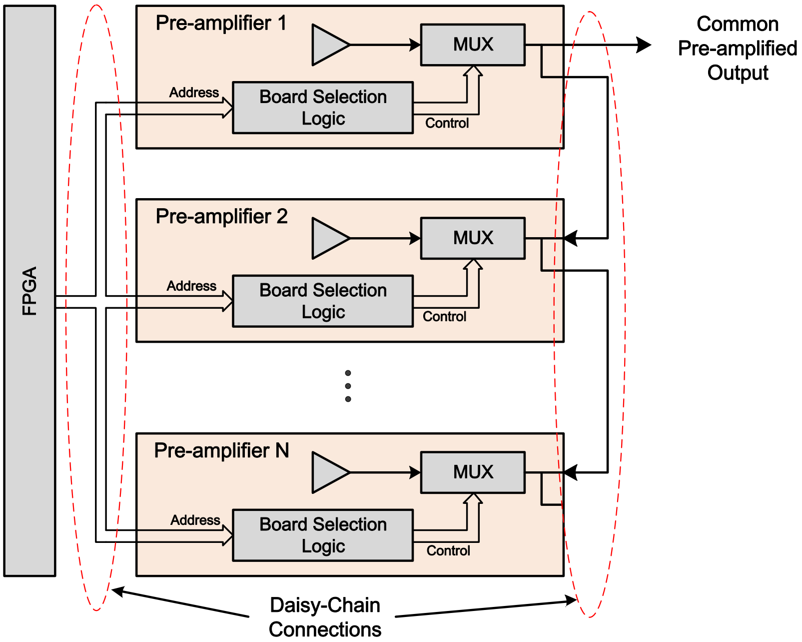

FIGURE 6.5: Conceptual block diagram of multiplexing scheme.

to the activated ultrasonic transducer. Both pre-defined board address and externally provided an address will be compared by the 8-bit comparator circuit. When both addresses match, the output of the comparator will transit from high to low level. For every high to low transition, the octal flip-flop circuit will be activated and data presented at its inputs (D0-D7) will be latched in flip-flop as shown in Fig.6.4(c). The address retrieval circuit loops back the on-board fixed address back to the FPGA. The on-board address circuit has the fixed 8-bit address. Thus, it is possible to attach maximum 256 pre-amplifier boards in cascading configuration via daisy chaining. Here all pre-amplifier boards have the same type of circuit configurations as shown in Fig.6.5. The input address connections of the all board selection logic circuits of pre-amplifier boards are connected together via daisy chaining. Likewise, the outputs of all multiplexure circuits are shorted together via daisy chaining. Therefore, the single multiplexed output of the activated pre-amplifier provides the amplified ultrasonic signal of the specific activated transducer.

6.2.2 Development of online GUI based signal processing software

The GUI has been implemented in visual software environment using visual C#. Once the appropriate connection between the host and the USB controller is established, the control endpoint is utilized to send/receive the sample data to/from the external device. The control endpoint is only one endpoint that serves as a bidirectional data connectivity. So before every transfer operation, the direction of control endpoint must be set. The *Request code* is also transmitted from host to device along with the control data.

The developed GUI software includes different sequential stages for imaging operations such as data fetching from the device, channel demultiplexing, noise suppression, base-line corrections, and scan conversion from raw data to different scan/image format (i.e. A-scan, B-scan, and C-scan). The N-channel raw data are fetched from the device and separated into the specific storage array. Thereafter, these raw data samples are fed to the envelope detection filter (EDF) based envelope generation block. The detailed explanation of EDF is provided below.

6.2.2.1 Real-time Envelope generation

Here the envelope detection filter (EDF) is adopted, proposed by Fritsch et al. [138] for the envelope generation of the ultrasonic data samples because it is fastest among others. An approximate value for a next sample of the envelope is gained from the two successive samples. Assume that input signal is $Y(t) = A(t)sin(2\pi f_c t + \phi)$, where f_c is the central frequency of the ultrasonic signal. For the sampling time period T_s, the k^{th} sample of signal $Y(t)$ can be represented as $Y_k = A_k sin(k\omega_0 + \phi) = A_k sin\phi_k$. The same way, $(k+1)^{th}$ sample is represented as $Y_{k+1} = A_k sin(\phi_k + \omega_0)$. Then, the next consecutive envelope amplitude $A_{k+1}(t)$ is given as

$$A_{k+1}(t) = \sqrt{Y_{k+1}^2 + \left(\frac{Y_k}{sin\omega_0} - \frac{Y_{k+1}}{tan\omega_0}\right)^2} \tag{6.1}$$

where, $\omega_0 = 2\pi f_c/f_s$ and f_s is the sampling rate of data acquisition. The main advantages of this filter are that it provides a good approximation of the ultrasonic signal envelope by only two successive samples of the data and the knowledge of the carrier frequency (f_c) and sampling frequency (f_s).

The FPGA plays a significant role for the N-channel ultrasonic processing unit that controls pulse transmission, channel multiplexing, data acquisition, pre-processing of the A-scan data sets and data transfer. Therefore, the FPGA code is appropriately designed and developed such that it is reconfigurable to re-optimize the speed and usage of the relevant resources in the multi-channel ultrasonic imaging system.

6.3 FPGA based Digital System

The block diagram of the FPGA (XC6SLX9-2CTQG144, Xilinx, CA) code for the $N(= 4)$ channel imaging system is shown in Fig.6.6. The code was written in VHDL based hardware description language (HDL). It comprises 4-channel pulser trigger generators that produce sequential pulses for the specific channels after getting the command from the USB controller. The ADC output is decoded as parallel, single-ended, and binary-offset outputs at 100 MHz speed. After that, the parallel data stream is synchronized with the system clock and stored in the Rx-A FIFO when the appropriate control signals are received from the FPGA master controller. Later, the data sets are transferred to the data averaging module for the coherent averaging process. The master controller handles the overall flow of the data and provides the reconfigurable feature of the code, which is ultimately controlled by the control signals from the USB controller. After completion of coherent averaging, it generates *Data_ready* signal. The master controller makes its decisions based on the trigger signal timing and *Data_ready* signal to control the Rx-A and Rx-B FIFO, pre-amplifier channel selection (enable/disable), and memory size. The functions of main blocks are summarized in the rest of this section.

6.3.1 Rx-A and Rx-B FIFO storage

The A-scan raw data samples are synchronized immediately before being accumulated in the Rx-A FIFO. The data sets from ADC are stored automatically to the FIFO input port at each rising edge of the sampling clock. It is considered that the outputs from the ADC are 8-bit quantized with 100 MHz sampling rate, and the length of Rx-A FIFO is 16384; which corresponds to a depth of penetration (D_p) in aluminium for the pulse-echo mode is calculated as

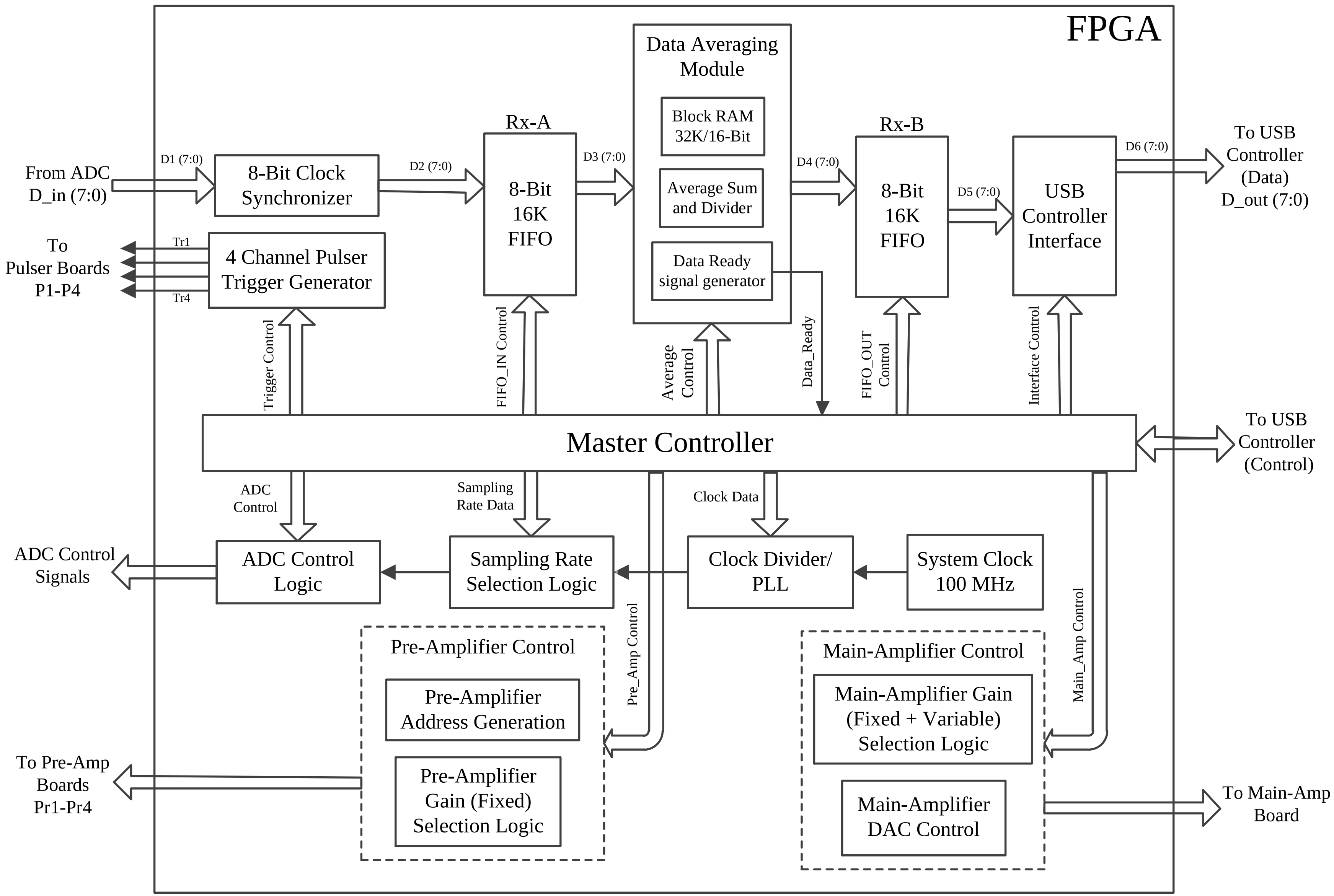

Figure 6.6: Block diagram of FPGA based digital system.

$$D_p = 16384 \times (6320\, m/s)/(100\, MHz \times 2) = 517.7\, mm \qquad (6.2)$$

where the acoustic velocity in aluminium is considered as $6320 m/s$. Note that this is for two-way travel of the ultrasonic wave for pulse-echo (P-E) mode; however, for T-R mode, 16384 byte FIFO length corresponds to double that distance, which is $1035.4\, mm$. Here the D_p of only solid material is considered as one usually skip the data acquisition of immersion path while imaging. On every trigger event, FIFO will be asynchronously reset by the master controller that initializes all internal pointers and output registers. The Rx-B FIFO is utilized to accumulate the averaged output data samples after the completion of N_{Avg} trigger events. The output of Rx-B FIFO is connected to the USB controller module via the parallel interface. Both Rx-A and Rx-B FIFOs have separate clock domains for both write and read data transmission.

6.3.2 USB Controller Interface and Control

The general purpose interface (GPIF II) of USB controller includes the necessary scheme to communicate with the FPGA board. The controller data bus and essential read/write control signals are connected to the FPGA. Some of these signals from FPGA are based on the scan-mode of imaging, acquisition speed, data transmission, and reset. Also, few signals are used to instruct the controller about the clock/phase synchronization, and whether the averaged data are ready from the FPGA. The GPIF II data bus of the controller is connected to the master controller of FPGA, which determines where to attach the corresponding channel by modifying the address of the corresponding channel and controlling the analog multiplexers of the pre-amplifier boards.

6.3.3 Overall scheme of data acquisition

To begin the acquisition process, a user interface control built up in a visual application is initialized first. The GUI software calculates the control parameters such as mode selection (P-E/T-R) sampling rate, acquisition memory size, number of coherent averages. During the running acquisition, it also calculates the control parameters for the front-end hardware such as pre-amplifier gain control, common-amplifier gain control, adjustable gain for VGA. These all parameters are calculated based on the respective transducer element and the scan type (i.e.,

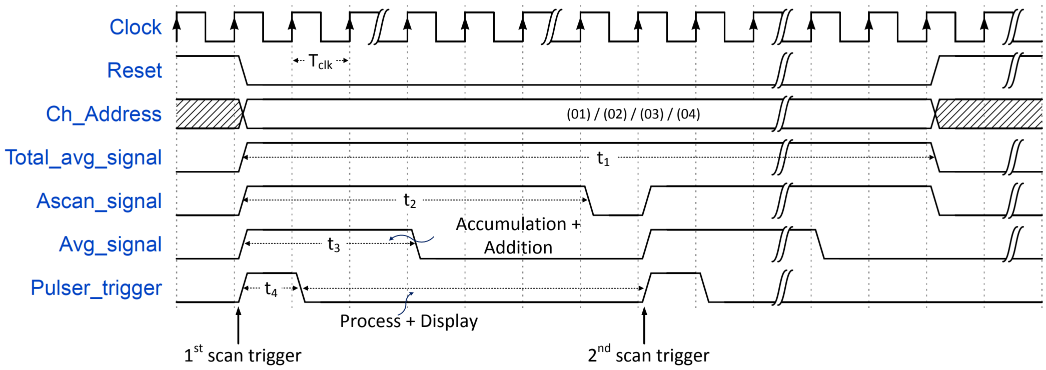

FIGURE 6.7: Timing diagram of the single channel (1-4) with N_{Avg} averages

A-scan, B-scan, and C-scan). After initialization, all parameters are downloaded into the USB controller via USB interface, which distributes them to the FPGA and front-end hardware. The pulse trigger signal to the next activated channel is fed via the FPGA after completion of the acquisition process of the formerly activated channel.

Once all parameter values are transferred to the FPGA, it triggers all the HV pulsers sequentially and simultaneously fills the receiving (Rx-A) FIFO with the corresponding A-scan stream of data until the *Full-Flag* signal is stimulated by the FIFO. After that, it waits for the next trigger pulse to start filling the FIFO again. This process is repeated for N_{Avg} times while the data sets of specific channels are averaged simultaneously and transferred immediately to another Rx-B FIFO. Afterwards, the accumulated data sets from Rx-B FIFO are transferred to the USB controller via parallel GPIF II interface. Once the controller receives all A-scan data sets, it will be transferred to the PC via USB interface. Thereafter, the post-processing operations like channel demultiplexing, envelope generation, and scan conversions are performed in host GUI. In the end, imaging is performed in three distinct modes: A-scan, B-scan, and C-scan.

6.3.4 Timing of control signals

The control unit of the averaging circuit uses four timing input signals as shown in Fig. 6.7. It presents the timing diagram of the pulse excitation, data acquisition and processing of the single channel configuration only and it will be repeated for the all N-channel operation. Here, the T_{clk} represents the pulse width of the clock signal. The *Total_avg_signal* determines the full data acquisition window width ($t_1 = N_{Avg} \cdot PRT$) and it totally depends on the number of averages. Likewise, the *Ascan_signal* represents the trigger pulse repetition width which is constant during each transducer excitation and *Avg_signal* describes the signal width of total accumulated acquisition samples in the FIFO. The time width t_2 ($= PRT - 1 \cdot T_{clk}$) describes the time span between each successive scan/trigger event of the transducer and it has to be wide enough such that the high voltage of negative spike pulses can get sufficient time to set in the initial state. The time width t_3 ($= \text{int}\,[N_R \cdot T_s]$) of each scan depends on the number of acquisition samples. The condition that applies to t_3 is that it must not exceed the available FIFO depth and it should be less than the PRT ($t_3 < PRT$). It is essential to decide the number of averages before the start of acquisition which is responsible for the time width t_3 and it is always greater than the PRT ($t_1 > (t_2, t_3)$). The t_4 ($= (1 \cdot T_{clk})$ to $(15 \cdot T_{clk})$) describes the pulse width of the pulser trigger signal.

The memory storage required by the implemented averaging architecture is only $2N_R$ bytes as displayed in Fig.6.6. The summing and division operation needs only 1 adder and 1 divisor, respectively. Therefore, The number of required memory storage and adders of the implemented averaging architecture is independent of the number of averages (N_{Avg}) and that allows the user to increase the number of averages and hence enhances SNR.

6.4 Results and Discussions

To validate this architecture, the 4-channel ultrasonic imaging system has been developed. However, the proposed architecture supports up to 256-ultrasonic channels. The detailed comparisons are given below.

TABLE 6.1: Comparisons between conventional and proposed architecture Assume that Pulse repetition time (PRT)= 1 ms

Parameter	4-Channel (Proposed)	8-Channel (Proposed)	4-Channel (Conventional)
Pulser (#)	4	8	4
Pre-amplifier (#)	4	8	4
Common-amplifier (#)	1	1	4
Digitizer (#)	1	1	4
Back-end hardware/complexity	1	1	4 times
Acquisition time (ms)	4	8	1

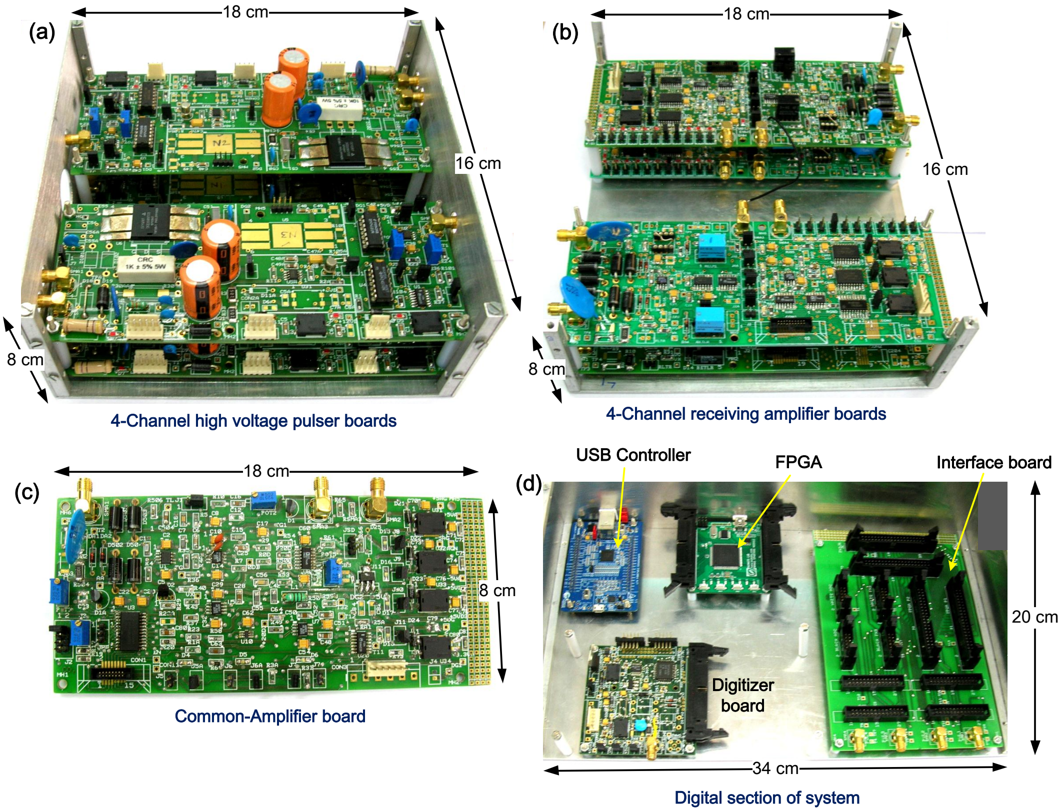

Figure 6.8: PCBs of the 4-channel ultrasonic imaging system with dimensions: (a) HV ultrasonic pulser boards, (b) Receiver pre-amplifier boards, (c) common-amplifier board, and (d) digital section of the imaging system that includes digitizer board, interface board, FPGA board and USB controller card.

6.4.1 FPGA resource utilization and power estimation

Table 6.2 illustrates the total FPGA resource utilization for the developed system. The power estimation of the various on-chip resources is also calculated using the Xilinx Power Estimator (XPE) tool (Xilinx, CA) as shown in Table 6.3. For the power estimation of the particular case, it is assumed that FPGA system clock frequency is $f_{sys} = 100MHz$, data acquisition rate is $f_{aq} = 100MHz$, and reading clock frequency for the FIFO (Rx-B) is $f_{rd} = 25MHz$. The total estimated power utilization in the FPGA is around 138 mW.

Table 6.2: Total FPGA resource utilization

Type	# Utilization	% Utilization
Slice Registers	983	8 %
Slice LUTs	725	12 %
LUT-FF pairs	438	34 %
IO buffers	49	48 %
Block-RAM/FIFO	16	50 %

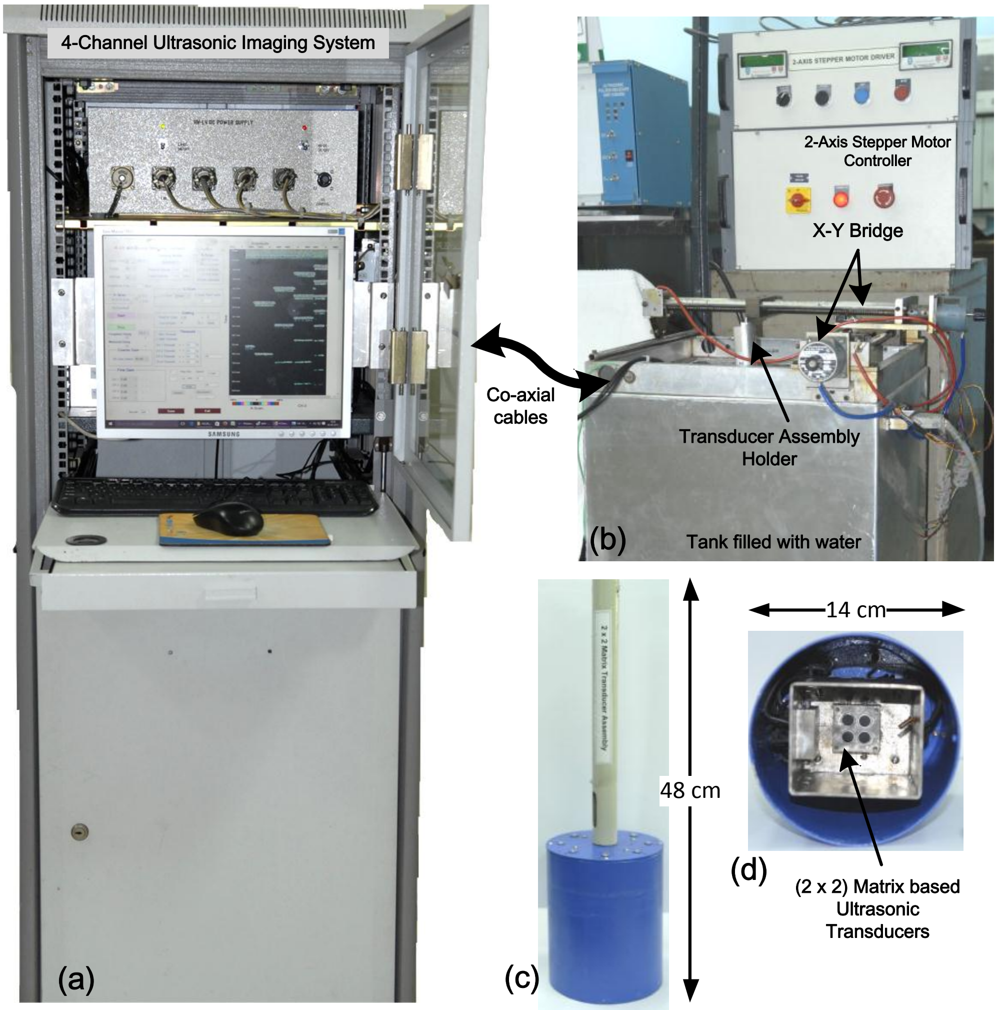

FIGURE 6.9: Experimental setup for immersion ultrasonic imaging (a) 4-Channel ultrasonic imaging system mounted in 14" rack, (b) Tank filled with water and X-Y automated scanner, (c) Transducer holder assembly and (d) Bottom view of transducer holder assembly.

6.4.2 Experimental setup

Photographs of the designed and developed electronic PCBs are shown in Fig. 6.8. It comprises the four HV pulser boards, four multi-stage pre-amplifier boards, common-amplifier board, digitizer board, FPGA module, and USB controller board. All boards are interfaced together and mounted in the 14" rack as shown in Fig. 6.9(a). The automated immersion scanner has been designed for the imaging of water-immersed structures and objects. This scanner (Fig. 6.9(b)) has two automated mechanical axes (X and Y) and a manual Z axis. The accurate ultrasonic transducer probe or assembly movement provided by the automated X and Y axes, along with the fine manual adjustments of transducer probe orientation with

TABLE 6.3: On-chip FPGA power estimation under the assumptions: $f_{sys} = 100MHz$, $f_{aq} = 100MHz$, and $f_{rd} = 25MHz$

On-chip	Power (W)
Clocks	0.012
Logics	0.005
Signals	0.005
BRAMs	0.006
IOs	0.092
Leakage	0.018
Total	**0.138**

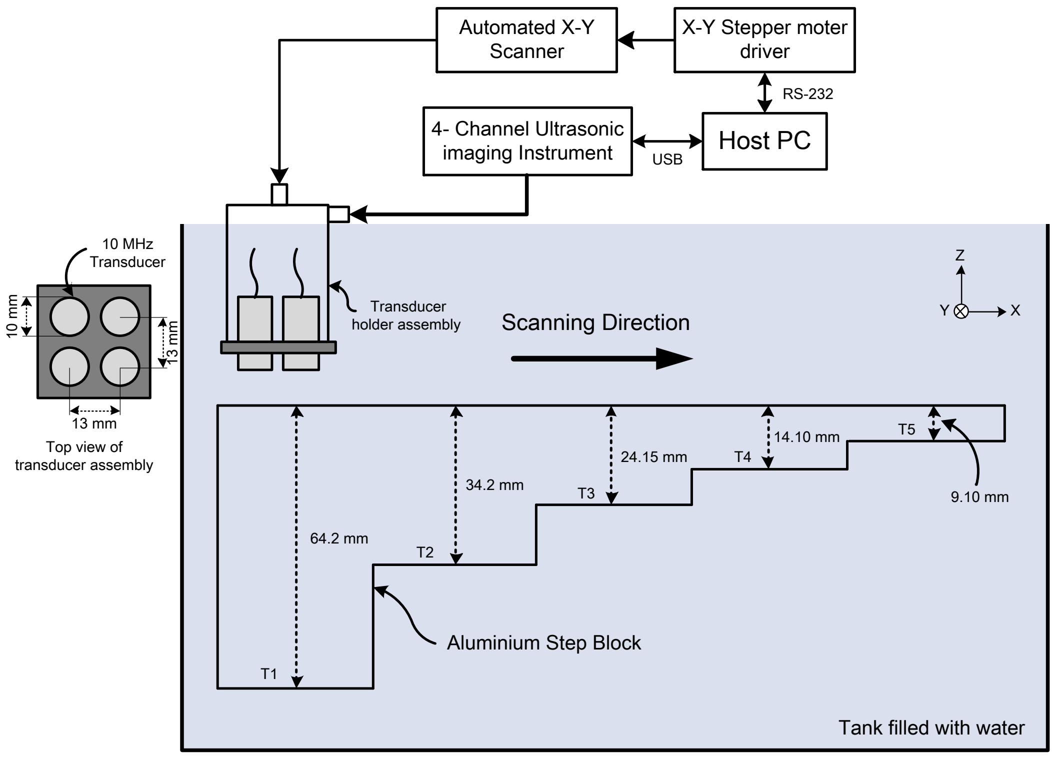

FIGURE 6.10: Calibrated aluminium Step block for B-scan imaging.

the Z-axis, enables precise and constant transducer probe positioning for imaging. This automated immersion scanner comprises the two-axis immersion tank, stepper motor drives, and motor controller unit. The automated axes are controlled by GUI software, which carries out axis displacements and scan patterns (B-scan/C-scan). The X-Y bridge of the scanner holds the 4-channel ultrasonic transducer holder assembly (Fig. 6.9 (c)). The holder assembly contains 4 water-immersible transducers of 10 MHz central frequency with 10 mm probe diameter and they are arranged in a matrix (2×2) configuration (Linear configuration can be used) as shown in Fig. 6.9 (d).

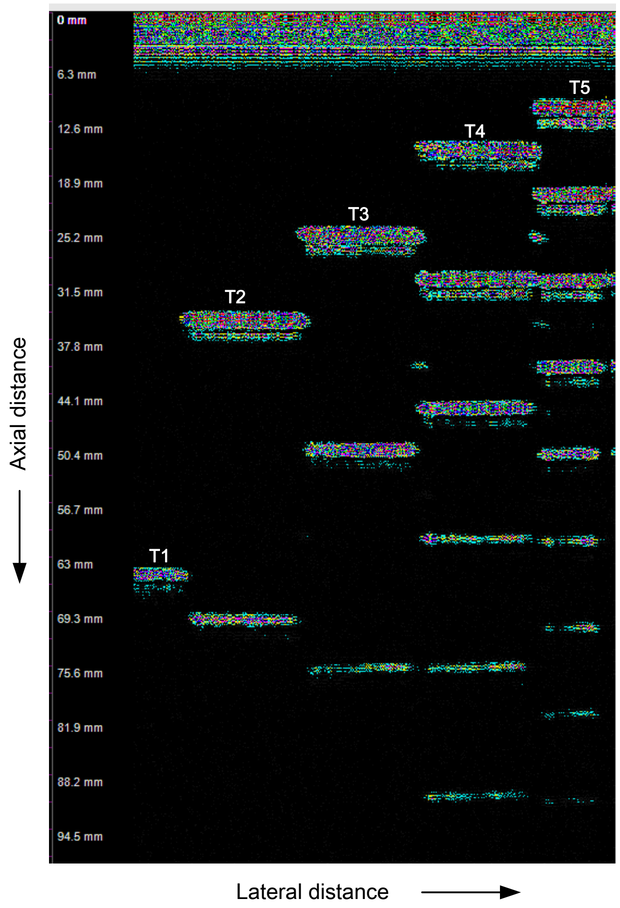

FIGURE 6.11: B-Scan image of the water-immersed aluminium step block. It shows B-Scan of the five steps ($T1$-$T5$) of step-block and its repetitive images.

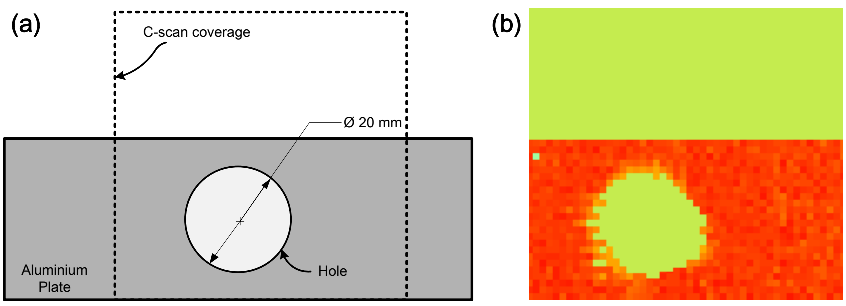

FIGURE 6.12: (a) Schematic diagram of aluminium sample plate with a drilled hole, (b) Acquired C-scan image of the aluminium plate.

6.4.3 B-Scan imaging of water immersed aluminium step block

The calibrated step block with 5 different steps has been used for the B-scan imaging as shown in Fig. 6.10. The automatic scanning in the X-axis direction has been performed starting from the maximum thickness (T1) to the minimum thickness (T5) of step block. As B-scan is a 2D representation, only two out of four transducers are used for the linear scanning of step block. The experimented B-scan image may contain the speckles or artifacts which degrades the quality of the image. But this image quality has been enhanced by using the hardware-based coherent averaging. The B-scan image of the step block with 16 coherent averages is shown in Fig. 6.11. It also shows the multiple/repetitive B-scan image of the step-block.

6.4.4 C-Scan imaging of water immersed aluminium plate

The aluminium sample plate of 2 mm thickness with 20 mm central drilled hole has been fabricated for immersion mode C-scan imaging. Fig. 6.12 (a) shows the schematic diagram of the aluminium plate with a C-scan coverage area (dotted line) for immersion imaging. The matrix (2×2) based ultrasonic transducers are utilized for c-scan imaging. The scanning has been performed with the X-Y bridge resolution of 1 mm in both X-Y directions. The Fig. 6.12 (b) shows the C-scan image of the aluminium sample. The resolution of the C-scan image can be further improved by raising the movement resolution of the X-Y automated scanner or increasing the number of transducers/channels of the immersion ultrasonic imaging system.

In the next chapter, the overall imaging scheme, design and development of the matrix-based (5×5) ultrasonic imaging is presented. This chapter provides the proposed matrix-based ultrasonic imaging scheme by performing real-time imaging of water-immersed mechanical components. Furthermore, the real-time imaging and bowing measurement of water-immersed FSA in the high-temperature environment is also presented.

Chapter 7

Matrix-based Ultrasonic Imaging for Immersion Applications

This chapter presents the ultrasonic imaging schemes using the matrix-based ultrasonic system. For that purpose, the beam-splitter based approach for both P-E and T-R mode of imaging is proposed. This beam-splitter based matrix-transducer approach allows the user to switch the mode of transmission from P-E to T-R or vice versa by using the same transducer holder/assembly. Furthermore, the overall imaging scheme of the matrix-based (5×5) ultrasonic imaging for immersion application is presented. The presented multi-channel ultrasonic imaging scheme combines sequential and parallel mode of acquisition and processing in real-time.

7.1 Beam-splitter based ultrasonic imaging

7.1.1 Reflection of a sound wave from thin plate and the penetration of it through thin plate

Consider that a thin plate with thickness d is placed between the two liquid semi-infinite medium as shown in below Fig. 7.1 and assume that a plane acoustic wave is incident at some arbitrary angle θ_i. The medium from which wave occurs, the plate, and the medium into which the wave penetrates are denoted by the numbers 1, 2 and 3, respectively. Here θ_l and θ_s indicate the angle of longitudinal and shear wave in the plate with the normal of the boundary layer. The reflected wave angle is denoted as θ_r. The angle formed by the transmitted wave is denoted as θ_t. The fluid medium acoustic density and acoustic velocity are indicated as ρ_f and

c_f respectively. Likewise, the thin plate medium acoustic density, longitudinal velocity, and shear velocity are indicated as ρ_b, c_l and c_f respectively.

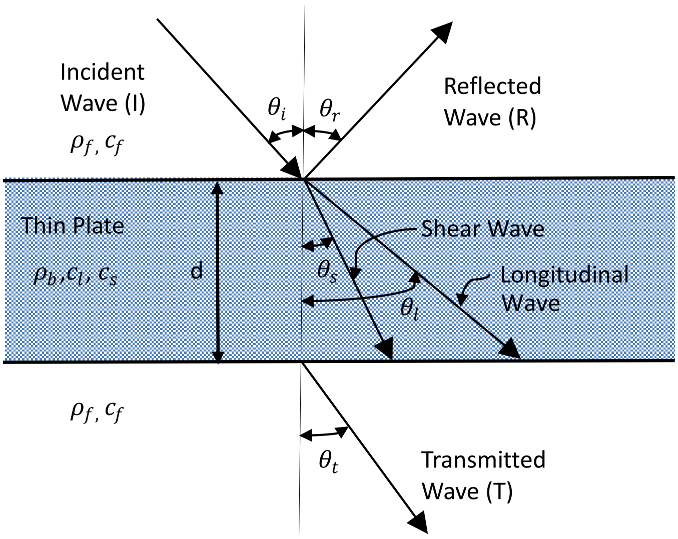

FIGURE 7.1: Reflection and Transmission of acoustic wave through a thin plate.

Here it is assumed that both side of plate have same liquid medium, i.e., $\rho_1 = \rho_2 = \rho_3$. Previously many authors have derived the equation for transmission and reflection and sound wave though then immersible plate [139–145]. The transmission coefficient W and reflection coefficient V are given by [144, 146],

$$\begin{aligned} V &= i\frac{M^2 - N^2 + 1}{2M + i\left(M^2 - N^2 - 1\right)} \\ W &= \frac{2N}{2M + i\left(M^2 - N^2 - 1\right)} \end{aligned} \tag{7.1}$$

where

$$\begin{aligned} M &= \frac{Z_l}{Z_f} cos^2\left(2\theta_s\right) cot\left(P\right) + \frac{Z_s}{Z_f} sin^2\left(2\theta_s\right) cot\left(Q\right) \\ N &= \frac{Z_l}{Z_f} cos^2\left(2\theta_s\right) sin\left(P\right) + \frac{Z_s}{Z_f} sin^2\left(2\theta_s\right) sin\left(Q\right) \end{aligned} \tag{7.2}$$

The parameters of (7.2) are given as

$$\begin{aligned}
\theta_l &= sin^{-1}\left[\frac{c_l}{c_f}sin(\theta_i)\right] \\
\theta_s &= sin^{-1}\left[\frac{c_s}{c_f}sin(\theta_i)\right] \\
Z_f &= \frac{\rho_f c_f}{cos(\theta_i)} \\
Z_l &= \frac{\rho_b c_l}{cos(\theta_l)} \\
Z_s &= \frac{\rho_b c_s}{cos(\theta_s)} \\
P &= \frac{2\pi f d}{c_l}cos(\theta_l) \\
Q &= \frac{2\pi f d}{c_s}cos(\theta_s)
\end{aligned} \tag{7.3}$$

Here quantities P and Q indicate the phase advances of the longitudinal and shear wave, respectively, over the thickness d of the plate. If the angle of incident θ_i does not exceed the angle of total internal reflection of the liquid-solid interference, either for the longitudinal wave or shear wave, then the angle θ_l and θ_s and coefficient V and W are real. The reflection power coefficient R and transmission power coefficient T are expressed by following equations,

$$\begin{aligned}
R = |V|^2 &= \frac{N^2 - M^2 - 1}{4M^2 + (N^2 - M^2 + 1)} \\
T = |W|^2 &= \frac{4N^2}{4M^2 + (N^2 - M^2 + 1)}
\end{aligned} \tag{7.4}$$

where $R + T = 1$, according to the law of conservation of energy.

It is assumed that while propagation of an acoustic wave through the plate, there is no attenuation and absorption of the acoustic wave in plate medium. It also assumed that there is the same liquid medium on both sides of the plate. Here water is considered as a liquid surrounding medium of the plate at room temperature. Fig. 7.2 shows the variation of acoustic transmitted energy from Stainless Steel (SS) plate to liquid medium with respect to the change in angle of incident θ_i and $f \times d$ (frequency-thickness) product. The acoustic density and velocity of SS are provided in Table 7.1.

From below Fig. 7.2, it is hereby stated that maximum transmission acoustic energy peak depends on the frequency-thickness product as well as on the incident angle of the acoustic wave. By increasing $f-d$ product $(f \times d)$ value and decreasing incident angle, the maximum transmission energy peak value decreases for the specific region as shown in Fig. **??**. For lower $f - d$ product value, the maximum energy peak is constant and also independent of the angle of incident.

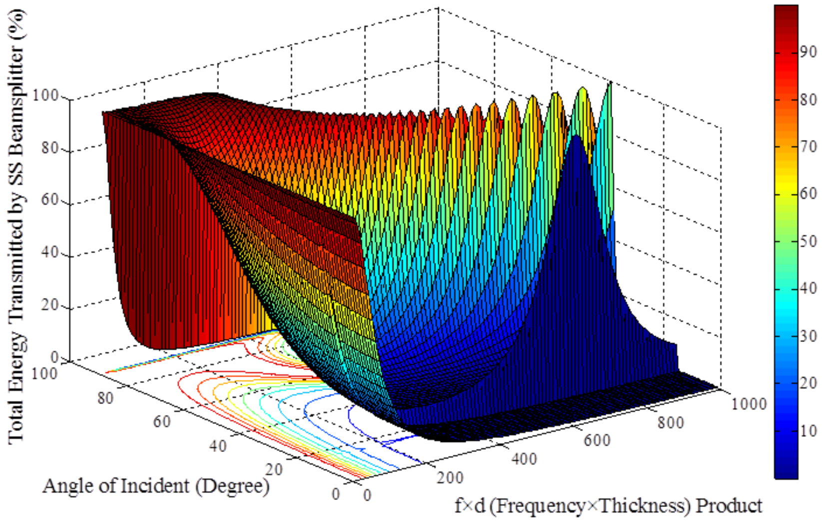

FIGURE 7.2: 3-D plot of acoustic transmission energy through SS beamsplitter with different incident angle and frequency-thickness product.

TABLE 7.1: Acoustic density and velocity of beam-splitter materials

Beam-splitter material	**Density** $\rho_b \times 10^3 kgm^{-3}$	**Longitudinal Velocity** $c_l \times 10^3 ms^{-1}$	**Shear Velocity** $c_s \times 10^3 ms^{-1}$
Stainless Steel	7.772	5.901	3.230
Aluminium	2.700	6.400	3.130

The acoustic density, longitudinal and shear velocity of different plate materials (stainless steel and aluminium) are shown in Table 7.1. From the above plotted graph, it is observed that transmitted energy is dependent on three parameters: angle of incidence (θ_i), frequency (f) and thickness of plate (d). To understand the effect of the individual parameter, the two parameters are kept as constant and one is kept as dependent.

7.1.2 Experimental results of matrix-based (2 × 2) ultrasonic imaging system using beam-splitter

The under-water experimental setup for the matrix-based ultrasonic imaging system is shown in Fig. 2.10(a). It consists of four high voltage ultrasonic pulser boards, four receiver amplifier boards, four digitizers, two FPGA cards, one USB

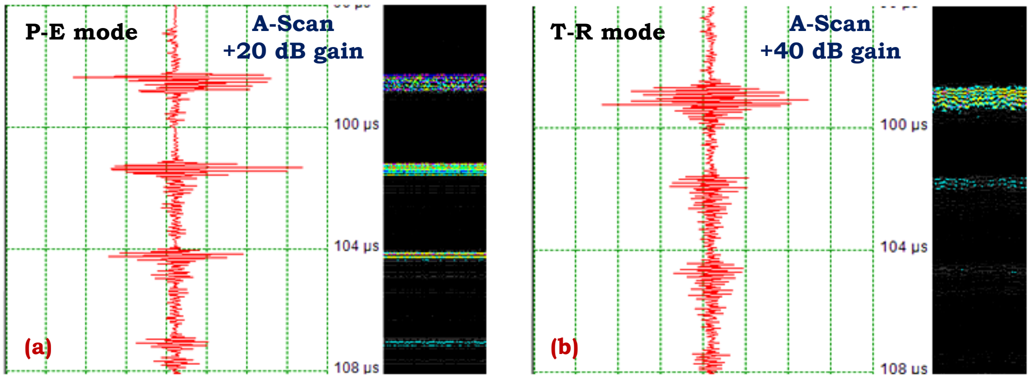

FIGURE 7.3: A-Scan Data and B-Scan images for P-E (a) and T-R (b) modes.

controller card, and a power supply unit. It also comprises 8-channel transducer assembly having two 2×2 matrix array transducers in which one array is needed for P-E mode and other is needed for T-R mode imaging. The prototype assembly is immersed in a water tank as shown in Fig. 2.10(b). Stainless Steel Beam-Splitter with 1 mm thickness is utilized for reflection and transmission of ultrasonic waves using P-E and T-R mode as depicted in Fig. 2.10(c). For experimentation purpose, 10 mm thick aluminium sheet is used, which has been submerged underneath the transducer assembly in the water tank. Fig. 7.3 shows the A-Scan data and B-Scan image results of one transducer of the matrix assembly unit for both P-E as well as T-R mode. From the A-scan results of both modes, it is observed that P-E mode has a high amplitude response with only 20 dB gain. From Fig. 7.3(b), it is observed that T-R mode requires higher gain (40 dB) compared to P-E mode, and it follows the results obtained from analytical equations as shown in Fig. 7.3(b). From the results, it is concluded that P-E mode has higher B-Scan image quality and detectability compared to T-R mode imaging. But axial resolutions and detection sensitivity of T-R mode images can be improved by increasing the receiver amplifier gain and signal processing of A-scan data. The same instrumentation setup is used for both P-E as well as T-R imaging modes having a matrix based transducer assembly and this instrumentation setup is scalable to higher channel matrix $(m \times n)$ based imaging applications.

7.2 Proposed real-time matrix-based (5×5) ultrasonic imaging using ultrasonic camera

7.2.1 Overall imaging scheme of multi-channel ultrasonic system

The matrix-based transducer arrangement is utilized for the multi-channel ultrasonic imaging. The entire matrix-based transducer assembly has Nr number of rows and Nc number of columns as shown in Fig 7.4 (a). The transducer numbers are given according to the respective row-column locations such as $T_{1,1}, T_{1,2}, ..., T_{Nr,Nc}$. Likewise, the T-R mode transducer assembly accommodates $NrNc$ number of ultrasonic transducers $(R_{1,1}, R_{1,2}, ..., R_{Nr,Nc})$. Here both parallel and sequential based mixed hardware approach are adopted for the data acquisition and processing. For that purpose, the Nc number of ultrasonic pulser receiver (UPR) modules are designed and developed for each column and each UPR module contains the Nr number of pulser-receiver circuits for each row. Here all the transducers in the single row are simultaneously selected. For the P-E mode, the ultrasonic pulse-echo signals from the same transducers are received by the hardware in a parallel manner. The data acquisitions and processing of the received signals also occur parallelly. Likewise, the transducers of every row are selected sequentially while at that time the transducers of remaining rows are non-selected as shown in Fig 7.5. For the T-R mode, separate transducers are used for the receiving purpose as shown in Fig 7.4 (b). So, here also the same kind of imaging scheme has been followed except that the ultrasonic transmitters and receivers have different sets for T-R mode.

7.2.2 System Description

The overall block diagram of the system is shown in Fig. 7.6. The system has a modular design which makes it easy to upgrade the number of channels in multiples of 5 and also DAQ parameters as per the requirement. Three types of customized hardware modules/units are used: 1) Transmitter-receiver unit, 2) Common amplifier unit and 3) Digital master/control unit. All modules are plugged into a mother-board (back-plane) and each module comprises the corresponding transducer connections that have been brought onto the front-fascia plate of every module via co-axial cable. The motherboard provides common DC power supply

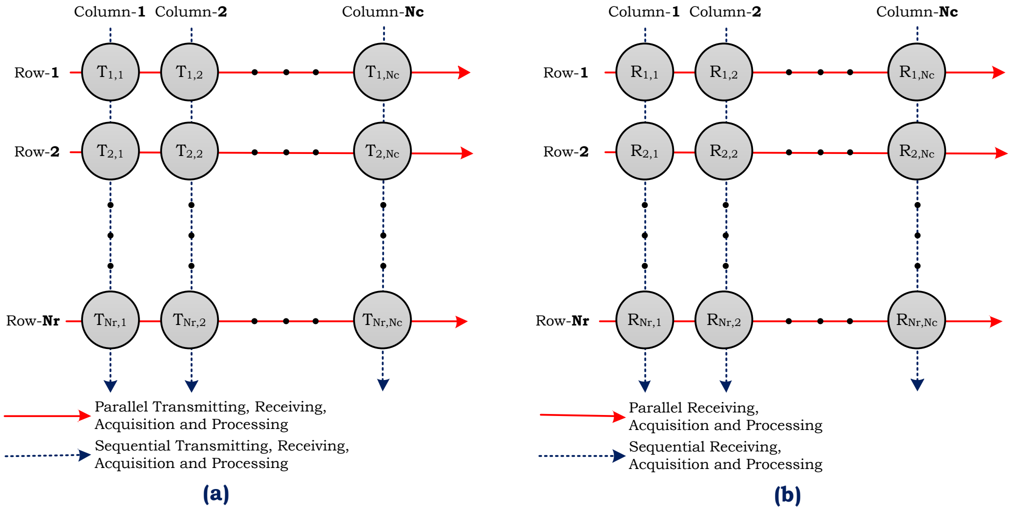

FIGURE 7.4: The schematic of $Nr \times Nc$ matrix-based ultrasonic transducers: (a) Transmitting and receiving transducers (Transmitters for P-E and T-R mode of imaging) and (b) Receiving transducers (Receivers for T-R mode of imaging).

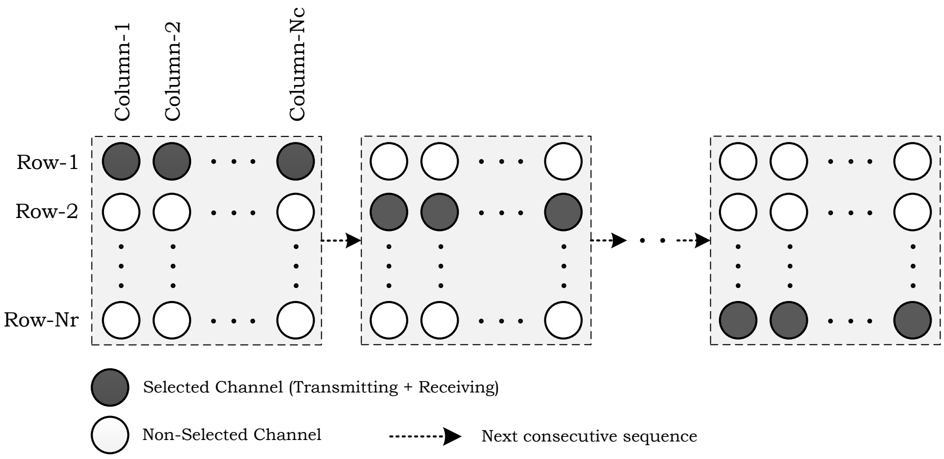

FIGURE 7.5: The sequence of ultrasonic selected channel (energization, acquisition and processing) and not-selected channel.

and ground plane to all the modules. The transmitter-receiver unit comprises multiple ultrasonic pulser-receiver (UPR) boards. Each customized UPR board has 5-channel spike pulsers, 5-channel pre-amplifiers, on-board pulse trigger generator and analog channel-multiplexing circuit for each signal.

The pulser section of the UPR board generates negative high-voltage (HV) spike pulses for energization of the transducers and echo signals received by the pre-amplifier section of the UPR board. The common-amplifier unit receives these

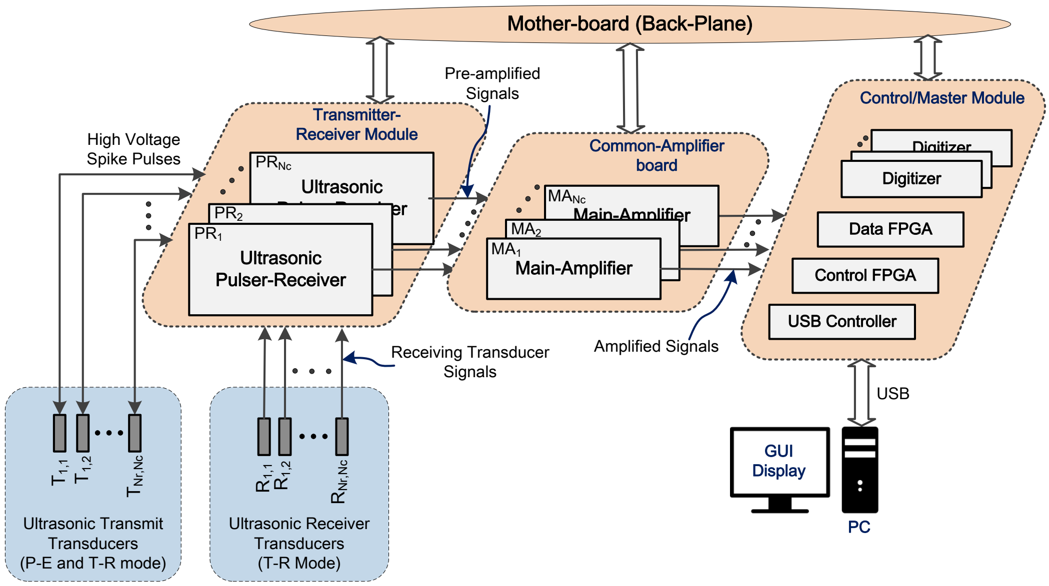

FIGURE 7.6: The overall block diagram ultrasonic imaging system for immersion applications.

amplified and buffered signals from the UPR boards for further amplification. The customized and designed ultrasonic main-amplifier board of common-amplifier unit contains high voltage (HV) input protection circuit (limiter), two stages of variable gain amplifiers (VGA) and fixed gain amplifiers connected in the cascaded configuration. The control/master unit holds the acquisitions circuits for analog signals, data FPGA, control-FPGA and USB controller board for the generation of control signals for the entire scanning and imaging process.

For the N $(Nr \times Nc)$-channel ultrasonic imaging system, it comprises three types of electronics boards interfaced with each-other and a PC based GUI software for post-processing and displaying of images. The imaging system has Nc numbers of UPR boards $(PR_1, PR_2, ..., PR_{Nc})$ which are connected to the total N $(Nr \times Nc)$ number of ultrasonic transducers $(T_{1,1}, T_{1,2}, ..., T_{Nr,Nc})$ for P-E and T-R mode. Same way, N $(Nr \times Nc)$ number of receiving transducers $(R_{1,1}, R_{1,2}, ..., R_{Nr,Nc})$ are also connected to UPR boards for T-R mode. The output signals of all Nr number of signals from each UPR board are amplified with the fixed gain and multiplexed together via daisy-chaining. Furthermore, this amplified single-ended output of each UPR board is provided to the common-amplifier board for further filtering and fine-gain amplification purpose. The common-amplifier board contains Nc number of main-amplifier circuits $(MA_1, MA_2, ..., MA_{Nc})$. The final filtered and amplified signals from the main-amplifier circuits are then connected to the digital control/master module for the digitization, processing and transferring of ultrasonic multi-channel data to PC. This digital control module contains Nc number of the digitizer units for the digitization of ultrasonic signals. The master module has two different FPGAs, one for data acquisition and transferring of digital data and other for controlling of other analog front-end boards and digital control module.

As shown in the system block diagram in Fig.7.6, the personal computer (PC) serves as the user interface. Upon each initiate signal provided through the graphical user interface (GUI), the processor inside the USB controller sequentially sends out required control signals to alternate blocks of the system such as data-FPGA and control-FPGA. The trigger generator circuit inside control-FPGA generates trigger signals to the UPR boards in sequential and parallel manner for the excitation of the respective transducer. The amplified echo signals are first digitized and later data aligned by the data-FPGA for further data processing. Afterwards, the processed data is transferred to the PC through the USB interface for display, measurement and analysis purpose. The GUI software is developed using Visual C# for the real-time display of A-scan waveforms and B-S can/C-Scan cross-sectional images.

7.2.3 Results and Discussions

7.2.3.1 Application 1: Real-time imaging of immersed mechanical components using matrix-based ultrasonic camera

For the matrix-based configuration, the individual 25 ultrasonic transducers have been arranged in the matrix form i.e. 5 rows and 5 columns (5×5) arrangement as shown in Fig. 7.7 (b). Each ultrasonic transducer has an operating frequency of 10 MHz, casing diameter of 10 mm. The 25-channel co-axial cables are used to connect this matrix-based transducer assembly with the ultrasonic camera system.

For the immersion-based ultrasonic imaging, an aluminium enclosure was filled with water and customized templates have been fabricated in aluminium plate of 2 mm thickness as shown in Fig. 7.7 (a). This fabricated plate is fitted in the middle of the box in such a way that it can be immersed in water. The three types of symbols or signs have been fabricated such as alphabet “P”, cross/plus sign and swastik sign. Furthermore, the customized aluminum object is also used for the real-time immersion imaging as shown in Fig. 7.12.

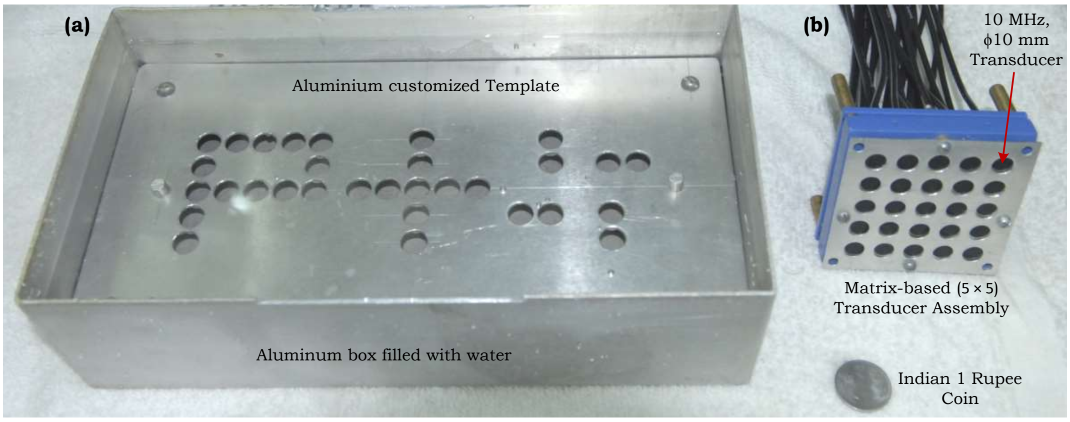

FIGURE 7.7: Customized immersion-based experimental setup: (a) Aluminium enclosure filled with water and three different templates fabricated on aluminium plate namely alphabet "P", cross sign and swastik sign, (b) Matrix-based (5 × 5) ultrasonic transducer assembly (P-E mode).

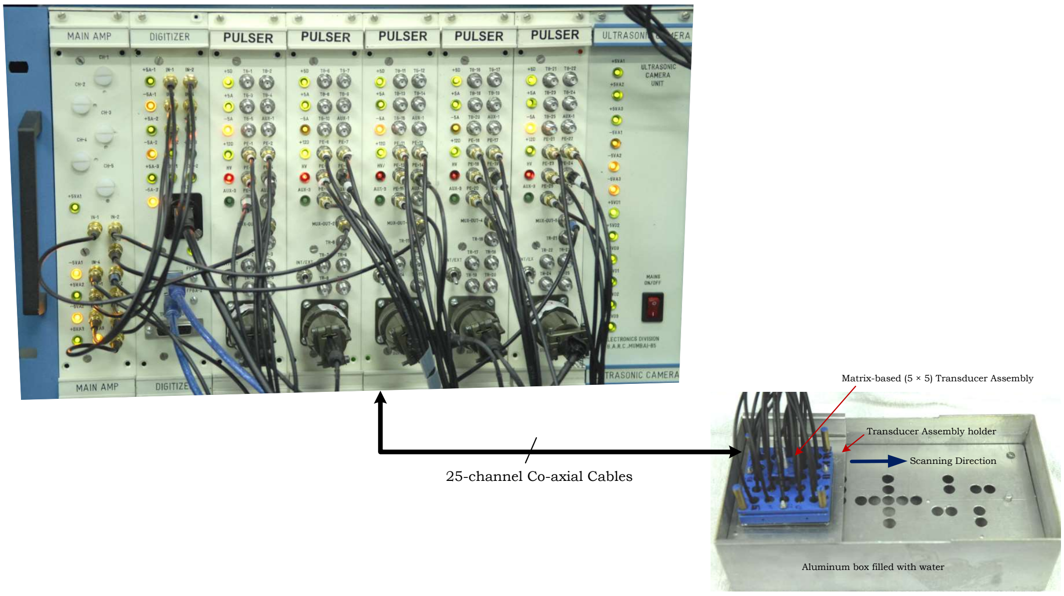

FIGURE 7.8: Ultrasonic imaging system connected with the matrix-based transducer holder assembly using 25-channel co-axial cables. The scanning movement of immersed transducer assembly is in the direction of left to right.

All matrix-based 25 ultrasonic transducers are connected with the respective 5 UPR boards via co-axial cables. For the excitation of the transducers, the negative spike pulses with the voltage of -500V, a pulse width of 100 ns and pulse repetition frequency (PRF) of 1 ms are applied. Since this is the P-E mode, the same transducers are utilized for the reception of echo signals. The received echo signals are amplified, filtered, digitized and processed through the different modules of the ultrasonic camera system. These all different signals have been processed again in real-time software environment and final matrix-based image have been generated

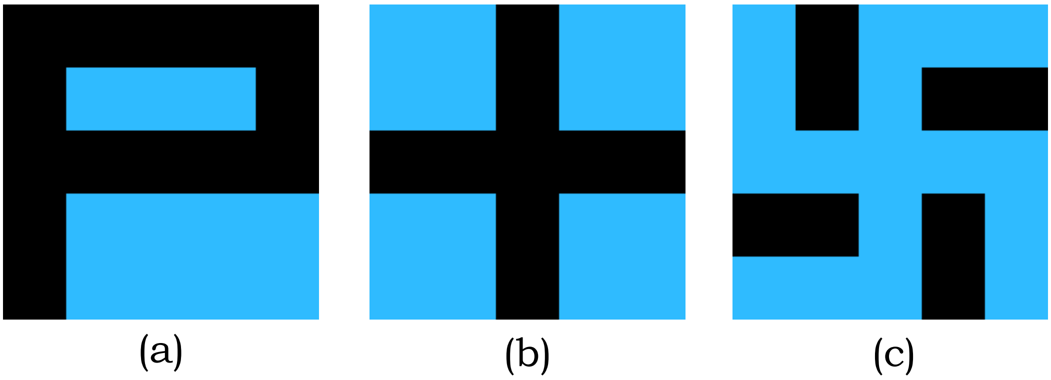

FIGURE 7.9: Real-time acquired C-Scan images of water-immersed templates using ultrasonic camera. The acquired images are: (a) alphabet “P”, (b) cross sign and (c) swastik sign.

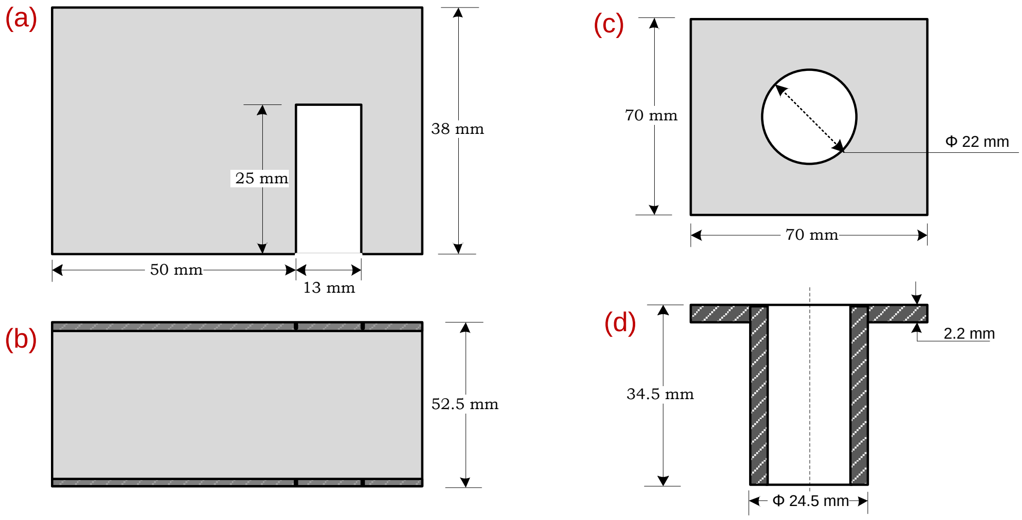

FIGURE 7.10: Customized mechanical object for immersion type imaging (a) Top view of asymmetric c-shaped aluminium object, (b) Front view of (a), (c) Top view of square object with drilled hole of 13 mm diameter and (d) Front view of (c).

and displayed in GUI software.

As shown in Fig. 7.8, the matrix-based ultrasonic transducer assembly has been manually shifted from the left to right direction to capture the depth-based c-scan images of all customized templates fabricated on the aluminium plate. The acquired real-time C-Scan images of three customized aluminium templates (7.7 (a)) are shown in Fig.7.9. Likewise, the real-time images of the two customized aluminum objects are shown in Fig. 7.16.

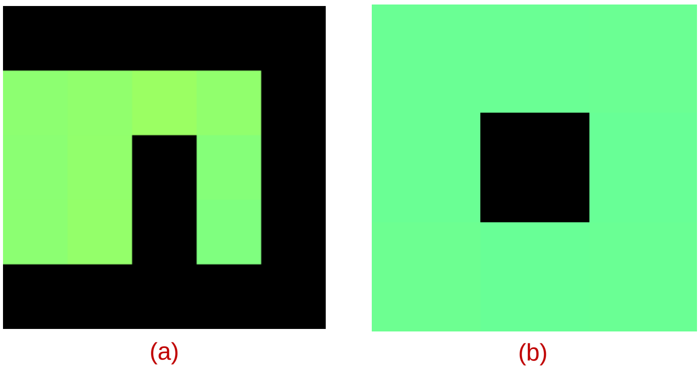

FIGURE 7.11: Real-time acquired images of customized and immersed aluminium object: (a) Image of object shown in Fig.7.10 (a) and (b) Image of object shown in Fig.7.10 (c)

.

7.2.3.2 Application 2: Real-time imaging of dummy FSA using 25-channel ultrasonic imaging system

For the real-time imaging of dummy FSA using the ultrasonic camera, the 19-channel ultrasonic transducer holder is developed and fabricated. This holder contains the 18 numbers of ultrasonic transducers in circumferences of the assembly and one transducer in center of the assembly as shown in Fig. 7.12. The circumference transducers are responsible for the imaging of the outer ring of the FSA and center transducer is responsible for the measurement of the hight of the FSA from the bottom-surface. The only 19-channels have been used from the 25-channel ultrasonic imaging system and connected through the 19-channel co-axial cables as shown in Fig. 7.12.

The tank is filled with water and heated by the two immersion heaters as shown in Fig. 7.13(a). A dummy hexagonal-shaped stainless-steel FSA of PFBR with the inner diameter of 110 mm and an outer diameter of 118 mm has been utilized for the ultrasonic imaging and bowing measurement. The both FSA and transducer holder assembly is immersed in the water tank and heated up to the 70 °C temperature.

The dummy hexagonal FSA of diameter d_f has been mechanically elevated in vertical direction from base level by the metallic rectangle plate of d_g thickness for the growth measurements as shown in Fig 7.14(b). For the growth measurement using the ultrasonic camera, the two aluminum plate with different thickness of 0.5 mm and 1 mm have been chosen. The same way for the bowing measurement, a small metallic object with the thickness of d_b has been kept under the FSA in

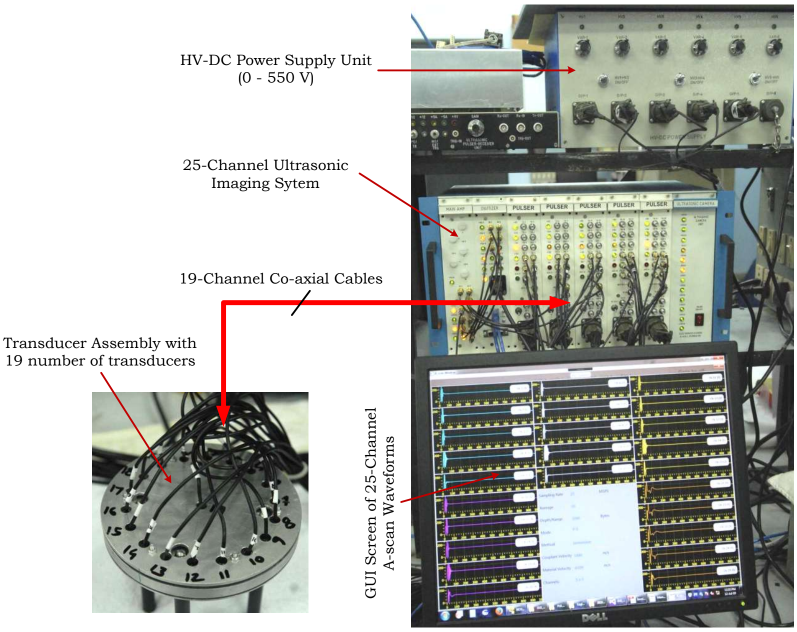

FIGURE 7.12: Fabricated transducer holder assembly for the measurement of bowing of FSA using 19 numbers of ultrasonic transducers and the wired connections between the transducer holder and 25-channel ultrasonic imaging system.

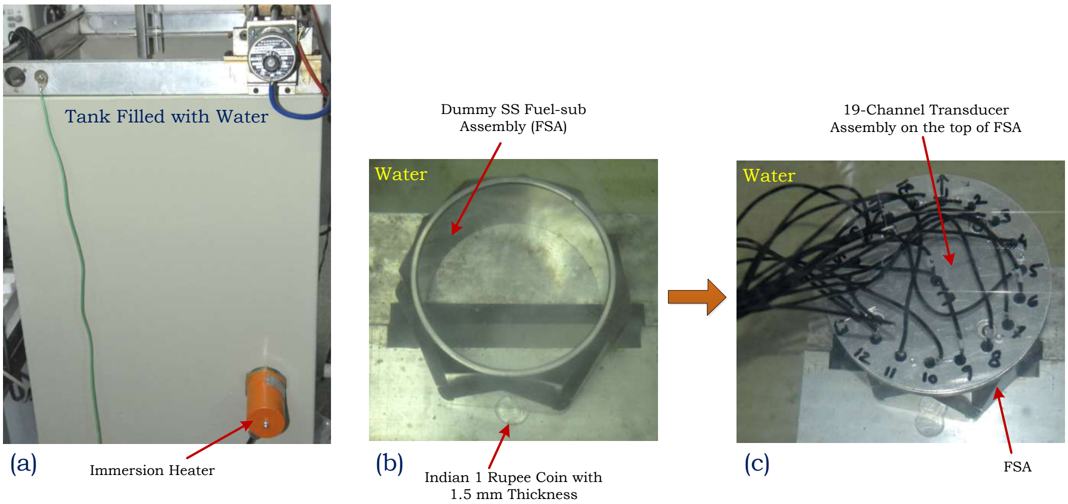

FIGURE 7.13: Experimental Setup for imaging of FSA (a) Tank filled with hot water at 70 °C which contains dummy FSA, traducer assembly and immersion heater, (b) dummy hexagonal FSA with 1 rupee Indian coin placed in the bottom of its one side and (c) Transducer holder assembly kept on the top of FSA with the distance of 30 mm.

one direction as shown in Fig. 7.14(c). The 1 rupee Indian coin with 1.5 mm thickness has been inserted under one of the hexagonal surfaces of dummy FSA for the bowing measurement of FSA as shown in Fig. 7.13(b).

Using the real-time ultrasonic camera, both qualitative and quantitative measurements of growth and bowing of FSAs have been presented. For the qualitative

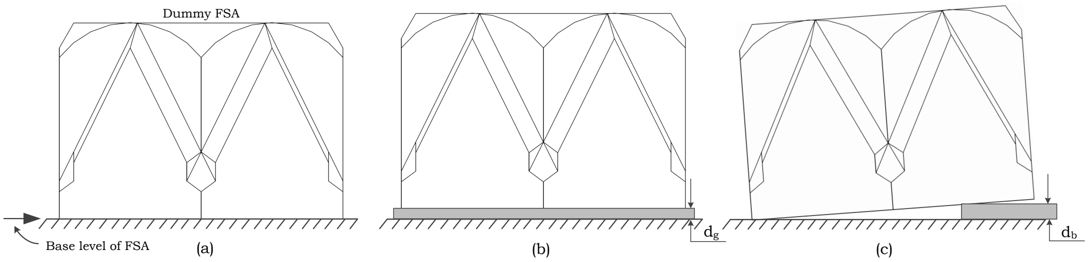

FIGURE 7.14: Artificially generated growth and bowing measurement of dummy FSA. (a) Dummy FSA rest on base level with average ring diameter of d_f, (b) Growth of FSA by metallic plate with d_g thickness and (c) Bowing of FSA by metallic object with d_b thickness

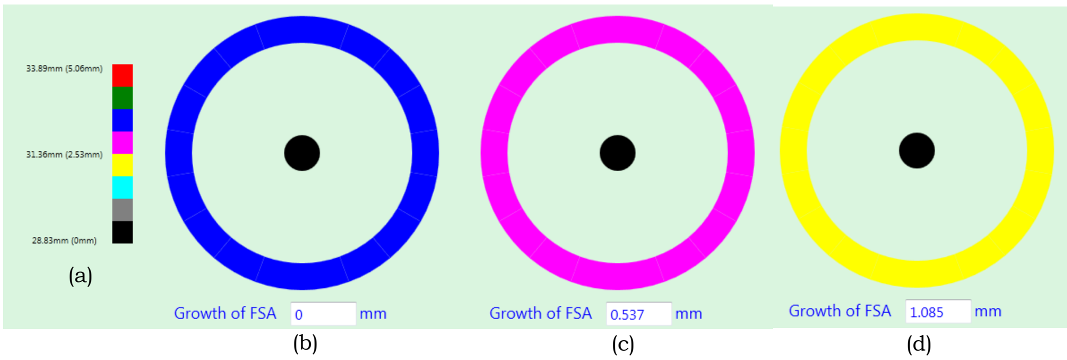

FIGURE 7.15: GUI screen-shot of real-time acquired depth-based c-scan images of immersed FSA for growth measurements with (a) $d_g = 0$mm, (b) $d_g = 0.5$mm and (c) $d_g = 1.0$ mm

measurement of growth and bowing of FSA, the color palette has been divided into the 8 number colors according to the width and position of the chosen and configured Gate. As displayed in Fig. 7.15(a), the exact (relative) values of start-point and end-point of the gate are 28.33 mm (0 mm) and 33.89 mm (5.06 mm), respectively.

Fig. 7.15(c) and (d) shows the real-time acquired images of the vertically elevated lifted FSA with the actual distance of 0.5 mm and 1 mm, respectively. It shows the qualitative measurements of the growth of FSA by visualizing the colors of FSA image. But for the quantitative measurements of growth, the relative average measured distance of each transducer is calculated with respect to the base level of FSA (*baseline*). The quantitative measured growth of FSA is also displayed in GUI as shown in Fig. 7.15(c) and (d). The error between the actual and measured growth is shown in Table 7.2.

The same way for the qualitative measurement of bowing of FSA, the color pallet (Fig. 7.16) has been set and the accurate (relative) distance values of start-point

TABLE 7.2: Quantitative growth and Bowing measurement using ultrasonic camera

Type	**Actual**	**Measured**	**Error**
	Growth		
Growth (mm)	0.500	0.537	0.037
	1.000	1.085	0.085
	Bowing		
Depth Diff. (mm)	1.500	1.540	0.040
Bowing (° Degree)	0.802	0.800	0.002

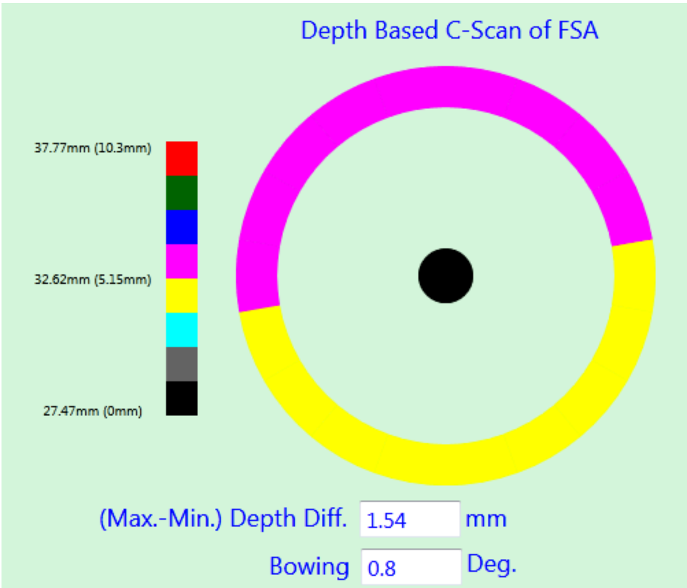

FIGURE 7.16: GUI screen-shot of real-time captured depth-based c-scan image of immersed FSA and measurements of depth difference and bowing.

and end-point of the gate are 27.44mm (0 mm) and 37.77 mm (10.3 mm), respectively. The real-time C-scan image of the immersed bowed FSA (Fig. 7.14(c)) is shown in Fig. 7.16. It is observed that the partial ring of FSA image contains different color and thus, it indicates the bow of FSA in a particular direction. For the quantitative measurement of bowing of FSA, a relative difference between the minimum and maximum distance from the FSA ring to transducer probes have calculated. The measured axial difference between the maximum and minimum distance point of the FSA top is equal to 1.54 mm. According to that, the measured bowing of the FSA is equal to 0.8°(degree). The error between the actual and measured value of the depth difference and bowing measurements are 0.04 and 0.002, respectively as shown in Table. 7.2.

TABLE 7.3: Major specifications of ultrasonic camera system

Parameter	**Value**
No. of Channels	#25 for P-E mode #50 for T-R mode
Acoustic Field of View	7 cm × 7 cm
Array Elements (P-E mode)	5 × 5
Array Elements (T-R mode)	5 × 5 and 5 × 5
Transducer Frequency	1-10 MHz
C-Scan Video Rate	10-30 frames per seconds
Thickness Range (Contact)	2500 mm (Aluminium) 2320 mm (Steel)
Thickness Range (Immersion)	600 mm (Water) 1000 mm (Sodium @ 200°C)
Sampling Rate	100 MSPS Max.
A-Scan	
A-Scan Rectification	Full, half, RF
A-Scan Gate Width	User selectable (4 gates)
A-Scan Gate Height	Variable from -100% to 100% FSH
Fixed Gain	0 to 90 dB
Variable Gain	0 to 80 dB (Total 0-170 dB)
Receiver Bandwidth	0.5 to 12 MHz @ -3 dB
Temporal Averages	# 2-256
Input Protection	1000 V Pk-Pk
Gate Type	Peak, Flank
Pulser	
Pulser Voltage	0 V to 550 V
PRF	1 KHz
Pulse Width	100 ns
Pulse Rise Time	<10 ns

7.2.4 Specifications of ultrasonic camera

The full system specifications of the ultrasonic camera are shown in Table 7.3. The achieved C-Scan imaging rate is around 9-10 frame per second. The maximum axial thickness range for the P-E contact method imaging is approximately 2500 mm for aluminum while for T-R contact mode the maximum axial thickness range will be double of the P-E mode i.e. 5000 mm for aluminium. The other specifications of camera are shown in Table 7.3. In the future, it is possible to enhance the resolution of the ultrasonic camera by increasing the number of channels of the array (25 × 25) and decreasing the element to element (pitch) distance.

Particularly for FBR applications, all previously developed ultrasonic imaging systems are not the real-time system as they usually take a long acquisition and processing time for the viewing of FSA such as system developed by Japan took approximately 3 minutes to take image using single transducer [26] and further it took approximately 7.2 seconds for one frame scan and several minutes to obtain image using the multi-channel imaging system [36]. The proposed circular-array based ultrasonic imaging system supports 10-30 frames per second depending upon the depth of the object.

Chapter 8

Conclusions and Future Scope

The thesis work emphasizes on simulation-modeling, implementation and experimentation of real-time ultrasonic imaging system intended for immersion applications. A novel real-time matrix-based ultrasonic imaging technique has been proposed which can enhance the inspection time and provide real-time images of immersed objects. In the first phase of research work, lossless and lossy spice modeling of a complete ultrasonic pulse-echo measurement system was completed specifically for immersion applications. The ultrasonic transducer is modeled by the leach model (transmission line and controlled sources) and propagation mediums and co-axial cables are modeled using the concept of the transmission line. Effects of non-ideal frequency-dependent behaviour of front-end transceiver electronics have been considered in simulation for practical ultrasonic NDT and imaging instruments. Results show that TOF and amplitude of lossy simulation, as well as experimental results, provide very close quantitative agreement in the time domain as well as in the frequency domain.

The two-stage noise filtering algorithm was proposed and implemented in the presence of both incoherent noise and coherent noise. The incoherent noise has been filtered by the coherent averaging algorithm (Stage-1) and subsequently, coherent noise was filtered by the EMD algorithm (Stage-2). In stage-1, real-time addressing based coherent averaging architecture was implemented using hardware adder, Radix-2 non-restoring divider and block-RAM on the FPGA platform. The proposed pipelined coherent averaging scheme requires minimum hardware (memory storage and adders) and also requires less execution time compared to the conventional averaging scheme. Furthermore, the amount of hardware requirement is totally independent of the number of averages and hence this architecture permits the user to increase the number of averages and hence enhances SNR. In stage-2, for coherent noise filtering, real-time implementation of an EMD algorithm based signal processing system was proposed. The PLI (Piece-wise Linear Interpolation) and CSI (Cubic Spline Interpolation) based EMD applications were implemented using the visual software environment. The total time complexity was calculated for both PLI-EMD and CSI-EMD methods and it is equal to $O(n \log n)$. The fully data-driven partial reconstruction scheme was adopted for signal filtering. The EMD software could correct the DC shift in the baseline and it reduced noise by extracting particular IMF (Intrinsic Mode Function) elements from the noisy ultrasonic signal. The proposed methodology has demonstrated significant improvement in SNR for ultrasonic pulse-echo signals.

For multichannel ultrasonic imaging applications, a reconfigurable embedded system was implemented which provides a dynamic, compliant and efficient platform for real-time acquisition and processing of multi-channel ultrasonic signals by utilizing reconfigurable and programmable hardware. By using an address-based analog multiplexing scheme, only a single DAQ unit and low size on-chip programmable memory was adequate for the configuration of the multi-channel imaging system. The proposed modular and reconfigurable ultrasonic system allows increment in the number of channels by changing only partial analog front-end hardware and reconfiguration parameters in the back-end embedded system.

A novel matrix-based real-time 50-Channel ultrasonic camera was configured for immersion-based imaging applications. By using the proposed address-based analog multiplexing scheme, both parallel-based and sequential-based mixed processing schemes were implemented for transducer excitation, signal acquisition, data processing and data transfer operation. For experimentation, a matrix-based (5×5) ultrasonic imaging system was designed and developed that has provided real-time data acquisition, processing, and imaging (A-Scan, B-Scan, C-Scan) system. For the user interface, a multi-threading software was developed for high-speed post-processing of data and displaying of cross-sectional images. The real-time images of the water-immersed mechanical components have been captured and these images provide a perfect physical shape of the mechanical specimen in real-time. Therefore, the ultrasonic camera developed for immersion applications facilitates to conduct real-time imaging of immersed structures and components that reduces inspection time and also provides geometrical identifications of the immersed object.

In the future, in order to acquire high-resolution images, it can be planned to implement and experiment with the high-resolution matrix-based (25×25) ultrasonic imaging system for real-time imaging of water-immersed metallic components. Furthermore, this ultrasonic camera can be scaled-up and qualified for EMI/EMC and environmental compliances to perform real-time viewing of under-sodium Fuel-Sub-Assemblies (FSAs) located in the core of Fast Breeder Reactor (FBR) during the shut-down stage.

Major outcomes/highlights of thesis

- The lossless and lossy modeling of the ultrasonic pulse-echo measurement system has been proposed and simulation and experimental validation using a single-channel real-time ultrasonic imaging system have been carried out.
- The two-stage noise filtering scheme for SNR enhancement has been proposed and real-time implementation of the noise filtering algorithms in programmable hardware/software environment have been carried out.
- Design and development of the reconfigurable embedded system using both sequential and parallel architecture for the multi-channel ultrasonic imaging have been completed.
- Design and development of the real-time matrix-based ultrasonic camera suitable for immersion applications has been completed.
- Ultrasonic camera system has been validated for immersion applications to visualize FSA top-heads in hot water at 70 °C.
- The real-time measurements of 0.5 mm growth and 0.8 deg. bowing of FSA top-head have been carried out using the matrix-based (5×5) ultrasonic camera.

  This application has paved way to carry out core-mapping of FBR at 200 °C, as a Fuel-Handling (FH) campaign, during shut-down stage of the reactor.

Appendix A

Spice Model of Components

```
*lossy aluminium model*
.SUBCKT Taluminium in out in1 out1
O1 in 0 out 0 MyLossyTline
.model MyLossyTline LTRA (len=30m R=2940.60 L=76.34m G=0 C=317.82n)
.ENDS Twater
*lossy water model*
.SUBCKT Twater in out in1 out1
O1 in 0 out 0 MyLossyTline
.model MyLossyTline LTRA (len=80m R=214.17 L=28.274m G=0 C=15.78u)
.ENDS Twater
*lossless water model*
.SUBCKT Twater lossless in out in1 out1
T2 in 0 out 0 Z0=42.326 TD=53.44u
.ENDS Twater lossless
*lossless aluminium model*
.SUBCKT Taluminium-lossless in out in1 out1
T1 in 0 out 0 Z0=490.10 TD=4.6729u
.ENDS Taluminium lossless
.SUBCKT RG174U-lossless in out in1 out1
*lossless 1 meter RG-174 cable*
O1 in 0 out 0 MyLossyTline
.model MyLossyTline LTRA (len=1 R=0 L=252.700n G=0 C=101.08p)
.ENDS RG174U-lossless
*lossless 2 meter RG-174 Cable*
.SUBCKT RG174U-2m-lossless in out in1 out1
O1 in 0 out 0 MyLossyTline
.model MyLossyTline LTRA ( len=2 R=0 L=252.700n G=0 C=101.08p)
.ENDS RG174U-2m-lossless
* lossy 2 meter RG-174 Cable*
.SUBCKT RG174U-2m in out in1 out1
O1 in 0 out 0 MyLossyTline
.model MyLossyTline LTRA (len=2 R=127.820u*sqrt(3.141592654*2*10000000)
L=252.700n G=0 +C=101.08p)
.ENDS RG174U-2m
```

```
* lossy 1 meter RG-174 Cable*
.SUBCKT RG174U in out in1 out1
O1 in 0 out 0 MyLossyTline
.model MyLossyTlineLTRA(len=1 R=127.820u*sqrt(3.141592654*2*10000000) L=252.700n
G=0 +C=101.08p)
.ENDS RG174U
*lossless PZT-5A transducer*
.SUBCKT PZT5A-lossless E B F
T1 B 1 F 1 Z0=953.187 TD=50n
V1 1 2
S3 2 0 4 0 1
V2 E 3
C0 3 0 955.46p
S1 0 3 V1 2.0
S2 0 4 V2 2.15e9
R1 4 0 1k
C1 4 0 1
.ENDS PZT5A-lossless
*lossy PZT-5A transducer*
.SUBCKT PZT5A E B F
O1 B 1 F 1 T1
.model T1 LTRA (len=217.5u R=183.41k L=219.12m G=0 C=241.175n)
V1 1 2
S3 2 0 4 0 1
V2 E 3
C0 3 0 955.46p
S1 0 3 V1 2.0
S2 0 4 V2 2.15e9
R1 4 0 1k
C1 4 0 1
.ENDS PZTR
*MUR4100EG Diode model* .SUBCKT MUR4100EG A K
d1 A K Dmur4100erl
.MODEL Dmur4100erl d (IS=1.45521e-06 RS=0.0590147 N=2.54768
+EG=1.16115 XTI=4 BV=1000 IBV=2.5e-05 CJO=7.02592e-11
+VJ=0.4 M=0.45039 FC=0.5 TT=1.62036e-07 KF=0 AF=1)
.ENDS MUR4100EG
*1N4148 Diode Model*
.SUBCKT 1N4148 1 2
R1 1 2 5.827E+9
D1 1 2 1N41481
.MODEL 1N41481 d
+ IS = 4.352E-9
+ N = 1.906
+ BV = 110
+ IBV = 0.0001
+ RS = 0.6458
+ CJO = 7.048E-13 + VJ = 0.869
+ M = 0.03
```

```
+ FC = 0.5
+ TT = 3.48E-9
.ENDS 1N4148
* IXRFD630/631 Model
.SUBCKT DVR 0 10
V_V1 12321 0
+PULSE 0 12 0n 2n 2n 130n 1m
C_C1 23432 12321 7n
R_R1 0 23432 0.1
L_L1 12321 34543 1n
R_R2 34543 10 0.1
L_L2 45654 56765 1n
C_C2 10 45654 1000p
R_R3 0 56765 .5
R_R4 0 10 1k
.ENDS DVR
*MOSFET Model .SUBCKT 08N120 10 20 30
* TERMINALS: D G S
M1 1 2 3 3 DMOS L=2U W=1U
RON 5 6 .5
DON 6 2 D1
ROF 5 7 1.0
DOF 2 7 D1
D1CRS 2 8 D2
D2CRS 1 8 D2
CGS 2 3 1.9N
RD 4 1 2.1
DCOS 3 1 D3
RDS 1 3 5.0MEG
LS 3 30 .5N
LD 10 4 1N
LG 20 5 1N
.MODEL DMOS NMOS (LEVEL=3 VTO=4 KP=10)
.MODEL D1 D (IS=.5F CJO=10P BV=1200 M=.5 VJ=.2 TT=1N)
.MODEL D2 D (IS=.5F CJO=20P BV=1200 M=.6 VJ=.6 TT=1N RS=10M)
.MODEL D3 D (IS=.5F CJO=60P BV=1200 M=.35 VJ=.6 TT=400N RS=10M)
.ENDS 08N120
```

Bibliography

[1] J. Krautkrämer and H. Krautkrämer, *Ultrasonic testing of materials*. Springer Science & Business Media, 2013.

[2] M. Berke, *Nondestructive material testing with ultrasonics: introduction to the basic principles*. Krautkamer GmbH & Company, 1996.

[3] "Ultrasonic transducers technical notes," Olympus NDT, Tech. Rep., 2006.

[4] L. J. Jacobs and J. O. Owino, "Effect of aggregate size on attenuation of rayleigh surface waves in cement-based materials," *Journal of Engineering Mechanics*, vol. 126, no. 11, pp. 1124–1130, 2000.

[5] "Standard guide for evaluating characteristics of ultrasonic search units, astm e1065 / e1065m-14," ASTM International, Tech. Rep., 2014.

[6] E. G. Tarpara, V. Patankar, V. Vijayan *et al.*, "Under sodium ultrasonic viewing for fast breeder reactors: a review," Bhabha Atomic Research Centre, Tech. Rep., 2016.

[7] E. Jasiūnienė, R. Raišutis, R. Šliteris, A. Voleišis, and M. Jakas, "Ultrasonic ndt of wind turbine blades using contact pulse-echo immersion testing with moving water container," *Ultragarsas*, vol. 63, no. 3, pp. 28–32, 2008.

[8] W. Deutsch, P. SCHULTE, M. JOSWIG, and R. KATTWINKEL, "Automated ultrasonic pipe weld inspection," in *WCNDT World Conference for Nondestructive Testing, Shanghai China*, 2008.

[9] B. W. Drinkwater and P. D. Wilcox, "Ultrasonic arrays for non-destructive evaluation: A review," *NDT & e International*, vol. 39, no. 7, pp. 525–541, 2006.

[10] G. Liaptsis, D. Liaptsis, P. Charlton, and B. Wright, "Focal law calculations for annular phased array transducers," *The e-Journal of NDT*, vol. 20, no. 2, 2015.

[11] C. Holmes, B. W. Drinkwater, and P. D. Wilcox, "Post-processing of the full matrix of ultrasonic transmit–receive array data for non-destructive evaluation," *NDT & e International*, vol. 38, no. 8, pp. 701–711, 2005.

[12] M. R. Lasser, M. Lasser, M. J. Gurney, M. J. Kula, and M. D. Rich, "Multiangle low cost ultrasound camera for ndt field applications," *Imperium, Inc. http://www. imperiuminc. com/PDF/ASNT-Paper-Sum-mary-2005. pdf.*

[13] R. S. Lasser, M. E. Lasser, and J. W. Gurney, “Multiangle ultrasound imager,” May 13 2008, uS Patent 7,370,534.

[14] “Dolphicam2 ultrasound imaging platform for ndt,” https://www.dolphitech.com/our-products/dolphicam2/.

[15] O. Balogun, B. Regez, H. F. Zhang, and S. Krishnaswamy, “Real-time full-field photoacoustic imaging using an ultrasonic camera,” *Journal of biomedical optics*, vol. 15, no. 2, p. 021318, 2010.

[16] Y. Zhou, G. Petculescu, I. Komsky, and S. Krishnaswamy, “A high-resolution real-time ultrasonic imaging system for ndi applications,” in *Health Monitoring and Smart Nondestructive Evaluation of Structural and Biological Systems V*, vol. 6177. International Society for Optics and Photonics, 2006, p. 617717.

[17] “Acoustocamtm i700 system specifications,” https://docs.wixstatic.com/ugd/806904_65aceb653e4f4fabb0de907867146037.pdf.

[18] “Dolphicam user manual,” https://www.dolphitech.com/wp-content/uploads/2014/12/DolphiCam-User-Manual-1.3.pdf.

[19] J. Krautkrämer and H. Krautkrämer, *Ultrasonic testing by determination of material properties*. Springer, 1990.

[20] V. Patankar, S. Lalwani, A. Agashe, G. Randale, R. Chaurasia, P. Jyothi, R. Jain, T. Ananthakrishnan, C. Pithawa, C. Asokane *et al.*, “Instrumentation & control system for under sodium ultrasonic scanner of pfbr,” in *Proceedings of the National Seminar & Exhibition on Non-Destructive Evaluation NDE 2011*, 2011, pp. 8–10.

[21] B. Raj, S. Mannan, P. V. Rao, and M. Mathew, “Development of fuels and structural materials for fast breeder reactors,” *Sadhana*, vol. 27, no. 5, pp. 527–558, 2002.

[22] S. Mannan, S. Chetal, B. Raj, and S. Bhoje, “Selection of materials for prototype fast breeder reactor,” *Transactions-Indian Institute of Metals*, vol. 56, no. 2, pp. 155–178, 2003.

[23] *Structural Materials for Liquid Metal Cooled Fast Reactor Fuel Assemblies-Operational Behaviour*, ser. Nuclear Energy Series. Vienna: INTERNATIONAL ATOMIC ENERGY AGENCY, 2012, no. NF-T-4.3.

[24] K. Swaminathan, A. Rajendran, and G. Elumalai, “The development and deployment of an ultrasonic under-sodium viewing system in the fast breeder test reactor,” *IEEE Transactions on nuclear science*, vol. 37, no. 5, pp. 1571–1577, 1990.

[25] R. Hans, E. Kranz, and H. Weiss, “Under sodium viewing-a method to identify objects in an opaque medium,” in *Liquid metal engineering and technology. 3 v. Proceedings of the 3. international conference held in Oxford on 9-13 April 1984*, 1984.

[26] J. Taguchi, N. Uesugi, T. Miyazawa, K. Sato, and S. Horikoshi, "An ultrasonic viewing system in liquid sodium," *IEEE transactions on Nuclear Science*, vol. 27, no. 1, pp. 821–825, 1980.

[27] R. Ord and R. Smith, "Development of an under-sodium ultrasonic scanner for in-reactor surveillance." Hanford Engineering Development Lab., Richland, Wash., Tech. Rep., 1972.

[28] L. J. Bond, J. W. Griffin, G. J. Posakony, R. V. Harris, and D. L. Baldwin, "Materials issues in high temperature ultrasonic transducers for under-sodium viewing," in *AIP Conference Proceedings*, vol. 1430, no. 1. AIP, 2012, pp. 1617–1624.

[29] J. W. Griffin, G. J. Posakony, R. V. Harris, D. L. Baldwin, A. M. Jones, and L. J. Bond, "High temperature ultrasonic transducers for in-service inspection of liquid metal fast reactors," in *2011 IEEE International Ultrasonics Symposium.* IEEE, 2011, pp. 1924–1927.

[30] V. Patankar, R. Jain, S. Lalwani, A. Agashe, G. Randale, P. Jyothi, P. Selvam, N. V. Varier, T. Ananthakrishnan, and C. Pithawa, "Sweep-arm scanning technique for core-mapping of fuel sub-assemblies of fast breeder reactor," in *Asia Pacific Conference on Non-Destructive Testing (14th APC-NDT).*

[31] L. Barrett, J. McKnight, and J. Forthergill, "Ultrasonic viewing in fast reactors," *Physics in Technology*, vol. 15, no. 6, p. 308, 1984.

[32] J. McKnight, E. Burton, and P. Fenemore, "Recent advances in the technology of under-sodium inspection in lmfbrs," in *Liquid metal engineering and technology. 3 v. Proceedings of the 3. international conference held in Oxford on 9-13 April 1984*, 1984.

[33] D. James and J. Ford, *Review of Fast Reactor In-service Inspection Practice.* European Commission, Directorate-General XIII, Telecommunications, 1996.

[34] F. Baque, "Review of in-service inspection and repair technique developments for french liquid metal fast reactors," *Nuclear technology*, vol. 150, no. 1, pp. 67–78, 2005.

[35] R. Hans, E. Kranz, and H. Weiss, "Under sodium viewing-a method to identify objects in an opaque medium," in *Liquid metal engineering and technology. 3 v. Proceedings of the 3. international conference held in Oxford on 9-13 April 1984*, 1984.

[36] H. Karasawa, M. Izumi, T. Suzuki, S. Nagai, M. Tamura, and S. Fujimori, "Development of under-sodium three-dimensional visual inspection technique using matrix-arrayed ultrasonic transducer," *Journal of nuclear science and technology*, vol. 37, no. 9, pp. 769–779, 2000.

[37] J. van Deventer, T. Lofqvist, and J. Delsing, "Pspice simulation of ultrasonic systems," *IEEE Transactions on Ultrasonics, Ferroelectrics, and Frequency Control*, vol. 47, no. 4, pp. 1014–1024, July 2000.

[38] A. Puttmer, P. Hauptmann, R. Lucklum, O. Krause, and B. Henning, "Spice model for lossy piezoceramic transducers," *IEEE Transactions on Ultrasonics, Ferroelectrics, and Frequency Control*, vol. 44, no. 1, pp. 60–66, Jan 1997.

[39] S. A. Morris and C. G. Hutchens, "Implementation of mason's model on circuit analysis programs," *IEEE Transactions on Ultrasonics, Ferroelectrics, and Frequency Control*, vol. 33, no. 3, pp. 295–298, May 1986.

[40] W. M. Leach, "Controlled-source analogous circuits and spice models for piezoelectric transducers," *IEEE Transactions on Ultrasonics, Ferroelectrics, and Frequency Control*, vol. 41, no. 1, pp. 60–66, Jan 1994.

[41] R. Guelaz, D. Kourtiche, and M. Nadi, "Ultrasonic piezoceramic transducer modeling with vhdl-ams: Application to ultrasound nonlinear parameter simulations," *IEEE Sensors Journal*, vol. 6, no. 6, pp. 1652–1661, Dec 2006.

[42] W. P. Mason, *Electromechanical transducers and wave filters*, 1948.

[43] W. P. Meson, *Physical acoustics: principles and methods.* Academic press, 1964.

[44] M. Redwood, "Transient performance of a piezoelectric transducer," *The journal of the acoustical society of America*, vol. 33, no. 4, pp. 527–536, 1961.

[45] R. Krimholtz, D. A. Leedom, and G. L. Matthaei, "New equivalent circuits for elementary piezoelectric transducers," *Electronics Letters*, vol. 6, no. 13, pp. 398–399, June 1970.

[46] Z. Wu, K. Xi, B. Zhu, H. Zheng, and Y. Tan, "Theoretical and experimental investigation of ultrasonic transducers with dual oppositely polarized pmn-pt layers in wide frequency range," *IEEE Transactions on Industrial Electronics*, vol. 63, no. 4, pp. 2313–2319, April 2016.

[47] X. Wei, Y. Yang, W. Yao, and L. Zhang, "Pspice modeling of a sandwich piezoelectric ceramic ultrasonic transducer in longitudinal vibration," *Sensors*, vol. 17, no. 10, p. ., 2017.

[48] M. K. Feldman, S. Katyal, and M. S. Blackwood, "Us artifacts," *RadioGraphics*, vol. 29, no. 4, pp. 1179–1189, 2009, pMID: 19605664.

[49] V. Matz, R. Smid, S. Starman, and M. Kreidl, "Signal-to-noise ratio enhancement based on wavelet filtering in ultrasonic testing," *Ultrasonics*, vol. 49, no. 8, pp. 752 – 759, 2009.

[50] J. Chen, Y. Shi, and S. Shi, "Noise analysis of digital ultrasonic nondestructive evaluation system," *International Journal of Pressure Vessels and Piping*, vol. 76, no. 9, pp. 619 – 630, 1999.

[51] J. Huang, J. K. Triedman, N. V. Vasilyev, Y. Suematsu, R. O. Cleveland, and P. E. Dupont, "Imaging artifacts of medical instruments in ultrasound-guided interventions," *Journal of Ultrasound in Medicine*, vol. 26, no. 10, pp. 1303–1322, 2007.

[52] P. Palanichamy, A. Joseph, T. Jayakumar, and B. Raj, “Ultrasonic velocity measurements for estimation of grain size in austenitic stainless steel,” *NDT & E International*, vol. 28, no. 3, pp. 179 – 185, 1995.

[53] A. Van Pamel, “Ultrasonic inspection of highly scattering materials,” 2015.

[54] M. Schrapp, T. Scharrer, M. Goldammer, S. J. Rupitsch, A. Sutor, H. Ermert, and R. Lerch, “Artifact reduction in non-destructive testing by means of complementary data fusion of x-ray computed tomography and ultrasonic pulse-echo testing,” *Measurement Science and Technology*, vol. 24, no. 12, p. 125403, 2013.

[55] S. H. C. Ortiz, T. Chiu, and M. D. Fox, “Ultrasound image enhancement: A review,” *Biomedical Signal Processing and Control*, vol. 7, no. 5, pp. 419 – 428, 2012.

[56] F. W. Kremkau and K. Taylor, “Artifacts in ultrasound imaging.” *Journal of ultrasound in medicine*, vol. 5, no. 4, pp. 227–237, 1986.

[57] S. H. C. Ortiz, T. Chiu, and M. D. Fox, “Ultrasound image enhancement: A review,” *Biomedical Signal Processing and Control*, vol. 7, no. 5, pp. 419 – 428, 2012.

[58] J. H. Rose, “Ultrasonic backscatter from microstructure,” in *Review of Progress in Quantitative Nondestructive Evaluation. Vol. 11B*, vol. 11, 1992, pp. 1677–1684.

[59] D. Benstock, F. Cegla, and M. Stone, “The influence of surface roughness on ultrasonic thickness measurements,” *The Journal of the Acoustical Society of America*, vol. 136, no. 6, pp. 3028–3039, 2014.

[60] A. Van Pamel, “Ultrasonic inspection of highly scattering materials,” Ph.D. dissertation, Imperial College London, 2015.

[61] J. Egerton, M. Lowe, and P. Huthwaite, “Automated and antidispersive coherent and incoherent noise reduction of waveforms that contain a reference pulse,” *NDT & E International*, vol. 105, pp. 35 – 45, 2019.

[62] F. Yan, R. L. Royer Jr, and J. L. Rose, “Ultrasonic guided wave imaging techniques in structural health monitoring,” *Journal of intelligent material Systems and Structures*, vol. 21, no. 3, pp. 377–384, 2010.

[63] N. M. Bilgutay, R. Murthy, U. Bencharit, and J. Saniie, “Spatial processing for coherent noise reduction in ultrasonic imaging,” *The Journal of the Acoustical Society of America*, vol. 87, no. 2, pp. 728–736, 1990.

[64] *Agilent InfiniiVision 2000 X-Series Oscilloscopes User’s Guide*, Agilent Technologies, Inc., 3 2012, fourth edition.

[65] *Keysight InfiniiVision 3000 X-Series Oscilloscopes User’s Guide*, Keysight Technologies, Inc., 4 2013, eighth edition.

[66] A. N. Kalashnikov, "Waveform measurement using synchronous digital averaging: Design principles of accurate instruments," *Measurement*, vol. 42, no. 1, pp. 18 – 27, 2009.

[67] R. Kaiser and W. Knight, "Digital signal averaging," *Journal of Magnetic Resonance (1969)*, vol. 36, no. 2, pp. 215 – 220, 1979.

[68] A. N. Kalashnikov, V. G. Ivchenko, R. E. Challis, and B. R. Hayes-Gill, "High-accuracy data acquisition architectures for ultrasonic imaging," *IEEE Transactions on Ultrasonics, Ferroelectrics, and Frequency Control*, vol. 54, no. 8, pp. 1596–1605, August 2007.

[69] U. Mahbub, T. Rahman, and A. B. M. H. Rashid, "Fpga implementation of real time acoustic noise suppression by spectral subtraction using dynamic moving average method," vol. 1, pp. 365–370, Oct 2009.

[70] U. Hassan and M. S. Anwar, "Reducing noise by repetition: introduction to signal averaging," *European Journal of Physics*, vol. 31, no. 3, p. 453.

[71] J. Banjac, "Fpga based data smoother for sensor data," CERN openlab, Tech. Rep., 2016. [Online]. Available: https://zenodo.org/record/159419/files/Report_JelenaBanjac.pdf

[72] J. Saniie, E. Oruklu, S. Gilliland, and S. Aslan, *Reconfigurable ultrasonic smart sensor platform for nondestructive evaluation and imaging applications*, S. Nihtianov, , and A. Luque, Eds. Woodhead Publishing, 2014.

[73] P. Govindan, V. Vasudevan, T. Gonnot, and J. Saniie, "Reconfigurable ultrasonic testing system development using programmable analog front-end and reconfigurable system-on-chip hardware," *Circuits and Systems*, vol. 6, no. 7, pp. 161 – 171, 2015.

[74] P. Govindan, S. Gilliland, T. Gonnot, and J. Saniie, "Reconfigurable ultrasonic system-on-chip hardware (rush) platform for real-time ultrasonic imaging applications," pp. 463–466, Oct 2012.

[75] P. Brandao, V. Infante, and A. Deus, "Thermo-mechanical modeling of a high pressure turbine blade of an airplane gas turbine engine," *Procedia Struct. Integrity*, vol. 1, pp. 189–196, January 2016.

[76] J. C. Lazaro, "Noise reduction in ultrasonic ndt using discrete wavelet transform processing," in *2002 IEEE Ultrasonics Symposium, 2002. Proceedings.*, vol. 1, Oct 2002, pp. 777–780 vol.1.

[77] Wei, Liang, Huang, Zuo-Ying, and P.-W. Que, "Sparse deconvolution method for improving the time-resolution of ultrasonic nde signals," *Ultrasonics*, vol. 49, no. 8, pp. 752–759, January 2009.

[78] E. Pardo, J. S. Emeterio, M. Rodriguez, and A. Ramos, "Noise reduction in ultrasonic ndt using undecimated wavelet transforms," *Ultrasonics*, vol. 44, pp. e1063–e1067, 2006.

[79] M. A. Rodriguez-Hernandez and J. L. S. Emeterio, "Noise reduction using wavelet cycle spinning: analysis of useful periodicities in the z-transform domain," *Signal, Image and Video Processing*, vol. 10, no. 3, pp. 519–526, Oct 2015.

[80] F. Boßmann, G. Plonka, T. Peter, O. Nemitz, and T. Schmitte, "Sparse deconvolution methods for ultrasonic ndt," *J. Nonde-struct. Eval*, vol. 31, no. 3, pp. 225–244, Sep 2012.

[81] N. Chakroun, M. A. Fink, and F. Wu, "Time reversal processing in ultrasonic nondestructive testing," *IEEE Trans. Ultrason. Ferroelectr. Freq. Control*, vol. 42, no. 6, pp. 1087–1098, Nov 1995.

[82] R. Drai, F. Sellidj, M. Khelil, and A. Benchaala, "Elaboration of some signal processing algorithms in ultrasonic techniques: application to materials ndt," *Ultrasonics*, vol. 38, no. 1-8, pp. 503–507, 2000.

[83] P. Karpur and O. J. Canelones, "Split spectrum processing: a new filtering approach for improved signal-to-noise ratio enhancement of ultrasonic signals," *Ultrasonics*, vol. 30, no. 6, pp. 351–357, 1992.

[84] R. Gongzhang, M. Li, B. Xiao, T. Lardner, and A. Gachagan, "Robust frequency diversity based algorithm for clutter noise reduction of ultrasonic signals using multiple sub-spectrum phase coherence," *AIP Conference Proceedings*, vol. 1581, no. 1, pp. 1948–1955, 2014.

[85] M. Izquierdo, M. Hernandez, O. Graullera, and L. Ullate, "Time frequency wiener filtering for structural noise reduction," *Ultrasonics*, vol. 40, no. 1-8, pp. 259–261, 2002.

[86] M. Rodriguez, J. S. Emeterio, J. Lazaro, and A. Ramos, "Ultrasonic flaw detection in nde of highly scattering materials using wavelet and wigner-ville transform processing," *Ultrasonics*, vol. 42, no. 1-9, pp. 847–851, 2004.

[87] N. Ruiz-Reyes, P. Vera-Candeas, J. Curpian-Alonso, R. Mata-Campos, and J. Cuevas-Martinez, "New matching pursuit-based algorithm for snr improvement in ultrasonic ndt," *NDT Int.*, vol. 38, no. 6, pp. 453–458, 2005.

[88] B. Wu, Y. Huang, and S. Krishnaswamy, "A bayesian approach for sparse flaw detection from noisy signals for ultrasonic ndt," *NDT Int.*, vol. 85, pp. 76–85, 2017.

[89] E. G. Tarpara, V. Patankar, and N. V. Varier, "Design and development of matrix based ultrasonic imaging instrumentation for immersion applications," in *15th Asia Pacific Conference for Non-Destructive Testing (APCNDT-2017)*, 2017.

[90] B. Mirshab, "Analog electronics design to improve performance of ultrasonic gas flow meter," p. ., 2015.

[91] E. Brunner, "Ultrasound system considerations and their impact on front-end components," *Analog Devices*, vol. 36, p. ., 2002.

[92] G. Reig, D. Kass, and T. Nelligan, "Application considerations in specifying high frequency ultrasonic transducers," pp. 25–29, 2006.

[93] A. Ramos, A. Ruíz, J. S. Emeterio, and P. Sanz, "Pspice circuital modelling of ultrasonic imaging transceivers including frequency-dependent acoustic losses and signal distortions in electronic stages," *Ultrasonics*, vol. 44, pp. e995 – e1000, 2006.

[94] J. Johansson, P. e. Martinsson, and J. Delsing, "Simulation of absolute amplitudes of ultrasound signals using equivalent circuits," *IEEE Transactions on Ultrasonics, Ferroelectrics, and Frequency Control*, vol. 54, no. 10, pp. 1977–1983, October 2007.

[95] N. Aouzale, A. Chitnalah, and H. Jakjoud, "Experimental validation of spice modeling diffraction effects in a pulse echo ultrasonic system," *IEEE Transactions on Circuits and Systems II: Express Briefs*, vol. 56, no. 12, pp. 911–915, Dec 2009.

[96] S. Hanane, C. Ahmed, A. Noureddine *et al.*, "P-spice modeling three-dimensional propagation of ultrasound diffraction considering a gaussian beam approach," *Journal of Vibration and Acoustics*, vol. 138, no. 1, p. 011019, 2016.

[97] N. Aouzale, A. Chitnalah, and H. Jakjoud, "Spice modeling nonlinearity effects on ultrasonic waves," *Journal of Vibration and Acoustics*, vol. 134, no. 5, p. 051003, 2012.

[98] N. Aouzale, A. Chitnalah, H. Jakjoud, and D. Kourtiche, "Pspice modelling of an ultrasonic setup for materials characterization," *Ferroelectrics*, vol. 372, no. 1, pp. 107–114, 2008.

[99] M. Nadi, R. Guelaz, D. Kourtiche, and P. Roth, "Double element ultrasonic piezoceramic transducer modeling with VHDL-AMS: application to B/A nonlinear ultrasonic parameter measurement in pulse-echo mode," *Technical Acoustics*, vol. 10, pp. ISSN 1819–2408, Apr. 2005, electronic journal, http://www.ejta.org.

[100] W. H. Hayt and J. A. Buck, *Engineering electromagnetics.* McGraw-Hill New York, 1981, vol. 6.

[101] G. S. Kino, *Acoustic waves: devices, imaging and analog signal processing*, 1987, no. 43 KIN.

[102] M. Kaufman and A. H. Seidman, *Handbook of electronics calculations for engineers and technicians.* McGraw-Hill Companies, 1988.

[103] K. Czuba and D. Sikora, "Temperature stability of coaxial cables," *Acta Phys. Pol. A*, vol. 119, no. EuCARD-PUB-2011-001, p. 553, 2011.

[104] R. Challis, A. Holmes, J. Harrison, and R. Cocker, "Digital signal processing applied to ultrasonic absorption measurements," *Ultrasonics*, vol. 28, no. 1, pp. 5 – 15, 1990.

[105] K. Scott, J.-Y. Kim, and L. J. Jacobs, "Signal processing methods for second harmonic generation in thin specimens," *NDT & E International*, vol. 95, pp. 57 – 64, 2018.

[106] R. E. Challis and R. I. Kitney, "Biomedical signal processing (in four parts)," *Medical and Biological Engineering and Computing*, vol. 28, no. 6, pp. 509–524, Nov 1990.

[107] R. Challis, T. Alper, R. Cocker, A. Holmes, and J. White, "Ultrasonic absorption and velocity dispersion measurements in thin adhesive layers," *Ultrasonics*, vol. 29, no. 1, pp. 22 – 28, 1991.

[108] A. N. Kalashnikov, R. E. Challis, M. E. Unwin, and A. K. Holmes, "Effects of frame jitter in data acquisition systems," *IEEE Transactions on Instrumentation and Measurement*, vol. 54, no. 6, pp. 2177–2183, Dec 2005.

[109] O. Rompelman and H. Ros, "Coherent averaging technique: A tutorial review part 1: Noise reduction and the equivalent filter," *Journal of Biomedical Engineering*, vol. 8, no. 1, pp. 24 – 29, 1986.

[110] O. Rompelmen and H. Ros, "Coherent averaging technique: A tutorial review part 2: Trigger jitter, overlapping responses and non-periodic stimulation," *Journal of Biomedical Engineering*, vol. 8, no. 1, pp. 30 – 35, 1986.

[111] J. Soto-Cajiga, J. Pedraza-Ortega, C. Rubio-Gonzalez, M. Bandala-Sanchez, and R. de J. Romero-Troncoso, "Fpga-based architecture for real-time data reduction of ultrasound signals," *Ultrasonics*, vol. 52, no. 2, pp. 230 – 237, 2012.

[112] S. Kumar and H. Furuhashi, "Characteristics of an ultrasonic phased array transmitter in medium range," *Ultrasonics*, vol. 82, pp. 331 – 335, 2018.

[113] P. Behrooz, "Computer arithmetic: Algorithms and hardware designs," *Oxford University Press*, vol. 19, pp. 512 583–512 585, 2000.

[114] N. E. Huang, Z. Shen, S. R. Long, M. C. Wu, H. H. Shih, Q. Zheng, N.-C. Yen, C. C. Tung, and H. H. Liu, "The empirical mode decomposition and the hilbert spectrum for nonlinear and non-stationary time series analysis," *Proc. R. Soc. Lond. A, Math. Phys. Eng. Sci.*, vol. 454, no. 1971, pp. 903–995, 1998.

[115] Y. Y. Hong and Y. Q. Bao, "Fpga implementation for real-time empirical mode decomposition," *IEEE Trans. Instrum. Meas.*, vol. 61, no. 12, pp. 3175–3184, Dec 2012.

[116] L. Wang, M. I. Vai, P. U. Mak, and C. I. Ieong, "Hardware-accelerated implementation of emd," in *in Proc. 3rd Int. Conf. Biomed. Eng. Informat.*, vol. 2, Oct 2010, pp. 912–915.

[117] M. H. Lee, K. K. Shyu, P. L. Lee, C. M. Huang, and Y. J. Chiu, "Hardware implementation of emd using dsp and fpga for online signal processing," *IEEE Trans. Ind. Electron.*, vol. 58, no. 6, pp. 2473–2481, June 2011.

[118] S. Cagdas and A. Celebi, "Fpga implementation of cubic spline interpolation method for empirical mode decomposition," in *Proc. IEEE Signal Process. Commun. Appl. Conf.*, April 2012, pp. 1–4.

[119] S. Shukla, S. Mishra, B. Singh, and S. Kumar, "Implementation of empirical mode decomposition based algorithm for shunt active filter," *IEEE Trans. on Ind. Appl.*, vol. 53, no. 3, pp. 2392–2400, May 2017.

[120] T.-L. Chen, P.-W. Que, Q. Zhang, and Q.-K. Liu, "Ultrasonic signal identification by empirical mode decomposition and hilbert transform," *Rev. Sci. Instrum.*, vol. 76, no. 8, p. 085109, 2005.

[121] Y. Mao and P. Que, "Noise suppression and flaw detection of ultrasonic signals via empirical mode decomposition," *Russian Journal of Nondestructive Testing*, vol. 43, no. 3, pp. 196–203, 2007.

[122] A. O. Boudraa and J. C. Cexus, "Emd-based signal filtering," *IEEE Trans. Instrum. Meas.*, vol. 56, no. 6, pp. 2196–2202, Dec 2007.

[123] M. Hjorth-Jensen, *Computational Physics*, University of Oslo, 2015. [Online]. Available: http://www.cec.uchile.cl/cinetica/pcordero/MC_libros/Hjorth-Jensen2008.pdf

[124] L. Thomas, *Elliptic problems in linear differential equations over a network*, 1949.

[125] P. Flandrin, G. Rilling, and P. Goncalves, "Empirical mode decomposition as a filter bank," *Signal Process. Lett.*, vol. 11, no. 2, pp. 112–114, Feb 2004.

[126] N. E. Huang, M.-L. C. Wu, S. R. Long, S. S. Shen, W. Qu, P. Gloersen, and K. L. Fan, "A confidence limit for the empirical mode decomposition and hilbert spectral analysis," *Proc. Royal. Soc. London. A*, vol. 459, no. 2037, pp. 2317–2345, 2003.

[127] Z. Wu and N. E. Huang, "A study of the characteristics of white noise using the empirical mode decomposition method," *Proc. R. Soc. London A*, vol. 460, no. 2046, pp. 1597–1611, 2004.

[128] Y.-H. Wang, C.-H. Yeh, H.-W. V. Young, K. Hu, and M.-T. Lo, "On the computational complexity of the empirical mode decomposition algorithm," *Phys. A Statist. Mech. Appl.*, vol. 400, pp. 159–167, 2014.

[129] Z. WU and N. E. HUANG, "Ensemble empirical mode decomposition: A noise-assisted data analysis method," *Adv. Adapt. Data Anal.*, vol. 01, no. 01, pp. 1–41, 2009.

[130] Z. Wu and N. E. Huang, "On the filtering properties of the empirical mode decomposition," *Adv. Adapt. Data Anal.*, vol. 02, no. 04, pp. 397–414, 2010.

[131] C. J.-H. Y. Benesty, J. and I. Cohen, *Noise reduction in speech processing*, 2009.

[132] P. Y. Chen, Y. C. Lai, and J. Y. Zheng, "Hardware design and implementation for empirical mode decomposition," *IEEE Trans. Ind. Electron.*, vol. 63, no. 6, pp. 3686–3694, June 2016.

[133] S. Langener, M. Vogt, H. Ermert, and T. Musch, "A real-time ultrasound process tomography system using a reflection-mode reconstruction technique," *Flow Measurement and Instrumentation*, vol. 53, pp. 107 – 115, 2017, process Tomography.

[134] L. Zhang, "A multichannel data acquisition system design for guided waves ultrasound testing," in *2014 IEEE Far East Forum on Nondestructive Evaluation/Testing*, June 2014, pp. 93–97.

[135] A. A. Assef, J. M. Maia, and E. T. Costa, "Initial experiments of a 128-channel fpga and pc-based ultrasound imaging system for teaching and research activities," in *2016 38th Annual International Conference of the IEEE Engineering in Medicine and Biology Society (EMBC)*, Aug 2016, pp. 5172–5175.

[136] I. Bolotina, A. Bulavinov, R. Pinchuk, and Y. Salchak, "Principles of construction of ultrasonic tomographs for solution of problems of nondestructive testing in mechanical engineering," *IOP Conference Series: Materials Science and Engineering*, vol. 124, no. 1, p. 012149, 2016.

[137] C. Risser, H. J. Welsch, H. Fonfara, W. Bost, S. Weber, H. Hewener, and S. Tretbar, "Very high frequency ultrasound beamformer for biomedical applications and non-destructive testing," in *2015 IEEE International Ultrasonics Symposium (IUS)*, Oct 2015, pp. 1–4.

[138] C. Fritsch, A. Ibanez, and M. Parrilla, "A digital envelope detection filter for real-time operation," *IEEE Transactions on Instrumentation and Measurement*, vol. 48, no. 6, pp. 1287–1293, Dec 1999.

[139] W. R. Davis, "Method for acoustic imaging of a tubular shape," Nov. 25 2003, uS Patent 6,651,502.

[140] D. E. Chimenti and A. H. Nayfeh, "Ultrasonic reflection and wave propagation in multilayered composite plates," in *Review of Progress in Quantitative Nondestructive Evaluation.* Springer, 1989, pp. 221–228.

[141] R. D. Fay and O. V. Fortier, "Transmission of sound through steel plates immersed in water," *The Journal of the Acoustical Society of America*, vol. 23, no. 3, pp. 339–346, 1951.

[142] T. J. Plona, L. E. Pitts, and W. G. Mayer, "Ultrasonic bounded beam reflection and transmission effects at a liquid/solid-plate/liquid interface," *The Journal of the Acoustical Society of America*, vol. 59, no. 6, pp. 1324–1328, 1976.

[143] G. Barnard, J. Bardin, and J. Whiteley, "Acoustic reflection and transmission characteristics for thin plates," *The Journal of the Acoustical Society of America*, vol. 57, no. 3, pp. 577–584, 1975.

[144] M. Osborne and S. Hart, "Transmission, reflection, and guiding of an exponential pulse by a steel plate in water. i. theory," *The Journal of the Acoustical Society of America*, vol. 17, no. 1, pp. 1–18, 1945.

[145] R. Fay, "Notes on the transmission of sound through plates," *The Journal of the Acoustical Society of America*, vol. 25, no. 2, pp. 220–223, 1953.

[146] L. Brekhovskikh, *Waves in layered media.* Elsevier, 2012, vol. 16.